Non-linear analysis of steel-concrete hybrid members with application to stability design

Pisey Keo

Thèse

THESE INSA Rennes
sous le sceau de l'Université européenne de Bretagne
pour obtenir le titre de
DOCTEUR DE L'INSA DE RENNES
Spécialité : Génie Civil (Mécanique des Structures)

présentée par
Pisey KEO
ECOLE DOCTORALE : *SDLM*
LABORATOIRE : *LGCGM*

Nonlinear Analysis of Steel-Concrete Hybrid Members with Application to Stability Design

Thèse soutenue le 27.11.2015
devant le jury composé de :

Ali LIMAM
Professeur, INSA de Lyon (France) / Président
Vincent DENOËL
Professeur, Université de Liège (Belgique) / Rapporteur
Enzo MARTINELLI
Professeur, University of Salerno (Italie) / Rapporteur
Luis COSTA NEVES
Professeur, Universidade de Coimbra (Portugal) / Examinateur
Philippe LE GROGNEC
Maître de Conférences (HDR), Ecole des Mines de Douai (France) / Examinateur
Quang-Huy NGUYEN
Maître de Conférences, INSA de Rennes (France) / Co-encadrant
Hugues SOMJA
Maître de Conférences, INSA de Rennes (France) / Co-encadrant
Mohammed HJIAJ
Professeur, INSA de Rennes (France) / Directeur de thèse

Nonlinear Anlysis of Steel-Concrete Hybrid Members with Application to Stability Design

Pisey KEO

Abstract

***

This thesis aims at developing simulation tools and a design method for hybrid beam-columns subjected to combined axial force, bending and shear. The thesis is divided in four main parts and comprises 6 chapters. In the first part, we develop a new finite element formulation based on the exact stiffness matrix for the linear elastic analysis of hybrid beam-columns in partial interaction taking into account the shear deformability of the encasing component. This element relies on the analytical solution of a set of coupled system of differential equations in which the primary variables are the slips and the shear deformation of the encasing beam. The latter is derived by combining the governing equations (equilibrium, kinematics, constitutive laws) and solved for a specific element with arbitrary boundary conditions and loading. Special care has been taken while dealing with the constants of integration. The second part of the thesis addresses a new finite element formulation for a large displacement analysis of elastic hybrid beam-columns taking into account the slips that occur at each steel-concrete interface. The co-rotational method is adopted in which the movement of the element is divided into a rigid body motion and a deformable portion in the local co-rotational frame which moves and rotates continuously with the element but does not deform with it. Appropriate selection of local kinematic variables along with corresponding transformation matrices allows transforming the linear finite element developed in Part 1 into a nonlinear one resulting in an efficient locking-free formulation. In Part 3, we derive a finite element formulation for materially nonlinear analysis of hybrid beam-columns with shear deformable en-

casing component, in partial interaction and subjected to the combined shear and bending. The fiber model is adopted with condensation of the 3D stress-strain relations which allow to account for confinement in a rigorous manner as well as the effect of the stirrups. Part 4 examines the adequacy of the moment magnification method given in Eurocode 2 and 4 to provide an accurate estimation of the ultimate load of hybrid columns subjected to a combination of axial load and uniaxial bending moment. The developed finite element model with a shear rigid encasing component is used to conduct a parametric study comprising 1140 cases to cover the various possible situations. The predictions of the model are compared against the values given by the simplified methods of Eurocode 2 and Eurocode 4. It is shown that these simplified methods does not give satisfactorily results. Based on the analysis of larger number of cases (2960 configurations), the moment magnification method has been calibrated for hybrid columns.

Keywords: hybrid steel-concrete columns, partial interaction, concrete confinement, co-rotational, interaction M-N, instability, moment magnification method.

Résumé

***

Le travail de cette thèse a pour but de développer des outils de simulation et une méthode de dimensionnement pour les poteaux hybrides soumis à des chargements combinés. La thèse est composée de 4 parties essentielles et comprend 6 chapitres. Dans la première partie, nous développons un élément fini poutre/poteau hybride élastique en interaction partielle avec matrice de raideur exacte. Cet élément fini découle de la solution analytique du système d'équations différentielles couplées obtenues en combinant les équations de champs (équilibre, cinématique et comportement). Les inconnues fondamentales sont les glissements aux interfaces et la déformation de cisaillement de l'élément principal. Ces équations sont résolues pour des conditions de chargement et des conditions aux limites arbitraires en accordant un soin particulier à la détermination des constantes d'intégration. Dans la seconde partie de cette thèse, nous proposons une formulation d'élément fini originale pour l'analyse en grand déplacement des poutres hybrides avec prise en compte des glissements qui se produisent à chaque interface acier-béton. La méthode co-rotationnelle est retenue. Dans cette approche, le mouvement de l'élément se décompose en un mouvement de corps rigide et en une partie déformable définie dans un repère co-rotationnel local qui se déplace de manière continue avec l'élément mais qui ne se déforme pas avec ce dernier. Un choix judicieux des variables cinématiques locales accompagné des matrices de transformation correspondantes permet de transposer l'élément linéaire développé en partie 1 en un élément géométriquement non-linéaire performant. La partie 3 est consacrée à l'analyse non linéaire matérielle par élément finis de poutres hy-

brides en interaction partielle et soumise aux forces combinées de flexion et de cisaillement. Dans la formulation élément fini proposée, nous adoptons la discrétisation par fibres et une modèle 3D de comportement du béton avec prise en compte des états plans ce qui permet de reproduire rigoureusement l'effet du confinement et l'action des étriers. En partie 4, nous évaluons la pertinence de la méthode d'amplification des moments proposées dans l'Eurocode 2 et 4 à évaluer la charge ultime de poteaux hybrides soumis à une combinaison de charge axiale et de moment de flexion uni-axial. Dans un premier temps, nous conduisons une étude paramétrique sur 1140 cas différents de poteaux hybrides; étude destinés à couvrir les différentes typologies possibles, afin de disposer d'une base de résultats permettant d'évaluer la pertinence des méthodes simplifiées de l'Eurocode 2 et de l'Eurocode 4 pour de tels éléments. Cette étude a été réalisée à l'aide d'un élément fini non-linéaire (géométrique et matériel), avec une hypothèse de Bernouilli pour tous les composants du poteau hybride. Il ressort de cette étude que ces méthodes simplifiées ne peuvent être appliquées aux poteaux hybrides. Sur base de l'analyse d'un nombre de cas plus important (2960 configurations), la méthode d'amplification des moments est calibrée pour les poteaux hybrides.

Mots clés : Poteaux hybrides acier-béton, interaction partielle, confinement du béton, co-rotationnel, interaction M-N, instabilité, méthode d'amplificatin des moments.

Acknowledgements

***

This thesis would not have been possible without the unconditional love and support of my parents, S. Navy Keo and Sokunmony Heng, my sisters, Kagna and Molika and undoubtedly with the encouragement of my beloved fiancee, Keosopanha. To them, I want to express all my love and my gratitude since all I am is because of them.

The completion of this research was made possible with the guidance, continuous support and endless patience of my supervisor, Professor Mohammed Hjiaj. I have felt privileged to work under his supervision and be extensively enjoyed working with and meeting him on a regular basis as well as a late hour of the day in the last three years. During this three-year period, he made a best conditions to make a possible achievement of this work and offered me to participate actively to European projects and actions. I also would like to express my sincere gratitude to my co-supervisors Dr. Hugues Somja and Dr. Quang-Huy Nguyen for the encouragements, discussions we had and their revisions of my thesis.

I would like to thank to my friends and colleagues for their friendship and unconditional support during my stay in France. Furthermore, special thank to Khmer Association, Solidarité Bretagne Cambodge, for providing me a sense of being home during my stay in Rennes.

This thesis was carried out with the financial support of French Government

scholarships and the European Commission (Research Fund for Coal and Steel) through the project SMARTCoCo (SMART COmposite COmponents: concrete structures reinforced by steel profiles) under grant agreement RFSR-CT-2012-00039.

Contents

***

List of Figures

***

List of Tables

***

Chapter 1

Introduction

***

A short overview of the high-rise building history and its construction and design alternative. The objective and the organization of the thesis.

1.1 High-rise building

High-rise buildings have long played a role in the perception of modern urbanized cities. The courage of building high is like to build the transcontinental railroad, discover the North Pole, scale Everest, or land on the moon which struggles to not only deepen the understanding but also to show the national and/or economic pride. The construction of high rise buildings is also influenced by ambition, ego, and other non-economic factors [1]. Constructing high-rise building remarkably boosts the research development. Throughout subsequent history there have been some tall structures like pyramids, towers, castle and cathedrals, but it was not until the middle of the nineteenth century that the skyscraper was born [2]. It is well known that modern high-rise buildings were originally invented in Chicago in 1885 with only 10 storeys, 55 meters high. It was regarded as the first high-rise

building in the world. Hereafter, with the development of economy and technology, many aspects of high-rise building have been improved. Those improvements include building height, style, architectural function, structural system and landscape art. As a result, the number of various high-rise buildings are growing rapidly around the world because of the great achievements in the construction economy and the science and technology.

1.2 Construction and design

The construction industry has a history of constant innovation as engineers and researchers strive to increase the safety, economy, and performance of our built environment. Engineers soon realized that combining different materials and/or methods of construction could produce a structure with enhanced strength, stiffness, ductility and fire protection. Over the past several decades, composite steel-concrete structural systems have gained popularity among the designers. The driving force behind employing composite steel-concrete systems is to combine the best attributes of steel and concrete to improve structural performance, erection time, economy of construction and occupant satisfaction in a way that might not be possible using only one of the materials and its associated construction techniques. On the one hand, reinforced concrete is inexpensive, massive and stiff with a fairly good ability to resist compressive actions in spite of its poor behavior in tension. On the other hand, steel members are lightweight, easy to assemble, strong under tensile forces and endowed with a long-span capability; but they have a low buckling and fire resistance. The most common examples of steel-concrete composite members are composite floor systems, composite beams and composite columns.

Composite steel-concrete constructions, as briefly described above, are just a part of a wider array of construction types involving concrete and steel. Over nearly a century, Steel Reinforced Construction (SRC) consisting of steel structural framing partially or totally encased in concrete has been adopted by engineers. Indeed,

the practice of encasing structural steel shapes in reinforced concrete columns or filling a tubular section of hot-rolled steel with concrete is common, mainly in the USA and Japan and dates back to the beginning of the 20th century. Various types of steel cross-section have been used such as H-shaped, I-shaped and a combination of angle and flat bars. The advantages of SRC over RC construction are: greater ductility, more compact cross-section, reduced creep deformation, and faster concrete casting [3]. Those over Steel construction are: multiple roles of concrete as structural, fireproofing and buckling-restraining elements, higher stiffness, and greater damping. Modern SRC members (hybrid members) commonly have extensive transverse and longitudinal reinforcement, and some use shear connectors between steel section and the surrounding concrete [4]. A wide

Figure 1.1: Structural arrangement of the IFC2 at Hong Kong.

variety of hybrid/mixed construction can be found in actual high-rise buildings such as structural systems involving steel framing partially or totally encased in concrete with reinforced concrete core or shear walls, for example the Interna-

tional Financial Center Tower 2 at Hong Kong (see Fig. 1.1 and Fig. 1.2 by Wong [5]). In mixed structural systems, the reinforced concrete core wall provides the

Figure 1.2: Composite columns encased with load-taking reinforced concrete, IFC2.

strength and stiffness for resisting lateral loads, while the steel frame is designed to resist gravity loads and provide the necessary ductility to absorb seismic energies. For buildings containing only concrete core wall to withstand the effects of the lateral load, the weight of the building would be heavy. In order to decrease the heavy weight of the building, the majority of that diminution has to be found in a reduction of the thickness of the concrete shear walls. This reduction could be achieved only by decreasing the wind-and earthquake-induced lateral forces resisted by those walls. As a result, to minimize the magnitude of the resultant lateral force acting on the core walls, the stiffness of the steel perimeter frame has to be increased so that it can absorb more loads. To combine the structural system of the core walls and perimeter frame, outriggers are introduced for high-rise building. The outriggers (belt trusses) are rigid horizontal structures connecting the building core to the perimeter columns. By making use of outrigger trusses

coupled to the columns of the mega-structure, an additional reduction would be realized. The lateral load transfer can be explained as follows. When the shear core tries to bend, the belt trusses act as lever arms that directly transfer axial stresses into the perimeter columns. The columns, in turn, act as struts to resist the lateral deflection of the core. This means that the core can fully develop the horizontal shear and then the belt trusses transfer the vertical shear from the core to the outrigger frame. Thus, the building is made to act as a unit that is very similar to a cantilever tube. These conceptual changes made possible the ability to design an efficient and economical structural system. However, it is worth mentioning that the core walls with reduced thickness as well as the perimeter columns may suffer the concentrated stresses and require well-detailed concentrated reinforcement to develop the necessary stiffness and/or buckling resistance. This often results in congestion in these heavily reinforced members, resulting in a laborious construction. To achieve strength and stiffness whilst restricting the size of the wall or column, the use of high strength construction materials is an option. In fact, increased demand on stiffness and strength dictates that the modulus of elasticity of the material should be as high as possible in order to limit small amplitude elastic displacements. Moreover, the need for rapid construction requires early age strength gain, a feature that may be offered readily by high strength concrete. On the other hand, the use of high strength reinforcing bars in structural members has several practical advantages, including reduction of congestion in heavily reinforced members, improved concrete placement, and savings in the cost of labor, reduction of construction time and, in some cases, enhanced resistance to corrosion [6]. The earthquake forces being directly proportional to the weight of the structure, the use of high strength concrete will produce lower seismic loads. The main disadvantage is the material cost and in some situations (very heavily loaded structures) it is no longer an effective solution and other alternatives must be found.

To overcome this issue, composite steel-concrete shear walls (CSW) where the steel sections serve as longitudinal reinforcement bars are used in replacement

of standard reinforced concrete walls. It was found that CSW can mitigate the disadvantages of RC and take advantage of the best properties of steel can offer [7]. Dan et al. [8] described the theoretical study and the experimental tests on CSW with several encased steel profiles and came to the following conclusions: composite steel-concrete shear walls have an important plastic resistance to compression, combined compression and bending and shear resistance; the amount of steel in composite wall cross-sections influences the value of ultimate shear force; the deformation ductility is similar for CSW with the same amount of the steel sections. For the same heavily loaded situation, the use of Steel Reinforced Concrete columns with multiple steel shapes seems to be a viable alternative considering the flexibility that one has in designing such members.

It must be stressed that significant variations in the behavior of composite members may be observed according to the range of relative proportions of steel and reinforced concrete. Some composite members are concrete-dominant and will more likely behave as a reinforced concrete member where steel sections act as reinforcement while others are steel-dominant and will more likely behave as structural steel members with concrete being placed in compressive zone to increase strength and stiffness, local stability or just used as fireproofing means.

The overall behavior of such member strongly depends on the stress transfer mechanisms between the steel and the concrete encasement, which may be accomplished by either bond, friction, shear connectors or plate bearings. Many factors influence the bond strength. In general, the latter reaches its capacity when the chemical adherence between the steel and the surrounding concrete is broken. It was observed that the amount of confining reinforcement affects the bond stress capacity only after significant slip has taken place [9, 10]. In most composite construction designs, the longitudinal shear strength at steel-concrete interface provided by bond and/or friction is mostly ignored. Thus, the force transfer from steel to concrete (or reverse) in SRC members is assumed to depend on mechanical transfer devices. Flexible shear studs are the most common

devices used to connect concrete to steel members but in some situations other types of shear connectors can be used. Rigid shear connectors develop full composite action between the components. Consequently, conventional principles of analysis of composite members can be employed. In most cases, connectors are flexible and relative displacements may occur at the interface of the two materials, resulting a so-called partial interaction.

Although a number of researches have focused on various aspects of hybrid structures, no design guidance exists for concrete structures reinforced locally by steel profiles or sections reinforced by several steel profiles. Gaps in knowledge are mostly related to the problem of force transfer between concrete and embedded steel profiles, a situation in which it is neither known how to combine the resistances provided by bond, by stud connectors and by plate bearings, nor how to reinforce the transition zones between classical reinforced concrete and concrete reinforced by steel profiles. Other elements of the same type exist:

- Connections of flat slabs to columns by shear keys comprised of metal profiles;

- Steel elements embedded in concrete in general, and particularly steel reinforcement around openings in the central cores, reinforcements of concrete columns with a steel profile on one level, reinforcements in walls in areas of discontinuity, and others.

To address these aspects, a research project called SMARTCoCo was mounted at European level bringing together the University of Liège, Imperial College London, INSA Rennes, ArcelorMittal and a Belgian company named BESIX. It aims to establish a design guide of hybrid elements. To do so, experimental tests and refined simulations have been conducted.

1.3 Objective and organization of the thesis

The main goal of this thesis is to develop simulation tools for concrete beam-columns reinforced by several embedded steel sections, so-called hybrid beam-columns. One of its main objectives is a part of the European project SMART-CoCo which is to formulate a design method for hybrid columns with more than one encased steel profile subjected to combined compression and bending. Those hybrid columns are neither RC columns in the sense of EN 1992-1-1 [11], nor composite columns in the sense of EN 1994-1-1 [12] where the design rules are provided only for a single encased steel profile. It is legitimate to raise the following question: can we use design rules given in Eurocode 2 or Eurocode 4 to design such columns? To answer this question, the present research work is carried out and reported in this thesis.

A brief description of the thesis layout is given in the following to provide a brief overview of what will be discussed. Chapter 2 presents an analytical solution and a new FE formulation for the analysis of hybrid beam-columns in partial interaction based on the exact stiffness matrix derived from the governing equations of the problems. The exact solution is based on solving the coupled system of differential equations where the slips and the shear deformation of the concrete component are considered as primary variables. This exact stiffness matrix can be used in a displacement-based procedure for the elastic analysis of hybrid beam-columns in partial interaction with arbitrary loading and support conditions. To illustrate the effects of shear deformability of the concrete component, the analyses based on both shear-rigid and shear-flexible models for the concrete component are carried out. Chapter 3 highlights a new FE formulation for a large displacement analysis of hybrid planar beam-columns taking into account the slips occurring at each steel-concrete interface. The co-rotational framework is adopted and the motion of the element is decomposed into a rigid body motion and a deformation part using a local co-rotational frame, which continuously translates and rotates with the element but does not deform with it. The analysis

of the performance and the accuracy of the new formulation is carried out considering several meaningful examples calculated in an elastic range. The constitutive modeling and time integration of the steel and concrete material as well as the shear connection are presented in Chapter 4. Chapter 5 outlines a nonlinear FE formulation for an analysis of hybrid planar beam-columns in partial interaction subjected to combined bending moment and shear force, based on a fiber model considering the triaxial stress state in the concrete component. The plane stress condition for the concrete component is enforced in order to condense the 3d formulation, derived from a 3d plastic model of the concrete material, into a 2d beam model. To assess the capability of the proposed formulation in reproducing the nonlinear behavior of hybrid beams subjected to combined loads, the experimental tests on the hybrid beams under 3-point flexural bending, conducted at Laboratory of Civil and Mechanical Engineering of INSA Rennes are selected to be compared against the results of the proposed model. Chapter 6 deals with numerical investigations on second-order effects in slender hybrid columns subjected to combined axial load and uniaxial bending moment about its strong axis. The first objective of this latter chapter is to point out that a straightforward application of the bending moment magnification method proposed in Eurocode 2 and Eurocode 4 to hybrid columns may lead to unsafe results. To remain consistent with the Eurocodes, a new version of bending moment magnification method for slender hybrid columns is proposed. To do so, the results of FE model will serve as references for a parametric study (1140 data sets) in which the simplified methods proposed in EC2 and EC4 are evaluated in case of hybrid columns. Based on an extended parametric study with 2960 data sets, new expressions for the moment magnification and the equivalent moment factor are proposed. The outcomes of this chapter has been contributed and published in the international scientific journal [13].

Chapter 2

Geometrically Linear Elastic Behavior

***

Analysis of partially connected hybrid beams with several embedded steel sections. Derivation of the exact stiffness matrix.

2.1 Introduction

The analysis of members consisting of semi-rigidly connected layers is complicated due to the partial transfer of shear force at the interface. Over the years, there has been a great deal of research conducted on the subject of elastic two-layered composite beams in partial interaction. The first contribution is commonly attributed to Newmark et al. [14] who investigated the behavior of a two-layered beam considering that both layers are elastic and deform according to Euler-Bernoulli kinematics. In their paper, a closed-form solution is provided for a simply supported elastic composite beam. Since then, numerous analytical models were developed to study different aspects of the composite behavior of

two-layered composite beams under more complicated situations. Several analytical formulations to investigate the behavior of elastic two-layered beams were proposed [15–23]. Significant development beyond that available from Newmark et al.'s paper [14] has been made in [22] by considering Timoshenko's kinematic assumptions for both layers. Beside these analytical works, several numerical models, mostly FE formulations have been developed to investigate the nonlinear behavior of both Bernoulli and Timoshenko two-layered beams with interlayer slip [24–35]. Most of the papers on layered beams in partial interaction are restricted to the case of two-layered beams, and multi-layered beams as well as hybrid beams reinforced by several embedded sections have received less attention. Chui and Barclay [36] and Schnabl et al. [37] proposed an exact analytical model for the case of three-layered beam where the thickness as well as the material of the individual layers are arbitrary. Sousa et al. [38] developed an analytical solution for statically determinate multi-layered beams with the assumption that the cross-section rotation is the same even if the shear-flexible components with different shear modulus are considered. The governing equations describing the behavior of such multi-layered beams consist of a coupled system of differential equations in which the slips are considered as the primary variables. Skec et al. [39] proposed mathematical models with analytical solutions for the analysis of linear elastic Reissner multi-layered beams. The models take into account the interlayer slip and the uplift of the adjacent layers, different material properties, independent transverse shear deformations, and different boundary conditions for each layer. Ranzi [40] proposed two types of displacement-based elements to analyse locking problems of multi-layered beams in partial interaction based on Euler-Bernoulli kinematics. For classical polynomial shape functions, it is shown that the element with internal node well characterizes the partial interaction behavior of multi-layered beams, while the element without internal node suffers from the curvature locking problems.

A formulation based on the exact stiffness matrix offers the possibility of generating a locking-free model. These elements are highly attractive due to their pre-

cision, computational efficiency and mesh independency. Heinisuo [41] proposed a finite element formulation using exact stiffness matrix for uniform, straight, linearly elastic beams with two faces and one core and with three symmetric faces and two identical cores. Sousa [42] developed the analytical formulation and derived the exact stiffness for partially connected multi-layered beams with the assumption that both the transverse displacement and cross-section rotation are the same for all layers. The model is based on the derivation of a flexibility matrix obtained from a statically determinate system.

The purpose of this chapter is to present an analytical solution and a new exact FE formulation for the analysis of shear-rigid (Euler-Bernoulli beam for all constituents) and shear-deformable (Euler-Bernoulli beam for embedded steel element and Timoshenko beam for encasing concrete component) hybrid beam-column in partial interaction based on the exact stiffness matrix derived from the governing equations of the problem. Due to the fact that the development of the analytical solution for shear-rigid hybrid beam-columns is a particular case of the shear-deformable one, in the following we present only the development of the analytical solution for shear-deformable hybrid beam-columns. The one for shear-rigid hybrid beam-columns can be found in detail in Appendix A. The features of the formulation presented in this chapter are as follows: (i) longitudinal partial interactions between the components are considered which provide a general description of the stresses and strains in the components; (ii) shear deformation of encasing concrete is considered for the shear-deformable hybrid beam model; (iii) exact stiffness matrix is used which provides accurate and stable results. The present models provide, therefore, an efficient tool for linear elastic analysis of shear-rigid and shear-deformable hybrid beam-columns with arbitrary supports and loading conditions.

The rest of the chapter is organized as follows. Section 2.2 deals with the field equations containing the kinematic relations and the equilibrium equations of the problems. In Section 2.3, the derivation of the governing equation is presented,

followed by the closed-form solution in Section 2.4 and the derivation of exact stiffness matrix in Section 2.5. Numerical examples are presented in Section 2.6 in order to assess the performance of the formulation and to support the conclusions drawn in Section 2.7.

2.2 Fundamental equations

The field equations describing the behavior of a linear elastic hybrid beam-column with "n" embedded steel sections in partial interaction are briefly outlined in this Section. All variables subscripted with "c" belong to the encasing concrete and those with subscript "s" belong to the embedded steel section. Quantities with subscript "sc" are associated with the shear connection. The following assumptions are commonly accepted in the models to be discussed in this work:

- connected components are made out of elastic, homogenous and isotropic materials;

- the cross-sections of all embedded sections remain plane and orthogonal to beam axis after deformation (Euler-Bernoulli);

- for the shear-deformable model, the cross-section of encasing concrete remains plane and not necessarily orthogonal to beam axis after deformation (Timoshenko);

- relative slip can develop along the interface between concrete component and embedded steel section and is considered at the centroid of the embedded cross-section;

- the lateral deflection v is assumed to be the same for all components (no uplift); and

- discretely located shear connectors are regarded as continuous.

2.2.1 Equilibrium

The equilibrium equations are derived by considering the free body diagram of a differential element dx located at an arbitrary position x in the hybrid beam-column, see Fig. 2.1. The interface connection between the embedded sections

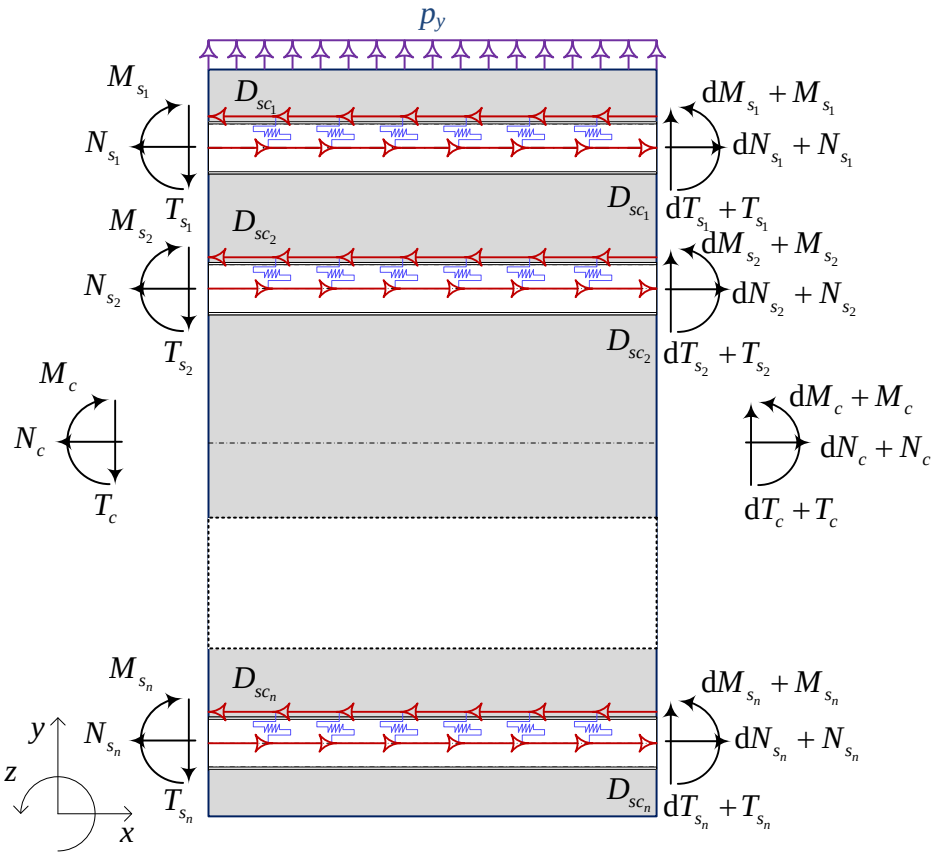

Figure 2.1: Equilibrium of a hybrid beam-column.

and the concrete component is modeled by continuously distributed spring. The

equilibrium conditions result in the following set of equations:

$$\partial N_{s_i} + D_{sc_i} = 0, \qquad i = 1, 2, \cdots n \tag{2.1}$$

$$\partial N_c - \sum_{j=1}^{n} D_{sc_j} = 0 \tag{2.2}$$

$$\partial M_c + T_c + \sum_{j=1}^{n} h_j D_{sc_j} = 0 \tag{2.3}$$

$$\partial M_{s_i} + T_{s_i} = 0, \qquad i = 1, 2, \cdots n \tag{2.4}$$

$$\partial T_c + \sum_{j=1}^{n} \partial T_{s_j} + p_y = 0 \tag{2.5}$$

where

- $\partial \bullet = \mathrm{d} \bullet / \mathrm{d}x$;
- N_{s_i}: normal force acting on the embedded section "i";
- N_c: normal force acting on the concrete beam;
- M_{s_i}: bending moments acting on the embedded section "i";
- M_c: bending moment acting on the concrete beam;
- T_c: shear force acting on the concrete beam;
- T_{s_i}: shear force acting on the embedded section "i";
- D_{sc_i}: interface shear stress at centroid of the embedded section "i"; and
- $h_i = y_{s_i} - y_c$ $(i = 1, 2, \cdots n)$: the distance between the centroid of the embedded section "i" and the concrete beam, see Fig. 2.2.

Combining Eqs. (2.3-2.5), one can rewrite the equilibrium equations as:

$$\partial N_{s_i} + D_{sc_i} = 0, \qquad i = 1, 2, \cdots n \tag{2.6}$$

$$\partial N_c - \sum_{j=1}^{n} D_{sc_j} = 0 \tag{2.7}$$

$$\partial M_c + \partial M_s + T + \sum_{j=1}^{n} h_j D_{sc_j} = 0 \tag{2.8}$$

$$\partial T + p_y = 0 \tag{2.9}$$

where

$$M_s = \sum_{j=1}^{n} M_{s_j} \tag{2.10}$$

$$T = \sum_{j=1}^{n} T_{s_j} + T_c \tag{2.11}$$

2.2.2 Compatibility

With the above assumptions, kinematic equations relating the displacement components (u_i, v, θ_i) to the corresponding strain components (ϵ_i, θ_i, γ_c, κ_i) are derived for each component of the hybrid beam-column (see Fig. 2.2) as follows:

$$\epsilon_i = \partial u_i \qquad i = s_1, s_2, \cdots, s_n, c \tag{2.12}$$

$$\theta_c = \partial v - \gamma_c \tag{2.13}$$

$$\kappa_c = \partial \theta_c \tag{2.14}$$

$$\theta_{s_i} = \partial v \qquad i = 1, 2, \cdots, n \tag{2.15}$$

$$\kappa_{s_i} = \partial \theta_{s_i} \qquad i = 1, 2, \cdots, n \tag{2.16}$$

in which γ_c is the shear deformation of the concrete component. The slip corresponds to the difference between the axial displacement of the embedded steel section and of the concrete beam which is expressed as:

$$g_i = u_c - u_{s_i} - h_i \theta_c, \qquad i = 1, 2, \cdots, n \tag{2.17}$$

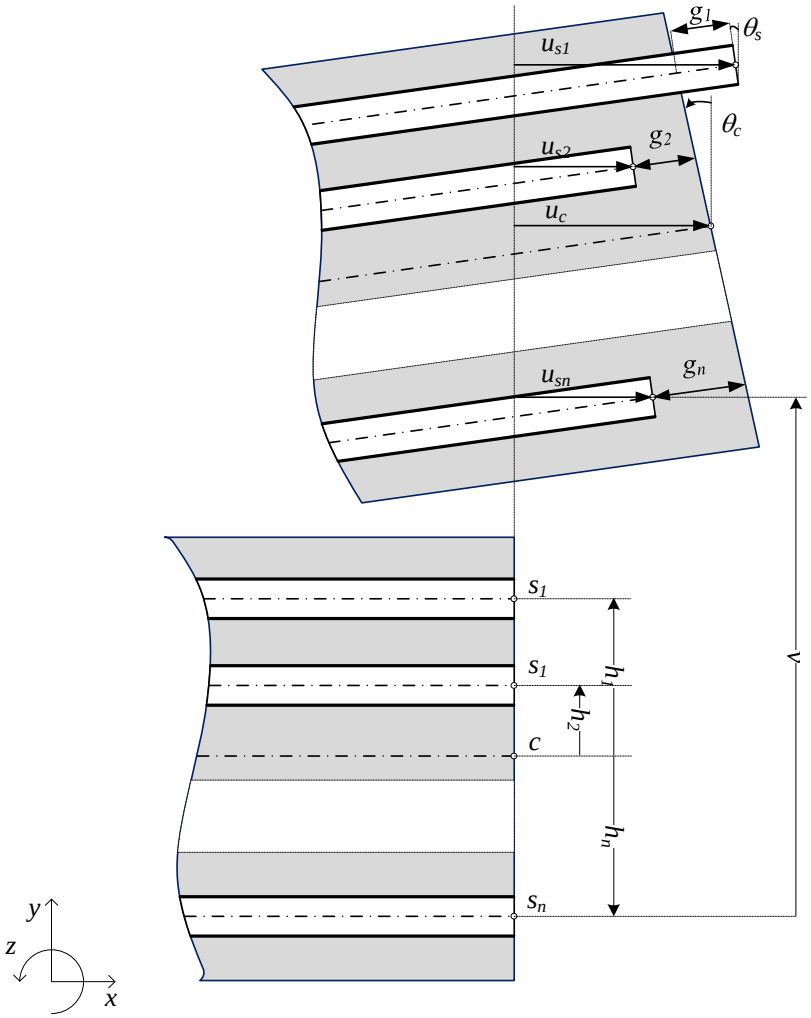

Figure 2.2: Displacement field of a hybrid beam-column.

2.2.3 Constitutive relationships

The generalized stress-strain relationships are simply obtained by integrating the appropriate uniaxial constitutive model over each cross-section. For a linear elas-

tic material, these relationships lead to the following set of equations:

$$N_i = \int_{A_i} \sigma \, \mathrm{d}A_i = (EA)_i \, \epsilon_i \tag{2.18}$$

$$M_i = -\int_{A_i} y \, \sigma \, \mathrm{d}A_i = (EI)_i \, \kappa_i \tag{2.19}$$

$$T_c = \int_{A_c} \tau \, \mathrm{d}A_c = (GA)_c \, \gamma_c \tag{2.20}$$

where

- $i = s_1, s_2, \cdots, s_n, c$
- $(EA)_i = E_i \, A_i$ is the axial stiffness of each component;
- $(EI)_i = E_i \, I_i$ is the flexural stiffness of each component;
- $(GA)_c = k_c \, G_c \, A_c$ is the shear stiffness of the concrete beam in which k_c is the shear correction factor.

E_i, G_i, A_i and I_i are elastic modulus, shear modulus, area of cross-section and second moment of area of cross-section of the component "i", respectively. The above relationships must be completed by the one between the longitudinal shear force D_{sc_i} and the slip g_i. The assumption of linear and continuous shear connection can be expressed by the following simple relationship between slip and shear flow:

$$D_{sc_i} = k_{sc_i} \, g_i, \qquad i = 1, 2, \cdots, n \tag{2.21}$$

where k_{sc_i} is the shear connection stiffness.

2.3 Derivation of the governing equations

The relationships introduced in Section 2.2 are now combined to derive the equations governing the behavior of a hybrid beam in partial interaction. Combining the kinematic relations Eqs. (2.12-2.14) with the elastic behavior Eqs. (2.18-2.21)

and inserting the outcome into the equilibrium equations Eqs. (2.6-2.8) produce the following set of differential equations:

$$(EA)_{s_i}\,\partial^2 u_{s_i} = -k_{sc_i}\,g_i, \qquad i = 1, 2, \cdots, n \tag{2.22}$$

$$(EA)_c\,\partial^2 u_c = \sum_{i=1}^{n} k_{sc_i}\,g_i \tag{2.23}$$

$$(EI)_0\,\partial^3 v = -T - \sum_{i=1}^{n} k_{sc_i}\,g_i\,h_i + (EI)_c\,\partial^2\gamma_c \tag{2.24}$$

The expression $(EI)_0$ denotes the sum of the flexural stiffness of each component i.e. $(EI)_0 = (EI)_s + E_c\,I_c$ in which $(EI)_s = \sum_{i=1}^{n} E_{s_i}\,I_{s_i}$.

Taking the derivative of the slip distribution Eq. (2.17) and making use of Eq. (2.13) and Eqs. (2.22-2.24), one arrives at the following equation:

$$\partial^2 g_i = \frac{k_{sc_i}}{(EA)_{s_i}}\,g_i + \sum_{j=1}^{n} k_{sc_j}\left[\frac{1}{(EA)_c} + \frac{h_i\,h_j}{(EI)_c}\right] g_j + h_i\frac{(GA)_c}{(EI)_c}\,\gamma_c \tag{2.25}$$

Inserting Eqs. (2.19-2.21) into Eq. (2.3) and making use of Eqs. (2.13-2.14) and Eq. (2.24), one gets

$$\partial^2\gamma_c = \sum_{j=1}^{n}\frac{h_j\,k_{sc_j}}{(EI)_c}g_j + \frac{(EI)_0(GA)_c}{(EI)_c(EI)_s}\gamma_c - \frac{T}{(EI)_s} \tag{2.26}$$

Combining Eq. (2.25) and Eq. (2.26), one arrives at the following coupled second-order system of differential equations where the primary unknown variables are the slip distribution and the shear deformation of the concrete beam:

$$\partial^2\mathbf{s} - \mathbf{A}\,\mathbf{s} = \mathbf{h} \tag{2.27}$$

where

$$\mathbf{s} = [\ g_1 \quad g_2 \quad \cdots \quad g_n \quad \gamma_c\ ]^{\mathrm{T}} \tag{2.28}$$

and

$$\mathbf{h} = [\ 0 \quad 0 \quad \cdots \quad 0 \quad -\frac{T}{(EI)_s}\ ]^{\mathrm{T}} \tag{2.29}$$

The components of the matrix $\mathbf{A}$ are given by

$$\mathbf{A} = \begin{bmatrix} k_{sc1}\left[\frac{1}{(EA)_{sc1}} + \frac{h_1^2}{(EI)_0}\right] & k_{sc2}\left[\frac{1}{(EA)_c} + \frac{h_1 h_2}{(EI)_0}\right] & \cdots & k_{scn}\left[\frac{1}{(EA)_c} + \frac{h_1 h_n}{(EI)_0}\right] & \frac{h_1\,(GA)_c}{(EI)_c} \\ k_{sc1}\left[\frac{1}{(EA)_c} + \frac{h_1 h_2}{(EI)_0}\right] & k_{sc2}\left[\frac{1}{(EA)_{sc2}} + \frac{h_2^2}{(EI)_0}\right] & \cdots & k_{scn}\left[\frac{1}{(EA)_c} + \frac{h_2 h_n}{(EI)_0}\right] & \frac{h_2\,(GA)_c}{(EI)_c} \\ \vdots & \vdots & \ddots & \vdots & \vdots \\ k_{sc1}\left[\frac{1}{(EA)_c} + \frac{h_1 h_n}{(EI)_0}\right] & k_{sc2}\left[\frac{1}{(EA)_c} + \frac{h_2 h_n}{(EI)_0}\right] & \cdots & k_{scn}\left[\frac{1}{(EA)_{scn}} + \frac{h_n^2}{(EI)_0}\right] & \frac{h_n\,(GA)_c}{(EI)_c} \\ \frac{h_1\,k_{sc1}}{(EI)_c} & \frac{h_2\,k_{sc2}}{(EI)_c} & \cdots & \frac{h_n\,k_{scn}}{(EI)_c} & \frac{(EI)_0(GA)_c}{(EI)_c(EI)_s} \end{bmatrix} \tag{2.30}$$

in which,

$$\frac{1}{(EA)_{sci}} = \frac{1}{(EA)_c} + \frac{1}{(EA)_{s_i}}, \qquad i = 1, 2, \cdots, n \tag{2.31}$$

It is worth mentioning that for shear-rigid model, the primary unknown variables in the coupled differential equations are only slip distributions since the shear deformation of concrete component is supposed negligible.

A diagonalization of the matrix $\mathbf{A}$ will uncouple the above system of differential equations Eq. (2.27) and produce a set of $n+1$ second-order ordinary equations. Let $\mathbf{A}_v$ and $\mathbf{A}_\lambda$ respectively be the matrix collecting the eigenvectors and the eigenvalues of $\mathbf{A}$. Then, we have the following relationship:

$$\mathbf{A}_\lambda = \mathbf{A}_v^{-1}\,\mathbf{A}\,\mathbf{A}_v. \tag{2.32}$$

Subsequently, we insert the vector $\mathbf{s}$ obtained by pre-multiplying the vector $\tilde{\mathbf{s}}$ by the matrix $\mathbf{A}_v$

$$\mathbf{s} = \mathbf{A}_v\tilde{\mathbf{s}} \tag{2.33}$$

into Eq. (2.27) and make use of Eq. (2.32) to produce an uncoupled differential equation system:

$$\partial^2\,\tilde{\mathbf{s}} - \mathbf{A}_\lambda\,\tilde{\mathbf{s}} = \bar{\mathbf{h}} \tag{2.34}$$

where $\bar{\mathbf{h}} = \mathbf{A}_v^{-1}\mathbf{h}$. By noting that the inverse matrix $\mathbf{A}_v^{-1}$ can be written as

$$\mathbf{A}_v^{-1} = \begin{bmatrix} \bar{a}_{11} & \bar{a}_{12} & \cdots & \bar{a}_{1(n+1)} \\ \bar{a}_{21} & \bar{a}_{22} & \cdots & \bar{a}_{2(n+1)} \\ \vdots & \vdots & \ddots & \vdots \\ \bar{a}_{(n+1)1} & \bar{a}_{(n+1)2} & \cdots & \bar{a}_{(n+1)(n+1)} \end{bmatrix} \tag{2.35}$$

the components i of vector $\bar{\mathbf{h}}$ can be written as:

$$\bar{h}_i = -\bar{a}_{i(n+1)} \frac{T}{(EI)_s}, \qquad i = 1, 2, \cdots, n+1 \tag{2.36}$$

Consequently, the system of differential equation (Eq. (2.34)) can be written as a set of $n+1$ uncoupled ordinary differential equations in variables $\tilde{s}_k$ as follows:

$$\partial^2 \tilde{s}_i - \lambda_i \tilde{s}_i = -\bar{a}_{i(n+1)} \frac{T}{(EI)_s}, \qquad i = 1, 2, \cdots, n+1 \tag{2.37}$$

where λ_i is the i^{th} eigenvalue of matrix $\mathbf{A}$.

2.4 Closed-form solution of the governing equations

In this section, we provide the analytical solution of the governing equations for the general case of the shear connection that is $0 < k_{sc_i} < \infty$. The governing differential equation involves the single unknown variable $\tilde{\mathbf{s}}$. It is worth mentioning that the exact solution of the governing differential equation (Eq. (2.37)) requires the distribution of the shear force $T(x)$ to be known. In order to simplify the development of the solution, we assume that the external distributed load on the element is uniform. As a result, the distribution of the shear force must be linear to ensure the overall transverse equilibrium Eq. (2.9).

$$T(x) = -p_y\, x + C_{2n+8} \tag{2.38}$$

where C_{2n+8} is the shear force at the left hand side of the beam and is considered to be a constant of integration. The kinematic variables can be determined once the expressions of $\tilde{s}_i$ are found by solving the differential equation. The general solution of $\tilde{s}_i$ $(i = 1, 2, \cdots, n+1)$ is given by

- For $\lambda_i > 0$

$$\tilde{s}_i = \tilde{C}_{2i-1} e^{\sqrt{\lambda_i} x} + \tilde{C}_{2i} e^{-\sqrt{\lambda_i} x} + \frac{\bar{a}_{i(n+1)}}{\lambda_i\, (EI)_s} (C_{2n+8} - p_y\, x) \tag{2.39}$$

- For $\lambda_i < 0$

$$\tilde{s}_i = C_{2i-1}\cos\sqrt{-\lambda_i}x + C_{2i}\sin\sqrt{-\lambda_i}x + \frac{\bar{a}_{i(n+1)}}{\lambda_i\,(EI)_s}(C_{2n+8} - p_y\,x) \tag{2.40}$$

- For $\lambda_i = 0$

$$\tilde{s}_i = C_{2i-1} + C_{2i}\,x - \frac{\bar{a}_{i(n+1)}}{(EI)_s}(C_{2n+8}\frac{x^2}{2} - p_y\,\frac{x^3}{6}) \tag{2.41}$$

The solution of $\tilde{s}_i$ in case $\lambda_i > 0$ involves exponential terms which may take a very large value. To avoid numerical ill-conditioning of the stiffness matrix, we replace the actual expressions of the constants of integration with the following ones:

$$\tilde{C}_{2i-1} = e^{-\sqrt{\lambda_i}L}\,C_{2i-1}, \qquad i = 1, 2, \cdots, n+1 \tag{2.42}$$

$$\tilde{C}_{2i} = C_{2i}, \qquad i = 1, 2, \cdots, n+1 \tag{2.43}$$

in which L is the length of the element.

All $\tilde{s}_i$ are collected in a vector so the analytical solution can be written in a matrix form as follows:

$$\tilde{\mathbf{s}} = \mathbf{X}_{\tilde{s}}\mathbf{C} + \mathbf{Z}_{\tilde{s}} \tag{2.44}$$

with

$$\tilde{\mathbf{s}} = [\,\tilde{s}_1\ \tilde{s}_2 \cdots \tilde{s}_{n+1}\,]^{\mathrm{T}} \tag{2.45}$$

and

$$\mathbf{C} = [\,C_1\ C_2 \cdots C_{2n+8}\,]^{\mathrm{T}} \tag{2.46}$$

The components of matrix $\mathbf{X}_{\tilde{s}}$ and $\mathbf{Z}_{\tilde{s}}$ are dependent on the eigenvalues of $\mathbf{A}$ and the external load p_y, respectively. In case $\mathbf{A}$ is positive definite i.e. $\lambda_i > 0$, we obtain the following expression for $\mathbf{X}_{\tilde{s}}$ and $\mathbf{Z}_{\tilde{s}}$ with $\alpha_i = \sqrt{\lambda_i}$.

$$\mathbf{X}_{\tilde{s}} = \begin{bmatrix} e^{\alpha_1(x-L)} & e^{-\alpha_1 x} & 0 & 0 & \cdots & 0 & 0 & 0 & 0 & 0 & 0 & \frac{\bar{a}_{1(n+1)}}{\lambda_1\,(EI)_s} \\ 0 & 0 & e^{\alpha_2(x-L)} & e^{-\alpha_2 x} & \cdots & 0 & 0 & 0 & 0 & 0 & 0 & \frac{\bar{a}_{2(n+1)}}{\lambda_2\,(EI)_s} \\ \vdots & \vdots & \vdots & \vdots & \ddots & \vdots & \vdots & \vdots & \vdots & \vdots & \vdots & \vdots \\ 0 & 0 & 0 & 0 & \cdots & e^{\alpha_{n+1}(x-L)} & e^{-\alpha_{n+1}x} & 0 & 0 & 0 & 0 & \frac{\bar{a}_{(n+1)(n+1)}}{\lambda_{n+1}\,(EI)_s} \end{bmatrix} \tag{2.47}$$

and

$$\mathbf{Z}_{\tilde{s}} = -\frac{p_y\, x}{(EI)_s}\left[\frac{\bar{a}_{1(n+1)}}{\lambda_1} \quad \frac{\bar{a}_{2(n+1)}}{\lambda_2} \quad \cdots \quad \frac{\bar{a}_{(n+1)(n+1)}}{\lambda_{n+1}}\right]^{\mathrm{T}} \tag{2.48}$$

Substituting Eq. (2.44) into Eq. (2.33), one gets

$$\mathbf{s} = \mathbf{X}_s\mathbf{C} + \mathbf{Z}_s \tag{2.49}$$

in which

$$\mathbf{X}_s = \mathbf{A}_v\mathbf{X}_{\tilde{s}} \qquad\qquad \mathbf{Z}_s = \mathbf{A}_v\mathbf{Z}_{\tilde{s}} \tag{2.50}$$

The vector $\mathbf{Z}_s$ as well as the matrix $\mathbf{X}_s$ is decomposed into two sub-vectors and sub-matrices, respectively in order to separate the distribution of slips g_i from the shear deformation of concrete beam γ_c. The first bloc collects the slip distribution g_i and the second one gathers the shear deformation γ_c:

$$\mathbf{g} = \mathbf{X}_g\mathbf{C} + \mathbf{Z}_g \tag{2.51}$$

$$\gamma_c = \mathbf{X}_{\gamma_c}\mathbf{C} + Z_{\gamma_c} \tag{2.52}$$

where $\mathbf{X}_s = [\ \mathbf{X}_g^{\mathrm{T}} \quad \mathbf{X}_{\gamma_c}^{\mathrm{T}}\ ]^{\mathrm{T}}$ and $\mathbf{Z}_s = [\ \mathbf{Z}_g^{\mathrm{T}} \quad Z_{\gamma_c}\ ]^{\mathrm{T}}$.

2.4.1 Determination of displacement fields

To determine the axial displacement of the concrete component and the deflection of the beam, we use the relationships in which the kinematic variables are expressed as a function of slip and shear deformation distribution Eqs. (2.23-2.24) developed in Section 2.3. Inserting Eqs. (2.51-2.52) into Eq. (2.24), one obtains:

$$\partial^3 v = \frac{1}{(EI)_0}\left(-\mathbb{I}_{2n+8} - \varrho\mathbf{X}_g + (EI)_c\,\partial^2\mathbf{X}_{\gamma_c}\right)\mathbf{C} + \frac{1}{(EI)_0}\left(p_y\, x - \varrho\mathbf{Z}_g + (EI)_c\,\partial^2 Z_{\gamma_c}\right) \tag{2.53}$$

where

$$\varrho = [\ h_1\, k_{sc_1} \quad h_2\, k_{sc_2} \quad \cdots \quad h_n\, k_{sc_n}\ ] \tag{2.54}$$

By making use of Eqs. (2.13-2.14), the curvature, the cross-section rotation and the deflexion can be derived by a successive integration of Eq. (2.53).

$$\kappa_s = \mathbf{X}_{\kappa_s}\mathbf{C} + Z_{\kappa_s} \tag{2.55}$$

$$\theta_s = \mathbf{X}_{\theta_s}\mathbf{C} + Z_{\theta_s} \tag{2.56}$$

$$v = \mathbf{X}_{v}\mathbf{C} + Z_{v} \tag{2.57}$$

where

$$\mathbf{X}_{\kappa_s} = \frac{1}{(EI)_0}\int \left[-\mathbb{I}_{2n+8} - \varrho\mathbf{X}_g + (EI)_c\,\partial^2\mathbf{X}_{\gamma_c}\right]\mathrm{d}x + \mathbb{I}_{2n+3} \tag{2.58}$$

$$\mathbf{X}_{\theta_s} = \int \mathbf{X}_{\kappa_s}\mathrm{d}x + \mathbb{I}_{2n+4} \tag{2.59}$$

$$\mathbf{X}_{v} = \int \mathbf{X}_{\theta_s}\mathrm{d}x + \mathbb{I}_{2n+5} \tag{2.60}$$

$$Z_{\kappa_s} = \frac{1}{(EI)_0}\int \left[p_y\,x - \varrho\mathbf{Z}_g + (EI)_c\,\partial^2 Z_{\gamma_c}\right]\mathrm{d}x \tag{2.61}$$

$$Z_{\theta_s} = \int Z_{\kappa}\mathrm{d}x \tag{2.62}$$

$$Z_{v} = \int Z_{\theta_s}\mathrm{d}x \tag{2.63}$$

$$\mathbb{I}_{2n+3} = [\overbrace{\begin{array}{cccc}0 & 0 & \cdots & 0\end{array}}^{2n+2}\ 1\ 0\ 0\ 0\ 0\ 0\ ] \tag{2.64}$$

$$\mathbb{I}_{2n+4} = [\ 0\ 0\ \cdots\ 0\ 0\ 1\ 0\ 0\ 0\ 0\ ] \tag{2.65}$$

$$\mathbb{I}_{2n+5} = [\ 0\ 0\ \cdots\ 0\ 0\ 0\ 1\ 0\ 0\ 0\ ] \tag{2.66}$$

$$\mathbb{I}_{2n+6} = [\ 0\ 0\ \cdots\ 0\ 0\ 0\ 0\ 1\ 0\ 0\ ] \tag{2.67}$$

$$\mathbb{I}_{2n+7} = [\ 0\ 0\ \cdots\ 0\ 0\ 0\ 0\ 0\ 1\ 0\ ] \tag{2.68}$$

$$\mathbb{I}_{2n+8} = [\ 0\ 0\ \cdots\ 0\ 0\ 0\ 0\ 0\ 0\ 1\ ] \tag{2.69}$$

Substituting Eq. (2.51) into Eq. (2.23) and integrating twice the outcome, one gets the axial displacement of the concrete beam as follow:

$$u_c = \mathbf{X}_{u_c}\mathbf{C} + Z_{u_c} \tag{2.70}$$

where

$$\mathbf{X}_{u_c} = \int \left[\int \left(\frac{1}{(EA)_c} \begin{bmatrix} k_{sc_1} & k_{sc_2} & \cdots & k_{sc_n} \end{bmatrix} \mathbf{X}_g \right) \mathrm{d}x \right] \mathrm{d}x + x\mathbb{I}_{2n+6} + \mathbb{I}_{2n+7} \tag{2.71}$$

$$Z_{u_c} = \int \left[\int \left(\frac{1}{(EA)_c} \begin{bmatrix} k_{sc_1} & k_{sc_2} & \cdots & k_{sc_n} \end{bmatrix} \mathbf{Z}_g \right) \mathrm{d}x \right] \mathrm{d}x \tag{2.72}$$

At this point, we have $2n + 8$ constants of integration which correspond to the number of degrees of freedom: $2n + 2$ axial displacements of each component, 2 cross-section rotations of the encasing component, 2 cross-section rotations of embedded components and 2 verticals displacement. Consequently, the remaining kinematic variables must be determined by using the kinematic relations. By inserting Eq. (2.52) and Eq. (2.57) into Eq. (2.13), the cross-section rotation of the concrete beam is obtained:

$$\theta_c = \mathbf{X}_{\theta_c}\,\mathbf{C} + Z_{\theta_c} \tag{2.73}$$

where

$$\mathbf{X}_{\theta_c} = \partial \mathbf{X}_v - \mathbf{X}_{\gamma_c} \qquad Z_{\theta_c} = \partial Z_v - Z_{\gamma_c} \tag{2.74}$$

We get the expression of the axial displacement of the embedded steel sections by inserting Eq. (2.51), Eq. (2.70) and Eq. (2.73) into Eq. (2.17) and solving for u_{s_i}:

$$u_{s_i} = \mathbf{X}_{us_i}\mathbf{C} + Z_{us_i}, \qquad i = 1, 2, \cdots, n \tag{2.75}$$

where

$$\mathbf{X}_{us_i} = \mathbf{X}_{u_c} - \mathbf{X}_{g_i} - h_i\,\mathbf{X}_{\theta_c} \qquad Z_{us_i} = Z_{u_c} - Z_g - h_i\,Z_{\theta_c} \tag{2.76}$$

2.4.2 Determination of internal forces

Once the displacement fields are defined, one can use the linear elastic relationship Eqs. (2.18-2.19) to obtain the nodal forces.

$$N_{s_i} = \mathbf{Y}_{Ns_i}\mathbf{C} + R_{Ns_i}, \qquad i = 1, 2, \cdots n \tag{2.77}$$

$$N_c = \mathbf{Y}_{N_c}\mathbf{C} + R_{N_c} \tag{2.78}$$

$$M_s = \mathbf{Y}_{M_s}\mathbf{C} + R_{M_s} \tag{2.79}$$

$$M_c = \mathbf{Y}_{M_c}\mathbf{C} + R_{M_c} \tag{2.80}$$

$$T = \mathbf{Y}_T\mathbf{C} + R_T \tag{2.81}$$

where

$$\mathbf{Y}_{Ns_i} = (EA)_{s_i}\,\partial\mathbf{X}_{us_i} \qquad R_{Ns_i} = (EA)_{s_i}\,\partial Z_{us_i}, \qquad i = 1, 2, \cdots n \tag{2.82}$$

$$\mathbf{Y}_{N_c} = (EA)_c\,\partial\mathbf{X}_{u_c} \qquad R_{N_c} = (EA)_c\,\partial Z_{uc} \tag{2.83}$$

$$\mathbf{Y}_{M_s} = (EI)_s\,\mathbf{X}_{\kappa_s} \qquad R_{M_s} = (EI)_s\,Z_{\kappa_s} \tag{2.84}$$

$$\mathbf{Y}_{M_c} = (EI)_c\,\partial\mathbf{X}_{\theta_c} \qquad R_{M_c} = (EI)_c\,Z_{\theta_c} \tag{2.85}$$

$$\mathbf{Y}_T = \mathbb{I}_{2n+8} \qquad R_T = -p_y\,x \tag{2.86}$$

$$M_s = \sum_{j=1}^{n} M_{s_j} \tag{2.87}$$

2.5 Exact stiffness matrix

The direct stiffness method is used to derive the exact stiffness of the hybrid beam-column with n embedded sections. It can be obtained starting from the general expressions of the internal forces and the displacement fields. Let a hybrid beam-column element of length L be considered. Since the same transverse displacement is assumed, this element has $(2n + 8)$ degrees of freedom, see Fig. 2.3. Applying the kinematic boundary conditions at $x = 0$ and $x = L$ leads to the relationship between the vector of constants of integration $\mathbf{C}$ and the vector of nodal displacements $\mathbf{q}$ as follows:

$$\mathbf{q} = \mathbf{X}\,\mathbf{C} + \mathbf{Z} \tag{2.88}$$

where

$$\mathbf{q} = [\ u_{s_1,0} \quad \cdots \quad u_{c,0} \quad v_{c,0} \quad \theta_{s,0} \quad \theta_{c,0} \quad u_{s_1,L} \quad \cdots \quad u_{c,L} \quad v_{c,L} \quad \theta_{s,L} \quad \theta_{c,L}\ ]^{\mathrm{T}} \tag{2.89}$$

$$\mathbf{X} = [\ \mathbf{X}_{us_1,0} \quad \cdots \quad \mathbf{X}_{\theta_s,0} \quad \mathbf{X}_{\theta_c,0} \quad \mathbf{X}_{us_1,L} \quad \cdots \quad \mathbf{X}_{\theta_s,L} \quad \mathbf{X}_{\theta_c,L}\ ]^{\mathrm{T}} \tag{2.90}$$

$$\mathbf{Z} = [\ \mathbf{Z}_{us_1,0} \quad \cdots \quad \mathbf{Z}_{\theta_s,0} \quad \mathbf{Z}_{\theta_c,0} \quad \mathbf{Z}_{us_1,L} \quad \cdots \quad \mathbf{Z}_{\theta_s,L} \quad \mathbf{Z}_{\theta_c,L}\ ]^{\mathrm{T}} \tag{2.91}$$

The nodal displacements being independent, so the matrix $\mathbf{X}$ is invertible. Thus, the constants C_i are obtained as a function of the nodal displacements q_i.

$$\mathbf{C} = \mathbf{X}^{-1}(\mathbf{q} - \mathbf{Z}) \tag{2.92}$$

The nodal forces can be expressed in compact form as:

$$\mathbf{Q} = \mathbf{Y}\,\mathbf{C} + \mathbf{R} \tag{2.93}$$

where,

$$\mathbf{Q} = [\ -N_{s_1,0} \quad \cdots \quad -M_{c,0} \quad N_{s_1,L} \quad \cdots \quad M_{c,L}\ ]^{\mathrm{T}} \tag{2.94}$$

$$\mathbf{Y} = [\ -\mathbf{Y}_{N_{s_1,0}} \quad \cdots \quad -\mathbf{Y}_{M_{c,0}} \quad \mathbf{Y}_{N_{s_1,L}} \quad \cdots \quad \mathbf{Y}_{M_{c,L}}\ ]^{\mathrm{T}} \tag{2.95}$$

$$\mathbf{R} = [\ -\mathbf{R}_{N_{s_1,0}} \quad \cdots \quad -\mathbf{R}_{M_{c,0}} \quad \mathbf{R}_{N_{s_1,L}} \quad \cdots \quad \mathbf{R}_{M_{c,L}}\ ]^{\mathrm{T}} \tag{2.96}$$

Inserting Eq. (2.92) into Eq. (2.93), one obtains:

$$\mathbf{K}\,\mathbf{q} = \mathbf{Q} + \mathbf{Q}_0 \tag{2.97}$$

where

$$\mathbf{K} = \mathbf{Y}\,\mathbf{X}^{-1} \tag{2.98}$$

represents the exact stiffness of the element and

$$\mathbf{Q}_0 = \mathbf{K}\,\mathbf{Z} - \mathbf{R} \tag{2.99}$$

represents the nodal force due to the uniform external load p_y.

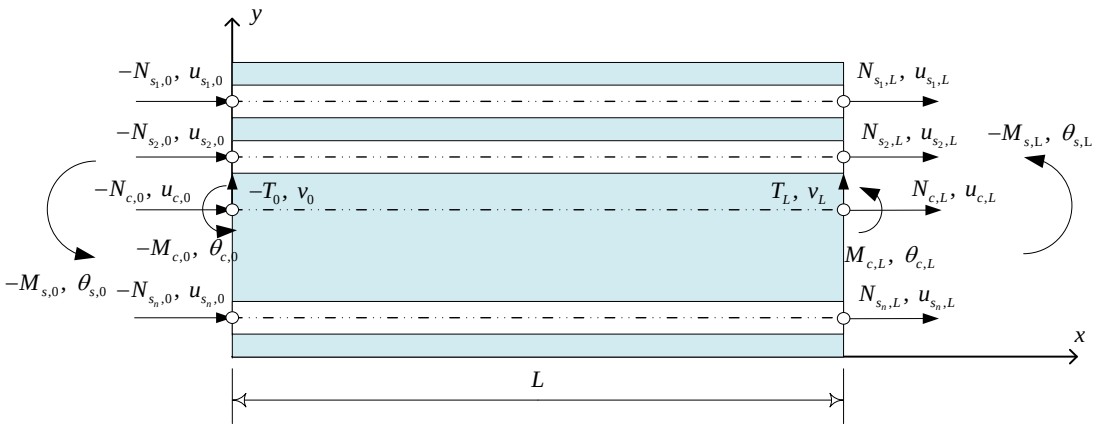

Figure 2.3: Nodal forces and displacements of hybrid beam element.

2.6 Numerical applications

The purpose of this section is to assess the capability of the proposed formulation in reproducing the linear elastic behavior of shear-rigid and shear-deformable hybrid beam-columns in partial interaction and to investigate the influence of the shear connection stiffness and span-to-depth ratio on mechanical responses of the beam-columns. To do so, the predictions of the exact finite element model for hybrid beam-columns with shear-rigid assumption are compared against the results obtained with the present exact model. The investigation is carried out considering three examples: simply supported sandwich beam, clamped-free hybrid column/shear-wall and two-span continuous hybrid beam.

2.6.1 Simply supported steel-reinforced concrete beam subjected to uniformly distributed load

Consider a concrete beam of breadth of 10 cm and depth of 20 cm (see Fig. 2.4) reinforced by two steel plates of equal thickness 2 cm attached, using shear connectors, to the top and bottom surfaces of the concrete beam. The latter is subjected to a uniformly distributed load p_y of intensity 10 kN/m. The elastic

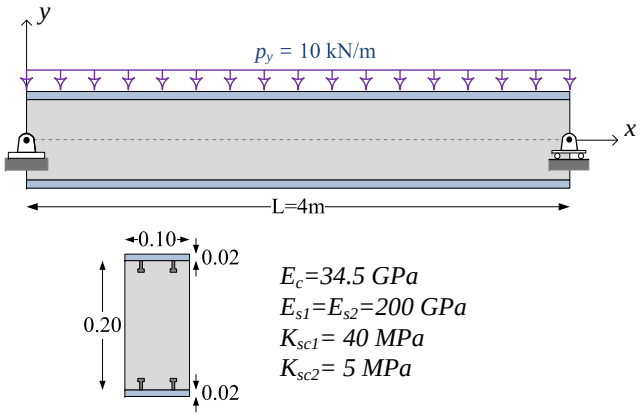

Figure 2.4: Sandwich beam with transversal loads (dimension in [m]).

Table 2.1: Numerical results.

	EB-Model		T-model	
	[42]	Present	[42]	Present
$\|\|v_{max}\|\|$ (mm)	10.87796015	10.87796014	10.91156269	10.93670002
$\|\|g_1\|\|$ (mm)	0.77821848	0.77821849	0.77821848	0.78028991
$\|\|g_2\|\|$ (mm)	1.00207365	1.00207366	1.00207365	1.00475539

modulus adopted for steel and concrete are 200 000 MPa and 34 500 MPa, respectively. The Poisson's ratio for the concrete core is taken equal to 0.2; and the value of shear correction factor is assumed to be equal to 1. The stiffness of the shear connection is taken equal to 40 MPa for the top layer and 5 MPa for the bottom layer. Such a distribution of the shear connection stiffness breaks the symmetry of the problem. The geometrically linear analysis of this beam problem was performed by Sousa Jr [42] using the exact flexibility matrix. To assess the capabilities of our formulation we perform a linear analysis with two exact finite elements. The exact stiffness is derived based on a linear shear force distribution (replacing T with $-p_y x + C_{2n+8}$ in Eq. (2.38)) so that the distributed load is considered without any approximation. A good agreement for the geometrically linear analysis with the results in [42] is obtained. The maximum deflection v_{max} occurring at mid-span of the beam along with the slips at the beam ends are

tabulated in Table 2.1 for both shear-rigid model (EB-model) and shear-flexible model (T-model).

2.6.2 Hybrid column/shear-wall

Consider a hybrid column/shear-wall consisting of a cross-section with breadth of 25 cm and depth of 90 cm reinforced by three embedded steel profiles, HEB100. The column/shear-wall is clamped at its base and free at its top. Equally spaced shear stud connectors are welded on both side of each web of steel sections. As a result, the shear connector stiffness k_{sc} for each sliding plane is equal. The shear correction factor for this example is taken equal to unity. The position of the centroid of the steel profile at mid-height of the hybrid cross-section coincides with the centroid of the concrete section. The geometrical and material characteristics of the column/shear-wall are reported in Fig. 2.5. The column/shear-wall is

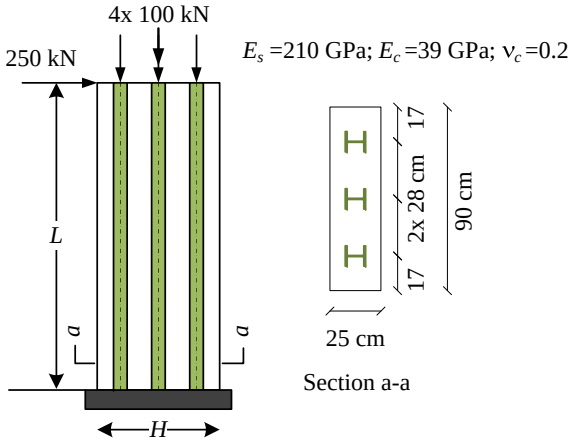

Figure 2.5: Hybrid column/shear-wall (dimension in [cm]).

subjected to a lateral load of 250 kN at the top and to equally distributed axial loads of 100 kN at the centroids of each component. The column/shear-wall is modeled using one element, which is the smallest number needed for this problem. It is worth mentioning that since the model is based on the exact stiffness

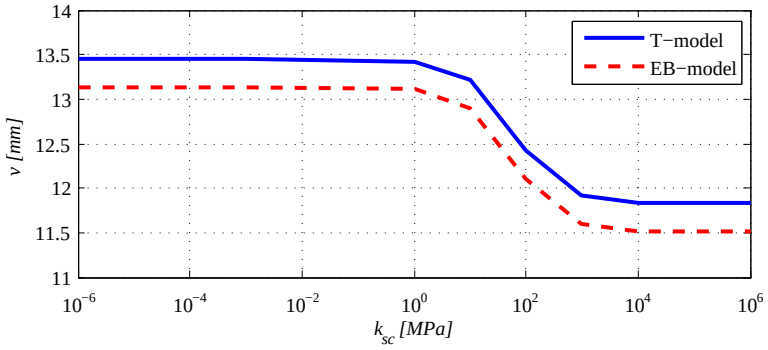

Figure 2.6: Deflection v as a function of shear connector stiffness with $L/H = 5$.

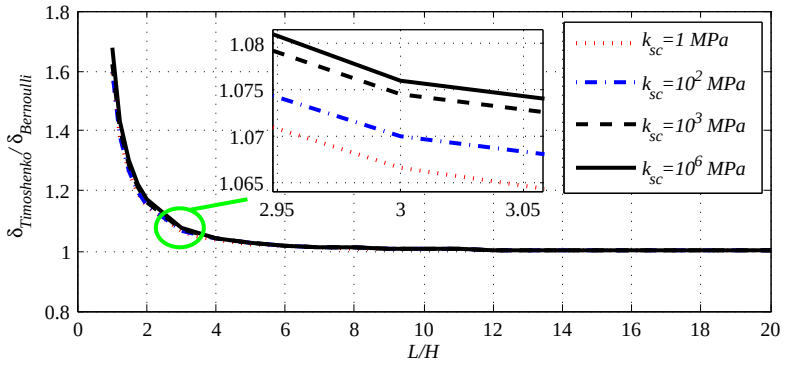

Figure 2.7: Lateral deflection ratio versus span-to-depth ratio for different shear connection stiffness.

matrix, considering more elements does not improve the results. The role of shear flexibility of the concrete component can be analyzed by comparing the mechanical response obtained with the shear-flexible model (T-model) against the corresponding response predicted by the shear-rigid model (EB-model). In particular, the comparison is carried out in terms of the lateral displacement (δ) evaluated by means of the two above-mentioned models. The degree of shear connection for a case where the span-to-depth ratio $L/H = 5$ is illustrated in Fig. 2.6 from which one can consider the shear connection as a loose connection for $k_{sc} = 1$ MPa and a full connection for $k_{sc} = 10^6$ MPa. Besides, one can observe from Fig. 2.6 that the distributions of the lateral displacement as a function of the shear connection stiffness for both models are almost "parallel".

Fig. 2.7 shows the lateral deflection ratio obtained with both models as a function of the span-to-depth ratios (L/H) for a different shear connection stiffness (k_{sc}). As expected, the deflection predicted by shear-flexible model is larger than the corresponding deflection evaluated using the shear-rigid model for any value of the ratio L/H. Moreover, the deflection ratio tends to infinity when the span-to-depth ratio tends to zero, and to unity when the span-to-depth ratio goes to infinity. It can be seen that the shear connection stiffness has almost no influence on the ratio between the lateral deflection obtained with the shear-flexible model and with the shear-rigid model. For both loose connection and full interaction, the deflection ratio as a function of the span-to-depth ratio are almost the same.

Further comparisons are also proposed in terms of end slips (see Fig. 2.8 and

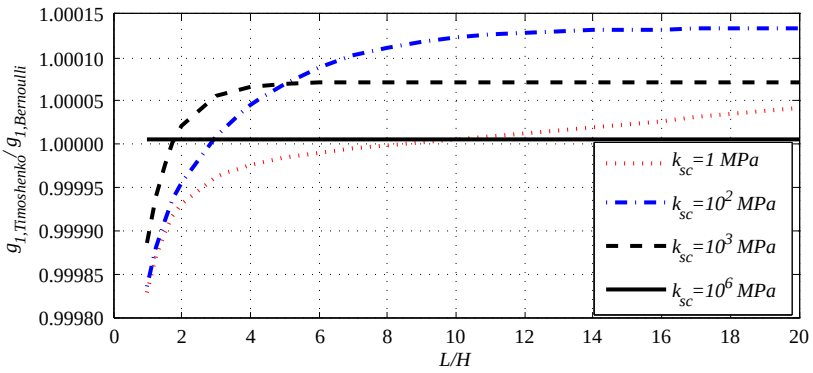

Figure 2.8: End beam slip strain ratio versus span-to-depth ratio for different shear connection stiffness.

Fig. 2.9). It is worth mentioning that by symmetry the slip g_2 at centroid of concrete cross-section is equal for both models. As a result, only distributions of g_1 and g_3 are discussed here. In contrast to the lateral deflection ratio that is influenced by the ratio L/H, one can observe that the slip ratio of both models does not vary significantly as a function of both L/H and k_{sc}. Due to the combination of the bending moment (depends on L/H ratio) and the axial force, the slip g_3 changes its sign at a specific value of L/H in partial interaction (low value

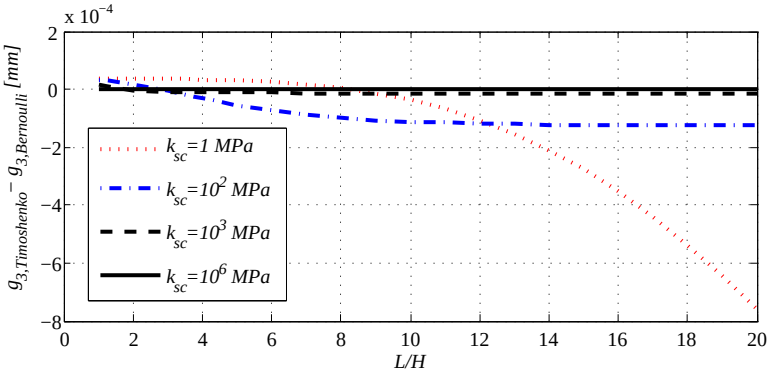

Figure 2.9: End beam slip ratio versus span-to-depth ratio for different shear connection stiffness.

of k_{sc}). At that specific value of L/H, the slip ratio tends to infinity and leads to discontinuity of the curve. As the result, the difference between the end slips of both models is provided.

2.6.3 Two-span continuous hybrid beam

Consider a concrete beam of 25 cm breadth and 90 cm depth (see Fig. 2.10) reinforced by two steel profiles HEB100 embedded in the concrete beam. The beam is subjected to a uniformly distributed load whose intensity is 100 kN/m. The elastic modulus adopted for steel and concrete are 200 000 MPa and 34 500 MPa, respectively. The Poisson's ratio for the surrounding concrete is taken equal to 0.2; and the unity value of shear correction factor is adopted. The shear connection stiffness is 50 MPa for the top connection between the concrete component and the embedded steel section and is 10 MPa for the bottom one. Such distribution of the shear connection stiffness breaks the symmetry of the problem. The values of end slips, transverse displacement at mid-span and the bending moment at the intermediate support are compared against those obtained with Euler-Bernoulli beam theory. The linear analysis with four elements using the exact stiffness matrix for both models is implemented and the results are presented in Table 2.2 for $L = 8$ m. One can see that the transverse displacement

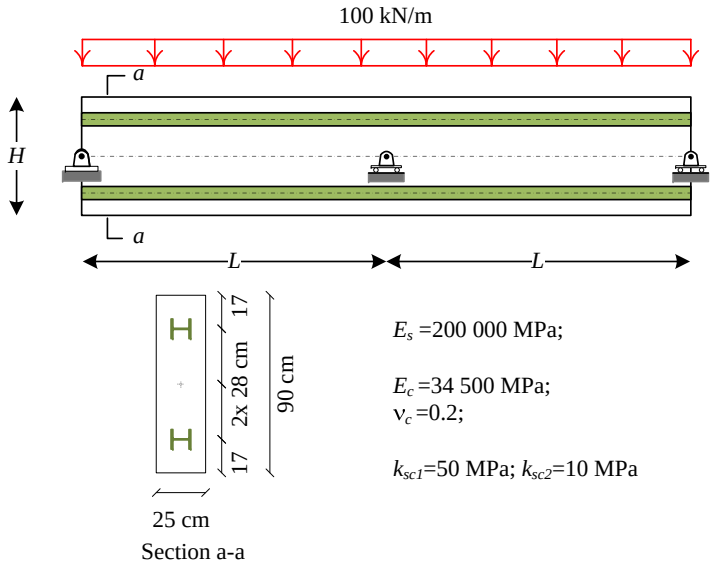

Figure 2.10: Two-span continuous hybrid beam (dimension in [cm]).

and the end slips obtained with the shear-flexible model (T-model) are greater than the ones from the shear-rigid model (EB-model). Nevertheless, the negative bending moment obtained from the T-model are smaller than the ones in the EB-model. Fig. 2.11 shows the influence of the degree of shear connection of both

Table 2.2: Numerical results

	EB-model	T-model
$v_{max}(mm)$	4.08807722	4.38853225
g_1 (mm)	0.35319143	0.35644706
g_2 (mm)	−0.49879217	−0.50751066
M_{max} (kN.m)	−795.62367844	−789.17254192

T-model and EB-model for the case where the span-to-depth ratio $L/H = 5$ and the same shear connection stiffness k_{sc} for both sliding planes. From Fig. 2.11, we can assume that for $k_{sc} = 0.1$ MPa we have a loose shear connection (without interaction) and for $k_{sc} = 10^5$ MPa we have a full interaction. Furthermore, the

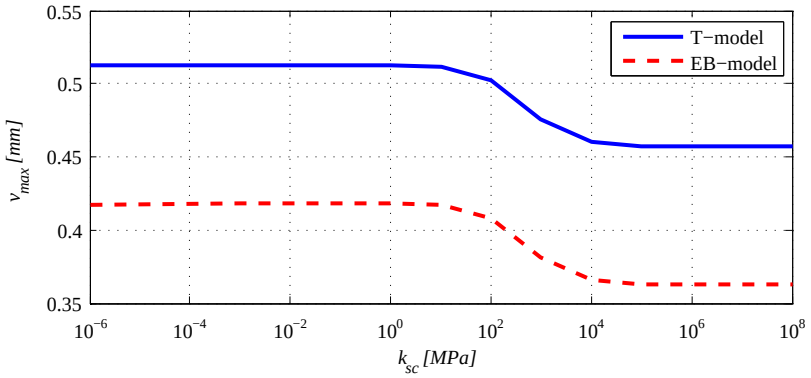

Figure 2.11: Deflection v_{max} as a function of shear connection stiffness with L/H=5.

ratio of the deflection at mid-span and the ratio of the bending moment at the intermediate support obtained with both T-model and EB-model are provided as a function of the longitudinal shear connection stiffness k_{sc} for four different values of the span-to-depth ratio L/H. The interface shear connection stiffness k_{sc} is considered as equal for both slipping planes. The curves illustrated in Fig. 2.12 confirm the important role of shear flexibility in the case of a low L/H ratio and a full connection. One can observe that the deflection ratio significantly increases,

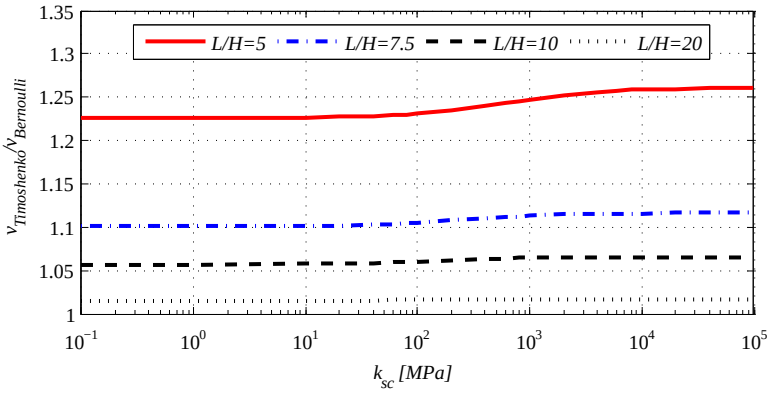

Figure 2.12: Mid-span deflection ratio versus shear connection stiffness for different span-to-depth ratios.

particularly for a low value of L/H ratio, when the value of k_{sc} varies from 0.1

MPa (almost no interaction) to 10^5 MPa (nearly full interaction). Nevertheless, increasing the value of k_{sc} has small effect on the deflection ratio for large values of L/H. For the latter case, the shear flexibility of the concrete component can be ignored which results an almost identical response of both models regardless of any value of shear connection stiffness. On the other hand, the comparison in terms of the bending moment at the intermediate support is also performed (Fig. 2.13). The four curves tend to a clear asymptotic value as k_{sc} approaches

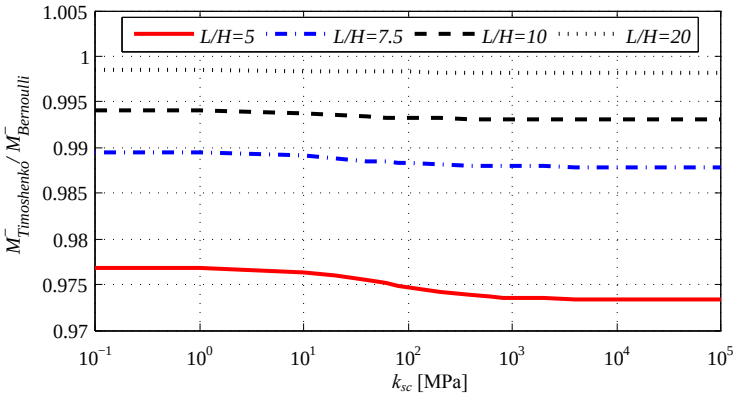

Figure 2.13: Bending moment ratio at intermediate support versus shear connection stiffness for different span-to-depth ratios.

infinity. Such limit values could be derived by analyzing the same hybrid beam adopted to Timoshenko and Bernoulli kinematic assumptions in full interaction. As expected, the beam is more flexible with the shear-flexible model than with the shear-rigid model (lower bending moment) for a short beam ($L/H = 5$) and the bending moment ratio tends to unity while the beam length gets larger.

2.7 Conclusion

In this chapter, the exact expression of the stiffness matrix has been developed for the hybrid beam-columns in partial interaction where the shear deformability of the encasing concrete component is taken into account. The exact stiffness matrix has been obtained by deriving a closed-form solution of the governing

equations of the problem. The exact solution is based on solving the coupled system of differential equations where the slips and the shear deformation of the concrete component are considered as primary variables. The proposed exact stiffness matrix can be used in a displacement-based procedure for the elastic analysis of shear-deformable hybrid beam-columns in partial interaction with arbitrary loading and support conditions.

The influence of the shear flexibility and the partial interaction on the overall behavior of the hybrid beam-columns has been investigated. A parametric analysis considering various values of the length-to-depth ratio and of the shear connection stiffness has been performed. It has been found out that transverse displacements are more affected by the shear flexibility than the slip. Indeed, the ratio of the deflection obtained from the shear-flexible model to the one obtained from the shear-rigid model varies slightly with the shear connection stiffness varying from low to high one value. On the other hand, the slenderness of the cross-section and the partial interaction have no significant effect on the slip ratio of both models.

Chapter 3

Geometrically Nonlinear Elastic Behavior

***

A new co-rotational finite element for a large displacement analysis of hybrid beam-columns.

3.1 Introduction

In contrast with a large body of literature devoted to mechanically nonlinear but geometrically linear problems of two-layered beam-columns in partial interaction, only a limited number of contributions have addressed the geometrically nonlinear behavior of layered beams. Assuming Euler-Bernoulli kinematics for each layer, linearized buckling loads have been computed by Girhammar and Gopu [15] using a modified second-order theory for two-layered beams with longitudinal slips. Hereafter, Girhammar and Pan [19] derived the exact expressions for buckling length coefficients of elastic composite beams with particular boundary conditions. A fully nonlinear analysis of steel-concrete composite beams and columns has been proposed by Pi et al. [43] considering Bernoulli kinematics for each layer. They proposed a monolithic element where an additional degree of freedom to

the deformed beam axis was added in order to describe small interlayer slips. Ranzi et al. [44] proposed a fully nonlinear kinematical model for planar composite beams including longitudinal partial interaction as well as vertical uplift. The co-rotational framework approach was considered by Battini et al. [32] and Hjiaj et al. [35] for the development of shear-rigid [32] and shear-deformable [35] beam-column element using the exact local elastic stiffness matrix. Sousa Jr et al. [45] developed a materially nonlinear displacement-based finite element model based on a total Lagrangian description considering large displacements, small strains and moderate rotations. A large displacement FE model for two-layered beam-column based on shear-rigid Reissner beam theory has been proposed by Hozjan et al. [46]. The latter model takes into account the exact geometrical and material nonlinearities as well as finite slip between the layers. Recently, Nguyen et al. [47] have presented a novel finite element model for the fully material and geometrical nonlinear analysis of shear-deformable two-layered composite planar beams with interlayer slip, using the co-rotational approach.

This chapter aims to present a new nonlinear finite element formulation for the large displacement analysis of hybrid planar beam-columns with several encased steel profiles taking into account the slips occurring at each steel-concrete interface. The co-rotational framework is adopted and the motion of the element is decomposed into a rigid body motion and a deformational part using a local co-rotational frame, which continuously translates and rotates with the element, but does not deform with it [48]. In comparison with the total and the updated Lagrangian formulations, a co-rotational element formulation has several relative advantages: (1) the co-rotational formulation is accurate and has good convergence properties for problems with large displacements and large rotations but small strains; and (2) the treatment of geometric nonlinearity is effectively undertaken at the level of discrete nodal variables with the transformation matrix between the local and global nodal entities being independent of the assumptions made for the local element. Thus many existing high-performance elements can be reused at the core of a co-rotational element formulation, and the resulting

formulation can be employed to solve large displacement and large rotation problems.

In the present work, the exact stiffness matrix derived from the analytical solution of the governing equations for hybrid beams developed in Chapter 2 will be used for the local formulation. As a result, internal nodes used to avoid the locking problem encountered in low order polynomial finite elements are not required. Therefore, this formulation is consistent with the co-rotational format. The features of the formulation presented in this chapter are as follows: (i) longitudinal partial interactions of the components are considered which provide a general description of the stresses and strains in the members; (ii) the small strain and large rotation formulation is developed which is an accurate representation of most structural behavior; (iii) exact local stiffness matrices are used, which provide accurate and stable results. The present model provides, therefore, an efficient tool for elastic nonlinear analyses of hybrid beam-columns with arbitrary support and loading conditions.

The rest of the chapter is organized as follows. Section 3.2 deals with the co-rotational framework, the derivation of the transformation matrices and issues related to eccentric nodes and forces. Five numerical examples are presented in Section 3.4 in order to assess the performance of the formulation and support the conclusions drawn in Section 3.5.

3.2 Co-rotational framework

We consider a hybrid beam with n embedded sections experiencing arbitrarily large displacements and rotations with respect to the global frame but strains are assumed to remain small. The main ingredients of a co-rotational formulation are: (i) the choice of co-rotating frame, (ii) the derivation of the relationships between the local variables and the global ones, and (iii) a variationally consistent internal force vector and the tangent stiffness matrix.

3.2.1 Beam kinematics

The co-rotational description of the motion of a deformable body finds its roots in the polar decomposition theorem [49] which states that the total deformation of a continuous body can be decomposed into a rigid body motion and a pure deformation part. In finite element implementations, this decomposition is performed by defining a local reference system attached to the element, which translates and rotates with the element but does not deform with it. With respect to the moving frame, local deformational displacements are defined and the geometrical nonlinearity induced by element large rigid-body motion is incorporated into the transformation matrix relating local and global displacements.

The origin of the co-rotational frame is taken at the node c_i which corresponds to the centroid of the concrete cross-section, see Fig. 3.1. The x_l-axis of the local coordinate system is defined by the line connecting c_i and c_j. The y_l-axis is orthogonal to the x_l-axis so that the result is right handed orthogonal coordinate system. The motion of the element from the original undeformed configuration to the actual deformed one can thus be separated into two parts. The first one, which corresponds to the rigid motion of the local frame, is the translation of the node c_i and the rigid rotation α of the x_l-axis. The second one refers to the deformations in the co-rotational element frame which remain small with respect to local frame. The strains and internal nodal forces of the element are calculated from these relative deformations. As a consequence, the linear beam theory defined in Chapter 2 can be used for describing the relative deformations, endowing the method with significant advantages in computational speed and programming simplicity.

The notations used in this chapter are defined in Fig. 3.1 and Fig. 3.2. All variables subscripted with "s_k" belong to the embedded steel element "s_k" and those with "c" belong to the encasing concrete component. The coordinates of the

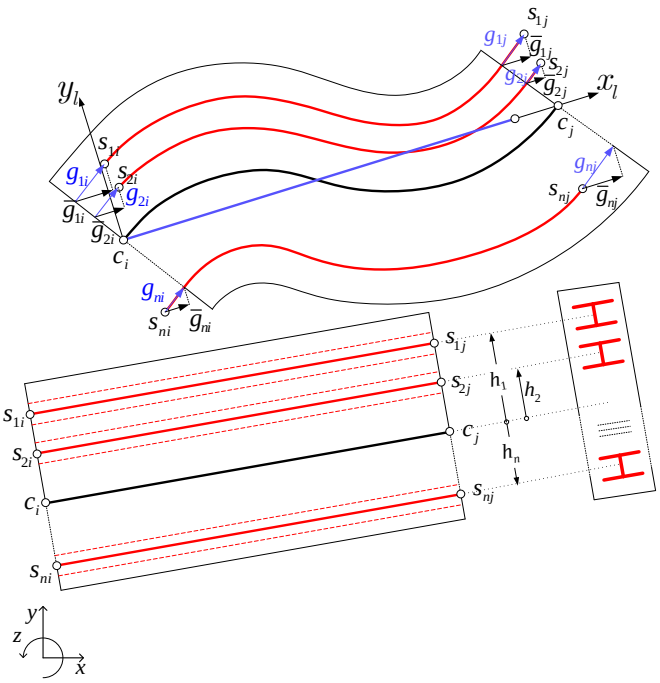

Figure 3.1: Co-rotational kinematic: slips.

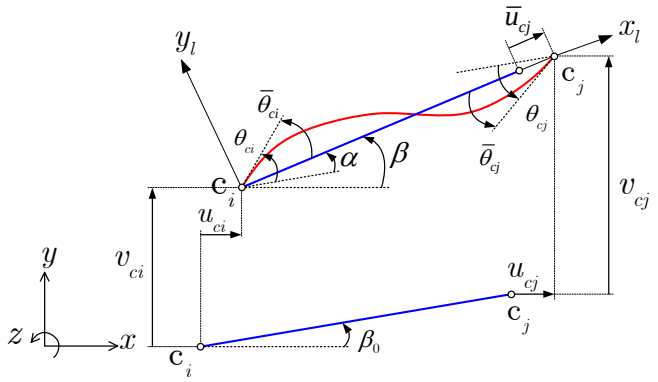

Figure 3.2: Co-rotational kinematic: displacement and rotations.

nodes c_i and c_j in the global coordinate system (x, y) are (x_{c_i}, y_{c_i}) and (x_{c_j}, y_{c_j}), respectively. The element has $2(n + 4)$ degrees of freedom: global displacements and rotations of the nodes (c_i and c_j) and slips (g_{ki}, g_{kj}) between the embedded steels "s_k" and the encasing concrete component "c" at both ends of the element. As the steel elements are surrounded by the concrete component, uplift cannot

occur. Thus, the rotations of each steel cross-section at the end nodes are equal (Bernoulli's assumption) and the slips ($g_{\mathrm{k}i}, g_{\mathrm{k}j}$) are perpendicular to the end cross-sections of the steel components.

The vectors of global and local displacements are respectively defined by Eq. (3.1) and Eq. (3.2)

$$\mathbf{p}_g = [u_{\mathrm{c}i}\ v_{\mathrm{c}i}\ \theta_{\mathrm{c}i}\ \theta_{\mathrm{s}i}\ g_{1i}\ g_{2i}\ \cdots\ g_{ni}\ u_{\mathrm{c}j}\ v_{\mathrm{c}j}\ \theta_{\mathrm{c}j}\ \theta_{\mathrm{s}j}\ g_{1j}\ g_{2j}\ \cdots\ g_{nj}]^{\mathrm{T}} \tag{3.1}$$

$$\mathbf{p}_l = [\bar{u}_{\mathrm{s}1i}\ \bar{u}_{\mathrm{s}2i}\ \cdots\ \bar{u}_{\mathrm{s}ni}\ \bar{u}_{\mathrm{c}i}\ \bar{v}_{\mathrm{c}i}\ \bar{\theta}_{\mathrm{s}i}\ \bar{\theta}_{\mathrm{c}i}\ \bar{u}_{\mathrm{s}1j}\ \bar{u}_{\mathrm{s}2j}\ \cdots\ \bar{u}_{\mathrm{s}nj}\ \bar{u}_{\mathrm{c}j}\ \bar{v}_{\mathrm{c}j}\ \bar{\theta}_{\mathrm{s}j}\ \bar{\theta}_{\mathrm{c}j}]^{\mathrm{T}} \tag{3.2}$$

The rigid rotation of the x_l-axis, α is obtained using the geometrical relation:

$$\sin\alpha = c_o\, s - s_o\, c \tag{3.3}$$

$$\cos\alpha = c_o\, c + s_o\, s \tag{3.4}$$

with

$$c_o = \cos\beta_o = \frac{1}{l_o}\,(x_{\mathrm{c}j} - x_{\mathrm{c}i}) \tag{3.5}$$

$$s_o = \sin\beta_o = \frac{1}{l_o}\,(y_{\mathrm{c}j} - y_{\mathrm{c}i}) \tag{3.6}$$

$$c = \cos\beta = \frac{1}{l_n}\,(x_{\mathrm{c}j} + u_{\mathrm{c}j} - x_{\mathrm{c}i} - u_{\mathrm{c}i}) \tag{3.7}$$

$$s = \sin\beta = \frac{1}{l_n}\,(y_{\mathrm{c}j} + v_{\mathrm{c}j} - y_{\mathrm{c}i} - v_{\mathrm{c}i}) \tag{3.8}$$

l_o and l_n being the element length in initial and deformed configuration, respectively:

$$l_o = [(x_{\mathrm{c}j} - x_{\mathrm{c}i})^2 + (y_{\mathrm{c}j} - y_{\mathrm{c}i})^2]^{1/2} \tag{3.9}$$

$$l_n = [(x_{\mathrm{c}j} + u_{\mathrm{c}j} - x_{\mathrm{c}i} - u_{\mathrm{c}i})^2 + (y_{\mathrm{c}j} + v_{\mathrm{c}j} - y_{\mathrm{c}i} - v_{\mathrm{c}i})^2]^{1/2} \tag{3.10}$$

Based on the definition of the co-rotating frame, the components of the local displacements $\mathbf{p}_l$ are computed according to:

$$\bar{u}_{ci} = 0 \tag{3.11}$$

$$\bar{v}_i = 0 \tag{3.12}$$

$$\bar{v}_j = 0 \tag{3.13}$$

$$\bar{u}_{cj} = l_n - l_o \tag{3.14}$$

$$\bar{\theta}_{si} = \theta_{si} - \alpha \tag{3.15}$$

$$\bar{\theta}_{ci} = \theta_{ci} - \alpha \tag{3.16}$$

$$\bar{\theta}_{sj} = \theta_{sj} - \alpha \tag{3.17}$$

$$\bar{\theta}_{cj} = \theta_{cj} - \alpha \tag{3.18}$$

$$\bar{u}_{ski} = -\bar{g}_{ki} - h_k\,\bar{\theta}_{ci} \tag{3.19}$$

$$\bar{u}_{skj} = -\bar{g}_{kj} + \bar{u}_{cj} - h_k\,\bar{\theta}_{cj} \tag{3.20}$$

where local slips $\bar{g}_{kl}$ are defined in local element formulation (see Section 3.4) and determined by

$$\bar{g}_{kl} = g_{kl}\,\cos\bar{\theta}_{sl}, \qquad l = i, j; \qquad k = 1, 2, \cdots n \tag{3.21}$$

3.2.2 Element formulation

A key step in the the co-rotational method is to establish the relationship between the local variables and the global ones. This is accomplished by performing a change of variables between the global quantities and the local ones. The second stage is to remove the rigid body motions from the element displacement field which is achieved by calculating the local displacements using Eqs. (3.11-3.21).

Let us consider two different coordinate systems with subscript i and j. Assume that the internal force vector $\mathbf{f}_i$ and tangent stiffness matrix $\mathbf{K}_i$ are consistent with the displacement vector $\mathbf{p}_i$ such that

$$\delta\mathbf{f}_i = \mathbf{K}_i\,\delta\mathbf{p}_i \tag{3.22}$$

Consider now that $\mathbf{p}_i$ is related to the displacement vector $\mathbf{p}_j$ through

$$\delta\mathbf{p}_i = \mathbf{B}_{ij}\,\delta\mathbf{p}_j \tag{3.23}$$

Then, by equating the virtual work in both systems, the internal force vector $\mathbf{f}_j$ consistent with $\mathbf{p}_j$ is defined by

$$\mathbf{f}_j = \mathbf{B}_{ij}^{\mathrm{T}}\,\mathbf{f}_i \tag{3.24}$$

The expression of the tangent stiffness matrix $\mathbf{K}_j$, consistent with $\mathbf{p}_j$ is obtained by differentiating Eq. (3.24) and combining the outcome with Eq. (3.22) and Eq. (3.23):

$$\mathbf{K}_j = \mathbf{B}_{ij}^{\mathrm{T}}\,\mathbf{K}_i\,\mathbf{B}_{ij} + \mathbf{H}_{ij} \qquad \mathbf{H}_{ij} = \left.\frac{\partial(\mathbf{B}_{ij}^{\mathrm{T}}\,\mathbf{f}_i)}{\partial\mathbf{p}_j}\right|_{\mathbf{f}_i} \tag{3.25}$$

From the idea described above, the element formulation can be obtained using three consecutive changes of variables and four different displacement vectors as follows:

$$\mathbf{p}_l = [\bar{u}_{\mathrm{s}1i}\ \bar{u}_{\mathrm{s}2i}\ \cdots\ \bar{u}_{\mathrm{sn}i}\ \bar{u}_{\mathrm{c}i}\ \bar{v}_{\mathrm{c}i}\ \bar{\theta}_{\mathrm{s}i}\ \bar{\theta}_{\mathrm{c}i}\ \bar{u}_{\mathrm{s}1j}\ \bar{u}_{\mathrm{s}2j}\ \cdots\ \bar{u}_{\mathrm{sn}j}\ \bar{u}_{\mathrm{c}j}\ \bar{v}_{\mathrm{c}j}\ \bar{\theta}_{\mathrm{s}j}\ \bar{\theta}_{\mathrm{c}j}]^{\mathrm{T}} \tag{3.26}$$

$$\mathbf{p}_e = [\ \bar{\theta}_{\mathrm{s}i}\ \ \bar{\theta}_{\mathrm{c}i}\ \ \bar{u}_{\mathrm{c}j}\ \ \bar{\theta}_{\mathrm{s}j}\ \ \bar{\theta}_{\mathrm{c}j}\ \ \bar{g}_{1i}\ \ \bar{g}_{2i}\ \ \cdots\ \ \bar{g}_{ni}\ \ \bar{g}_{1j}\ \ \bar{g}_{2j}\ \ \cdots\ \ \bar{g}_{nj}\ ]^{\mathrm{T}} \tag{3.27}$$

$$\mathbf{p}_a = [\ \bar{\theta}_{\mathrm{s}i}\ \ \bar{\theta}_{\mathrm{c}i}\ \ \bar{u}_{\mathrm{c}j}\ \ \bar{\theta}_{\mathrm{s}j}\ \ \bar{\theta}_{\mathrm{c}j}\ \ g_{1i}\ \ g_{2i}\ \ \cdots\ \ g_{ni}\ \ g_{1j}\ \ g_{2j}\ \ \cdots\ \ g_{nj}\ ]^{\mathrm{T}} \tag{3.28}$$

$$\mathbf{p}_g = [u_{\mathrm{c}i}\ v_{\mathrm{c}i}\ \theta_{\mathrm{c}i}\ \theta_{\mathrm{s}i}\ g_{1i}\ g_{2i}\ \cdots\ g_{ni}\ u_{\mathrm{c}j}\ v_{\mathrm{c}j}\ \theta_{\mathrm{c}j}\ \theta_{\mathrm{s}j}\ g_{1j}\ g_{2j}\ \cdots\ g_{nj}]^{\mathrm{T}} \tag{3.29}$$

For the sake of clarity in representing the transformation matrices, we present in the following the formulations of hybrid beam-column with three embedded steel sections. Nevertheless, the concepts are also applicable to general case of n embedded steel sections. The first change of variables between $\mathbf{p}_l$ and $\mathbf{p}_e$ is based on the linear equations (Eqs. (3.11-3.13 and Eqs. (3.19-3.20)). Then, the transformation matrices giving $\mathbf{f}_e$ and $\mathbf{K}_e$ as function of $\mathbf{f}_l$ and $\mathbf{K}_l$ are easily

obtained:

$$\mathbf{B}_{le} = \begin{bmatrix} 0 & -h_1 & 0 & 0 & 0 & -1 & 0 & 0 & 0 & 0 & 0 \\ 0 & -h_2 & 0 & 0 & 0 & 0 & -1 & 0 & 0 & 0 & 0 \\ 0 & -h_3 & 0 & 0 & 0 & 0 & 0 & -1 & 0 & 0 & 0 \\ 0 & 0 & 0 & 0 & 0 & 0 & 0 & 0 & 0 & 0 & 0 \\ 0 & 0 & 0 & 0 & 0 & 0 & 0 & 0 & 0 & 0 & 0 \\ 1 & 0 & 0 & 0 & 0 & 0 & 0 & 0 & 0 & 0 & 0 \\ 0 & 1 & 0 & 0 & 0 & 0 & 0 & 0 & 0 & 0 & 0 \\ 0 & 0 & 1 & 0 & -h_1 & 0 & 0 & 0 & -1 & 0 & 0 \\ 0 & 0 & 1 & 0 & -h_2 & 0 & 0 & 0 & 0 & -1 & 0 \\ 0 & 0 & 1 & 0 & -h_3 & 0 & 0 & 0 & 0 & 0 & -1 \\ 0 & 0 & 1 & 0 & 0 & 0 & 0 & 0 & 0 & 0 & 0 \\ 0 & 0 & 0 & 0 & 0 & 0 & 0 & 0 & 0 & 0 & 0 \\ 0 & 0 & 0 & 1 & 0 & 0 & 0 & 0 & 0 & 0 & 0 \\ 0 & 0 & 0 & 0 & 1 & 0 & 0 & 0 & 0 & 0 & 0 \end{bmatrix} \tag{3.30}$$

Consequently,

$$\mathbf{H}_{le} = \mathbf{0} \tag{3.31}$$

For the second change of variables from $\mathbf{p}_e$ to $\mathbf{p}_a$, the transformation matrices giving $\mathbf{f}_a$ and $\mathbf{K}_a$ as function of $\mathbf{f}_e$ and $\mathbf{K}_e$ are derived using Eq. (3.21).

$$\mathbf{B}_{ea} = \begin{bmatrix} 1 & 0 & 0 & 0 & 0 & 0 & 0 & 0 & 0 & 0 & 0 \\ 0 & 1 & 0 & 0 & 0 & 0 & 0 & 0 & 0 & 0 & 0 \\ 0 & 0 & 1 & 0 & 0 & 0 & 0 & 0 & 0 & 0 & 0 \\ 0 & 0 & 0 & 1 & 0 & 0 & 0 & 0 & 0 & 0 & 0 \\ 0 & 0 & 0 & 0 & 1 & 0 & 0 & 0 & 0 & 0 & 0 \\ -g_{1i}\sin\bar{\theta}_{si} & 0 & 0 & 0 & 0 & \cos\bar{\theta}_{si} & 0 & 0 & 0 & 0 & 0 \\ -g_{2i}\sin\bar{\theta}_{si} & 0 & 0 & 0 & 0 & 0 & \cos\bar{\theta}_{si} & 0 & 0 & 0 & 0 \\ -g_{3i}\sin\bar{\theta}_{si} & 0 & 0 & 0 & 0 & 0 & 0 & \cos\bar{\theta}_{si} & 0 & 0 & 0 \\ 0 & 0 & 0 & -g_{1j}\sin\bar{\theta}_{sj} & 0 & 0 & 0 & 0 & \cos\bar{\theta}_{sj} & 0 & 0 \\ 0 & 0 & 0 & -g_{2j}\sin\bar{\theta}_{sj} & 0 & 0 & 0 & 0 & 0 & \cos\bar{\theta}_{sj} & 0 \\ 0 & 0 & 0 & -g_{3j}\sin\bar{\theta}_{sj} & 0 & 0 & 0 & 0 & 0 & 0 & \cos\bar{\theta}_{sj} \end{bmatrix} \tag{3.32}$$

Then,

$$\mathbf{H}_{ea}^{\mathrm{T}} = \left[\begin{array}{ccc} \mathbf{H}_{ea}(1) & \cdots & \mathbf{H}_{ea}(11) \end{array} \right] \tag{3.33}$$

where the non-zero components are

$$\mathbf{H}_{ea}(1)^{\mathrm{T}} = \left[\begin{array}{c} -\sum_{k=1}^{3} g_{ki} f_e(5+k) \cos\bar{\theta}_{\mathrm{s}i} \\ 0 \\ 0 \\ 0 \\ 0 \\ -\sin\bar{\theta}_{\mathrm{s}i}\, f_e(6) \\ -\sin\bar{\theta}_{\mathrm{s}i}\, f_e(7) \\ -\sin\bar{\theta}_{\mathrm{s}i}\, f_e(8) \\ 0 \\ 0 \\ 0 \end{array} \right] ; \quad \mathbf{H}_{ea}(4)^{\mathrm{T}} = \left[\begin{array}{c} 0 \\ 0 \\ 0 \\ -\sum_{k=1}^{3} g_{kj} f_e(8+k) \cos\bar{\theta}_{\mathrm{s}j} \\ 0 \\ 0 \\ 0 \\ 0 \\ -\sin\bar{\theta}_{\mathrm{s}j}\, f_e(9) \\ -\sin\bar{\theta}_{\mathrm{s}j}\, f_e(10) \\ -\sin\bar{\theta}_{\mathrm{s}j}\, f_e(11) \end{array} \right] \tag{3.34}$$

$$\mathbf{H}_{ea}(6)^{\mathrm{T}} = [\ -\sin\bar{\theta}_{\mathrm{s}i}\, f_e(6) \quad 0 \quad 0 \quad 0 \quad 0 \quad 0 \quad 0 \quad 0 \quad 0 \quad 0 \quad 0\ ] \tag{3.35}$$

$$\mathbf{H}_{ea}(7)^{\mathrm{T}} = [\ -\sin\bar{\theta}_{\mathrm{s}i}\, f_e(7) \quad 0 \quad 0 \quad 0 \quad 0 \quad 0 \quad 0 \quad 0 \quad 0 \quad 0 \quad 0\ ] \tag{3.36}$$

$$\mathbf{H}_{ea}(8)^{\mathrm{T}} = [\ -\sin\bar{\theta}_{\mathrm{s}i}\, f_e(8) \quad 0 \quad 0 \quad 0 \quad 0 \quad 0 \quad 0 \quad 0 \quad 0 \quad 0 \quad 0\ ] \tag{3.37}$$

$$\mathbf{H}_{ea}(9)^{\mathrm{T}} = [\ 0 \quad 0 \quad 0 \quad -\sin\bar{\theta}_{\mathrm{s}j}\, f_e(9) \quad 0 \quad 0 \quad 0 \quad 0 \quad 0 \quad 0 \quad 0\ ] \tag{3.38}$$

$$\mathbf{H}_{ea}(10)^{\mathrm{T}} = [\ 0 \quad 0 \quad 0 \quad -\sin\bar{\theta}_{\mathrm{s}j}\, f_e(10) \quad 0 \quad 0 \quad 0 \quad 0 \quad 0 \quad 0 \quad 0\ ] \tag{3.39}$$

$$\mathbf{H}_{ea}(11)^{\mathrm{T}} = [\ 0 \quad 0 \quad 0 \quad -\sin\bar{\theta}_{\mathrm{s}j}\, f_e(11) \quad 0 \quad 0 \quad 0 \quad 0 \quad 0 \quad 0 \quad 0\ ] \tag{3.40}$$

with

$$\mathbf{f}_e^{\mathrm{T}} = [f_e(1)\ f_e(2)\ \cdots\ f_e(11)] \tag{3.41}$$

The third change of variables from $\mathbf{p}_a$ to $\mathbf{p}_g$ is performed using Eqs. (3.14-3.18). After some algebraic manipulations (see e.g. [48]), the transformation matrices giving $\mathbf{f}_g$ and $\mathbf{K}_g$ as function of $\mathbf{f}_a$ and $\mathbf{K}_a$ are obtained. The transformation

matrices are given as follows.

$$\mathbf{B}_{ag} = \begin{bmatrix} -s/l_n & c/l_n & 0 & 1 & 0 & 0 & 0 & s/l_n & -c/l_n & 0 & 0 & 0 & 0 & 0 \\ -s/l_n & c/l_n & 1 & 0 & 0 & 0 & 0 & s/l_n & -c/l_n & 0 & 0 & 0 & 0 & 0 \\ -c & -s & 0 & 0 & 0 & 0 & 0 & c & s & 0 & 0 & 0 & 0 & 0 \\ -s/l_n & c/l_n & 0 & 0 & 0 & 0 & 0 & s/l_n & -c/l_n & 0 & 1 & 0 & 0 & 0 \\ -s/l_n & c/l_n & 0 & 0 & 0 & 0 & 0 & s/l_n & -c/l_n & 1 & 0 & 0 & 0 & 0 \\ 0 & 0 & 0 & 0 & 1 & 0 & 0 & 0 & 0 & 0 & 0 & 0 & 0 & 0 \\ 0 & 0 & 0 & 0 & 0 & 1 & 0 & 0 & 0 & 0 & 0 & 0 & 0 & 0 \\ 0 & 0 & 0 & 0 & 0 & 0 & 1 & 0 & 0 & 0 & 0 & 0 & 0 & 0 \\ 0 & 0 & 0 & 0 & 0 & 0 & 0 & 0 & 0 & 0 & 0 & 1 & 0 & 0 \\ 0 & 0 & 0 & 0 & 0 & 0 & 0 & 0 & 0 & 0 & 0 & 0 & 1 & 0 \\ 0 & 0 & 0 & 0 & 0 & 0 & 0 & 0 & 0 & 0 & 0 & 0 & 0 & 1 \end{bmatrix} \tag{3.42}$$

and

$$\mathbf{H}_{ag} = f_a(3)\frac{\mathbf{z}\,\mathbf{z}^{\mathrm{T}}}{l_n} + (f_a(1) + f_a(2) + f_a(4) + f_a(5))\frac{\mathbf{r}\,\mathbf{z}^{\mathrm{T}} + \mathbf{z}\,\mathbf{r}^{\mathrm{T}}}{l_n^2} \tag{3.43}$$

where

$$\mathbf{z}^{\mathrm{T}} = [s \;\; -c \; 0 \; 0 \; 0 \; 0 \; 0 \;\; -s \; c \; 0 \; 0 \; 0 \; 0 \; 0] \tag{3.44}$$

$$\mathbf{r}^{\mathrm{T}} = [-c \;\; -s \; 0 \; 0 \; 0 \; 0 \; 0 \; c \; s \; 0 \; 0 \; 0 \; 0 \; 0] \tag{3.45}$$

$$\mathbf{f}_a^{\mathrm{T}} = [f_a(1) \;\; f_e(2) \;\; \cdots \;\; f_e(11)] \tag{3.46}$$

and c, s defined in Eqs. (3.7) and (3.8).

3.2.3 Eccentric nodes and forces

The boundary conditions for composite and hybrid beams may be complicated to define and depend strongly on how the member is connected to the rest of the structure. In general, one could distribute the external load among the different constituent according to some rules among which, the relative stiffness. This would lead to the same axial displacement of each constituent at the beginning of the load step. Another option is to assume no slip at the beam end and the load

is applied at an arbitrary point within the cross-section. This section presents the possibility to deal with those options in the proposed formulation.

The choice of the slips as the degrees of freedom is indispensable for the robustness of the formulation. Due to this choice (see Eq. (3.1)) the boundary conditions require a special treatment in case external concentrated loads are not applied to the node located at the centroid of the beam cross-section (origin of the local frame) but somewhere else on the cross-section.

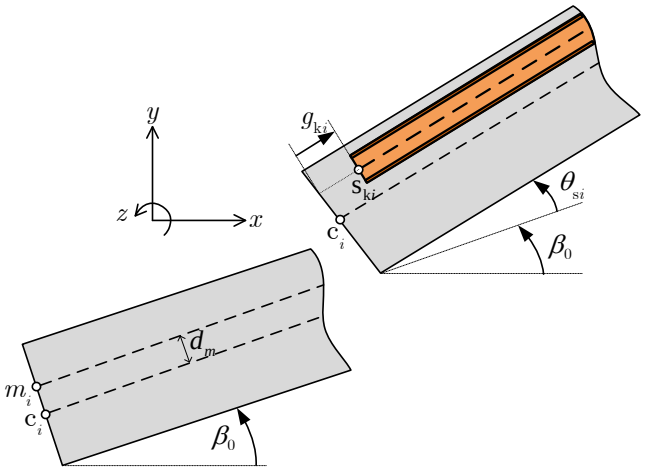

Figure 3.3: Eccentric nodes and forces.

3.2.3.1 Eccentric nodes

Let us first consider (see Fig. 3.3) that prescribed displacement or rotation are applied at node m_i. This situation requires a rigid link between the nodes c_i and m_i and a change of degrees of freedom from $\mathbf{p}_g$ to $\mathbf{p}_m$ with

$$\mathbf{p}_m = [u_{\mathrm{m}i}\ v_{\mathrm{m}i}\ \theta_{\mathrm{c}i}\ \theta_{\mathrm{s}i}\ g_{1i}\ g_{2i}\ \cdots\ g_{ni}\ u_{\mathrm{c}j}\ v_{\mathrm{c}j}\ \theta_{\mathrm{c}j}\ \theta_{\mathrm{s}j}\ g_{1j}\ g_{2j}\ \cdots\ g_{nj}]^{\mathrm{T}} \tag{3.47}$$

The displacements of the node m_i can easily be obtained as

$$\begin{bmatrix} u_{\mathrm{m}i} \\ v_{\mathrm{m}i} \end{bmatrix} = \begin{bmatrix} u_{\mathrm{c}i} \\ v_{\mathrm{c}i} \end{bmatrix} + \begin{bmatrix} \cos\theta_{\mathrm{c}i} - 1 & -\sin\theta_{\mathrm{c}i} \\ \sin\theta_{\mathrm{c}i} & \cos\theta_{\mathrm{c}i} - 1 \end{bmatrix} \begin{bmatrix} -\sin\beta_o \\ \cos\beta_o \end{bmatrix} d_{\mathrm{m}} \tag{3.48}$$

which, after differentiation, gives

$$\begin{bmatrix} \delta u_{\mathrm{m}i} \\ \delta v_{\mathrm{m}i} \end{bmatrix} = \begin{bmatrix} \delta u_{\mathrm{c}i} \\ \delta v_{\mathrm{c}i} \end{bmatrix} - \begin{bmatrix} \cos(\beta_o + \theta_{\mathrm{c}i}) \\ \sin(\beta_o + \theta_{\mathrm{c}i}) \end{bmatrix} d_{\mathrm{m}}\, \delta\theta_{\mathrm{c}i} \tag{3.49}$$

The internal force vector and tangent stiffness matrix consistent with $\mathbf{p}_m$ are then obtained, see Section 3.2.2, using the transformation matrix $\mathbf{B}_{gm}$. This gives

$$\delta\mathbf{p}_g = \mathbf{B}_{gm}\,\delta\mathbf{p}_m \quad \mathbf{f}_m = \mathbf{B}_{gm}^{\mathrm{T}}\,\mathbf{f}_g \quad \mathbf{K}_m = \mathbf{B}_{gm}^{\mathrm{T}}\,\mathbf{K}_g\,\mathbf{B}_{gm} + \mathbf{H}_{gm} \tag{3.50}$$

with

$$\mathbf{B}_{gm\,(k,k)} = 1 \qquad k = 1, 2, \cdots, 2n+8 \tag{3.51}$$

$$\mathbf{B}_{gm\,(1,3)} = \cos(\beta_o + \theta_{\mathrm{c}i})\, d_{\mathrm{m}} \tag{3.52}$$

$$\mathbf{B}_{gm\,(2,3)} = \sin(\beta_o + \theta_{\mathrm{c}i})\, d_{\mathrm{m}} \tag{3.53}$$

and the only non zero term in the matrix $\mathbf{H}_{gm}$ is

$$\mathbf{H}_{gm\,(3,3)} = -\sin(\beta_o + \theta_{\mathrm{c}i})\, d_{\mathrm{m}}\, f_g(1) + \cos(\beta_o + \theta_{\mathrm{c}i})\, d_{\mathrm{m}}\, f_g(2) \tag{3.54}$$

3.2.3.2 Eccentric forces

Let us now consider that two external force vectors $\mathbf{f}_{\mathrm{c}i}$ and $\mathbf{f}_{\mathrm{sk}i}$ defined by

$$\mathbf{f}_{\mathrm{c}i} = [\ f_{\mathrm{c}i}(1) \quad f_{\mathrm{c}i}(2) \quad f_{\mathrm{c}i}(3)\ ]^{\mathrm{T}}; \quad \mathbf{f}_{\mathrm{sk}i} = [\ f_{\mathrm{sk}i}(1) \quad f_{\mathrm{sk}i}(2) \quad f_{\mathrm{sk}i}(3)\ ]^{\mathrm{T}} \tag{3.55}$$

are applied at the nodes c_i and $\mathrm{s}_{\mathrm{k}i}$. $f_{\mathrm{c}i}(1), f_{\mathrm{sk}i}(1)$ are horizontal forces (in the local frame); $f_{\mathrm{c}i}(2)$, $f_{\mathrm{sk}i}(2)$ are vertical forces and $f_{\mathrm{c}i}(3)$, $f_{\mathrm{sk}i}(3)$ are moments. These loads require a special treatment since the degrees of freedom of the element are $\mathbf{p}_m$, see Eq. (3.47). The idea is to calculate the loads applied at node m_i which perform the same external virtual work.

For the load $\mathbf{f}_{\mathrm{m}i}$, it gives

$$[\,\delta u_{\mathrm{m}i}\,\delta v_{\mathrm{m}i}\,\delta\theta_{\mathrm{c}i}\,]\,\mathbf{f}_{\mathrm{m}i} = [\,\delta u_{\mathrm{c}i}\,\delta v_{\mathrm{c}i}\,\delta\theta_{\mathrm{c}i}\,]\,\mathbf{f}_{\mathrm{c}i} \tag{3.56}$$

Using Eq. (3.49), one gets

$$\mathbf{f}_{\mathrm{m}i} = \begin{bmatrix} 1 & 0 & 0 \\ 0 & 1 & 0 \\ \cos(\beta_o + \theta_{ci})\, d_{\mathrm{m}} & \sin(\beta_o + \theta_{ci})\, d_{\mathrm{m}} & 1 \end{bmatrix} \mathbf{f}_{ci} \tag{3.57}$$

Differentiating Eq. (3.57) gives the stiffness correction term $\mathbf{K}_{sm}$ associated to $[\, u_{\mathrm{m}i}\, v_{\mathrm{m}i}\, \theta_{ci}\,]$, which must be subtracted from the tangent stiffness matrix of the structure, as

$$\mathbf{K}_{sm} = \begin{bmatrix} 0 & 0 & 0 \\ 0 & 0 & 0 \\ 0 & 0 & A \end{bmatrix}; \quad A = -\sin(\beta_o + \theta_{ci})\, d_{\mathrm{m}}\, f_{ci}(1) + \cos(\beta_o + \theta_{ci})\, d_{\mathrm{m}}\, f_{ci}(2) \tag{3.58}$$

In the case external loads are applied to an embedded section $\mathbf{f}_{\mathrm{sk}i}$, the calculations are more complicated since the slip $g_{\mathrm{k}i}$ is involved. Equating the external virtual work performed by both force vectors gives

$$[\ \delta u_{\mathrm{m}i} \quad \delta v_{\mathrm{m}i} \quad \delta\theta_{ci} \quad \delta\theta_{\mathrm{s}i} \quad \delta g_{\mathrm{k}i}\ ]\, \mathbf{f}_{\mathrm{m}i} = [\ \delta u_{\mathrm{sk}i} \quad \delta v_{\mathrm{sk}i} \quad \delta\theta_{\mathrm{s}i}\ ]\, \mathbf{f}_{\mathrm{sk}i} \tag{3.59}$$

The displacements of the node $\mathrm{s}_{\mathrm{k}i}$ can be obtained as (see Fig. 3.3)

$$\begin{bmatrix} u_{\mathrm{sk}i} \\ v_{\mathrm{sk}i} \end{bmatrix} = \begin{bmatrix} u_{\mathrm{m}i} \\ v_{\mathrm{m}i} \end{bmatrix} + \begin{bmatrix} \cos\theta_{ci} - 1 & -\sin\theta_{ci} \\ \sin\theta_{ci} & \cos\theta_{ci} - 1 \end{bmatrix} \begin{bmatrix} -\sin\beta_o \\ \cos\beta_o \end{bmatrix} h_{\mathrm{m}} + \begin{bmatrix} \cos(\beta_o + \theta_{si}) \\ \sin(\beta_o + \theta_{si}) \end{bmatrix} g_{\mathrm{k}i} \tag{3.60}$$

with $h_{\mathrm{m}} = h_{\mathrm{k}} - d_{\mathrm{m}}$. After differentiation, it gives

$$\begin{bmatrix} \delta u_{\mathrm{sk}i} \\ \delta v_{\mathrm{sk}i} \end{bmatrix} = \begin{bmatrix} \delta u_{\mathrm{m}i} \\ \delta v_{\mathrm{m}i} \end{bmatrix} - \begin{bmatrix} \cos(\beta_o + \theta_{ci}) \\ \sin(\beta_o + \theta_{ci}) \end{bmatrix} h_{\mathrm{m}}\, \delta\theta_{ci} - \begin{bmatrix} \sin(\beta_o + \theta_{\mathrm{s}i})\, g_{\mathrm{k}i} \\ -\cos(\beta_o + \theta_{\mathrm{s}i})\, g_{\mathrm{k}i} \end{bmatrix} \delta\theta_{\mathrm{s}i} + \begin{bmatrix} \cos(\beta_o + \theta_{\mathrm{s}i}) \\ \sin(\beta_o + \theta_{\mathrm{s}i}) \end{bmatrix} \delta g_{\mathrm{k}i} \tag{3.61}$$

By inserting Eq. (3.61) into Eq. (3.59), one obtains

$$\mathbf{f}_{\mathrm{m}i} = \begin{bmatrix} 1 & 0 & 0 \\ 0 & 1 & 0 \\ -\cos(\beta_o + \theta_{\mathrm{c}i})\, h_{\mathrm{m}} & -\sin(\beta_o + \theta_{\mathrm{c}i})\, h_{\mathrm{m}} & 0 \\ -\sin(\beta_o + \theta_{\mathrm{s}i})\, g_{\mathrm{k}i} & \cos(\beta_o + \theta_{\mathrm{s}i})\, g_{\mathrm{k}i} & 1 \\ \cos(\beta_o + \theta_{\mathrm{s}i}) & \sin(\beta_o + \theta_{\mathrm{s}i}) & 0 \end{bmatrix} \mathbf{f}_{\mathrm{sk}i} \tag{3.62}$$

Differentiating Eq. (3.62) gives the stiffness correction term $\mathbf{K}_{ssk}$ associated to $[\, u_{\mathrm{m}i}\, v_{\mathrm{m}i}\, \theta_{\mathrm{c}i}\, \theta_{\mathrm{s}i}\, g_{\mathrm{k}i}]$, which must be subtracted from the tangent stiffness matrix of the structure, as

$$\mathbf{K}_{ssk} = \begin{bmatrix} 0 & 0 & 0 & 0 & 0 \\ 0 & 0 & 0 & 0 & 0 \\ 0 & 0 & A & 0 & 0 \\ 0 & 0 & 0 & B & C \\ 0 & 0 & 0 & C & 0 \end{bmatrix} \tag{3.63}$$

with

$$A = f_{\mathrm{sk}i}(1)\, h_m\, \sin(\beta_o + \theta_{\mathrm{c}i}) - f_{\mathrm{sk}i}(2)\, h_m\, \cos(\beta_o + \theta_{\mathrm{c}i}) \tag{3.64}$$

$$B = -f_{\mathrm{sk}i}(1)\, g_{\mathrm{k}i}\, \cos(\beta_o + \theta_{\mathrm{s}i}) - f_{\mathrm{sk}i}(2)\, g_{\mathrm{k}i}\, \sin(\beta_o + \theta_{\mathrm{s}i}) \tag{3.65}$$

$$C = f_{\mathrm{sk}i}(2)\, \cos(\beta_o + \theta_{\mathrm{s}i}) - f_{\mathrm{sk}i}(1)\, \sin(\beta_o + \theta_{\mathrm{s}i}) \tag{3.66}$$

3.3 Local linear element

During the past decades, several finite element formulations for two-layered beams have been proposed, see for instance [17, 18, 20, 22, 27, 28, 32, 35, 41, 45]. It has been found that the locking phenomena occur in low order displacement-based finite element models particularly for a short element with a stiff shear connection. In order to avoid locking problem in two-nodes beam element, the stiffness matrix $\mathbf{K}_l$ in the local coordinate system for shear-flexible as well as shear-rigid model which is constructed based on the exact solution of the governing equations of a hybrid beam with deformable shear connectors (see Chapter 2) can be used.

3.4 Numerical examples

The purpose of this section is to assess the capability of the proposed formulation in reproducing the nonlinear behavior of hybrid beams in partial interaction and to investigate the influence of the shear connection stiffness on the geometric nonlinear effects. The analysis of the performance and the accuracy of the present formulation is carried out by considering four numerical examples. To study the effect of shear deformability of the concrete element, the numerical analysis results obtained from the present model (T-model) are compared to the ones obtained from the shear-rigid model (EB-model), see Appendix B, in which the exact stiffness matrix developed in Appendix A is used for the local frame.

3.4.1 Buckling of a shear deformable beam-column

The buckling load of a column depicted in Fig. 3.4 is studied here by considering a

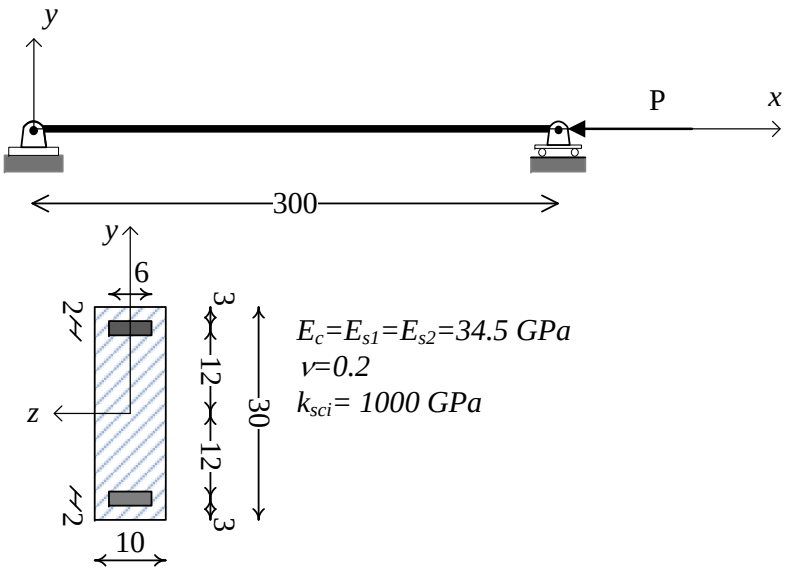

Figure 3.4: Buckling of a shear deformable column (dimension in [cm]).

high shear connection stiffness $k_{sc} = 10^6$ MPa. Restraints are applied in order to

avoid bucking about the y-axis. The buckling loads of the column obtained with different meshes are presented in Table 3.1. A very good agreement compared to

Table 3.1: Numerical results.

Number of elements	2	4	8	16	20
$P_{cr}/P_{cr,T}$	1.2319	1.0672	1.0274	1.0173	1.0158

the analytical solution, Engesser's buckling load [50]

$$P_{cr,T} = \frac{\pi^2\, EI/L^2}{1 + \dfrac{\pi^2\, EI/L^2}{GA}},$$

is obtained. A further investigation on the effect of the shear connection stiffness on the critical load has been carried out. The critical load is obtained by performing a nonlinear analysis using 20 elements. It can be seen from Fig. 3.5 that the critical load obtained from the FE analysis using the proposed formulation (P_{cr}) is lower than Euler's critical load ($P_{cr,T}$) for low shear connection stiffness. The magnitude of P_{cr} increases with increasing value of shear connection stiffness. However, P_{cr} remains constant for a shear connection stiffness k_{sc} beyond a critical value (about 10^4 MPa) where the full interaction can be assumed.

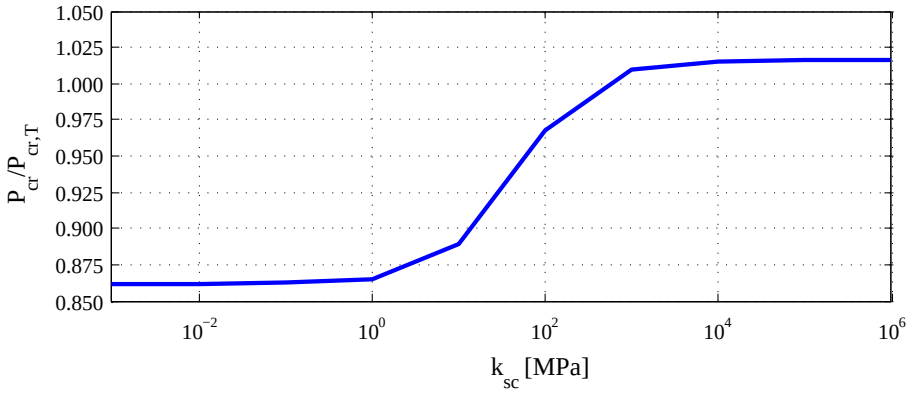

Figure 3.5: Ratio between the predicted ultimate load and the Engesser's buckling load in function of shear connection stiffness.

3.4.2 Simply supported steel-reinforced concrete beam subjected to uniformly distributed load

Consider a sandwich beam (see Fig. 3.6) subjected to a uniformly distributed

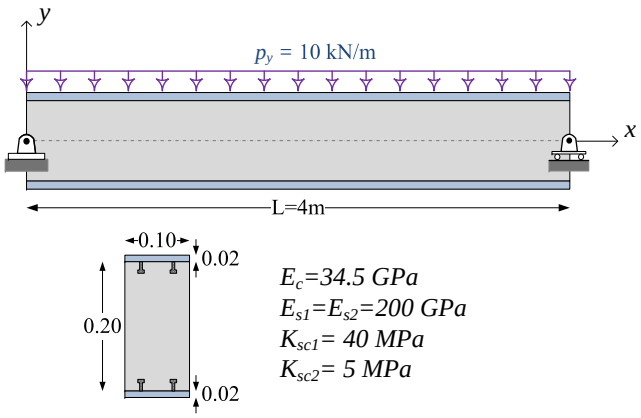

Figure 3.6: Three-layered beam with transversal loads (dimension in [m]).

load p_y of intensity 10 kN/m. The elastic modulus adopted for steel and concrete are 200 000 MPa and 34 500 MPa, respectively. The Poisson coefficient for the concrete core is taken equal to 0.2; and the unity value of shear correction factor is adopted. The stiffness of the shear connection is taken equal to 40 MPa for the top layer and 5 MPa for the bottom layer. A large displacement analysis with 20 elements is performed in which the distributed load is replaced with concentrated nodal forces. As expected larger slips occur at the interface between the bottom steel plate and the core beam (see Fig. 3.7 for distributed load $p_y = 10$ kN/m). The maximum deflection v_{max} occurring at the mid-span of the beam along with the slips at the beam ends are tabulated in Table 3.2 for both shear-rigid model (EB-model) and shear-flexible model (T-model). For the present case where the sandwich beam can be considered as a slender beam, the results given by both EB-model and T-model are not significantly distinct. Nonlinear analyses with a large amplitude of distributed load are performed in order to capture the geometrically nonlinear behavior of the sandwich beam. It can be seen that the

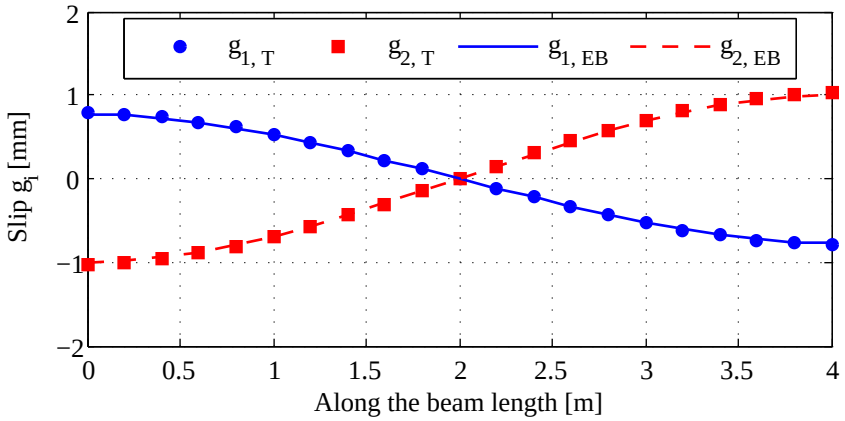

Figure 3.7: Slips between concrete and steel beams.

Table 3.2: Numerical results.

	EB-Model	T-model
$\|\|v_{max}\|\|$ (m)	0.0109	0.0111
$\|\|g_1\|\|$ (mm)	0.7759	0.7817
$\|\|g_2\|\|$ (mm)	1.0000	1.0224

sandwich beam behaves linearly below 600 kN/m. Beyond that load, the non-linear behavior become significantly apparent. One can observe that for a large amplitude of the loading, the magnitude of the transverse displacement given by the geometrically nonlinear analysis is significantly below the one predicted by a geometrically linear analysis. This behavior is similar to what has been observed in a non-linear bending of simply supported beams with a constant homogenous cross-section carrying uniformly distributed load (see [51]). In such a problem, the large displacement produces axial forces which increase the stiffness of the system requiring larger loads for the same displacement. To illustrate this behavior, the nonlinear load-deflection curve (GNA) is compared to the linear one (GLA) (see Fig. 3.8) where v_{max} is the transverse displacement at the mid-span.

Furthermore, the effect of cross-section slenderness is investigated by consider-

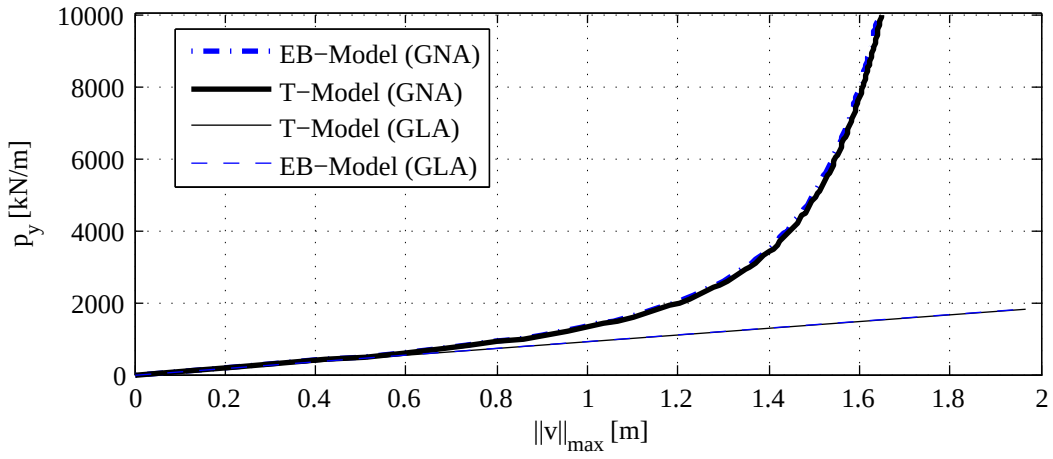

Figure 3.8: Load-deflection curve with L/H=16.67.

ing a large depth of the concrete core with a value of 60 cm. Both geometrically nonlinear analyses of EB-model and T-model are performed. It can be observed from Fig. 3.9 that the shear deformability of the concrete core influences significantly the response of the short beam with a slender cross-section.

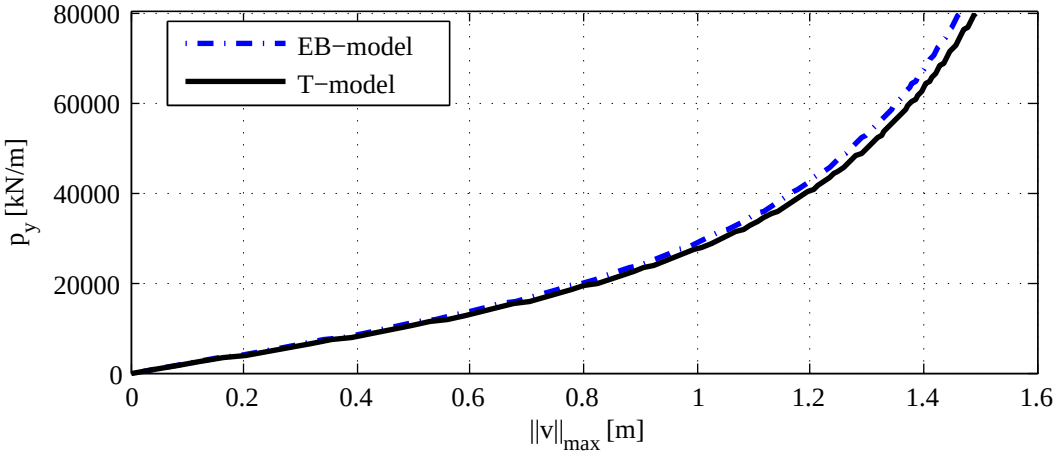

Figure 3.9: Load-deflection curve with L/H=6.25.

3.4.3 Hybrid Beam with 3 embedded sections subjected to axial and transversal loads

Consider a pinned hybrid beam consisting of a concrete beam of breadth $b = 0.25$ m and depth $h = 0.80$ m (see Fig. 3.10) reinforced by three steel profiles. Equally spaced stud connectors are welded on both side of each steel beam flanges. The details of the geometrical and material characteristics are reported in Fig. 3.10. The Poisson coefficient for the concrete component is taken equal to 0.15; and the

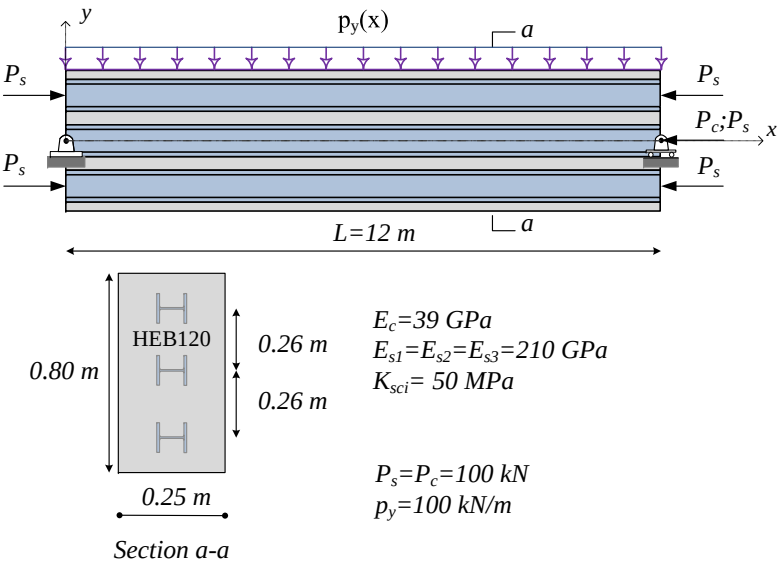

Figure 3.10: Beam with axial and transversal loads.

value of shear correction factor is assumed to be equal to 1. The beam is subjected to both axial and transversal loads. Each layer of the hybrid beam is loaded by an axial force. The position of the centroid of the steel beam at mid-height of the hybrid section coincides with the centroid of the concrete section. However, those centroid nodes are distinct in the FE formulation. For this problem, a nonlinear analysis is required in order to take into account the second-order effect induced by the axial loads. The degree of shear connection for the shear-flexible model is evaluated by analyzing the deflection at the mid-span with the variation of the shear connection stiffness k_{sc}, see Fig. 3.11. For a shear connection stiffness k_{sc}

lower than 10^3 MPa, the beam is in partial interaction. The numerical results

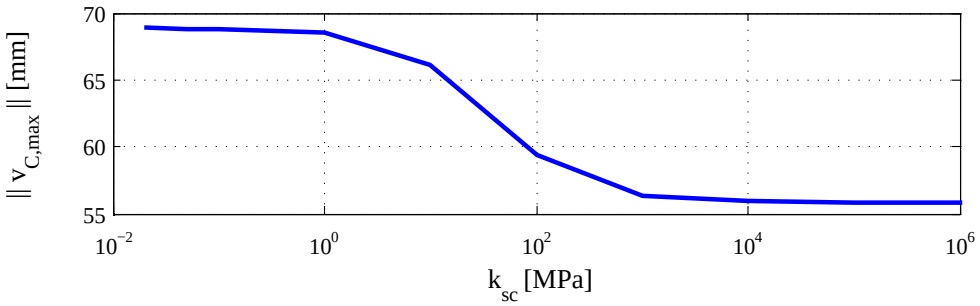

Figure 3.11: Degree of shear connection.

for the slips at the beam end and the deflection at the mid-span are provided in Table 3.3 for both shear-rigid model (EB-model) and shear-flexible model (T-

Table 3.3: Numerical results.

	EB-model	T-model
$\|\|v_{C,max}\|\|$ (mm)	60.8698	61.4415
g_1 (mm)	2.8225	2.8225
g_2 (mm)	0.7447	0.7432
g_3 (mm)	-1.3331	-1.3361

model) considering $k_{sc} = 50$ MPa. These results have been obtained with a mesh consisting of 20 elements. The slip distributions between the encasing concrete and the steel beams are illustrated in Fig. 3.12. One can observe that although the hybrid section is symmetric, the slip distribution at top steel profile is not symmetric with respect to the one at bottom steel profile. As a result of the interaction between bending moment and normal forces, the slip at the mid-height of the cross-section is not equal to zero. Indeed, two axial forces are applied at each cross-section centroid (at mid-height), one at the steel section (steel node) and another one at the concrete section (concrete node). These two axial forces

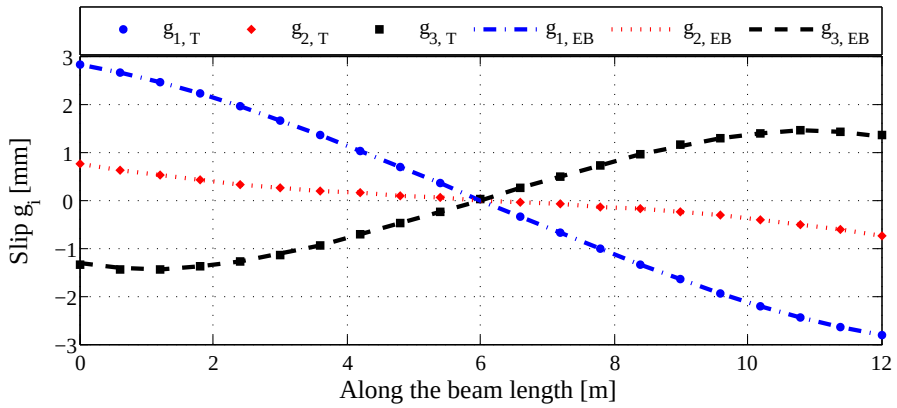

Figure 3.12: Slips between concrete and steel beams.

accompanied by the bending moment produce different axial displacements of both nodes which result the non-zero slip (g_2) along the beam length. On the other hand, the deformed shapes of the hybrid beam obtained from both models are depicted in Fig. 3.13. As expected, the deflection obtained from T-model is

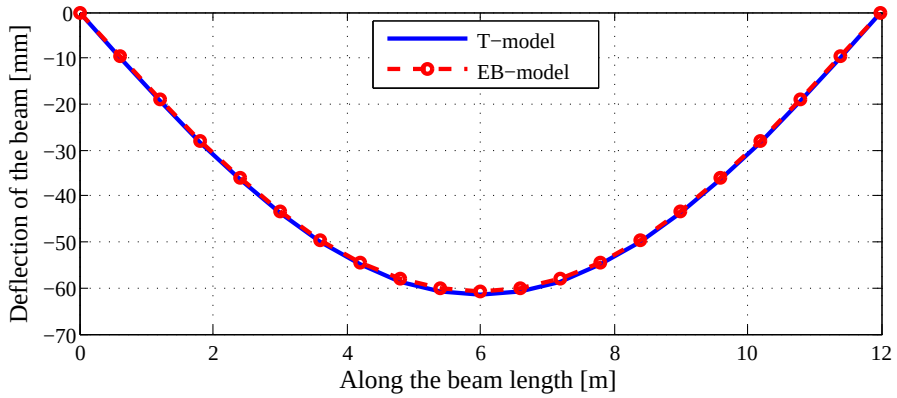

Figure 3.13: Deformed shape of the beam.

slightly greater than the one from EB-model. It is worth mentioning that the responses of the T-model is almost identical to the ones of EB-model. This is due to the relatively large length-to-depth ratio of the considered beam setup $L/H = 15$.

3.4.4 Uniform bending of cantilever beam

To highlight the performance of the co-rotational formulation dealing with a large displacement analysis, we consider a classical problem where three cantilever steel beams (s_i) are embedded in the concrete beam (c) and freely deform in their longitudinal axis (without shear connection), see Fig. 3.14. Those beams are subjected to an end moment M such that the deformed shape of the beam (c) is a quarter of circle. For that reason, the results obtained from the co-rotational model are compared against the analytical solutions in which the shear deformability of the concrete beam is ignored. The analytical end moment required to deform the

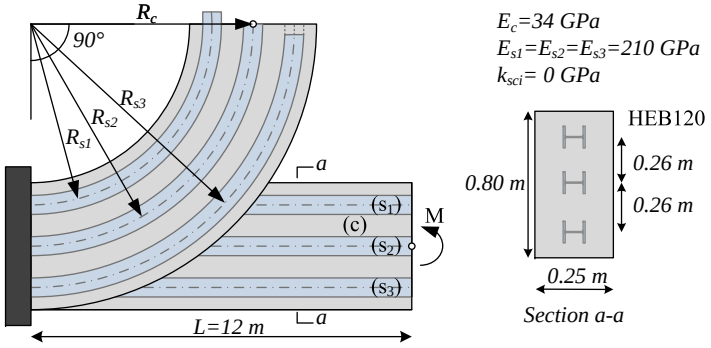

Figure 3.14: Uniform bending of cantilever beam.

beam (c) is

$$M_c = \frac{(EI)_c}{R_c}, \quad R_c = \frac{2L}{\pi} \tag{3.67}$$

The beams (s_i) have to bend into the concentric arcs, which require the end moments

$$M_{si} = \frac{(EI)_{si}}{R_{si}}, \quad R_{si} = R_c - h_i \qquad i = 1, 2, 3 \tag{3.68}$$

The required total moment is therefore $M = M_c + M_{s1} + M_{s2} + M_{s3}$ and the slip between those beams at the free end are

$$g_i = -(R_c - h_i)\frac{(R_c - R_{si})L}{R_c\, R_{si}} \qquad i = 1, 2, 3 \tag{3.69}$$

Table 3.4: Numerical results.

	Analytical	FE model	FE/Analytical
v_C (m)	7.6394	7.6473	1.0010
u_C (m)	-4.3606	-4.3527	0.9982
g_1 (m)	-0.4084	-0.4097	1.0031
g_2 (m)	0.0000	$-7.2905 \cdot 10^{-18}$	–
g_3 (m)	0.4084	0.4097	1.0031
M (MN.m)	45.7204	45.7202	1.0000
$max \parallel V(x) \parallel$ (N)	0.0000	$9.4995 \cdot 10^{-7}$	–
$max \parallel N(x) \parallel$ (N)	0.0000	$1.6075 \cdot 10^{-6}$	–

The results of the FE analysis obtained with 10 elements are presented in Table 3.4. A very good agreement with analytical solution is obtained.

3.5 Conclusion

In this chapter, a new finite element formulation for a large displacement analysis of hybrid beam-columns with several encased steel profiles in partial interaction has been presented. To describe the geometrical nonlinearity, the co-rotational framework was adopted and the motion of the element decomposed into a rigid body motion and a deformational part using a local co-rotational frame, which continuously translates and rotates with the element but does not deform with it. The treatment of geometric nonlinearity is effectively undertaken at the level of discrete nodal variables with the transformation matrix between the local and global nodal entities being independent of the assumptions made for the local element. To avoid locking problems encountered in two-node element (low order elements), the exact stiffness matrix was used for the local formulation. The performance of the formulation has been illustrated in four numerical examples. It was shown that the proposed formulation provides a robust and reliable option for a large displacement analysis of hybrid beam-columns.

Chapter 4

Constitutive Modeling

***

Material laws adopted in the thesis.

4.1 Introduction

In general, the inelastic analysis of framed structures can be categorized into two main types: (1) concentrated plasticity and (2) distributed plasticity. For the former, the nonlinear behavior of a beam-column element is lumped in nonlinear springs typically at the extremities of a linear-elastic element. In most lumped plasticity models, the axial force, shear force and bending moment relationships are described by a yield surface for the stress resultants and an associated flow rule according to the classical plasticity theory. The drawback of plastic hinge methods is that the axial force, shear force and bending moment interaction is separated from the element behavior. Consequently, it often does not well represent frame response. On the other hand, distributed plasticity models account for the nonlinear interaction of the internal forces along the entire element by numerically integrating force-deformation response at a finite number of control sections. The nonlinear behavior at these sections is derived by subdividing the cross-section into fibers and integrating the material constitutive model. The

distributed inelasticity models are computationally more demanding. This is because the detailed coupling between bending, axial and shear deformations due to partial cross-section plasticity is difficult to capture by distributed plasticity models.

This chapter presents the nonlinear constitutive models for the steel material, the concrete material and the shear connection, as required for material nonlinear analysis. For the reinforcing bar as well as the embedded steel section, shear deformations are ignored (Bernoulli kinematic assumptions); as a result, a uniaxial stress-strain relationship is employed. The longitudinal shear transfer mechanisms by bond and by shear stud connector are recalled. The behavior of shear stud connector is described through three existing models in literature: (1) an elastic-perfectly plastic model; (2) the model by Ollgaard et al. [52] and (3) the model by Salari [24]. For the concrete material, the 3d plasticity model and the uniaxial stress-strain relationship are highlighted.

4.2 Uniaxial behavior of steel material

Engineering materials (like steel and concrete) have their qualitatively distinct mechanical responses. However, those materials share some important features of their phenomenological behavior that make them possible to be modeled by the theory of plasticity. To illustrate such common features, a uniaxial tensile test where a steel coupon is loaded monotonically in a quasi-static manner up to failure is discussed in this section. The response of the steel material is typically depicted in Fig. 4.1, where the axial stress, σ, is plotted against the axial strain, ε. Some important phenomenological properties of this response can be described as the following:

- **The linear elastic range**: During the initial stage of loading, the stress varies linearly with the strain up to a proportional limit referred to as the elastic limit. In this region, the stress is proportional to the strain with the constant of proportionality being the modulus of elasticity or Young

modulus, denoted E. As strain is increased, steel material deviates from this linear proportionality to enter the non-linear reversible domain up to the yield point, σ_y, where plasticity starts to develop.

- **The yield plateau**: For strain demand exceeding the the yielding strain ε_y, the stress is maintained at the yield stress value for a moderate increase in strain. At yield point, the evolution of plastic strains (plastic flow) takes place.

- **The strain-hardening range**: At the end of the yield plateau, the stress starts to increase again with increasing value of the total strain. In this region, an evolution of the yield stress is observed. This phenomenon is known as hardening.

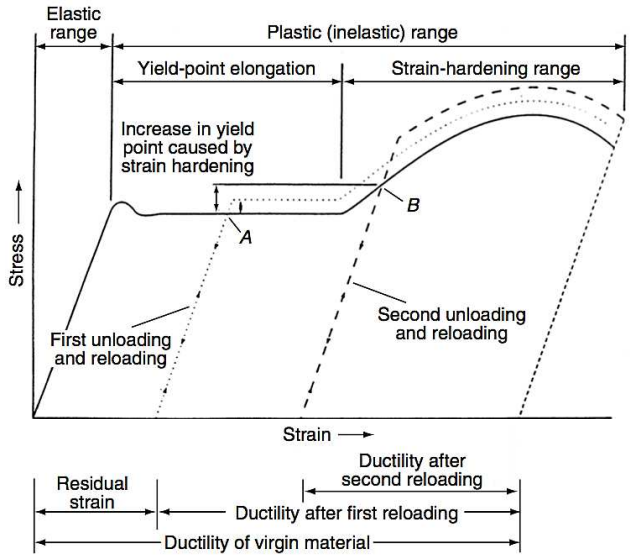

Figure 4.1: Effect of prior tensile loading on tensile stress-strain behavior.

The phenomenological characteristics observed in steel material above is also discovered in a wide variety of materials such as concrete, rocks, soils and many others. These phenomenological behaviors can be described with sufficient accuracy by the mathematical theory of plasticity that will be discussed in the

following.

After the steel coupon is loaded beyond its yield limit and subsequently, completely unloaded, there still remains a deformation that is not recoverable in the steel coupon. This unrecoverable deformation is called plastic strain, ε^p. During the reloading state, the behavior of the steel coupon is considered to be linear elastic and the uniaxial stress corresponding to a configuration with total strain ε is given by

$$\sigma = E\,(\varepsilon - \varepsilon^p) \tag{4.1}$$

It is worth to mention that the difference between the total strain and the current plastic strain is fully reversible; that is, upon complete unloading, $\varepsilon - \varepsilon^p$ is fully recovered without further evolution of plastic strains. In this manner, the total strain, ε, can be decomposed into the sum of an elastic (or reversible) strain, ε^e, and a plastic (or permanent) strain, ε^p at restrictions to small strains:

$$\varepsilon = \varepsilon^e + \varepsilon^p \tag{4.2}$$

where the elastic strain has been defined as

$$\varepsilon^e = \varepsilon - \varepsilon^p \tag{4.3}$$

Following the above definition of the elastic axial strain, the constitutive law for the axial stress can be expressed as

$$\sigma = E\,\varepsilon^e. \tag{4.4}$$

This relation is also known as Hooke's law for linear elastic behavior. For plastic material behavior, no more explicit relation between stress and strain is given since the strain state is also dependent on the loading history. In spite of that, the plastic material behavior can be described by a yield condition, a flow rule and a hardening law.

By assuming that the yield stress, σ_y is identical in the tensile and compressive regime, the elastic domain delimited by the yield stress can be expressed as

$$|\sigma| - \sigma_y < 0 \tag{4.5}$$

in which no change in plastic strain takes place, i.e., $\dot{\varepsilon}^p = 0$. A change in ε^p can take place only if the relevant body is under plastic loading where

$$|\sigma| - \sigma_y = 0 \tag{4.6}$$

It is worth mentioning that, at any stage, no stress level is allowed above the current yield stress, i.e. plastically admissible stresses lie either in the elastic domain or on the yield limit. The following notation is introduced to designate the set of *admissible stresses*:

$$\mathbb{E}_\sigma = \{\sigma \in \mathbb{R} \,|\, f(\sigma, \sigma_y) = |\sigma| - \sigma_y \leq 0\} \tag{4.7}$$

Then, the *yield condition* that enables one to determine whether the relevant material suffers only elastic or also plastic strains at a certain stress state is:

$$f(\sigma, \sigma_y) = |\sigma| - \sigma_y \leq 0 \tag{4.8}$$

4.2.1 Flow rule

In the plastic range, the relevant body experiences the plastic strain rate. Let $\dot{\lambda} \geq 0$ be the absolute value of the plastic strain rate (it is also called as plastic multiplier or consistency parameter). Then the preceding physical assumption takes the form

$$\dot{\varepsilon}^p = \dot{\lambda}\,\mathrm{sign}(\sigma) \tag{4.9}$$

which is the *plastic flow rule* for the uniaxial model. sign is the signum function defined as

$$\mathrm{sign}(\sigma) = \begin{cases} +1 & \text{if } \sigma > 0 \\ 0 & \text{if } \sigma = 0 \\ -1 & \text{if } \sigma < 0 \end{cases} \tag{4.10}$$

4.2.2 Loading/unloading conditions

With the observation made above, the yield condition defines not only the set of permissible stresses, but also the conditions for which plastic deformations can continue to occur. Whereas all elastic stress states are located inside the yield surface and defined uniquely by the elastic strain i.e. $\dot{\lambda} = 0$ and $f(\sigma, \sigma_y) < 0$, plastic deformations can occur as long as the stress point is located on the yield surface i.e. $\dot{\lambda} > 0$ and $f(\sigma, \sigma_y) = 0$. It follows that

$$\dot{\lambda}\, f(\sigma, \sigma_y) = 0 \tag{4.11}$$

This condition goes by the name of Kuhn-Tucker condition. Thus the loading/unloading conditions of the elasto-plastic model are defined as follows:

$$f(\sigma, \sigma_y) \leq 0, \qquad \dot{\lambda} \geq 0, \qquad \dot{\lambda}\, f(\sigma, \sigma_y) = 0 \tag{4.12}$$

In addition to above conditions, $\lambda \geq 0$ satisfies the consistency requirement below:

$$\dot{\lambda}\, \dot{f}(\sigma, \sigma_y) = 0 \tag{4.13}$$

In classical literature, conditions (4.12) and (4.13) go by the names *loading/unloading* and *consistency conditions*, respectively.

4.2.3 Hardening law

The complete characterisation of the uniaxial model is achieved with the introduction of the hardening law which allows the consideration of the influence of material hardening on the yield condition and the flow rule. As remarked in the experimental test of steel coupon, an evolution of the yield stress accompanies the evolution of the plastic strain in strain-hardening range. Whereas for perfect plasticity the closure of the elastic range $\mathbb{E}_\sigma$ remains unchanged, $\mathbb{E}_\sigma$ expands with the amount of plastic flow in the system for the strain hardening model. This expansion can be incorporated into the uniaxial model by simply assuming that the yield stress σ_y is a given function

$$\sigma_y = \sigma_y(\zeta) \tag{4.14}$$

of the internal variable. In this case the accumulated axial plastic strain, ζ is defined as

$$\zeta = \int_0^t |\dot{\varepsilon}^p| \mathrm{d}t \tag{4.15}$$

It is straightforward that in a monotonic tensile test, we have

$$\zeta = |\varepsilon^p| \tag{4.16}$$

which, in view of the plastic flow rule, gives

$$\dot{\zeta} = \dot{\lambda} \tag{4.17}$$

The relations (4.14) and (4.17) define the *hardening law* of the material subjected to the monotonic loading.

4.2.4 Tangent elasto-plastic modulus

The consistency condition enables us to solve explicitly for $\dot{\lambda}$ and relate stress rates to strain rates as follows. By taking the time derivative of the yield function and making use of Eq. (4.8), (4.9) and (4.16), along with the elastic stress-strain relationship Eq. (4.1), we have

$$\begin{aligned} \dot{f} &= \frac{\partial f}{\partial \sigma}\,\dot{\sigma} + \frac{\partial f}{\partial \zeta}\,\dot{\zeta} \\ &= \mathrm{sign}(\sigma)\, E\,(\dot{\varepsilon} - \dot{\varepsilon}^p) - H\,\dot{\varepsilon}^p\,\mathrm{sign}(\sigma) \\ &= \mathrm{sign}(\sigma)\, E\,\dot{\varepsilon} - \dot{\lambda}\,[E + H] \end{aligned} \tag{4.18}$$

where H is called the hardening modulus, or hardening slope, and is defined as

$$H = H(\zeta) = \frac{\mathrm{d}\sigma_y}{\mathrm{d}\zeta} \tag{4.19}$$

The consistency condition (Eq. (4.13)) implies that the rate of f vanishes whenever plastic yielding occurs. Then the plastic multiplier, $\dot{\lambda}$, is uniquely determined during plastic yielding as

$$\dot{\lambda} = \frac{E}{H + E}\,\dot{\varepsilon}\,\mathrm{sign}(\sigma) \tag{4.20}$$

Then the rate form of the elastic relationship Eq. (4.1) along with Eq. (4.20) yields

$$\dot{\sigma} = \begin{cases} E\,\dot{\varepsilon} & \text{if } \dot{\lambda} = 0, \\ \dfrac{E\,H}{E+H}\,\dot{\varepsilon} & \text{if } \dot{\lambda} > 0. \end{cases} \tag{4.21}$$

in which the quantity $E\,H/(E+H)$ is called the *elasto-plastic tangent modulus*.

4.3 Constitutive modeling with internal variables: multi axial stress-strain models

For elastic body, the strain at any point of the body is defined by the current stress. On the contrary, the current strain or stress in inelastic body depends not only on the current value of state variables but also on the past history through the present value of a set of internal state variables which account for the internal restructuring taking place during the dissipative process. These phenomena were well observed in one-dimensional tensile test described in the previous section. In this section, we apply the straightforward extension of the one-dimensional model into two- and three-dimensional situations. The notations used here are the following.

- The symmetric second-order tensors are represented as six-dimensional vectors and denoted by bold letters.
- A set of numbers are denoted by the capital doubled letter.
- The rate of an internal variable, also called velocity, is denoted by a superimposed dot.

The following set of state variables is assumed for the thermodynamic state at any time t:

$$\{\boldsymbol{\epsilon},\, \boldsymbol{\epsilon}^p,\, \boldsymbol{\zeta}\}$$

where $\boldsymbol{\epsilon}$ is total strain vector, $\boldsymbol{\epsilon}^p$ plastic strain vector and $\boldsymbol{\zeta}$ is a set of internal variables containing, in general, entities of scalar, vectorial and tensorial nature associated with dissipative mechanisms. The number and the mathematical nature (tensor, vector or scalar) of the internal variables depend on the model under consideration.

4.3.1 State equations

In the framework of thermodynamics, the constitutive equations are generally developed in order to prevent violation of physical principles. They consist mostly of a state equation and evolution equations. The state equation describes the relationship between the stress $\boldsymbol{\sigma}$, total strain $\boldsymbol{\epsilon}$, plastic strain $\boldsymbol{\epsilon}^p$, temperature T and state variable $\boldsymbol{\zeta}$, which represents the microstructural state of the material. We assume that the temperature remains constant with time and is uniform in space so that it will not be considered hereafter. The material state may then be quantified in terms of ($\boldsymbol{\epsilon}$, $\boldsymbol{\epsilon}^p$, $\boldsymbol{\zeta}$) as follow:

$$\boldsymbol{\sigma} = \boldsymbol{\sigma}(\boldsymbol{\epsilon},\, \boldsymbol{\epsilon}^p,\, \boldsymbol{\zeta}) \tag{4.22}$$

In the definition of the state variables characterizing the state of the system, we refer only to the so-called strain-like variables (kinematic variables) whereas the corresponding stress-like variables are obtained by duality. The state equations defining the relationship between static and kinematic internal variables can be formally written as:

$$\boldsymbol{\sigma} = \boldsymbol{\sigma}(\boldsymbol{\epsilon}^e) \quad , \quad \boldsymbol{\mathcal{Z}} = \boldsymbol{\mathcal{Z}}(\boldsymbol{\zeta}) \tag{4.23}$$

where $\boldsymbol{\mathcal{Z}}$ is the dual of $\boldsymbol{\zeta}$. Assuming linear elasticity and strictly positive hardening with no coupling, the above relation can be equivalently written as follows:

$$\boldsymbol{\sigma} = \frac{\partial \psi_e}{\partial \boldsymbol{\epsilon}^e} \quad \text{and} \quad \boldsymbol{\mathcal{Z}} = \frac{\partial \psi_p}{\partial \boldsymbol{\zeta}} \tag{4.24}$$

where $\psi_e(\boldsymbol{\epsilon}^e)$ is the stored energy due to elastic strain and $\psi_p(\boldsymbol{\zeta})$ is the unrecoverable stored energy due the internal variables describing hardening. Under the aforementioned assumptions, $\psi_e(\boldsymbol{\epsilon}^e)$ and $\psi_p(\boldsymbol{\zeta})$ are both proper strictly convex

functions. The sum of the two ($\psi_e(\boldsymbol{\epsilon}^e)$ and $\psi_p(\boldsymbol{\zeta})$) give the so-called Helmholtz energy function:

$$\psi(\boldsymbol{\epsilon}^e, \boldsymbol{\zeta}) = \psi_e(\boldsymbol{\epsilon}^e) + \psi_p(\boldsymbol{\zeta}) \tag{4.25}$$

The potential form of the state law (4.24) will ensure that the Clausius-Duhem is fulfilled for any admissible thermodynamic process, i.e.:

$$\left(\boldsymbol{\sigma} - \frac{\partial \psi_e}{\partial \boldsymbol{\epsilon}^e}\right) \cdot \boldsymbol{\epsilon}^e + \boldsymbol{\sigma} \cdot \dot{\boldsymbol{\epsilon}}^p - \boldsymbol{\mathcal{Z}} \cdot \dot{\boldsymbol{\zeta}} \geqslant 0 \tag{4.26}$$

4.3.2 Elastic domain and yield criterion

Recall that in the uniaxial yield criterion, the plastic flow takes place when the uniaxial stress attains a critical value. This phenomenon could be expressed by means of a yield function which is negative or zero. Herein, we extend this concept to the three-dimensional case by defining the yield function $f : \mathbb{S} \times \mathbb{R}^m \to \mathbb{R}$ and constraining the admissible state $\{\boldsymbol{\sigma}, \boldsymbol{\mathcal{Z}}\} \in \mathbb{S} \times \mathbb{R}^m$ in stress space to lie in the set $\mathbb{E}_\sigma$ defined as:

$$\mathbb{E}_\sigma := \{(\boldsymbol{\sigma}, \boldsymbol{\mathcal{Z}}) \in \mathbb{S} \times \mathbb{R}^m \,|\, f(\boldsymbol{\sigma}, \boldsymbol{\mathcal{Z}}) \leq 0\} \tag{4.27}$$

where the scalar yield function, f, is now a function of the stress vector and a set of internal stress-like variables, $\boldsymbol{\mathcal{Z}}$ which are functions of $\boldsymbol{\zeta}$. We denote $\text{int}(\mathbb{E}_\sigma)$ the interior of $\mathbb{E}_\sigma$ defined as

$$\text{int}(\mathbb{E}_\sigma) := \{(\boldsymbol{\sigma}, \boldsymbol{\mathcal{Z}}) \in \mathbb{S} \times \mathbb{R}^m \,|\, f(\boldsymbol{\sigma}, \boldsymbol{\mathcal{Z}}) < 0\} \tag{4.28}$$

which describes the elastic domain. The set of stresses for which plastic yielding may occur is the boundary of the elastic domain, denoted by $\partial\mathbb{E}_\sigma$ as follow:

$$\partial\mathbb{E}_\sigma := \{(\boldsymbol{\sigma}, \boldsymbol{\mathcal{Z}}) \in \mathbb{S} \times \mathbb{R}^m \,|\, f(\boldsymbol{\sigma}, \boldsymbol{\mathcal{Z}}) = 0\}. \tag{4.29}$$

4.3.3 Evolution rules

While the evolution of the strain can be controlled externally, the internal variables evolve according to some additional rules called *evolution laws* which complement the state equations. These laws, which describe the evolution of the

internal modifications, establish relationships between the rate of change of each internal variable $\boldsymbol{\Xi}$ (generalized velocity) and each generalized stress $\boldsymbol{\Sigma}$.

For standard plasticity models with an associative flow rule, the rate formulation is the most popular. In this formulation, the direction of the velocity vector is given by the gradient to the yield surface expressed in the generalized stresses space and its magnitude by the plastic multiplier:

$$\dot{\boldsymbol{\Xi}} = \dot{\lambda}\frac{\partial f}{\partial \boldsymbol{\Sigma}} \tag{4.30}$$

Then, the flow rule and hardening law are defined respectively as the following

$$\dot{\boldsymbol{\epsilon}^p} = \dot{\lambda}\,\mathbf{N} \tag{4.31}$$

$$\dot{\boldsymbol{\zeta}} = \dot{\lambda}\,\mathbf{H} \tag{4.32}$$

where the vector

$$\mathbf{N} = \frac{\partial f}{\partial \boldsymbol{\sigma}} \tag{4.33}$$

is termed the flow vector and the function

$$\mathbf{H} = -\frac{\partial f}{\partial \boldsymbol{\mathcal{Z}}} \tag{4.34}$$

is the generalised hardening modulus which defines the evolution of the hardening variables. The plastic multiplier is required to satisfy the following complementarity relations which are the same as Eq. (4.11-4.13) but σ_y is replaced by $\boldsymbol{\mathcal{Z}}$ in this case:

$$f(\boldsymbol{\sigma},\, \boldsymbol{\mathcal{Z}}) \leq 0\ ,\ \dot{\lambda} \geq 0\ ,\ \dot{\lambda} f(\boldsymbol{\sigma},\, \boldsymbol{\mathcal{Z}}) = 0. \tag{4.35}$$

In addition to conditions (4.35) above, $\dot{\lambda} \geq 0$ satisfies the consistency requirement as below:

$$\dot{\lambda}\, \dot{f}(\sigma,\, \boldsymbol{\mathcal{Z}}) = 0 \tag{4.36}$$

4.4 Steel stress-strain explicit 1D model

A number of researchers have proposed models to characterize the response of steel under monotonic/cyclic loading. The simplest and most computationally efficient model for predicting the steel behavior is based on the aforementioned plasticity theory. Based on the results of experimental reversed cyclic loading tests, the plastic deformation and an unloading stiffness, approximately equal to the initial elastic material stiffness, are accumulated. The phenomenon that characterizes the increased strength under increasing plastic strain can be described by the isotropic strain hardening. Furthermore, the premature yielding associated with the Bauschinger effect may be characterized by a plasticity model that incorporates a kinematic strain hardening.

A uniaxial constitutive model developed based on the plasticity theory with linear isotropic and kinematic strain hardening is defined by the following set of equations:

$$f(\sigma, \zeta) = |\sigma - \chi| - \sigma_y(\zeta) \leq 0 \tag{4.37}$$

$$\dot{\varepsilon}^p = \dot{\lambda}\,\mathrm{sign}(\sigma - \chi) \tag{4.38}$$

$$\dot{\zeta} = \dot{\lambda} \tag{4.39}$$

$$\chi = \dot{\lambda}\,H\,\mathrm{sign}(\sigma - \chi) \tag{4.40}$$

$$\sigma_y(\zeta) = \sigma_y + K\,\zeta \tag{4.41}$$

where ζ, K and H are the back stress, the isotropic and kinematic hardening parameters, respectively.

A more representative model for steel stress-strain behavior can be achieved through the use of phenomenological models in which nonlinear stress-strain relationships are calibrated based on the experimental data such as the well-known Ramberg-Osgood model. The model proposed by Ramberg and Osgood [53] uses a single nonlinear relation to describe the observed curvilinear response of reinforcing steel under monotonic loading. This model defines the normalized strain

to be a function of the normalized stress. Various other models have been developed to characterize the behavior of reinforcing steel. Menegotto and Pinto [54] propose a model in which the steel behavior is defined by the following nonlinear equation:

$$\bar{\sigma} = b\,\bar{\varepsilon} + \frac{(1-b)\bar{\varepsilon}}{(1+\bar{\varepsilon}^R)^{1/R}} \tag{4.42}$$

where $\bar{\varepsilon}$ is the effective strain defined by

$$\bar{\varepsilon} = \frac{\varepsilon - \varepsilon_r}{\varepsilon_0 - \varepsilon_r} \tag{4.43}$$

and $\bar{\sigma}$ is the effective stress given by

$$\bar{\sigma} = \frac{\sigma - \sigma_r}{\sigma_0 - \sigma_r} \tag{4.44}$$

The constant b is the ratio of the initial to final tangent stiffness and R is a parameter that defines the shape of the unloading curve which takes the following form:

$$R = R_0 - \frac{a_1\,\xi}{a_2 + \xi} \tag{4.45}$$

where ξ is updated following a strain reversal; R_0 the value of the parameter R during first loading; and a_1, a_2 are experimentally determined parameters to be defined together with R_0. The Menegotto-Pinto steel model is represented in Fig. 4.2. Let us consider the transition of two branches with asymptote line (a) and (b). σ_0 and ε_0 are the stress and strain at the point where the two asymptotes meet (point B); similarly, σ_r and ε_r are the stress and strain at the point where the last strain reversal with stress of equal sign took place (point A). As indicated in Fig. 4.2, (σ_0, ε_0) and (σ_r, ε_r) are updated after each strain reversal. A number of models have been developed based on the work done by Menegotto and Pinto [54]. Stanton and McNiven [55] proposed a steel model which improves the computational efficiency of Menegotto-Pinto model by assuming that the reference curves for steel subjected to cyclic loading follows the monotonic envelope. Filippou et al. [56] observed that Menegotto-Pinto model prohibits its

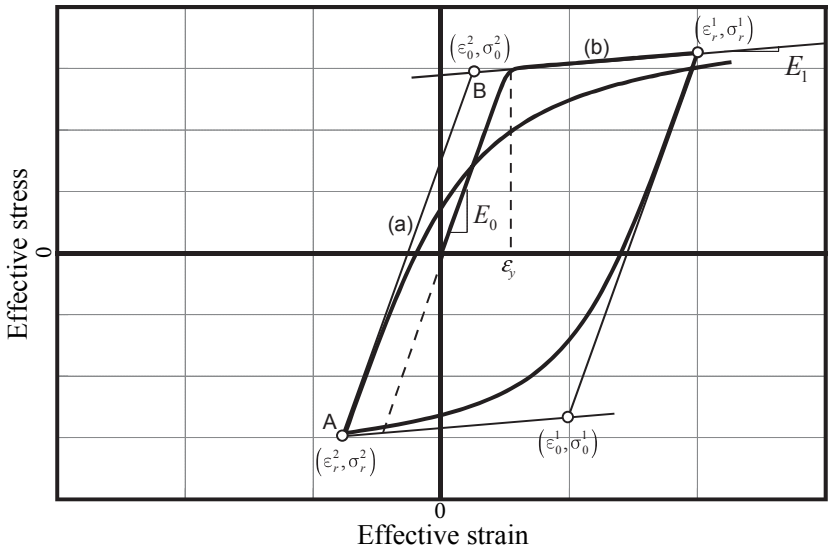

Figure 4.2: Menegotto-Pinto steel model.

failure from allowing the isotropic hardening. To take into account this drawback, they proposed a stress shift in linear yield asymptote as a function of the maximum plastic strain as follow:

$$\sigma_{st} = a_3 \left[\frac{\varepsilon_{max}}{\varepsilon_y} - a_4 \right] \sigma_y \tag{4.46}$$

where ε_{max} is the absolute maximum strain at the instant of strain reversal; ε_y and σ_y are respectively the strain and stress at yield point; and a_3 and a_4 are experimentally determined parameters.

In the model code for concrete structures, CEB-FIP 2010 [57], the stress-strain diagram used for modeling the steel material can be adopted to the one provided by manufacturer. In some design codes, the steel constitutive model is considerably simple. EN 1992-1-1 [11] proposes a bilinear stress-strain diagram with isotropic hardening for modeling the reinforcing steel bar whilst EN 1993-1-1 [58] recommends to adopt an appropriate stress-strain curve for structural steel members but the elastic perfectly plastic stress-strain diagram may be used.

4.5 Concrete constitutive model

Concrete is a common engineering composite material which is made of cement, water and aggregates. Experimental tests show that concrete is a highly nonlinear material under uniaxial compression stress. The stress-strain curve observed from the compressive experimental test, has a nearly linear form up to about 30 percent of the maximum compressive strength, f'_c. For stress beyond this limit, the curve shows a gradual increase up to about $0.75f'_c$ to $0.90f'_c$. At stress above this point, the curve bends more sharply before approaching the peak stress f'_c beyond which the concrete undergoes strain softening described by a descending branch of the curve until the failure point at some ultimate strain ε_u. When concrete is under uniaxial tensile stress, the similar characteristic of stress-strain curve as the one under uniaxial compression has been observed. However, the tensile strength of the concrete material is significantly low compared to the compressive one. The constitutive behavior of concrete under biaxial or triaxial states of stress is different from the constitutive behavior under uniaxial loading conditions. Richart et al. [59] and Balmer [60] conducted trial tests at low to high volumetric compression (or confining) stress levels. The results showed that concrete can act as a quasi-brittle, plastic-softening, or plastic-hardening material depending on the confining stress. Moreover, the maximum compressive strength of concrete increases with increasing confining pressure.

4.5.1 Concrete plasticity model

Plasticity theory has been successfully applied to model the concrete behavior. Several plasticity models have been developed to characterize the behavior of concrete under multi-axial loading [61–69]. The main characteristics of the concrete plasticity models include pressure sensitivity, associative or non-associative flow rule, work or strain hardening and limited tensile strength. These main characteristics lead to different numbers of model parameters and different the shape of the yield surface in principal stress space. One parameter model of the maximum tensile stress criterion of Rankine, dating from 1876, is generally accepted

today to determine whether a tensile or a compressive type of failure has occurred for concrete. According to this criterion, brittle fracture of concrete takes place when the maximum principal stress at a point inside the material reaches a value equal to the tensile strength of the material as found in a simple tension test, regardless of the normal or shearing stresses that occur on other planes through the point. This surface is generally referred to as a tension cutoff surface. Mohr-Coulomb and Drucker-Prager failure surfaces are two-parameter models which take into account the pressure dependence on the failure criterion of concrete. The shortcoming of these surfaces are the linear relationship between $\sqrt{J_2}$ and I_1 and the independence of the deviatoric section on the Lode angle θ. However, the experimental results have showed that the relationship between $\sqrt{J_2}$ and I_1 is nonlinear and the trace of the failure surface on deviatoric sections is not circular but depends on the Lode angle θ. William and Warnke [61] proposed three- and five-parameter model for concrete in the multi axial stress state. Both models have non circular cross sections but straight meridians for three-parameter model and curved meridians for five-parameter model. Ottosen [62] suggested a failure surface with a four-parameter criterion where the meridians are nonlinear curve and cross section is not circular. The modern development of concrete model have been addressed to a cap model [70, 71]. The cap model to be discussed in the following is elasto-perfectly plastic with an associated flow rule and a smooth yield surface that closes in the hydrostatic compression. The shortcoming of the cap model is that it can represent the concrete behavior in the hydrostatic compression. The envelope failure surface function of the smooth cap model is defined as

$$F_f(I_1) = \alpha - \theta I_1 \tag{4.47}$$

where I_1 is the first invariant of the stress tensor, $I_1 = Trace(\sigma)$, and α and θ are model parameters.

The cap surface of the model is based on the non-dimensional functional form

given by Pelessone [72] as:

$$F_c = 1 - \frac{(I_1 - k_0)(-|I_1 - k_0| + I_1 - k_0)}{2(X_0 - k_0)^2} \tag{4.48}$$

where $X_0 = k_0 - R\,F_f(k_0)$, k_0 and R are material parameters. The function F_c, is unity for I_1 less than k_0 and elliptical for $k_0 > I_1 > X_0$.

The smooth cap model, shown in Fig. 4.3, is formed by multiplying the envelop failure and cap surface functions to form a smoothly varying (continuous derivative) function given by

$$f_1(I_1, J_2) = J_2 - F_f^2\,F_c \tag{4.49}$$

where J_2 is the second invariant of the deviatoric stress tensor, $J_2 = \frac{1}{2}\mathbf{s}^{\mathrm{T}}\mathbf{s}$ with $\mathbf{s} = \boldsymbol{\sigma} - \frac{I_1}{3}\,\mathbf{1}$ and $\mathbf{1} = [1,\,1,\,1,\,0,\,0,\,0]^{\mathrm{T}}$. One can observe that the yield criterion

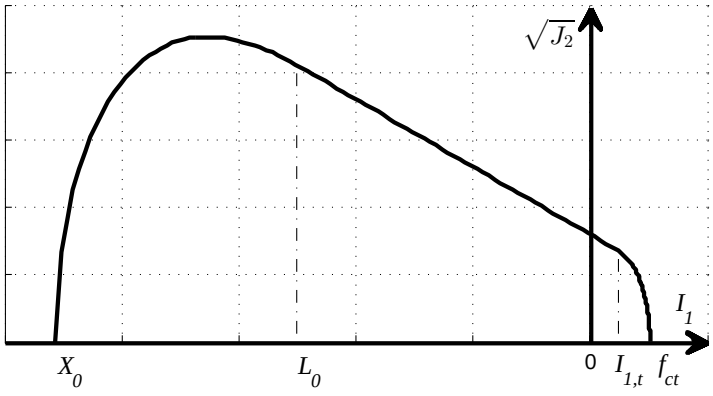

Figure 4.3: Smooth cap yield surface.

of concrete is defined by Drucker-Prager yield surface when the concrete is under the stress state where its first invariant is greater than k_0, see Fig. 4.3, beyond that hydrostatic compression point, the yield criterion of concrete is controlled by the cap surface. To characterize the tensile failure of the concrete, the tension cutoff surface may be considered. However, the yield function on the intersection point of the latter surface with the envelop yield surface is not smooth and one

has to deal with a so-called corner region. It has been recognized that this region can cause both numerical and material instabilities [73]. In the present work, this problem is solved by introducing an elliptical surface on the tension side which is chosen to smoothly intersect the failure envelope. This tension surface is expressed as:

$$f_2 = \frac{(I_1 - a)^2}{R_t^2} + J_2 - b^2 \tag{4.50}$$

where $a = f_{ct} - R_t\, b$; R_t is the aspect ratio of the ellipse; b corresponds to the ellipse vertical radius; and f_{ct} is a material constant referred to as the tensile strength. The ellipse radius b and intersection point $I_{1,t}$ of the tension elliptical surface and the failure envelope curve are given by

$$b = \frac{\alpha - \theta\, f_{ct}}{\sqrt{\theta^2\, R_t^2 + 1} - \theta\, R_t} \tag{4.51}$$

$$I_{1,t} = \frac{\alpha\, \theta\, R_t^2 + f_{ct} - R_t\, b}{\theta^2\, R_t^2 + 1} \tag{4.52}$$

4.5.1.1 Material constants

The envelop yield surface (Drucker-Prager yield function) as viewed in three-dimensional principal-stress space, is a cone with the space diagonal as its axis, while the Mohr-Coulomb criterion is a pyramid with an irregular hexagonal base and the space diagonal as its axis. Two of the most common approximations used to match the Drucker-Prager yield surface with the Mohr-Coulomb surface are outer edges fitting and inner edges fitting. The coincidence at the outer edges is obtained when

$$\theta = \frac{2\sin\phi}{\sqrt{3}(3 - \sin\phi)}, \quad \alpha = \frac{6\, c\, \cos\phi}{\sqrt{3}(3 - \sin\phi)}, \tag{4.53}$$

whereas, coincidence at the inner edges is given by

$$\theta = \frac{2\sin\phi}{\sqrt{3}(3 + \sin\phi)}, \quad \alpha = \frac{6\, c\, \cos\phi}{\sqrt{3}(3 + \sin\phi)} \tag{4.54}$$

in which ϕ and c are the angle of internal friction and the cohesion, respectively. Moreover, we can match the two criteria with the simple tensile strength f_{ct}

and the simple compressive strength f'_c of the concrete material. The material constants α and θ of Drucker-Prager for this case are determined as:

$$\theta = \frac{1}{\sqrt{3}} \sin\phi, \quad \alpha = \frac{2}{\sqrt{3}} c \cos\phi \tag{4.55}$$

where the parameters ϕ and c have to be chosen as:

$$\phi = \sin^{-1}\left(\frac{f'_c - f_{ct}}{f'_c + f_{ct}}\right), \quad c = \frac{f'_c f_{ct}}{f'_c - f_{ct}} \tan\phi. \tag{4.56}$$

However, there have been several discussion on how to determine accurately the concrete cohesion c while using the finite element analysis. Chen [74] adopted the cohesion of the concrete block as $c = f'_c/4$ to verify the nonlinear finite element analysis. Doran et al. [75] proposed the following equation to determine the cohesion of concrete after calibrating the results of several finite element applications to concrete:

$$c = 0.231 \ln(E_c d_{max}^2) - 0.60 \tag{4.57}$$

where E_c [MPa] is the elastic modulus of concrete and d_{max} [mm] represents the maximum aggregate size in the concrete mix. A thorough investigation on the concrete cohesion has been carried out by Arslan [76]. The following equation to determine the concrete cohesion is proposed [76]:

$$c = \begin{cases} 4.35(f'_c)^{0.31}(\frac{a}{d})^{-1.33}\exp(0.12\rho)(\frac{d}{d_{max}})^{-0.30}, & \text{for } a/d < 2.5 \\ \frac{2}{3}(f'_c)^{0.31}(\frac{a}{d})^{0.75}\exp(0.12\rho)(\frac{d}{d_{max}})^{-0.30}, & \text{for } a/d \geq 2.5 \end{cases} \quad \text{[MPa]} \tag{4.58}$$

where a is the shear span; d is the depth of the cross-section; and ρ is the tensile steel reinforcement.

In this thesis, we adopt Eq. (4.58) to determine the cohesion of concrete and for the cap parameter X_0, the following equation is used [77]:

$$X_0 = 8.769178.10^{-3}(f'_c)^2 - 7.3302306.10^{-2}(f'_c) + 84.85 \quad \text{[MPa]} \tag{4.59}$$

4.5.1.2 Integration algorithm of concrete constitutive law-Return mapping algorithm

The return mapping algorithm basically consists of two major steps, the formulation of the elastic trial stress $\boldsymbol{\sigma}^{tr}_{n+1}$, also referred to as an elastic predictor and the return mapping to the yield surface, which can be interpreted as a closest point projection of the trial stress onto the yield surface, also referred to as a plastic corrector. This strategy involves an implicit approximation of the governing equations, leading to a nonlinear system of algebraic equations in the stresses and updated internal variables. Details can be found in the following section, with complete accounts presented in several textbooks existing already on the subject, see [78–80] among others. For multi-surface plasticity application of an implicit backward Euler integration scheme on the generalized flow rule yields the following return mapping algorithm

$$\boldsymbol{\epsilon}^{p}_{n+1} = \boldsymbol{\epsilon}^{p}_{n} + \Delta\boldsymbol{\epsilon}^{p}_{n+1} = \boldsymbol{\epsilon}^{p}_{n} + \sum_{i=1}^{2} \Delta\lambda_{i,n+1}\partial_{\boldsymbol{\sigma}} f_{i,n+1} \tag{4.60}$$

$$\boldsymbol{\sigma}^{tr}_{n+1} = \mathbf{C}\,(\boldsymbol{\epsilon}_{n+1} - \boldsymbol{\epsilon}^{p}_{n}) \tag{4.61}$$

$$\boldsymbol{\sigma}_{n+1} = \mathbf{C}\,(\boldsymbol{\epsilon}_{n+1} - \boldsymbol{\epsilon}^{p}_{n+1}) = \boldsymbol{\sigma}^{tr}_{n+1} - \mathbf{C}\,\Delta\boldsymbol{\epsilon}^{p}_{n+1} \tag{4.62}$$

where $\Delta\lambda_{i,n+1} = \dot{\lambda}_i \Delta t$ and $\mathbf{C}$ is the elastic stiffness matrix. Eq. (4.62) can be expanded as

$$I_{1,n+1} = I^{tr}_{1,n+1} - 3K\,\Delta\bar{I}^{p}_{1,n+1} \tag{4.63}$$

$$\mathbf{s}_{n+1} = \mathbf{s}^{tr}_{n+1} - 2G\,\Delta\mathbf{e}^{p}_{n+1} \tag{4.64}$$

where $\bar{I}^{p}_{1,n+1}$, $\Delta\mathbf{e}^{p}_{n+1}$, K and G are respectively first invariant of plastic strain, deviatoric plastic strain, bulk modulus and shear modulus.

The next step is to determine the active part of the yield surface. On the basis of the elastic trial stress state, we can distinguish three possibilities:

1. Stress point lies inside the yield surface - elastic state.
2. Stress point lies on the smooth cap surface - plastic state.
3. Stress point lies on the tension elliptical surface - plastic state.

4.5.1.3 Loading on the smooth cap surface mode

Loading on the smooth cap surface is characterized by $f^{tr}_{1,n+1} > 0$, $\Delta\lambda_{1,n+1} > 0$ and $\Delta\lambda_{2,n+1} = 0$ or in the numerical implementation ($I^{tr}_1 < I_{1,t}$, $f^{tr}_{1,n+1} > 0$, $\sqrt{J^{tr}_2} > \frac{1}{\theta} I^{tr}_1 - (\theta + \frac{1}{\theta}) f_{ct} + \alpha$). From the flow rule, we have

$$\Delta\boldsymbol{\epsilon}^p_{n+1} = \Delta\lambda_{1,n+1}\partial_{\boldsymbol{\sigma}} f_{1,n+1}. \tag{4.65}$$

Substituting Eq. (4.65) into Eq. (4.62), we get:

$$\boldsymbol{\sigma}_{n+1} = \boldsymbol{\sigma}^{tr}_{n+1} - \Delta\lambda_{1,n+1}\,\mathbf{C}\,\partial_{\boldsymbol{\sigma}} f_{1,n+1}. \tag{4.66}$$

In the plastic regime, the solution of above equation (4.66) involves the introduction of an additional variable which is the incremental consistency parameter $\Delta\lambda_{1,n+1}$. Hence we need an additional equation to solve the system of equations, and that is the yield function evaluated at time t_{n+1}

$$f_{1,n+1} = 0. \tag{4.67}$$

To solve this system of equations, functions are evaluated at time t_{n+1}. This system is typically solve by a Newton-Raphson type iteration. The unknown variables are cast into one vector which is

$$\mathbf{x} = \left[\boldsymbol{\sigma}_{n+1}\ \Delta\lambda_{1,n+1}\right]^{\mathrm{T}}. \tag{4.68}$$

The residual vector is defined as

$$\mathbf{r} = \begin{bmatrix} \mathbf{r}_{\boldsymbol{\sigma}} \\ r_f \end{bmatrix} = \begin{bmatrix} \boldsymbol{\sigma}_{n+1} - \boldsymbol{\sigma}^{tr}_{n+1} + \Delta\lambda_{1,n+1}\,\mathbf{C}\,\partial_{\sigma} f_{1,n+1} \\ f_{n+1} \end{bmatrix}. \tag{4.69}$$

Solving the linearized equations, we get at $(k+1)^{th}$ iteration:

$$\mathbf{x}^{(k+1)} = \mathbf{x}^{(k)} + \Delta\mathbf{x} \tag{4.70}$$

where $\Delta\mathbf{x} = -\left(\frac{\partial\mathbf{r}}{\partial\mathbf{x}}|^{(k)}\right)^{-1}\mathbf{r}^{(k)}$. The solution can be written as the following.

$$\Delta^2\lambda^{(k)}_1 = \frac{r^{(k)}_f - \partial_{\boldsymbol{\sigma}} f^{\mathrm{T}\,(k)}_{1,n+1}\,\boldsymbol{\Xi}_{1,n+1}\,\mathbf{C}^{-1}\,r^{(k)}_{\boldsymbol{\sigma}}}{\partial_{\boldsymbol{\sigma}} f^{\mathrm{T}\,(k)}_{1,n+1}\,\boldsymbol{\Xi}_{1,n+1}\,\partial_{\boldsymbol{\sigma}} f^{(k)}_{1,n+1}} \tag{4.71}$$

$$\Delta\boldsymbol{\sigma}^{(k)} = -\boldsymbol{\Xi}_{1,n+1}\left(\partial_{\boldsymbol{\sigma}} f^{(k)}_{1,n+1}\,\Delta^2\lambda^{(k)}_1 + \mathbf{C}^{-1}\,r^{(k)}_{\boldsymbol{\sigma}}\right) \tag{4.72}$$

where $\boldsymbol{\Xi}_{1,n+1} = \left[\mathbb{I} + \Delta\lambda^{(k)}_{1,n+1}\,\mathbf{C}\,\partial^2_{\boldsymbol{\sigma}\boldsymbol{\sigma}} f^{(k)}_{1,n+1}\right]^{-1}\mathbf{C}$ and $\mathbb{I}$ is unity matrix. Hence, the next iteration step is given by

$$\Delta\lambda^{(k+1)}_{1,n+1} = \Delta\lambda^{(k)}_{1,n+1} + \Delta^2\lambda^{(k)}_1 \tag{4.73}$$

$$\boldsymbol{\sigma}^{(k+1)}_{n+1} = \boldsymbol{\sigma}^{(k)}_{n+1} + \Delta\boldsymbol{\sigma}^{(k)} \tag{4.74}$$

4.5.1.4 Loading on the tensile elliptical surface

Loading is on the tensile elliptical surface while $f^{tr}_{2,n+1} > 0$, $\Delta\lambda_{2,n+1} > 0$ and $\Delta\lambda_{1,n+1} = 0$ or in the numerical implementation ($I^{tr}_1 \geq I_{1,t}$, $f^{tr}_{2,n+1} > 0$, $\sqrt{J^{tr}_2} < \frac{1}{\theta}\,I^{tr}_1 - (\theta + \frac{1}{\theta})\,f_{ct} + \alpha$). The computation algorithm for this case is similar to the previous one.

4.5.1.5 Consistent tangent operator

Use of tangent operator, consistent with the integration algorithm is essential in order to preserve the quadratic rate of convergence that characterizes Newton methods. In contrast to continuum elasto-plastic tangent operator, which is obtained by enforcing the consistency condition on the continuum problem, consistent algorithmic tangent operator is obtained by enforcing consistency on the discrete algorithmic problem.

4.5.1.5.1 Consistent tangent operator for smooth cap yield surface

Differentiation of the elastic stress-strain relationship Eq. (4.62) and the discrete flow rule Eq. (4.60) yields

$$\mathrm{d}\boldsymbol{\sigma}_{n+1} = \mathbf{C}\left(\mathrm{d}\boldsymbol{\epsilon}_{n+1} - \mathrm{d}\boldsymbol{\epsilon}^p_{n+1}\right) \tag{4.75}$$

$$\mathrm{d}\boldsymbol{\epsilon}^p_{n+1} = \mathrm{d}\left(\Delta\lambda_{1,n+1}\right)\partial_{\boldsymbol{\sigma}} f_{1,n+1} + \Delta\lambda_{1,n+1}\partial^2_{\boldsymbol{\sigma}\boldsymbol{\sigma}} f_{1,n+1}\mathrm{d}\boldsymbol{\sigma}_{n+1} \tag{4.76}$$

Combining these two equations gives

$$\mathrm{d}\boldsymbol{\sigma}_{n+1} = \boldsymbol{\Xi}_{1,n+1}\left(\mathrm{d}\boldsymbol{\epsilon}_{n+1} - \mathrm{d}\left(\Delta\lambda_{1,n+1}\right)\partial_{\boldsymbol{\sigma}} f_{1,n+1}\right) \tag{4.77}$$

where $\boldsymbol{\Xi}_{1,n+1} = [\mathbb{I} + \Delta\lambda_{1,n+1}\,\mathbf{C}\,\partial^2_{\boldsymbol{\sigma}\boldsymbol{\sigma}} f_{1,n+1}]^{-1}\,\mathbf{C}$. The coefficient $\mathrm{d}\,(\Delta\lambda_{1,n+1})$ in Eq. (4.77) can be obtained by differentiating $f_{1,n+1} = 0$

$$\partial_{\boldsymbol{\sigma}} f^{\mathrm{T}}_{1,n+1}\,\mathrm{d}\boldsymbol{\sigma}_{n+1} = 0 \tag{4.78}$$

Substituting Eq. (4.77) into Eq. (4.78) and solving for $\mathrm{d}\,(\Delta\lambda_{1,n+1})$, we get

$$\mathrm{d}\,(\Delta\lambda_{1,n+1}) = \frac{\partial_{\boldsymbol{\sigma}} f^{\mathrm{T}}_{1,n+1}\,\boldsymbol{\Xi}_{1,n+1}\,\mathrm{d}\boldsymbol{\epsilon}_{n+1}}{\partial_{\boldsymbol{\sigma}} f^{\mathrm{T}}_{1,n+1}\,\boldsymbol{\Xi}_{1,n+1}\,\partial_{\boldsymbol{\sigma}} f_{1,n+1}} \tag{4.79}$$

Inserting Eq. (4.79) into Eq. (4.77), we obtain the consistent tangent operator as below

$$\mathbf{C}^{ep}_{n+1} = \boldsymbol{\Xi}_{1,n+1} - \frac{\boldsymbol{\Xi}_{1,n+1}\,\partial_{\boldsymbol{\sigma}} f_{1,n+1} \otimes \partial_{\boldsymbol{\sigma}} f^{\mathrm{T}}_{1,n+1}\,\boldsymbol{\Xi}_{1,n+1}}{\partial_{\boldsymbol{\sigma}} f^{\mathrm{T}}_{1,n+1}\,\boldsymbol{\Xi}_{1,n+1}\,\partial_{\boldsymbol{\sigma}} f_{1,n+1}} \tag{4.80}$$

where $\otimes$ is vectorial product operation of two vectors.

4.5.1.5.2 Consistent tangent operator for tensile elliptical yield surface

The procedure determining the consistent tangent operator is the same as previously described in Section 4.5.1.5.1. In this case, the following expressions are obtained.

$$\mathrm{d}\,(\Delta\lambda_{2,n+1}) = \frac{\partial_{\boldsymbol{\sigma}} f^{\mathrm{T}}_{2,n+1}\,\boldsymbol{\Xi}_{2,n+1}\,\mathrm{d}\boldsymbol{\epsilon}_{n+1}}{\partial_{\boldsymbol{\sigma}} f^{\mathrm{T}}_{2,n+1}\,\boldsymbol{\Xi}_{2,n+1}\,\partial_{\boldsymbol{\sigma}} f_{2,n+1}} \tag{4.81}$$

$$\mathbf{C}^{ep}_{n+1} = \boldsymbol{\Xi}_{2,n+1} - \frac{\boldsymbol{\Xi}_{2,n+1}\,\partial_{\boldsymbol{\sigma}} f_{2,n+1} \otimes \partial_{\boldsymbol{\sigma}} f^{\mathrm{T}}_{2,n+1}\,\boldsymbol{\Xi}_{2,n+1}}{\partial_{\boldsymbol{\sigma}} f^{\mathrm{T}}_{2,n+1}\,\boldsymbol{\Xi}_{2,n+1}\,\partial_{\boldsymbol{\sigma}} f_{2,n+1}} \tag{4.82}$$

4.5.2 Concrete stress-strain explicit 1D model

Many different explicit stress-strain models exist to describe the unconfined and confined concrete stress-strain behavior. Popovics [81] proposed a stress-stain model of unconfined concrete requiring three material parameters to control the entire pre and post peak behavior of concrete. Popovics model represents adequately the behavior of most normal-strength concrete ($f'_c < 50$ MPa), but it

is short of a necessary control over the slope of the post-peak branch for high-strength concrete. Thorenfeldt et al. [82] modified the Popovics model to take into account the high-strength concrete behavior after the post-peak where the descending branch drop off more sharply. Mander et al. [83] adopted a failure criteria based on a 5-parameter model of William and Warnke [61] along with data from Schickert and Winkler [84] to define the confined compressive strength of concrete and adopted the 3-parameter equation proposed by Popovics [81] to describe the entire uniaxial stress-strain curve they. Bing et al. [85] proposed a three branch stress-strain model for high strength concrete confined by either normal or high-yield strength transverse reinforcement based on the experimental tests conducted by the same authors [86]. One model which is often used in nonlinear elasticity is the Kent and Park [87] model, later modified by Scott et al. [88] to include the strength and ductility enhancement due to confinement effects and the effect of strain rate. The stress-strain relationship of the modified Kent and Park concrete model is as follow:

$$\sigma_c = \begin{cases} K\, f'_c \left[\dfrac{2\varepsilon_c}{0.002K} - \left(\dfrac{\varepsilon_c}{0.002K} \right)^2 \right] & \text{for } \varepsilon_c \leq 0.002K \\ K\, f'_c \left[1 - Z_m \left(\varepsilon_c - 0.002K \right) \right] \geq 0.2K\, f'_c & \text{for } \varepsilon_c > 0.002K \end{cases} \tag{4.83}$$

For a low strain rate the coefficients K and Z_m are defined as

$$K = 1 + \frac{\rho_s\, f_{yh}}{f'_c} \tag{4.84}$$

$$Z_m = \frac{0.5}{\dfrac{3 + 0.29 f'_c}{145 f'_c - 1000} + \dfrac{3}{4}\rho_s \sqrt{\dfrac{h''}{s_h}} - 0.002K} \tag{4.85}$$

and for a high strain rate,

$$K = 1.25 \left[1 + \frac{\rho_s\, f_{yh}}{f'_c} \right] \tag{4.86}$$

$$Z_m = \frac{0.625}{\varepsilon_{50c} - 0.002K} \tag{4.87}$$

where ρ_s is the ratio of volume of rectangular steel hoop to volume of concrete core measured to the outside of the peripheral hoop, h'' the width of concrete core measured to the outside of the peripheral hoop, s_h the center to center spacing of

hoop sets, f_{yh} the yield strength of the hoop reinforcement, ε_{50c} strain at $0.5f'_c$ on falling branch of stress-strain curve for confined concrete, and f'_c is the cylinder compressive strength in MPa.

For nonlinear analysis of reinforced concrete structures, EN 1992-1-1 [11] proposes the following stress-strain relationship for normal strength concrete:

$$\frac{\sigma_c}{f_{cm}} = \frac{k\left(\frac{\varepsilon_c}{\varepsilon_{c1}}\right) - \left(\frac{\varepsilon_c}{\varepsilon_{c1}}\right)^2}{1 + (k-2)\left(\frac{\varepsilon_c}{\varepsilon_{c1}}\right)} \tag{4.88}$$

where ε_{c1} is the deformation at pick stress and k is determined by

$$k = \frac{1.1\, E_{cm}\, \varepsilon_{c1}}{f_{cm}} \tag{4.89}$$

in which f_{cm} is the mean value of concrete cylinder compressive strength and E_{cm} is the relative secant modulus calculated conventionally at a stress of $0.4f_{cm}$. Upon the ultimate strain, ε_{cu}, the model proposed by EN 1992-1-1 [11] gives no expression of stress-strain curve and is not adapted to a high strength concrete which shows a more ductile behavior than normal concrete. For confined concrete, EN 1992-1-1 [11] proposes a parabolic-rectangular stress-strain curve where the increased characteristic strength and strains are defined by

$$f_{ck,c} = \begin{cases} f_{ck}\left(1.000 + 5.0\dfrac{\sigma_2}{f_{ck}}\right) & \text{for } \sigma_2 \leq 0.05 f_{ck} \\ f_{ck}\left(1.125 + 2.5\dfrac{\sigma_2}{f_{ck}}\right) & \text{for } \sigma_2 > 0.05 f_{ck} \end{cases} \tag{4.90}$$

$$\varepsilon_{c2,c} = \varepsilon_{c2}\left(\frac{f_{ck,c}}{f_{ck}}\right)^2 \tag{4.91}$$

$$\varepsilon_{cu2,c} = \varepsilon_{cu2} + 0.2\frac{\sigma_2}{f_{ck}} \tag{4.92}$$

in which f_{ck} is the characteristic compressive cylinder strength of concrete at 28 days, $\sigma_2 (= \sigma_3)$ the effective lateral compressive stress due to confinement and ε_{c2} and ε_{cu2} are defined by EN 1992-1-1 [11].

4.6 Constitutive law for shear connection

The overall behavior of the composite steel-concrete member strongly depends on the stress transfer mechanism between the steel and the concrete encasement which may be accomplished by three main mechanisms: a) chemical bonding (bond between the cement paste and the surface of the steel: b) friction (assumed proportional to the normal force at the interface): c) mechanical interaction (due to embossments, ribs or shear stud connectors). The role of shear connection is essential, without them, there is no collaboration between the steel and concrete material. They limit the slip that may occur along the steel-concrete interface. Thus ensuring a resumption of longitudinal shear, they allow to obtain a composite section with two components working together. However, superposition of force transfer mechanisms is not generally permitted as the experimental data indicate that direct bearing or shear connection often does not initiate until after direct bond interaction has been breached, and little experimental data is available regarding the interaction of direct bearing and shear connection via steel anchors.

4.6.1 Shear transfer by bond strength between the steel and concrete component

At low loads, most longitudinal shear stresses are transferred by the chemical bond at the interface of steel-concrete whilst the chemical bond breaks down and cannot be restored [89] at high load. In general, the bond strength is a function of the normal confining pressure exerted by the surrounding concrete on the steel surface which is known as the friction mechanism. The bond stress capacity is commonly evaluated as the maximum average bond stress, which is the maximum load transferred between the steel and concrete, divided by the total surface area of steel cross-section embedded in the concrete. Experimental tests of composite structures without mechanical connector devices [90–92] have shown that the bond stress distribution is not necessarily uniform over the entire cross-section.

The earliest push-out tests by Bryson and Mathey [90] studied the effect of the steel surface condition on the bond stress capacity. The surfaces of the embedded steel beams were either freshly sandblasted, sandblasted and allowed to rust, or left with normal rust and mill scale. The steel surfaces that were sandblasted and allowed to rust, developed a larger maximum average bond stress than those with mill scale. It has been observed that once the slip was produced at the steel-concrete interface, the post slip bond stress was similar for all surface conditions. Later, Hawkins [91] examined the position of concrete casting and the relative size of reinforcement. The test results showed that specimens cast in the horizontal position had smaller bond capacity than those cast in the vertical position. This was attributed to the segregation of aggregate and accumulation of water under the lower flange of the horizontal steel section. On the other hand, the amount of confining reinforcement did not consistently affect the bond strength prior to significant slip, but an increase in confining reinforcement increased the bond resistance after slip. Moreover, the size of the steel cross-section had no effect on the bond behavior for specimens with the same ratio of the embedment length to the steel core depth. Another push-out test by Roeder [92] considered the distribution of bond stress over the member length. It has been discovered that the bond stress is primarily contributed by the flanges and the maximum bond stress is a function of the concrete strength. Based on the results of the tests, the value of the allowable load for the encased shape can be estimated by

$$P_{sl} = \frac{3.6\, b_f\, (0.09\, f'_c - 95)\, l_e}{k}, \quad \text{(in lb)} \tag{4.93}$$

where b_f is steel flange width of encased shape (in.), f'_c concrete compressive strength (psi), l_e encased length of steel shape (in.) and k is a constant equal to 5. Converting to an average ultimate bond stress using only the flange surfaces as being effective and applying a safety factor of five as reported in the tests, one obtains:

$$\tau_{max} = 0.9\, (0.09\, f'_c - 95), \quad \text{(in psi)} \tag{4.94}$$

Hamdan and Hunaiti [93] examined the effects of the concrete strength, steel surface condition, and the tie reinforcement on the maximum average bond stress.

According to the test results, the concrete strength had no effect on the bond strength but the maximum average bond stress increases by adding tie reinforcement to specimens with sandblasted steel surfaces. The same conclusions have been made by Hotta et al. [94]. Wium and Lebet [95] examined encased composite columns. They postulated that bond stress can be separated into two stages. The first stage occurs prior to complete slip and is governed by adhesion or chemical bonding between the cement paste and the steel. The second stage occurs after complete slip and is characterized as a purely frictional phenomenon. The tests showed that an increase in flange cover from 50 mm to 150 mm (2-6 in.) increased the force transfer after chemical debonding by 50%. They suggested to use only the bond stress due to friction in the design and analysis of composite structures. This bond strength depends on four major parameters: thickness of the concrete cover, amount of hoop reinforcement, size of the steel section (depth of section) and concrete shrinkage. Lam et al. [96] conducted the pullout tests on the steel plate embedded in reinforced concrete beam. The results showed that the maximum bond stress that could be developed in the specimens was about 0.6 MPa. It was observed that the bond stress dropped slowly as the interface slip increased, and the value could be maintained at slightly above 0.5 MPa at large slips. In some design codes for encased composite members [97, 98], the shear transfer between the steel and concrete is based entirely on the direct bearing. No allowance is made for natural bond between the steel and concrete. EN 1994-1-1 [12] permits the use of natural bond of 0.3 MPa for encased composite members, over the entire perimeter of the section.

For natural bond condition, the experimental results tested by Roeder et al. [99] indicated that the bond stress can be determined by using the following equation in which the maximum average bond stress was reduced by 2 standard deviations providing an estimated confidence of 97.7%:

$$f_{s(2\sigma)} = 2.52 - 0.39\frac{L}{d} - 19.12\rho, \quad \text{(in MPa)} \tag{4.95}$$

where L and d are the length and depth of the steel section; $\rho = \frac{A_s}{A_t}$; A_s and A_t are the areas of the steel section to the total cross section of the composite

member. Eq. (4.95) indicates that no bond is available when the L/d ratio is greater than approximately 6 or when ρ is greater than 0.125. It is tempting to use the longest bond length, but this will not necessarily produce the largest load transfer capacity. An optimization of the maximum load capacity computed from Eq. (4.95) found that the maximum capacity will occur when:

$$\frac{L}{d} = 3.22 - 24.52\,\rho \tag{4.96}$$

In practice, nearly all columns will use this critical length for defining their bond stress capacity, and therefore Eq. (4.96) can be introduced into Eq. (4.95) for these practical applications. Then,

$$f_{s(2\sigma)} = 1.26 - 9.54\,\rho, \quad \text{(in MPa)} \tag{4.97}$$

At the ultimate load performance level, this bond stress can be uniformly distributed over the perimeter of the section and a length equal to the lesser of either the column length or the length defined by Eq. (4.96). The tests reported that under cyclic loading the interface is deteriorated after the initial slip between the steel and concrete occurs. Thus, at the serviceability performance level, it is proposed that the triangular bond stress distribution to be used over the length of the member is equal to two times the depth of the encased sections. The maximum average bond stress defined in Eq. (4.95) is also used for the serviceability limit state, because it leads to a conservative estimation of the serviceability behavior.

According to the experimental tests [99], the concrete confinement did not have a dramatic effect on the maximum average bond stress, but it affected the post-slip deterioration. The observations during the experimental tests suggested that a minimum confinement is necessary to assure satisfactory post slip behavior, but that large amounts of confining steel are not needed to achieve a good bond performance. Further, these experiments supported the observations that the bond stress is distributed exponentially over the column length under service load, and the distribution approaches a uniform value for loads approaching the maximum

capacity. In spite of the individual previous studies suggesting that the surface condition of the steel affected the bond stress capacity, it is still recommended by Roeder et al. [99] that the bond stress should be employed only with blast cleaned surface. Moreover, the bond stress capacity does not appear to be related to the strength of the concrete.

4.6.2 Shear transfer by shear stud connector

Headed steel stud connectors welded to a steel section and encased in concrete have been the most common mechanical devices for transferring forces between the steel and concrete materials in composite construction [100]. This type of connectors has been investigated by numerous researchers worldwide, starting in the 1950s. The critical load of the stud was presented on the basis of push-out tests (see Fig. 4.4) which are commonly used to determine the load-slip behavior of the shear connectors. The shear connection capacity is assumed to be the failure load divided by the number of connectors. The first push-out test was conducted by Viest [101] who carried out 12 experimental tests with varying ratios of the effective depth-to-stud diameter (h/d), where h is the stud height from its base to the underside of the stud head. Three types of failure were observed: steel failures, where the stud diameter reached its yield point and failed; concrete failures, where the concrete surrounding the headed stud crushed; and mixed failures that included failure of both materials. Moreover, the first formulas to assess the shear strength of headed studs of composite structures was proposed as follow:

$$P_u = \begin{cases} 5.25\, d^2\, f'_c \sqrt{\frac{4000}{f'_c}} & \text{if } d < 1\,\text{in.} \\ 5\, d\, f'_c \sqrt{\frac{4000}{f'_c}} & \text{if } d > 1\,\text{in.} \end{cases} \tag{4.98}$$

where f'_c is the cylinder compressive strength of the concrete (psi) and P_u is stud shear bearing capacity (lbf). Driscoll and Slutter [102] observed that the total depth-to-stud diameter, h/d for studs embedded in normal-weight concrete should be equal to or larger than 4.2 if the full shear strength of the anchor had to be developed. As a consequence, they proposed a modification of Viest's equation

as follow.

$$P_u = \begin{cases} 932\, d^2 \sqrt{f'_c} & \text{if } h/d > 4.2\,\text{in.} \\ 222\, h\, d \sqrt{f'_c} & \text{if } h/d < 4.2\,\text{in.} \end{cases}, \quad \text{(kips)} \tag{4.99}$$

The following equations in EN 1994-1-1 [12] state the design strength of the stud shear connectors while welded automatically:

$$P_u = \min \begin{cases} \dfrac{0.8\, f_u\, \pi\, d^2/4}{\gamma_v} \\ \dfrac{0.29\, \alpha\, d^2 \sqrt{f'_c\, E_c}}{\gamma_v} \end{cases} \tag{4.100}$$

with:

$$\alpha = 0.2 \left(\frac{h}{d} + 1 \right) \qquad \text{for } 0 \leq h/d \leq 4 \tag{4.101}$$

$$\alpha = 1 \qquad \text{for } h/d > 4 \tag{4.102}$$

where γ_v is the partial factor with recommended value of 1.25 and f_u is the specified ultimate tensile strength of the material of the stud but not greater than 500 N/mm^2.

Other researchers performed push-out tests to investigate the behavior of small headed studs in a composite beam with a solid slab and with/without profile steel sheeting. Chinn [103] and Valente and Cruz [104] carried out push-out tests to evaluate the behavior of shear connection between steel and lightweight concrete. The connection behavior was analysed in term of its load-slip relation and the failure modes were identified. Davies [105] studied group effects for several headed studs in push-out tests. Mainston and Menzies [106] carried out tests on 83 push-out specimens covering the behavior of headed anchors under both static and fatigue loads. Hawkins and Mitchell [107] conducted 13 push-out tests to study the behavior of headed stud shear connectors in composite beams with profiled steel sheeting perpendicular to the beam. An and Cederwall [108] presented push-out tests of studs in normal and high strength concrete. Topkaya

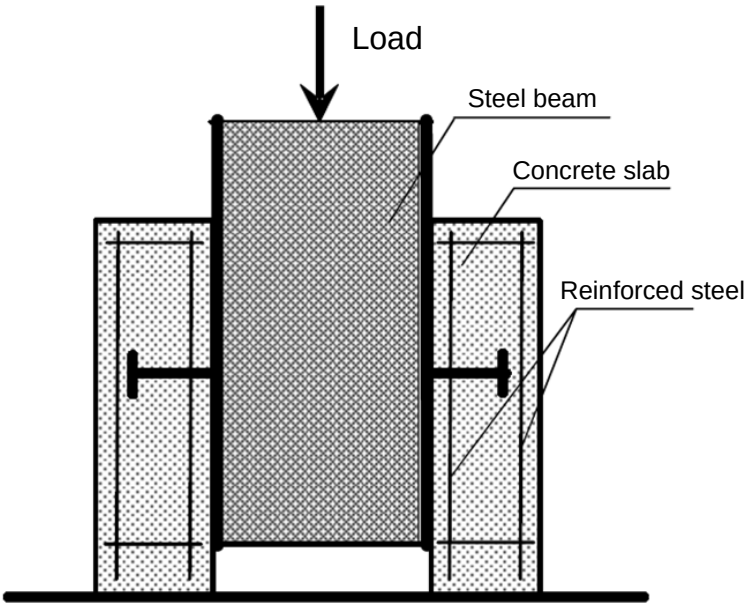

Figure 4.4: Push-out test specimen.

et al. [109] tested 24 specimens in order to describe the behavior of headed studs at early concrete ages. In brief, from the results of the experimental tests shear stud connectors are influenced by several parameters, with major factors categorized into shank diameter, height and tensile strength of studs, compressive strength and elastic modulus of concrete, reinforcement detailing, and direction of concrete casting.

In the high shear areas of steel girder bridge, many studs with typical diameter (< 25 mm) should be welded to the top flanges to satisfy the design requirements. However, this relatively large number of studs may have several disadvantages [110–112]. Among them are 1) long installation time; 2) difficult deck removal that may damage the studs as well as the girder top flange; and 3) little room on the top flange for the construction workers to walk, which raises safety concerns. For this reason, the use of large studs, which are larger than 25 mm in diameter, in composite beams can simplify the structure, save the construction time and make steel and concrete work together better. Several researchers have

investigated the behavior of shear stud connectors with large diameter. Badie et al. [110] conducted push-off tests on large studs of 31.8 mm in diameter and provided information on the development, welding, quality control, and the application of large studs. Shim et al. [111] and Lee et al. [112] investigated the static and fatigue behavior of large stud shear connectors up to 30 mm in diameter, which were beyond the limitation of current design codes. The ultimate strength of the shear connection showed that the design shear strength in Eurocode 4 gives conservative values for large studs.

With regard to the law of a welded shear stud connector behavior, Ollgaard et al. [52] proposed, following a series of 48 push-out tests in lightweight and normal-weight concrete with an effective embedment depth ratio (h/d) of 3.26, the explicit shear-slip relationship as follow (see Fig. 4.5a):

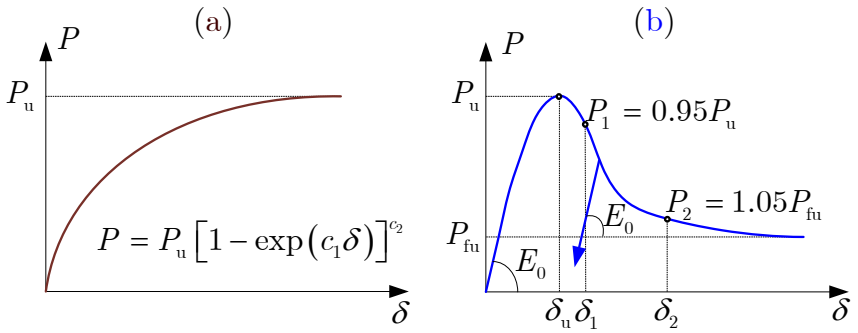

Figure 4.5: Shear stud constitutive law: (a) Ollgaard-model; (b) Salari-model.

$$P = P_u \left(1 - \mathrm{e}^{-c_1|\delta|}\right)^{c_2} \tag{4.103}$$

where P_u is the ultimate strength of shear connector, δ is the slip in mm, $c_2 = 0.4$, and $c_1 = 0.7$ mm^{-1}. This model became the basis of several design methods in codes. Aribert and Labib [113] provided a combination of $c_2 = 0.8$, $c_1 = 0.7$ mm^{-1}, while Johnson et al. [114] presented values of $c_2 = 0.558$, $c_1 = 1.0$ mm^{-1}, and also $c_2 = 0.989$, $c_1 = 1.535$ mm^{-1}. An improvement was given by Gattesco and Giuriani [115] to simulate the actual behavior of the connectors, Eq. (4.104)

with $c_2 = 0.97$, $c_1 = 1.3$ mm^{-1} and $c_3 = 0.0045$ mm^{-1}.

$$P = P_u \left[c_2 \left(1 - \mathrm{e}^{\frac{-c_1 |\delta|}{c_2}} \right)^{0.5} + c_3 |\delta| \right] \tag{4.104}$$

More recently, Salari [116] proposed an explicit model of the nonlinear behavior of cyclic studs. This model is capable of taking into account the loss of strength and stiffness of the connector during cyclic loading (see Fig. 4.5b). The envelope curve is given by the following formulas.

$$P = P_u \alpha_1 \overline{\delta} \exp\left(-\alpha_2 \overline{\delta}^{\alpha_3} \right) \qquad \text{for} \qquad 0 \leq \overline{\delta} = \frac{\delta}{\delta_u} \leq 1 \tag{4.105}$$

$$P = P_u \beta_1 \exp\left(-\beta_2 \left(\overline{\delta} - 1 \right)^{\beta_3} \right) + P_{fu} \qquad \text{for} \qquad \overline{\delta} = \frac{\delta}{\delta_u} > 1 \tag{4.106}$$

with:

$$\alpha_1 = \frac{E_0 \delta_u}{P_u} \qquad \beta_1 = 1 - \frac{P_u}{P_{fu}}$$

$$\alpha_2 = \mathrm{Ln}(\alpha_1) \qquad \beta_2 = -\frac{\mathrm{Ln}(R_1)}{(\overline{\delta}_1 - 1)^{\beta_3}}$$

$$\alpha_3 = \frac{1}{\alpha_2} \qquad \beta_3 = \frac{\mathrm{Ln}(R_1) - \mathrm{Ln}(R_2)}{\mathrm{Ln}(\overline{\delta}_1 - 1) - \mathrm{Ln}(\overline{\delta}_2 - 1)}$$

$$R_i = \frac{P_i - P_{fu}}{P_u - P_{fu}} \qquad \overline{\delta}_i = \frac{\delta_i}{\delta_u}\,, \;\; i = 1, 2$$

In these formulas, we denote by:

- δ_u the slip corresponding to the ultimate force P_u;
- P_{fu} is the adhesive strength related to the friction;
- δ_1 is the slip corresponding to the force $P_1 = 0.95 P_u$ after peak;
- δ_2 is the slip corresponding to the force $P_2 = 1.05 P_{fu}$ after peak;

Another shear-slip relationship of the shear stud connector, which is fairly simple, is elastic perfectly plastic model, (Fig. 4.6).

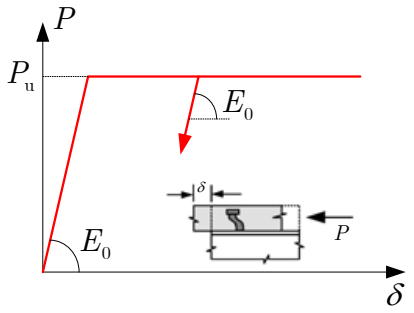

Figure 4.6: Elastic-perfectly plastic shear stud model.

4.7 Conclusion

In this thesis, the concrete plastic Cap model is adopted for characterizing the 3D stress state of concrete in the shear-flexible model. The outcome of the cap model is that it can represent the concrete behavior in the hydrostatic compression that can arrive for highly confined concrete. For structural steel shape and reinforcement bar, the elastic perfectly plastic and elasto-plastic with linear hardening constitutive law are adopted, respectively. The shear connection is modeled as a distributed spring in this thesis. The equivalent distributed shear strength and stiffness are calculated by dividing the strength and stiffness of a single row of shear studs by their spacing along the beam length. The elastic perfectly plastic constitutive law is adopted for shear connection. This adoption in the forthcoming numerical model may give a more flexible response of the beam compared to the model with a nonlinear constitutive law of shear connection. However, both constitutive law may give the same ultimate.

Chapter 5

Nonlinear Finite Element Analysis

***

Nonlinear analysis of hybrid beam-column using displacement-based approach.

5.1 Introduction

In comparison to the case of the hybrid member under combined compression and bending, the nonlinear behavior of hybrid member under high shear stresses has not been extensively investigated. Indeed, the classical fiber beam element model considering only the axial stresses acting on the cross-section is not capable to accurately describe the response of the structural member under the coupling between shear, axial and bending action. Over the years, there has been a great deal of research on the development of the fiber element model to overcome this limitation by adopting the Timoshenko beam theory or even the exact beam theory. The differences between the models proposed in the literature are related to the shear kinematic assumptions taken at the sectional level, the type of multi-axial constitutive relations and also to the FE formulation based on

the stiffness or flexibility approach [117–126]. Vecchio and Collins [117] adopted the smeared crack approach and proposed the modified compression field theory (MCFT) which assumes the cracked concrete in reinforced concrete can be treated as a new material with empirically defined uniaxial stress-strain behavior, representing the average stress versus strain constitutive laws in the element. This model includes an additional set of equilibrium equations designed to satisfy the longitudinal equilibrium of each fiber which enables to determine numerically the shear strain profile. Bentz et al. [118] then improves upon this model and entitled it the Simplified Modified Compression Field Theory (SMCFT) by providing an accurate shear calculation while making the overall shear design method less complicated. Ranzo and Petrangeli [119] adopted the nonlinear truss model to identify the monotonic shear response of the reinforced concrete beam (a hysteretic stress-strain relationship) and then implemented the latter straightforwardly into the classical fiber element model. Thereafter, Petrangeli et al. [120] adopted the micro-plane theory to model the shear mechanism at each concrete fiber of the cross-section by imposing the equilibrium between the concrete and the transverse steel reinforcement to determine the transverse strains. A contribution by Guner and Vecchio [123] is quite similar in terms of the shear strain distribution and the assumption of zero clamping stresses in the transverse direction. Recently, Navarro-Gregori et al. [126] presented a model based on Timoshenko beam theory with a variable shear strain distribution on the cross-section in order to effectively capture the phenomenon of diagonal cracking. Apart from the assumption of the shear strain distribution on the cross-section, a sectional model based upon a displacement field to take into account the effects of warping and distortion in the cross-section has been proposed by Bairan and Mari [121] and Mohr et al. [124]. A further modeling strategy attempting to capture the mechanics of the phenomena is addressed to the triaxial constitutive model of the concrete coupling with/without the damage mechanic model. Saritas and Filippou [122] developed a beam element model by condensing the 3d formulation derived from a 3d plastic-damage material model with the plane stress conditions. Likewise, a force-based Timoshenko-type 3d beam element with the

softened membrane constitutive model was developed by Mullapudi and Ayoub [125] to analyze concrete members subjected to combined loadings including torsion. They emphasized the accuracy of the model in representing both global and local behavior of concrete member parameters as well as the proper failure mode.

This chapter aims to develop a new finite element formulation based on a fiber model considering the triaxial stress state in the concrete component, motivated by a large range of the research on the shear failure of reinforced concrete members as cited above. The plane stress condition for the concrete component is applied in order to condense the 3d formulation, derived from a 3d plastic model of the concrete material, into a 2d beam model. To do so, we apply the strategy proposed by Klinkel and Govindjee [127] where the stresses that need to be set equal to zero on the 3d material model are linearized. Consequently, the out-of-plane strain components are updated. This allows a quadratic convergence rate in the local iteration scheme. The consistent tangent stiffness are provided by the standard static condensation of the 3d material tangent stiffness. To take into account the contribution of the transverse reinforcement on confinement effects of the concrete material, we extend this algorithm by imposing the transversal equilibrium between the concrete fiber and the transverse steel.

The organization of this chapter is as follows. In Section 5.2, the equilibrium and the kinematic equations are introduced in matrix forms. Next, the development of the displacement-based finite element formulation is presented in Section 5.3. Section 5.4 is devoted to the sectional formulation where the procedure of determining the consistent tangent stiffness is highlighted. Finally, the numerical applications are presented in Section 5.5 to assess and illustrate the performance of the developed formulations.

5.2 Equation field

The field equations in matrix form describing the behavior of hybrid beam with n embedded sections in partial interaction are briefly outlined in this section. All variables with subscript c belong to the encasing component (concrete) and those with subscript s belong to the embedded element (steel). Quantities with subscript sc are associated with the shear connection.

5.2.1 Kinematic relations

From the kinematic relations Eqs. (2.12-2.16), the vector $\hat{\mathbf{e}}$ denoting the generalized sectional strain is related to the displacement field by the kinematic relations as follow:

$$\hat{\mathbf{e}} = \hat{\partial}\mathbf{d} \tag{5.1}$$

where

$$\hat{\mathbf{e}}^{\mathrm{T}} = [\epsilon_{s_1}\ \epsilon_{s_2}\ \cdots\ \epsilon_{s_n}\ \kappa_s\ \epsilon_c\ \kappa_c\ \gamma_c\ g_1\ g_2\ \cdots\ g_n]\,, \tag{5.2}$$

$$\mathbf{d}^{\mathrm{T}} = [u_{s_1}\ u_{s_2}\ \cdots\ u_{s_n}\ u_c\ v\ \theta_c] \tag{5.3}$$

and the expression of $\hat{\partial}$ is given by

$$\hat{\partial}^{\mathrm{T}} = \begin{bmatrix} \partial & 0 & \cdots & 0 & 0 & 0 & 0 & 0 & -1 & 0 & \cdots & 0 \\ 0 & \partial & \cdots & 0 & 0 & 0 & 0 & 0 & 0 & -1 & \cdots & 0 \\ \vdots & \vdots & \ddots & \vdots & \vdots & \vdots & \vdots & \vdots & \vdots & \vdots & \ddots & \vdots \\ 0 & 0 & \cdots & \partial & 0 & 0 & 0 & 0 & 0 & 0 & \cdots & -1 \\ 0 & 0 & \cdots & 0 & 0 & \partial & 0 & 0 & 1 & 1 & \cdots & 1 \\ 0 & 0 & \cdots & 0 & \partial^2 & 0 & 0 & \partial & 0 & 0 & \cdots & 0 \\ 0 & 0 & \cdots & 0 & 0 & 0 & \partial & -1 & -h_1 & -h_2 & \cdots & -h_n \end{bmatrix} \tag{5.4}$$

The superscript $\bullet^{\mathrm{T}}$ denotes matrix transposition.

5.2.2 Equilibrium relations

The equilibrium equations (Eqs. (2.1-2.5)) can be cast in compact form as follow:

$$\widetilde{\partial}\mathbf{D} + \mathbf{P}_e = 0 \tag{5.5}$$

in which

$$\mathbf{D}^{\mathrm{T}} = [N_{s_1}\ N_{s_2} \cdots N_{s_n}\ M_s\ N_c\ M_c\ T_c\ D_{sc_1}\ D_{sc_2} \cdots D_{sc_n}]\,, \tag{5.6}$$

$$\mathbf{P}_e^{\mathrm{T}} = [0\ 0 \cdots 0\ 0\ p_y\ 0] \tag{5.7}$$

and the expression of $\widetilde{\partial}$ is as follow:

$$\widetilde{\partial} = \begin{bmatrix} \partial & 0 & \cdots & 0 & 0 & 0 & 0 & 0 & 1 & 0 & \cdots & 0 \\ 0 & \partial & \cdots & 0 & 0 & 0 & 0 & 0 & 0 & 1 & \cdots & 0 \\ \vdots & \vdots & \ddots & \vdots & \vdots & \vdots & \vdots & \vdots & \vdots & \vdots & \ddots & \vdots \\ 0 & 0 & \cdots & \partial & 0 & 0 & 0 & 0 & 0 & 0 & \cdots & 1 \\ 0 & 0 & \cdots & 0 & 0 & \partial & 0 & 0 & -1 & -1 & \cdots & -1 \\ 0 & 0 & \cdots & 0 & -\partial^2 & 0 & 0 & \partial & 0 & 0 & \cdots & 0 \\ 0 & 0 & \cdots & 0 & 0 & 0 & \partial & 1 & h_1 & h_2 & \cdots & h_n \end{bmatrix} \tag{5.8}$$

5.2.3 Variational formulation

For the sake of simplicity, the element distributed loads (body forces) are omitted. The variational formulations of equilibrium equations are then as follow:

$$\int_L \delta d^{\mathrm{T}}\, \widetilde{\partial}\mathbf{D}\, \mathrm{d}x = 0 \tag{5.9}$$

Applying integration by parts, the above equation is rewritten as

$$\int_L \delta\hat{\mathbf{e}}^{\mathrm{T}}\, \mathbf{D}\, \mathrm{d}x = \delta\mathbf{q}^{\mathrm{T}}\, \mathbf{Q} \tag{5.10}$$

The left hand side is the virtual works of internal forces while the right one is of external forces. The latter can be written as

$$\delta\mathbf{q}^{\mathrm{T}}\mathbf{Q} = \left[\sum_{j=1}^{n} \delta u_{s_j}\, N_{s_j} + \delta u_c\, N_c + \delta\theta_s\, M_s + \delta\theta_c\, M_c + \delta v\, T\right]_0^L \tag{5.11}$$

in which $T = T_c + \sum_{i=1}^{n} T_{s_i}$ is the total shear force at the considered point on the directrix of the beam.

The consistent matrix formulations are obtained by using Newton-Raphson iterative procedure. In the interval of $(i-1)^{th}$ to i^{th} iteration, the linear behavior is assumed which gives:

$$\mathbf{D}^i = \mathbf{D}^{i-1} + \mathbf{k}^{i-1}\, \Delta\hat{\mathbf{e}} \tag{5.12}$$

where k^{i-1} is the linear tangent stiffness matrix of the section at the $(i-1)^{th}$ iteration.

At the i^{th} iteration, Eq. (5.10) is rewritten as:

$$\int_L \left(\delta\hat{\mathbf{e}}^T \left(\mathbf{D}^{i-1} + \mathbf{k}^{i-1}\, \Delta\hat{\mathbf{e}}\right)\right) \mathrm{d}x = \delta\mathbf{q}^T\mathbf{Q} \tag{5.13}$$

5.3 Displacement based formulation

Let the hybrid beam be divided into finite number of elements. The continuum displacement vector within an element is discretized such that

$$\mathbf{d} = \sum_{i=1}^{\alpha} N_i\, \mathbf{q}_i \tag{5.14}$$

where N_i is the shape function of node i; α is number of nodes in an element and $\mathbf{q}_i$ is the generalized displacement vector corresponding to the i^{th} node of an element. The above relation is expressed in matrix form as

$$\mathbf{d} = \mathbf{N}\,\mathbf{q} \tag{5.15}$$

where $\mathbf{N}$ is element shape function matrix and $\mathbf{q}$ is element nodal displacement vector, see Fig. 5.1. The deformation field, $\hat{\mathbf{e}}$ can be expressed in terms of nodal displacement vector, $\mathbf{q}$ as

$$\hat{\mathbf{e}} = \mathbf{B}\,\mathbf{q} \tag{5.16}$$

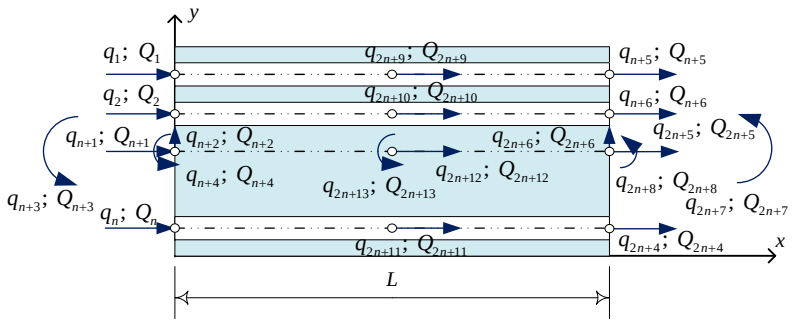

Figure 5.1: Nodal forces and displacements of hybrid beam element.

where $\mathbf{B} = \hat{\partial}\mathbf{N}(x)$. By substituting Eq. (5.16) back into Eq. (5.13), one obtains:

$$\delta\mathbf{q}^{\mathrm{T}} \int_L \left[\mathbf{B}^{\mathrm{T}} \left(\mathbf{D}^{i-1} + \mathbf{k}^{i-1}\mathbf{B}\Delta\mathbf{q}\right)\right] \mathrm{d}x = \delta\mathbf{q}^T\mathbf{Q}, \qquad \forall\delta\mathbf{q} \tag{5.17}$$

which must hold for any kinematically admissible variations $\delta\mathbf{q}$. Therefore, this equation may be simplified in the following form

$$\int_L \left[\mathbf{B}^{\mathrm{T}} \left(\mathbf{D}^{i-1} + \mathbf{k}^{i-1}\,\mathbf{B}\,\Delta\mathbf{q}\right)\right] \mathrm{d}x = \mathbf{Q} \tag{5.18}$$

which can be rewritten as

$$\mathbf{K}^{i-1}\Delta\mathbf{q}^i = \mathbf{Q}^i - \mathbf{Q}_R^{i-1} \tag{5.19}$$

where $\mathbf{K}^{i-1} = \int_L \mathbf{B}^{\mathrm{T}}\,\mathbf{k}^{i-1}\,\mathbf{B}\,\mathrm{d}x$ is element tangent stiffness matrix and $\mathbf{Q}_R^{i-1} = \int_L \mathbf{B}^{\mathrm{T}}\,\mathbf{D}^{i-1}\,\mathrm{d}x$ is the nodal forces due to the lack of equilibrium at the element level. In the present work, we adopt Hermite polynomial function for the transversal displacement v and the quadratic interpolation functions for axial displacement u_i of each constituent and for sectional rotation θ_c of encasing component. Such shape functions will prohibit the analysis result from the shear locking problem. The shape function, $\mathbf{N}$ used for interpolation of displacement field is defined as follow.

$$\mathbf{N}^{\mathrm{T}} = \begin{bmatrix} \mathbf{N}_{us_1}^{\mathrm{T}} & \mathbf{N}_{us_2}^{\mathrm{T}} & \cdots & \mathbf{N}_{us_n}^{\mathrm{T}} & \mathbf{N}_{u_c}^{\mathrm{T}} & \mathbf{N}_{v}^{\mathrm{T}} & \mathbf{N}_{\theta_c}^{\mathrm{T}} \end{bmatrix} \tag{5.20}$$

where

$$
\begin{aligned}
N_{us_1} &= \Big[A_u \;\; 0 \;\; \cdots \;\; 0 \;\; 0 \;\; 0 \;\; 0 \;\; 0 \;\; B_u \;\; 0 \;\; \cdots \;\; 0 \;\; 0 \;\; 0 \;\; 0 \;\; 0 \;\; C_u \;\; 0 \;\; \cdots \;\; 0 \;\; 0 \;\; 0\Big] \\
N_{us_2} &= \Big[0 \;\; A_u \;\; \cdots \;\; 0 \;\; 0 \;\; 0 \;\; 0 \;\; 0 \;\; 0 \;\; B_u \;\; \cdots \;\; 0 \;\; 0 \;\; 0 \;\; 0 \;\; 0 \;\; 0 \;\; C_u \;\; \cdots \;\; 0 \;\; 0 \;\; 0\Big] \\
N_{us_n} &= \Big[0 \;\; 0 \;\; \cdots \;\; A_u \;\; 0 \;\; 0 \;\; 0 \;\; 0 \;\; 0 \;\; 0 \;\; \cdots \;\; B_u \;\; 0 \;\; 0 \;\; 0 \;\; 0 \;\; 0 \;\; 0 \;\; \cdots \;\; C_u \;\; 0 \;\; 0\Big] \\
N_{uc} &= \Big[0 \;\; 0 \;\; \cdots \;\; 0 \;\; A_u \;\; 0 \;\; 0 \;\; 0 \;\; 0 \;\; 0 \;\; \cdots \;\; 0 \;\; B_u \;\; 0 \;\; 0 \;\; 0 \;\; 0 \;\; 0 \;\; \cdots \;\; 0 \;\; C_u \;\; 0\Big] \\
N_{v} &= \Big[0 \;\; 0 \;\; \cdots \;\; 0 \;\; 0 \;\; A_v \;\; A_{\theta_s} \;\; 0 \;\; 0 \;\; 0 \;\; \cdots \;\; 0 \;\; 0 \;\; B_v \;\; B_{\theta_s} \;\; 0 \;\; 0 \;\; 0 \;\; \cdots \;\; 0 \;\; 0 \;\; 0\Big] \\
N_{\theta_c} &= \Big[0 \;\; 0 \;\; \cdots \;\; 0 \;\; 0 \;\; 0 \;\; 0 \;\; A_{\theta_c} \;\; 0 \;\; 0 \;\; \cdots \;\; 0 \;\; 0 \;\; 0 \;\; 0 \;\; B_{\theta_c} \;\; 0 \;\; 0 \;\; \cdots \;\; 0 \;\; 0 \;\; C_{\theta_c}\Big]
\end{aligned}
\tag{5.21}
$$

in which

$$
\begin{aligned}
A_u(x) &= A_{\theta_c}(x) = 1 - \frac{3x}{L} + \frac{2x^2}{L^2} & B_u(x) &= B_{\theta_c}(x) = -\frac{x}{L} + \frac{2x^2}{L^2} \\
A_v(x) &= 1 - \frac{3x^2}{L^2} + \frac{2x^3}{L^3} & B_v(x) &= \frac{3x^2}{L^2} - \frac{2x^3}{L^3} \\
A_{\theta_s}(x) &= x - \frac{2x^2}{L} + \frac{x^3}{L^2} & B_{\theta_s}(x) &= -\frac{x^2}{L} + \frac{x^3}{L^2} \\
C_u &= C_{\theta_c} = \frac{4x}{L} - \frac{4x^2}{L^2}
\end{aligned}
\tag{5.22}
$$

5.4 Section formulation

The nonlinear behavior of a hybrid beam subjected to a combined load largely depends on the hypotheses made for the stress and strain distribution on the cross-section. It is here assumed that the longitudinal reinforcing bar and steel sections are subjected to only axial stresses whereas the concrete component is under generalized 3d stress field. As a consequence, a uniaxial stress-strain relationship for the longitudinal reinforcing bar and the steel profile can be used and a 3d constitutive model of concrete has to be adopted. Because of the complexity of the latter, the following section is only devoted to the description of the concrete component.

5.4.1 Fibre state determination

In the framework of the sectional level, the two translations of any point on the cross-section of concrete component $\overline{\mathbf{d}}_i^{\mathrm{T}} = [\overline{u}_i\ \overline{v}_i]$ are related to the generalized displacements at the reference point of the cross-section by the following expressions.

$$\begin{aligned} \overline{u}_c(x,y) &= u_c(x) - y\theta_c(x) \\ \overline{v}_c(x,y) &= v_c(x) = v(x) \end{aligned} \tag{5.23}$$

Given the generalized sectional strain vector $\hat{\mathbf{e}}_c = [\epsilon_c,\ \kappa_c,\ \gamma_c]^{\mathrm{T}}$, the fiber longitudinal strains (parallel to the beam axis) and shear strains of concrete component can be found using suitable shape functions. In particular, for the longitudinal strain field, the plane section hypothesis has to be retained, whereas for the shear strain field different shear shape functions can be used. Another fashion of an analytical procedure is to approximate the shear stress distributions. Despite no guarantee of compatibility between fibers, it gives a satisfactory approximate analysis that allows for a better computational speed in sectional level, see [117]. Comparing the numerical results of both uniform shear stress and parabolic shear strain assumption against the results of a rigorous procedure, Vecchio and Collins [117] showed that using the former assumption led to a conservative value of the ultimate load and the latter resulted in an un-conservative value of the failure load. For the sake of simplicity and computational efficiency for implementing and applying the concrete plasticity model, in this study a uniform shear strain distribution γ_{xy}^c along the concrete section is assumed in spite of the fact that this assumption may overestimate the ultimate load:

$$\gamma_{xy}^c = \gamma_c \tag{5.24}$$

In this manner, the plane section hypothesis is restrained. By these means and using the equilibrium, compatibility and constitutive equations, the complete 2d stress-strain state and the stiffness matrix of the fiber are determined.

5.4.1.1 Plane stress

The constitutive equations of 2d stress-strain state for concrete fiber are obtained by prescribing the in-plane strains and enforcing the plane beam constraint on the 3d constitutive law, and then obtaining, as a result, the active stresses and out-of-plane strains. In the transverse direction (y-direction as well as z-direction), the transversal reinforcement is assumed to be uniformly distributed in the concrete with a volumetric ratio ρ^{st}. This assumption is made in order to take into account the confinement effects in the concrete. When imposing the equilibrium between concrete and steel in transverse direction, we can choose the solution within two extreme options [120] which are 1) impose equilibrium at each fiber separately and 2) impose equilibrium over the whole cross-section. The former option is more advantageous from a computational point of view because the iterations are carried out separately at each fiber, according to the degree of nonlinearity of the fiber behavior. Therefore, the total number of fiber state determinations are reduced to a minimum, avoiding iteration of the whole cross-section (option 2), when highly nonlinear behavior takes place in only a few fibers. Moreover, within option 1, it is possible to define a different effective transverse steel area for each fiber, depending on the stirrup configuration. Hence, the option 1 is adopted in this study. Compatibility requirements impose that the transverse strain ϵ_y^c and lateral strain ϵ_z^c in concrete is equal to the strain in the transversal reinforcement ϵ_y^{st} and ϵ_z^{st}, respectively, see Fig. 5.2. The resultant stresses along the y-direction

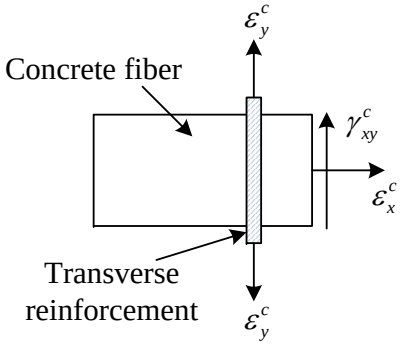

Figure 5.2: Concrete fiber mechanics.

and z-direction are the additions of the axial stresses in the transversal steel σ_y^{st} and σ_z^{st} to the axial stresses in concrete σ_y^c and σ_z^c, respectively:

$$\sigma_y = \sigma_y^c + \rho_y^{st}\,\sigma_y^{st} \tag{5.25}$$

$$\sigma_z = \sigma_z^c + \rho_z^{st}\,\sigma_z^{st} \tag{5.26}$$

where $\rho_\alpha^{st} = \frac{A_\alpha^{st}}{b_\alpha\, s_{st}}$; $\sigma_\alpha^{st} = E_\alpha^{st}\,\epsilon_\alpha^c$; $E_\alpha^{st} = \frac{\partial \sigma_\alpha^{st}}{\partial \epsilon_\alpha^{st}}$; A_α^{st} the area of transversal steel; b_α the width/height of the cross-section with $\alpha = y$, z and s_{st} is the longitudinal spacing of the stirrups. Therefore, the 3d stress-strain relationship from the 3d problem can be written as:

$$\begin{bmatrix} \sigma_x^c \\ \sigma_y \\ \sigma_z \\ \tau_{xy}^c \end{bmatrix} = \left(\begin{bmatrix} C_{11}^{ep} & C_{12}^{ep} & C_{13}^{ep} & C_{14}^{ep} \\ C_{21}^{ep} & C_{22}^{ep} & C_{23}^{ep} & C_{24}^{ep} \\ C_{31}^{ep} & C_{32}^{ep} & C_{33}^{ep} & C_{34}^{ep} \\ C_{41}^{ep} & C_{42}^{ep} & C_{43}^{ep} & C_{44}^{ep} \end{bmatrix} + \begin{bmatrix} 0 & 0 & 0 & 0 \\ 0 & \rho_y^{st}\,E_y^{st} & 0 & 0 \\ 0 & 0 & \rho_z^{st}\,E_z^{st} & 0 \\ 0 & 0 & 0 & 0 \end{bmatrix} \right) \begin{bmatrix} \epsilon_x^c \\ \epsilon_y^c \\ \epsilon_z^c \\ \gamma_{xy}^c \end{bmatrix} \tag{5.27}$$

where $\mathbf{C}^{ep}$ is the 3d consistent tangent stiffness of the concrete section.

In the following, the nested Newton return-mapping iteration for plane beam enforcement is restricted to for the reason that the original three-dimensional algorithm can be used without modification. In order to describe the procedure, it is convenient to employ the matrix notation of active stresses and in-plane strains as follows:

$$\overline{\boldsymbol{\sigma}}^c = \left[\sigma_x^c\ \tau_{xy}^c\right]^{\mathrm{T}} \tag{5.28}$$

$$\overline{\boldsymbol{\epsilon}}^c = \left[\epsilon_x^c\ \gamma_{xy}^c\right]^{\mathrm{T}} \tag{5.29}$$

During a typical equilibrium iteration, the in-plane displacements are prescribed and so is the in-plane strain array $\overline{\boldsymbol{\epsilon}}^c$. Instead of giving $\overline{\boldsymbol{\epsilon}}^c$ as the input of an augmented algebraic system, we proceed as follows. Firstly, we define some initial guesses for the unknown out-of-plane strains ($\overline{\boldsymbol{\epsilon}}_p^c = [\epsilon_y^c,\ \epsilon_z^c]^{\mathrm{T}}$). One possible guess can be the previously (equilibrium) converged out-of-plane strains, i.e. we can set

$$\overline{\boldsymbol{\epsilon}}_p^c = \overline{\boldsymbol{\epsilon}}_{p,0}^c. \tag{5.30}$$

Next, we use the augmented strain array $\left[\overline{\boldsymbol{\epsilon}}^{c,\mathrm{T}},\ \overline{\boldsymbol{\epsilon}}_p^{c,\mathrm{T}}\right]^{\mathrm{T}}$ as the input of the integration algorithm for the 3d case i.e. for $\widehat{\boldsymbol{\epsilon}}^c = \left[\epsilon_x^c\ \epsilon_y^c\ \epsilon_z^c\ \gamma_{xy}^c\right]^{\mathrm{T}}$ case. After application of the 3d return-mapping procedure, the corresponding routine will return the augmented stress array $\left[\overline{\boldsymbol{\sigma}}^{c,\mathrm{T}}\ \overline{\boldsymbol{\sigma}}_p^{\mathrm{T}}\right]^{\mathrm{T}}$ where $\overline{\boldsymbol{\sigma}}_p^{\mathrm{T}} = [\sigma_y\ \sigma_z]$. If $\|\overline{\boldsymbol{\sigma}}_p\| = 0$ (or, in computational terms, $\|\overline{\boldsymbol{\sigma}}_p\| \leq Tol$) then the guesses $\overline{\boldsymbol{\epsilon}}_p^c$ indeed solves the plane beam problem, and the solution obtained by the 3d problem is the one we are looking for. Otherwise, we apply a Newton-Raphson correction to obtain another guess

$$\overline{\boldsymbol{\epsilon}}_p^c = \overline{\boldsymbol{\epsilon}}_p^c - \mathbf{C}_{pp}^{-1}\overline{\boldsymbol{\sigma}}_p \tag{5.31}$$

where $\mathbf{C}_{pp}$ is the component of the modified 3d consistent tangent matrix obtained from Eq. (5.27) as follows:

$$\begin{bmatrix} \overline{\boldsymbol{\sigma}}^c \\ \overline{\boldsymbol{\sigma}}_p \end{bmatrix} = \begin{bmatrix} \mathbf{C}_{mm} & \mathbf{C}_{mp} \\ \mathbf{C}_{pm} & \mathbf{C}_{pp} \end{bmatrix} \begin{bmatrix} \overline{\boldsymbol{\epsilon}}^c \\ \overline{\boldsymbol{\epsilon}}_p^c \end{bmatrix}. \tag{5.32}$$

We repeat this process until we find the out-of-plane strains $\overline{\boldsymbol{\epsilon}}_p^c$ that, together with the in-plane strains kinematically prescribed by the global equilibrium iteration, results in zeros (or sufficiently small) the non-active stresses $\overline{\boldsymbol{\sigma}}_p$ upon application of the 3d algorithm.

To obtain the tangent operator consistent with the above nested iteration algorithm, we first differentiate the residual equation $\overline{\boldsymbol{\sigma}}_p = 0$ of the plane beam enforcement loop. This together with Eq. (5.32) gives

$$\mathrm{d}\overline{\boldsymbol{\sigma}}_p = \mathbf{C}_{pm}\,\mathrm{d}\overline{\boldsymbol{\epsilon}}^c + \mathbf{C}_{pp}\,\mathrm{d}\overline{\boldsymbol{\epsilon}}_p^c = 0, \tag{5.33}$$

which renders

$$\mathrm{d}\overline{\boldsymbol{\epsilon}}_p^c = -\mathbf{C}_{pp}^{-1}\mathbf{C}_{pm}\,\mathrm{d}\overline{\boldsymbol{\epsilon}}^c. \tag{5.34}$$

Substitution of above equation into Eq. (5.32) results in the following consistent tangent relation between the active stresses and strains components

$$\frac{\mathrm{d}\overline{\boldsymbol{\sigma}}^c}{\mathrm{d}\overline{\boldsymbol{\epsilon}}^c} = \overline{\mathbf{k}}^c \tag{5.35}$$

where $\overline{\mathbf{k}}^c = \mathbf{C}_{mm} - \mathbf{C}_{mp}\mathbf{C}_{pp}^{-1}\mathbf{C}_{pm}$.

5.4.1.2 Plane strain

In case the lateral deformations of concrete are restrained, the plane strain conditions can be used. The original three-dimensional algorithm can be then used without modification by imposing the out-of-plan strains equal to zero. From the 3d problem, we have the 3d stress-strain relationship as follows:

$$\begin{bmatrix} \sigma_x^c \\ \sigma_y^c \\ \sigma_z^c \\ \tau_{xy}^c \end{bmatrix} = \begin{bmatrix} C_{11}^{ep} & C_{12}^{ep} & C_{13}^{ep} & C_{14}^{ep} \\ C_{21}^{ep} & C_{22}^{ep} & C_{23}^{ep} & C_{24}^{ep} \\ C_{31}^{ep} & C_{32}^{ep} & C_{33}^{ep} & C_{34}^{ep} \\ C_{41}^{ep} & C_{42}^{ep} & C_{43}^{ep} & C_{44}^{ep} \end{bmatrix} \begin{bmatrix} \epsilon_x^c \\ 0 \\ 0 \\ \gamma_{xy}^c \end{bmatrix} \tag{5.36}$$

The consistent tangent stiffness of the concrete fiber for the plane strain conditions is then:

$$\overline{\mathbf{k}}^c = \begin{bmatrix} C_{11}^{ep} & C_{14}^{ep} \\ C_{41}^{ep} & C_{44}^{ep} \end{bmatrix}. \tag{5.37}$$

5.4.2 Section response

The relation between internal forces $\mathbf{D}$ and generalized strains $\hat{\mathbf{e}}$ depends on the material properties and the cross-section geometry of the beam. For hybrid beam in partial interaction with nonlinear material behavior, this relation can be expressed in general form as

$$\mathbf{D} = \Omega(\hat{\mathbf{e}}) \tag{5.38}$$

where Ω represents a general function that permits the computation of internal forces for given generalized strains. The linearization of Eq. (5.38) gives the tangent stiffness matrix of the section $\mathbf{k}$ which is

$$\mathbf{k} = \begin{bmatrix} \mathbf{k}_s & \mathbf{0} & \mathbf{0} \\ \mathbf{0} & \mathbf{k}_c & \mathbf{0} \\ \mathbf{0} & \mathbf{0} & \mathbf{k}_{sc} \end{bmatrix} \tag{5.39}$$

The components of the consistent tangent stiffness of the section are:

$$\mathbf{k}_s = \begin{bmatrix} \overline{EA}_{s_1} & 0 & \cdots & 0 & -\overline{ES}_{s_1} \\ 0 & \overline{EA}_{s_2} & \cdots & 0 & -\overline{ES}_{s_2} \\ \vdots & \vdots & \ddots & \vdots & \vdots \\ 0 & 0 & \cdots & \overline{EA}_{s_n} & -\overline{ES}_{s_n} \\ -\overline{ES}_{s_1} & -\overline{ES}_{s_2} & \cdots & -\overline{ES}_{s_n} & \overline{EI}_s \end{bmatrix}, \tag{5.40}$$

$$\mathbf{k}_c = \begin{bmatrix} \int_{A_c} \overline{k}^c_{11} \mathrm{d}A + \overline{EA}_{sl} & -\int_{A_c} (y-y_c)\overline{k}^c_{11} \mathrm{d}A - \overline{ES}_{sl} & \int_{A_c} \overline{k}^c_{12} \mathrm{d}A \\ -\int_{A_c} (y-y_c)\overline{k}^c_{11} \mathrm{d}A - \overline{ES}_{sl} & \int_{A_c} (y-y_c)^2 \overline{k}^c_{11} \mathrm{d}A + \overline{EI}_{sl} & \int_{A_c} (y-y_c)\overline{k}^c_{12} \mathrm{d}A \\ \int_{A_c} \overline{k}^c_{21} \mathrm{d}A & -\int_{A_c} (y-y_c)\overline{k}^c_{21} \mathrm{d}A & \int_{A_c} \overline{k}^c_{22} \mathrm{d}A \end{bmatrix}, \tag{5.41}$$

and

$$\mathbf{k}_{sc} = \begin{bmatrix} k_{sc_1} & 0 & \cdots & 0 \\ 0 & k_{sc_2} & \cdots & 0 \\ \vdots & \vdots & \ddots & \vdots \\ 0 & 0 & \cdots & k_{sc_n} \end{bmatrix} \tag{5.42}$$

where $\overline{EA}_\alpha = \int_{A_\alpha} E_{\alpha,t} \mathrm{d}A$, $\overline{ES}_\alpha = \int_{A_\alpha} E_{\alpha,t}\,(y-y_\alpha)\mathrm{d}A$, $\overline{EI}_\alpha = \int_{A_\alpha} E_{\alpha,t}\,(y-y_\alpha)^2 \mathrm{d}A$ for $\alpha = s_1, \cdots, s_n$ with the Young's tangent modulus $E_{\alpha,t} = \dfrac{\partial \sigma_\alpha}{\partial \epsilon_\alpha}$, $\overline{EA}_{sl} = \int_{A_{sl}} E_{sl,t} \mathrm{d}A$, $\overline{ES}_{sl} = \int_{A_{sl}} E_{sl,t}\,(y-y_c)\mathrm{d}A$, and $\overline{EI}_{sl} = \int_{A_{sl}} E_{sl,t}\,(y-y_c)^2 \mathrm{d}A$ with the Young's tangent modulus $E_{sl,t} = \dfrac{\partial \sigma_{sl}}{\partial \epsilon_{sl}}$ in which the contribution of the longitudinal reinforcement in concrete component is explicitly considered.

5.5 Numerical application

The purpose of this section is to assess the capability of the proposed formulation in reproducing the nonlinear behavior of hybrid beams subjected to combined loads and to investigate the influence of the partial interaction on the general behavior of the members. The Gauss integration method (5 Gauss-Lobatto integration points) is used to integrate the resultant section forces and section stiffness along the element, while the return mapping algorithm is employed to integrate the stresses and material stiffness within the fiber of the concrete cross-section.

5.5.1 Beams under three-point flexural bending

The experimental tests consisting of two hybrid beams under 3-point flexural bending, conducted at Laboratory of Civil and Mechanical Engineering of INSA Rennes [128] are selected in order to assess the accuracy of the proposed model. The hybrid-beam specimens (CW and CWHC) are reinforced by three HEB100 steel profiles totally encased in the RC cross-section reinforced with eight 20 mm diameter longitudinal reinforcing bars. All specimens had a length of 5 m and a 25×90 cm^2 rectangular cross-section. The transverse reinforcement consisting of 14 mm reinforcing bars was made in form of stirrups. The stud connectors (Nelson H3L16) with spacing 20 cm are welded at both sides of the web of the steel section ensuring the force transfer between the concrete and the steel profile. The reinforcing bar arrangement is the same in all specimens except the stirrup spacing (10 cm for CW and 20 cm for CWHC). The geometry and reinforcement of the beams are represented in Fig. 5.3 and the main characteristics of the experimental tests are summarized in Table 5.1 in which the cylinder

Table 5.1: Main characteristic of the materials.

	Concrete		Long. bar		Stirrup		Steel	
Specimen	f_{cm}	E_{cm}	f_s	E_s	f_{st}	E_{st}	f_y	E_y
CW	32.00	31187	383.91	210740	633.26	207460	462.7	214450
CWHC	31.63	31078	383.91	210740	633.26	207460	462.7	214450

in MPa

strength of concrete is measured at the day of test and the elastic modulus of concrete is determined using the EC2 formulation. The specimens were supported by two pins at point A and B (62.5 cm from the right and left extremity of the beam, respectively) and were loaded at mid-span until failure under displacement controlled conditions. The response of the beams was monitored as schematically represented in Fig. 5.4: deflection displacements were measured at five points; two concrete strain gauges were pasted to the top concrete surface; twenty two strain

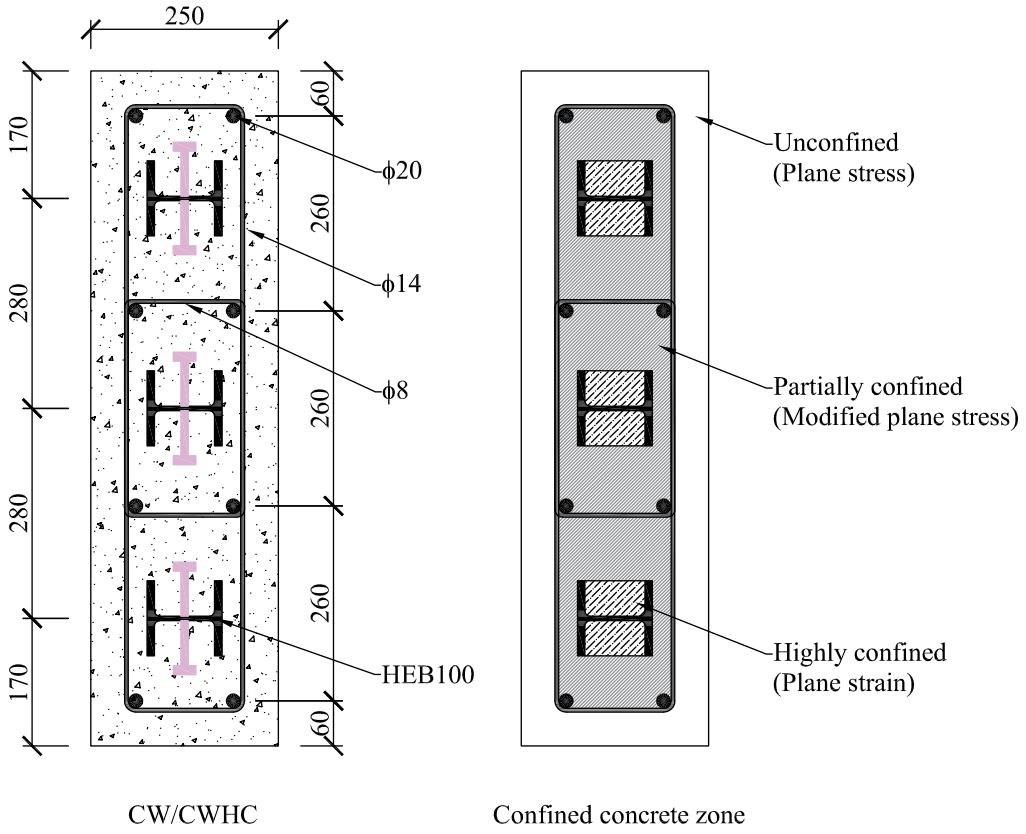

Figure 5.3: Cross-section of the CW and CWHC specimens.

gauges were pasted to reinforcement steel and nine rosette strain gauges composed of 0, 45 and 90 degree were pasted to steel profiles. For the numerical simulation, the specimens are modeled by implementing the present FE model into the co-rotational frame, developed in Chapter 3, using 12 elements. The degrees of freedom corresponding to the internal nodes in the local frame are statically condensed out to obtain the local displacement vector containing only the degrees of freedom at the element ends. The self-weight of the beams are considered through the distributed loads applied at the element level, see Eq. (5.5). In an analysis step with the displacement control, the vertical displacement at mid-span was incrementally applied in the model up to failure. Concerning the constitutive law, we adopt the following stress-strain relationship: the cap model is adopted for concrete; and the elastic-perfectly plastic for the structural steel, the reinforcing

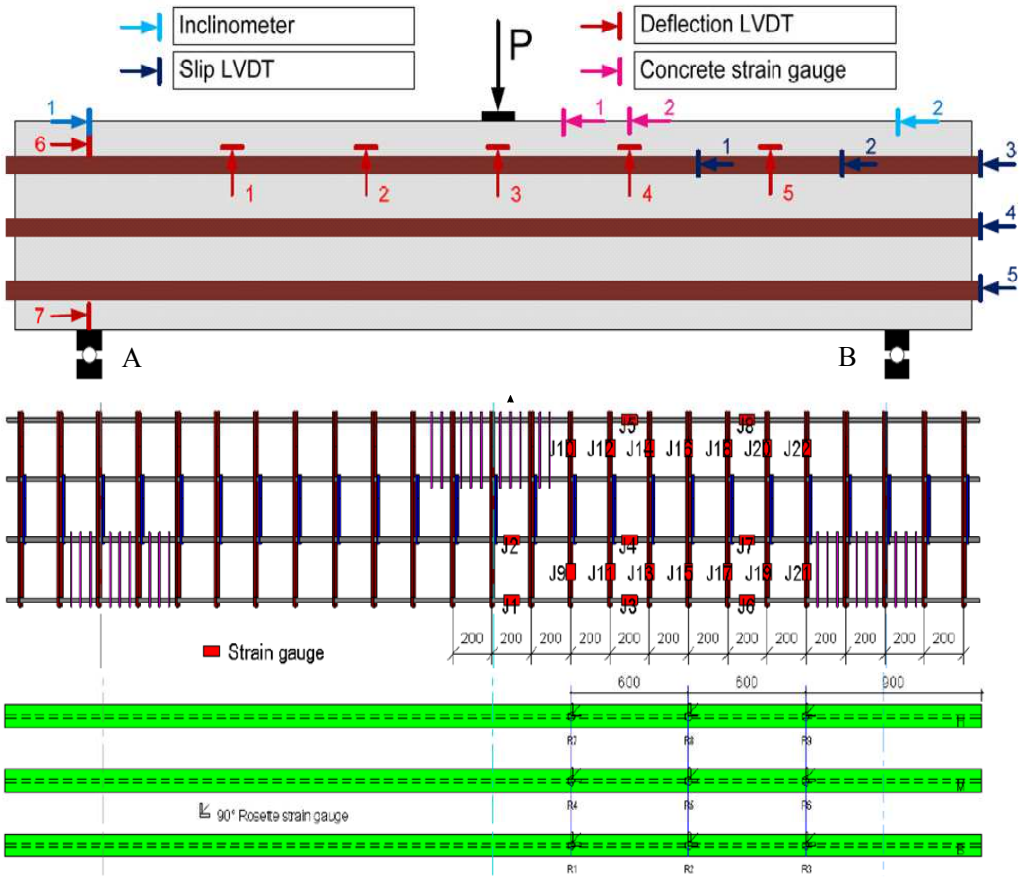

Figure 5.4: Detailed arrangement of measuring devices.

bar and the shear connection. The parameters used in the concrete cap model are presented in Table 5.2 in which the parameters for envelop curve is fitted with

Table 5.2: Concrete cap model parameters.

Specimen	$\alpha^{\dagger}$	θ	$X_0^{\dagger}$	R	$f_t^{\dagger}$
CW	1.3789	0.4729	-91.4840	5	2.0630
CWHC	1.3740	0.4729	-91.3046	5	2.0470

† in MPa

Mohr-Colomb model (matched with a simple tensile and compressive strength)

and the concrete Poisson's ratio of 0.15 is adopted. For the reason of the lack of experimental test on the shear stud behavior used in the hybrid beams, we adopt the formulation provided by EC4 [12] to determine the ultimate shear strength of the connector in which the partial factor is assumed to be equal to 1; and we assume that the slip at the ultimate shear strength of the connector is 2 mm. The load-displacement curves obtained from the FE models, compared against the ones obtained from the experimental tests are depicted in Fig. 5.5 and Fig. 5.6 for CW and CWHC, respectively. The confined concrete zone in the FE models is divided into three zones as illustrated in Fig. 5.3. Four FE models are considered:

- the model with the confined concrete zone defined in Fig. 5.3 (FE1);
- the model without the highly confined concrete zone (FE2);
- the model without confinement (FE3);
- and the Euler-Bernoulli beam model (EB-Model, see Appendix B).

The parabolic rectangular model for concrete (with limited concrete strain at crushing strength) is adopted in the latter FE model. The curves of the exper-

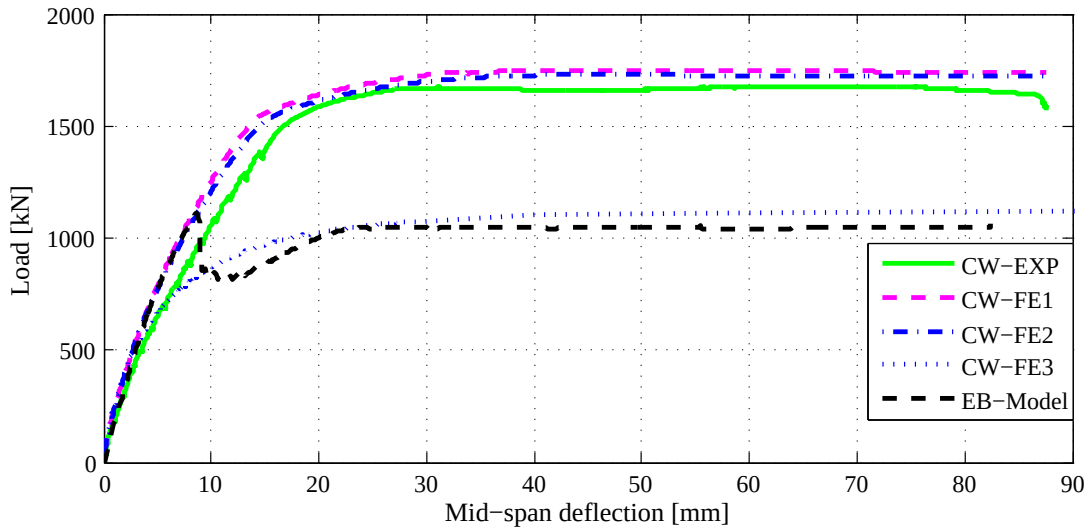

Figure 5.5: Load-displacement curve at mid-span of CW specimen.

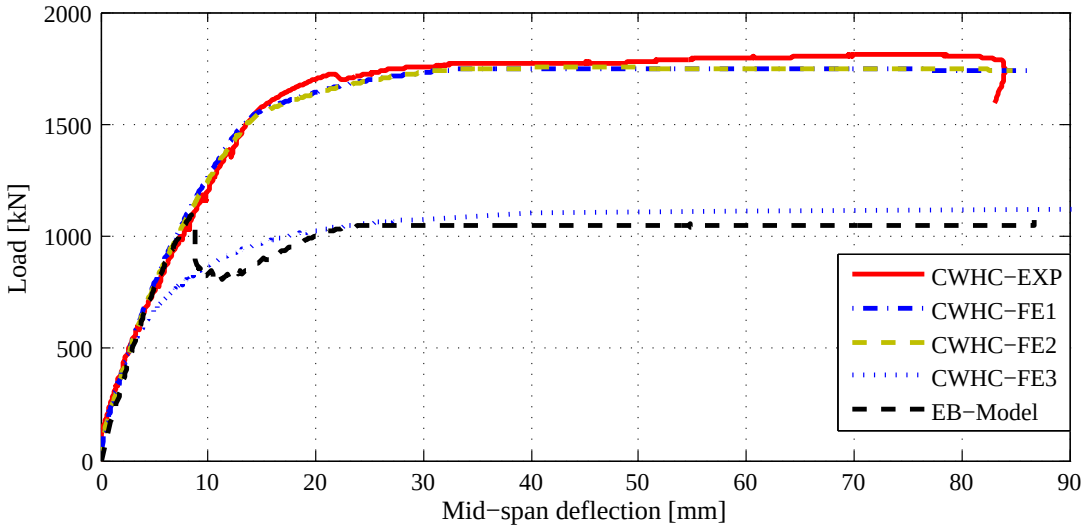

Figure 5.6: Load-displacement curve at mid-span of CWHC specimen.

imental results show that the specimens can deform with a large displacement showing their ductile behavior while subjected to a monotonic loading. The ultimate loads of CW and CWHC predicted by FE analysis (FE1 model) agree well with those of the experimental results (1.0461 and 0.9737 for CW and CWHC, respectively). It can be observed that there is a slight effect of the highly confined concrete zone (considered in the FE1 model) on the response of the beam when compared with the response of FE2 model. Otherwise, when considering the plane stress condition on the concrete cross-section without taking into account the effects of the transverse reinforcement (FE3 model), the predicted ultimate load of the beam drops significantly. Nevertheless, the ultimate loads predicted by the FE3 model agree well with those of EB-model. It is worth mentioning that the ultimate load in EB-model is defined by the crushing of concrete. After concrete crushing occurs, the softening response is observed. This is due to the brutal decreasing of tangent stiffness of concrete cross-section. It is noteworthy to mention that the steel sections have not completely reached their limit elasticity while the crushing of concrete occurs.

5.5.2 Effects of partial interaction

A hybrid beam under three-point bending (see Fig. 5.4) with the same cross-section configuration as CW specimen is considered, but in this case there is no shear connector placed at the interface of the steel and the concrete component. The force transfer mechanism between the concrete and the steel component is based on the bond strength which is a function of the normal confining pressure exerted by the encasing concrete on the steel surface. Most of the design codes provide the ultimate strength of the bond stress between the concrete and steel interface rather than the stiffness. The design longitudinal shear strength by friction is assumed to be equal to 0.3 MPa in EN 1994-1-1:6.7.4.3(3) for a completely concrete encased steel section. For a C30 concrete, the design value of the ultimate bond stress between a ribbed bar and concrete component according to EN 1992-1-1:8.2 is seven times (about 2.1 MPa) greater than the one of the steel embedded section in EC4. However, according to EN 1994-1-1:6.7.4.3(4) a higher value of bond strength of steel embedded section may be used for a concrete cover greater than 40 mm and with an adequate reinforcement. In this case, the bond strength is 0.75 MPa for the present cross-section configuration. The corresponding ultimate longitudinal distributed shear force is then 420 N/mm. In this study, four values of shear connection stiffness are considered in the finite element model. This specimen is denoted by BW with the stirrup spacing of 20 cm along the beam length. The material characteristics of the specimen are reported in Table 5.3 and the parameters used in the concrete cap model are presented in

Table 5.3: Main characteristic of the materials.

	Concrete		Long.	bar	Stirrup		Steel	
Specimen	f_{cm}	E_{cm}	f_y	E_y	f_{yst}	E_{yst}	f_s	E_s
BW	31.50	31040	383.91	210740	633.26	207460	462.7	214450

in MPa

Table 5.4 in which the parameter for envelop curve is fitted with Mohr-Colomb

Table 5.4: Concrete cap model parameters.

Specimen	$\alpha^{\dagger}$	θ	$X_0^{\dagger}$	R	$f_t^{\dagger}$
BW	1.3722	0.4729	-91.2422	5	2.0414

† in MPa

model (matched with a simple tensile and compressive strength) and the concrete Poisson coefficient of 0.15 is adopted.

Fig. 5.7 shows the comparisons between the load-deflection curve obtained from

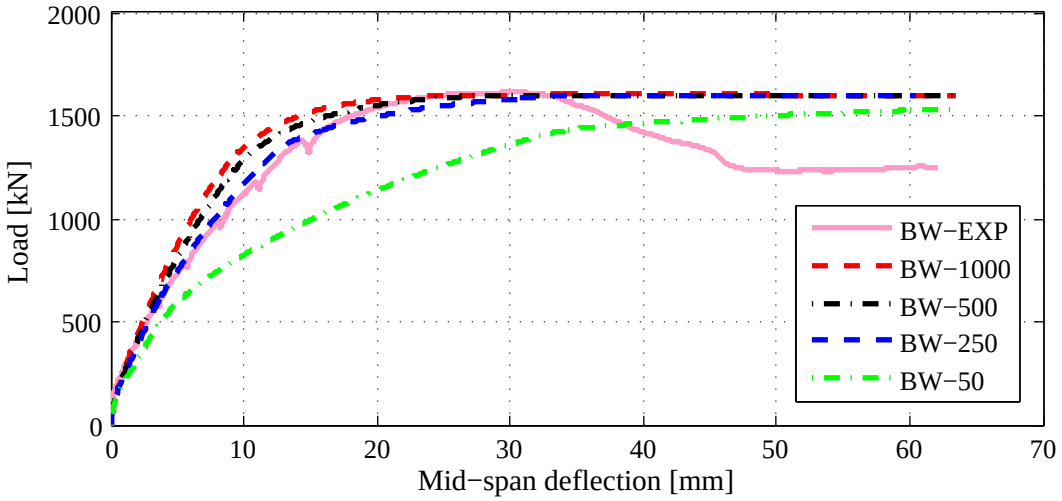

Figure 5.7: Load-displacement curve at mid-span of the BW specimen.

the experimental test [128] and the FE analysis with several values of the shear connection stiffness (1000, 500, 250 and 50 MPa denoted by BW-1000, BW-500, BW-250 and BW-50, respectively). It can be seen that the shear connection stiffness plays a crucial role in the flexibility of the hybrid beam. With a low shear connection stiffness, the hybrid beam is more flexible compared to the one with a high shear connection stiffness. However, all cases of shear connection stiffness used in the FE model lead to the same ultimate load of the beam which agrees well with the experimental result. Nevertheless, the FE model fails to capture

the softening part of the beam behavior which is observed in the experimental test. This softening part is due to the failure of the bond strength. To reproduce this descending part, the softening laws of the shear bond strength has to be employed.

5.6 Conclusion

In this chapter, the nonlinear FE model of hybrid beam under combined load has been developed based on the fiber beam model where the shear deformability of the concrete component is considered. To take into account the confinement effects, the 3d constitutive law for the encasing concrete component is adopted. Then, the plane stress condition for the concrete component is applied in order to condense the 3d formulation, derived from a 3d plastic model of the concrete material, into the 2d beam model. The developed FE model is implemented into the local frame of the co-rotational framework developed in Chapter 3. The static condensation has been applied in order to obtain the consistent tangent matrix in the local co-rotational formulation. The FE model has been validated by comparing its predictions against the experimental results of the hybrid beams conducted at Laboratory of Civil and Mechanical Engineering of INSA Rennes. Moreover, the influence of the partial interaction on the overall behavior of the hybrid beams has been investigated. It has been found that the ultimate loads predicted by FE analysis agree well with those of the experimental results and that the shear connection stiffness plays an important role in the flexibility of the hybrid beam. The proposed formulation can thus provide a robust and reliable option for determining the ultimate load in a large displacement analysis of hybrid beam-columns subjected to combined loads.

Chapter 6

Simplified Design Method for Slender Hybrid Columns

***

Numerical investigations on second-order effects in slender hybrid columns subjected to combined axial load and uniaxial bending moment. Comparison between the results obtained with FE analysis and Eurocode simplified methods. New expressions for the correction factors involved in the determination of the effective flexural stiffness EI.

6.1 Introduction

Hybrid structures composed of steel members encased in reinforced concrete have been used at an increasing rate for mid-to-high rise buildings as they effectively

combine structural steel and reinforced concrete members to their best advantage. For instance, composite columns have significant economic advantages over either pure structural steel or reinforced concrete (RC) alternatives. For a given cross sectional dimension, composite columns also have higher strength and stiffness therefore leading to reduced slenderness and increased buckling resistance. In the early time of hybrid construction, these systems were built by first erecting a steel skeleton and selected columns or entire bays of the steel framing were encased in reinforced concrete to increase, at minimal cost, their strength, stiffness as well as their fire resistance. Sooner these systems became very popular in seismic prone area and nowadays it is commonly accepted within the engineering community that composite and hybrid systems offer an economical method to develop the required strength and stiffness. Several hybrid systems have been developed and for some design rules need to be devised.

In high-rise buildings, slender RC columns containing multiple encased profiles as reinforcement are often used to resist horizontal loads by bending about their strong axes when standard reinforcement with rebars is not sufficient to sustain such extreme loads. Those composite steel-concrete columns are called "hybrid columns" because they are neither RC columns in the sense of EC2 [11], nor composite columns in the sense of EC4 [12] where the design rules are provided only for a single encased steel profile. Nevertheless, it is legitimate to raise the following question: can we use design rules given in EC2 or EC4 to design such column? For columns being sensitive to instability, both EC2 and EC4 propose simplified design methods based on moment magnification approach. The latter can be written in general form as $M_{Ed,2} = k\, M_{Ed,1}$ where $M_{Ed,2}$ is second-order bending moment; $M_{Ed,1}$ is first-order bending moment; and k is the so-called moment magnification factor. Different expressions for the factor k have been proposed (see for example [11, 12, 97, 129, 130]). A large number of expressions for k proposed in the technical literature can be (re)written in the following form: $k = \beta/(1 - N_{Ed}/N_{cr})$ where N_{Ed} is the design axial load; N_{cr} is the elastic critical normal force; and β is the equivalent uniform moment factor. The

accuracy of moment magnification method strongly depends on, as included in N_{cr}, the effective flexural stiffness EI which depends on, among other factors, the nonlinearity of the concrete stress-strain curve, the creep and the cracking along the column length, and on the factor β. The expression for EI used to design reinforced concrete and composite columns has been studied for decades. There is a vast amount of expressions for the effective flexural stiffness EI in the literature. Mavichak and Furlong [131] considered the relative normal force as a single parameter in their expression for EI. Mirza [132] suggested to take into account the eccentricity, the slenderness ratio, and the creep factor related to the sustained load. The latter was further enhanced by Tikka and Mirza [133–136] taking into account the reinforcement ratio in their proposed EI equation. The above-mentioned factors including the strength of concrete are also considered in [129, 137]. Bonet et al. [130] extended their work to propose a new EI equation valid for arbitrary cross-section shape. Similarly, many authors proposed an expression for the equivalence uniform moment factor β. The most adopted expression by the codes was proposed by Austin [138] in linear form of eccentricity ratio (r_m) at the extremities of the column. It was deduced from the solution of linear elastic analysis. Robinson et al. [139] proposed other formula in quadratic form of (r_m). Trahair [140] and Duan et al. [141] considered eccentricity ratio and axial force level in their expression for β. Sarker and Rangan [142] explained that the expression provided by Austin [138] is unsafe for columns of low and medium slenderness and they proposed another expression for β which is valid for short-term load and for normal to high strength concrete. Tikka and Mirza [143] maintained that the expression proposed by Austin [138] which is used in ACI-318 [97] is safe. ACI-318 [97] proposes β equal to 1.0 for column subjected to transverse load, and EC2 [11] does not define the β factor explicitly.

This chapter deals with numerical investigations on second-order effects in slender hybrid columns reinforced by several steel sections subjected to combined axial load and uniaxial bending moment about strong axis. The first objective of this study is to point out that a straightforward application of the bending moment

magnification method proposed in EC2 and EC4 to hybrid columns may lead to unsafe results. To remain consistent with the Eurocodes, a new version of bending moment magnification method for slender hybrid columns is proposed. To do so, our FE model is used in which the geometrical/material nonlinearities, the geometrical imperfections, the residual stresses in steel profiles as well as the partial interaction effect between steel profiles and the surrounding concrete are taken into account. Since slender hybrid columns subjected to combined axial load and bending moment are considered, the effects of shear deformability of concrete component can be ignored. As the result, Euler-Bernoulli beam kinematics and the uniaxial stress-strain behavior for each component (steel and concrete) of the hybrid beam-column element are adopted. Moreover, the developed model based on Euler-Bernoulli kinematic assumption is consistent with the finite element model proposed in the general methods of Eurocodes (EC2 and EC4) for designing a column subjected to combined axial load and bending moment. The developed FE model, see Appendix B, is validated through the comparison with the experimental results of standard composite columns (due to lack of experimental results of hybrid columns) and will serve as references for an extensive parametric study (1140 data sets) in which the simplified methods proposed in EC2 and EC4 are evaluated in case of hybrid columns. Based on the extended parametric study with 2960 data sets, new expressions for the coefficient k and β are proposed. The organization of this chapter is as follows. The recommendations for the design of columns in EC2 and EC4 are briefly recalled in Section 6.2. Section 6.3 is devoted to the parametric study in which the hypotheses considered for material laws and geometrical and material imperfections are deduced from Eurocode recommendations for FE analysis and from the background of these methods. Finally, the design method for slender hybrid column is proposed and validated based on the results obtained from FE analysis in Section 6.4.

6.2 Eurocode design methods for slender columns

In the design of slender structures, the second-order effect needs to be considered. Eurocodes provide guidance on how to consider these effects in structural analysis using either a first-order analysis with appropriate amplification factors or a more precise second-order analysis. Nevertheless, second-order effects may be ignored if they are significantly less than the corresponding first-order ones, for instance less than 10% as stated in EN 1992-1-1: 5.8.2(6) and in EN 1994-1-1: 5.2.1(3). This implies that the designer would first check the second-order effects before ignoring them. EC2 and EC4 provide simplified criteria to verify if a global second-order analysis of the structure must be carried out in global structural analysis. If the answer to the question is "yes", EC2 refers to its Appendix H for the evaluation of the global second-order effects using magnified horizontal forces, where the rigidity of bracing elements is determined by taking into account concrete cracking. Members sensitive to second-order effects will then be checked separately using the internal forces given by the global structural analysis. EN 1994-1-1: 5.2.2(3) states that individual stability checks of composite columns can be ignored if their individual imperfection and their reduced stiffness are fully accounted for in the global structural analysis.

Once the second-order effects (including cracking, material nonlinearity and creep) need to be accounted for, EC2 and EC4 propose both a simplified method, called "Moment Magnification Method", in which the first-order bending moment M_{Ed} is modified by a magnification factor k to obtain the second-order bending moment. The factor k largely depends on the flexural stiffness and the equivalent moment distribution. Hence, the procedure involves two steps. The first stage is to compute the effective stiffness EI and the second one is to estimate the first-order moment magnification factor based on the shape of bending moment diagram. In general, not only the factors mentioned previously influence the flexural stiffness of the columns but also the column slenderness, the eccentricity, the magnitude of normal force and the reinforcement ratio. The expression of EI can be written

in the following form:

$$EI = K_c E_c I_c + K_s E_s I_s + K_a E_a I_a \tag{6.1}$$

where the contribution of concrete, rebars and steel sections with subscript c, s and a respectively are multiplied by a correction factor and summed up. The correction factors K_c, K_s and K_a can be calibrated using more or less sophisticated models, to give the agreement between the proposed method and FE analysis.

6.2.1 The Moment Magnification Method in Eurocode 2

According to EC2, the second-order bending moment can be obtained using two different simplified methods. The first one, based on the nominal stiffness, can be applied in all situations. The second one is based on the nominal curvature and is primarily suitable for isolated members with constant normal force. Since EC4 also proposes an approach based on the nominal stiffness for the moment magnification method, therefore this method seems to be a good candidate for hybrid column design.

The total design moment, including second order moment, may be determined by multiplying the first-order moment including the effect of imperfections by the magnification factor k (EN1992-1-1: 5.8.7.3(1)) which is expressed as

$$k = 1 + \frac{\beta}{\frac{N_B}{N_{Ed}} - 1} \tag{6.2}$$

where

- β is a factor which depends on distribution of 1^{st} and 2^{nd} order moments. For isolated columns with constant cross section and axial load, $\beta = 1.233$ for a constant first order moment distribution, 1.028 for a parabolic distribution and 0.822 for a symmetric triangular distribution;

- N_{Ed} is the design value of the axial load; and

- $N_{\mathrm{B}} = \dfrac{\pi^2 EI}{l_0^2}$ is the buckling load based on nominal stiffness EI defined by the following expressions (EN 1992-1-1: 5.8.7.2(1))

$$EI = K_c E_{cd} I_c + K_s E_s I_s \tag{6.3}$$

in which l_0 is the effective length of the column; K_c is a factor for effects of cracking, creep and material nonlinearity; and K_s is a factor related to the contribution of reinforcement. Provided the geometric reinforcement ratio is greater than 0.2%, they are determined by the following expressions (EN 1992-1-1: 5.8.7.2(2)):

$$K_c = \sqrt{\frac{f_{ck}}{20}} \min\left(\frac{N_{\mathrm{Ed}}}{A_c f_{cd}} \frac{\lambda}{170}; 0.2\right) \frac{1}{1+\varphi_{ef}} \text{ and } K_s = 1 \tag{6.4}$$

where φ_{ef} is the effective creep ratio and λ is the slenderness ratio.

6.2.2 The Moment Magnification Method in Eurocode 4

According to EC4, the second-order effects in composite columns can be accounted for by multiplying the largest first-order design bending moment M_{Ed} by a magnification factor k given by:

$$k = \frac{\beta}{1 - \dfrac{N_{Ed}}{N_{cr,eff}}} \tag{6.5}$$

where

- $\beta = 1$ if M_{Ed} is the maximum bending moment within the column length ignoring the second-order effect (the column is subjected to the lateral load). Otherwise $\beta = \max(0.66 + 0.44\, r_m; 0.44)$ in which r_m is the ratio between bending moments acting at the column extremities ($-1 \leq r_m \leq 1$);
- N_{Ed} is the total design normal force;
- $N_{cr,eff}$ is the buckling load computed with the effective stiffness $(EI)_{\mathrm{eff,II}}$ defined by the following expression (EN 1994-1-1: 6.7.3.4(2))

$$(EI)_{\mathrm{eff,II}} = 0.9(E_a I_a + E_s I_s) + 0.45 E_{cm} I_c \tag{6.6}$$

In order to take into account the influence of long-term effects on the effective elastic flexural stiffness, EC4 proposes to reduce the modulus of elasticity of concrete E_{cm} to the value $E_{c,eff}$ in accordance with the following expression:

$$E_{c,eff} = E_{cm} \frac{1}{1 + (N_{G,Ed}/N_{Ed})\varphi_t} \tag{6.7}$$

where φ_t is the creep coefficient; and $N_{G,Ed}$ is the part of total design normal force N_{Ed} that is permanent.

6.2.3 Plastic resistance of hybrid cross-sections

The plastic resistance of the hybrid cross-section is required to be verified against the second-order bending moment obtained from the application of the moment magnification method. However, nowadays no design standard provides the guidance on how to determine properly the plastic resistance of reinforced concrete with more than one embedded steel profile. For reinforced concrete, a classical approach in reproducing the bending moment-axial force interaction curve is the pivot method. This method is similar to the simplified method proposed by EC4 in determining the interaction curve for classical composite sections. Due to this similarity, Bogdan et al. [144] proposed the pivot method to compute the plastic resistance of the hybrid cross-sections by making the following assumptions:

- plane section remains plane;
- slip occurred at the steel and concrete interface is ignored;
- parabola rectangle stress-strain relationship of concrete is adopted as proposed by EC2; and
- bilinear law of steel is used.

Fig. 6.1 shows the possible strain distribution in ultimate limit state of a hybrid cross-section with three pivots named A, B and C. The pivot A represents the strain distribution where the reinforcement bars at the bottom reach their limit strain in tension. The point where the top fiber of concrete reaches its ultimate

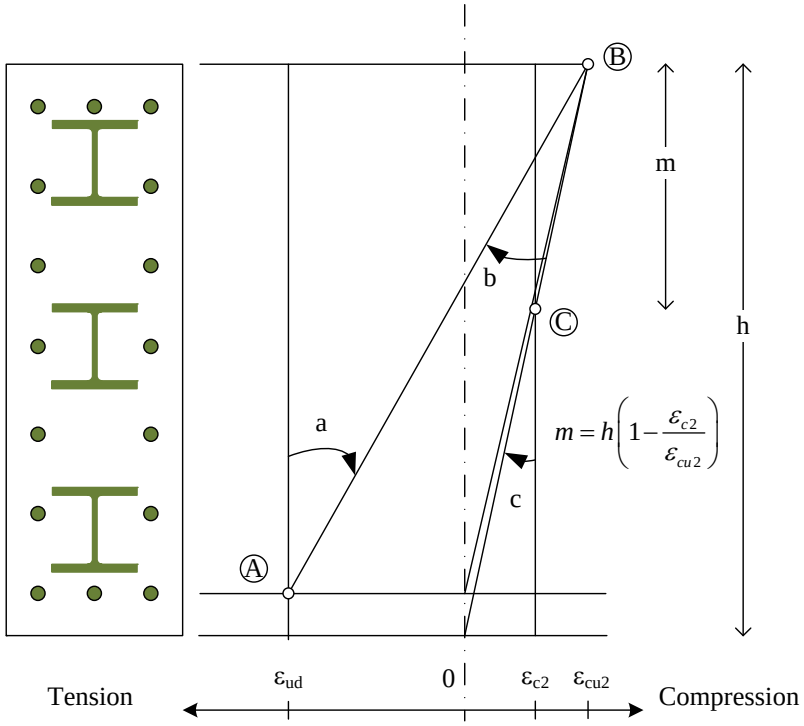

Figure 6.1: Possible strain distribution in ultimate limit state of a hybrid cross-section.

limit strain in compression defines the pivot B. The last pivot C is treated to the strain limit in pure compression of concrete. The assessment of the pivot method was carried out by Bogdan et al. [144]. It was shown that this method provides sufficient accuracy in determining the interaction curve of hybrid cross-sections.

6.3 Parametric study and assessment of simplified methods of EC2 and EC4

In this section, the developed FE model which was successfully validated above is used to conduct an extensive parametric study in order to assess the applicability of moment magnification methods of EC2 and EC4 for hybrid column design. To do so, the ultimate load of slender hybrid columns with different types of cross-sections are computed using the proposed FE model and also calculated

using Eurocode simplified methods. The obtained results of calculation methods are compared against each other to assess the applicability of Eurocode simplified methods to hybrid column designs. Five different hybrid cross-section configurations (HSRCC1-5) are considered. The cross-sections HSRCC1 and HSRCC2 are built with 3 steel profiles HEB120. In the first configuration (HSRCC1) the weak-axis of the profiles is parallel to the bending axis whereas in the second configuration (HSRCC2) they are orthogonal to the bending axis (see Fig. 6.2a and Fig. 6.2b). Hybrid cross-sections HSRCC3 and HSRCC5 correspond to the so-called mega-column which contains 4 steel profiles, HD400x1086, located at each corner of the cross-section (see Fig. 6.2c and Fig. 6.2d). The last hybrid cross-section (HSRCC4) has also 3 steel profiles but with larger steel cross-section, HEB200. For cross-sections HSRCC1, HSRCC2 and HSRCC5, the diameter of the reinforcement rebar is 20 mm whereas 32 mm and 12 mm for HSRCC3 and HSRCC4 respectively. Due to symmetry, only half-section of mega-column (HSRCC3 and HSRCC5) is modeled. For all cases considered in this study, the limit of elasticity for steel profile is restricted to 355 MPa and for reinforcement bar is 500 MPa. Three classes of concrete strength C35, C60 and C90 are considered. Note that hybrid columns HSRCC4 and HSRCC5 with a significantly high value of steel contribution ratio δ, are modeled with concrete class C35. Although the hybrid column HSRCC4 is not totally realistic, it is considered here for maximizing the ratio δ.

In high-rise buildings, there is a significant amount of long term loads (approximately 75% of total loads). Therefore, the effect of sustained loads has to be considered. In this work, the effective creep ratio is taken equal to 1.5. As a consequence, the concrete stress-strain curve is modified following EC2 recommendation. For columns subjected to axial compression and bending moment, three different relative slenderness $\bar{\lambda}$ are considered for each cross-section configuration with or without taking into account the creep effect. The relative slenderness $\bar{\lambda}$ is determined according to the EC4 formulation. From the value

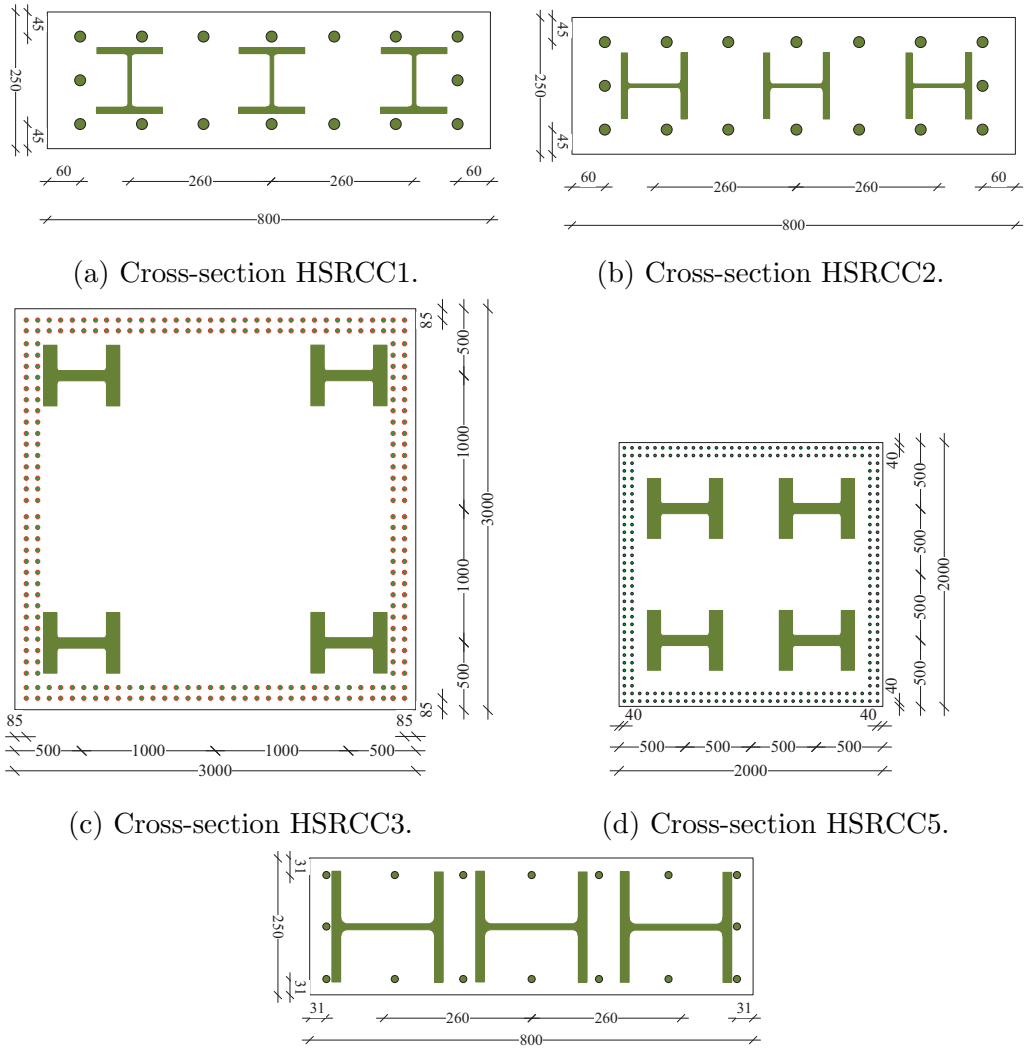

(a) Cross-section HSRCC1.

(b) Cross-section HSRCC2.

(c) Cross-section HSRCC3.

(d) Cross-section HSRCC5.

(e) Cross-section HSRCC4.

Figure 6.2: Cross-sections considered in parametric study.

of relative slenderness and geometry of the cross-section, the column length can be deduced. For columns subjected to compressive load only, the whole range of possible relative slenderness is covered. The parametrical study is summarized in Table 6.1.

In this study, bending is considered to take place about the strong axis. This situation corresponds to the case where the extreme load produced by wind or

Table 6.1: Summary of case-studies.

Section	S1; S2; S3; S4; S5
Concrete	C35/45; C60/75; C90/105
f_{sk}	500 MPa
f_y	355 MPa
$\bar{\lambda}$	0.5; 1.0; 2.0
$\frac{e}{h}$	0.0-3.0
δ	0.2-0.62
φ_{ef}	0; 1.5

seismic load in that direction and the motion of the column is restrained on the other direction.

6.3.1 Material laws

In order to evaluate the accuracy of the safety level when applying the simplified design methods proposed in EC2 and EC4 for hybrid column design, the general design methods (using nonlinear FE analysis) suggested by the Eurocodes should be adopted. Nonlinear material models as well as the safety format have to be properly described. The comparison of the results provided by the simplified method of EC2 against FE analysis is readily achieved by using the stress-strain relationship based on the design values of the constitutive model parameters as it is clearly defined in EN 1992-1-1: 5.8.6. Regarding the safety format for nonlinear FE analysis, the Eurocode for composite structures recommends to use the stress-strain relationships defined in EC2 and EC3 as stated in EN 1994-1-1: 6.7.2(8). Therefore, the material constitutive laws and the partial factors recommended by EC2 and EC3 are adopted. The descriptions of the stress-strain relationships are recalled in the following.

EN 1992-1-1: 5.8.6(3) recommends to use the concrete stress-strain relationship expressed by Eq. (6.8) (EN 1992-1-1: 3.1.5(1)) where the tension part of concrete is ignored. The bilinear stress-strain relationship for reinforcing bar is suggested by the code.

$$\frac{\sigma_c}{f_{cm}} = \frac{k\eta - \eta^2}{1 + (k-2)\eta} \tag{6.8}$$

where

- $\eta = \epsilon_c/\epsilon_{c1}$;
- ϵ_{c1} is the strain at peak stress according to EN 1992-1-1; and
- $k = 1.05E_{cm}\,|\epsilon_{c1}|/f_{cm}$($f_{cm}$ according to EN 1992-1-1).

Eq. (6.8) is valid for $0 < |\epsilon_c| < |\epsilon_{cu1}|$ where ϵ_{cu1} is the nominal ultimate strain. According to EN 1992-1-1: 5.8.6(4), creep can be taken into account by multiplying all strain values in the concrete stress-strain diagram with a factor $(1 + \varphi_{ef})$, where φ_{ef} is the effective creep ratio. According to EN 1994-1-1: 3.2(2), the design value of the modulus of elasticity E_s of reinforcing rebar may be taken equal to the value for structural steel given in EN 1993-1-1: 3.2.6.

Incremental FE model based on fiber discretization requires appropriate uniaxial stress-strain relationships for each material with the design values of strengths. This requirement is consistent with the stress-strain relationship given by the code. The stiffness of the element is then derived from these stress-strain curves.

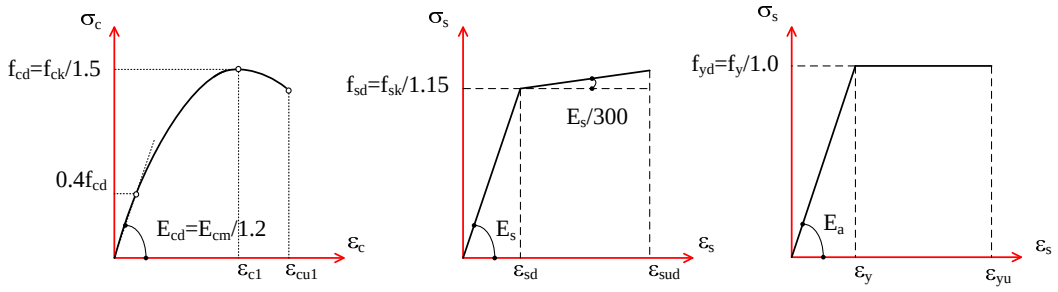

Figure 6.3: Stress-strain relationship used for FE analysis.

Since there is dependency between strength and stiffness in FE analysis, the partial factors for concrete, rebar reinforcement and steel profile are taken respectively equal to 1.5, 1.15 and 1; and the partial factor for design modulus of elasticity of concrete is taken equal to 1.2 (following EN 1992-1-1: 5.8.6(3)). The design stress-strain curves for each material are illustrated in Fig. 6.3.

6.3.2 Geometric imperfection and residual stresses

Second-order analysis requires the definition of an imperfection. Those imperfections found their sources in both the geometric imperfection as well as the residual stresses. The definition of this initial deformed shape strongly affects the behavior of slender columns. For concrete columns, EC2 recommends to consider a geometric imperfection equal to $l_0/400$ whereas for steel columns EC3 not only suggests to adopt a geometric imperfection equal to $l_0/1000$ but also to take into account the effects of the residual stress distribution. The imperfect shape of composite columns is governed by the steel component and therefore by the residual stress distribution within this component (see Fig. 6.4). Accordingly, an

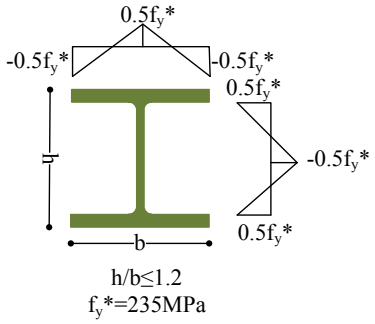

Figure 6.4: Residual stress distribution of steel profile.

initial imperfection $l_0/1000$ has to be considered and the geometric effects of the residual stress distribution must be considered. To simplify the calculation, EC4 suggests to replace the residual stresses by an equivalent initial bow imperfection. However, Bergmann and Hanswille [145] have shown that this simplification produces an approximate value of the ultimate resistance in axial compression. The

hybrid column being built as a concrete column; to ensure the best accuracy of the results we adopt an initial imperfection in parabolic shape with an amplitude of w_0 equal to $l_0/400$, combined with an explicit representation of the residual stress distribution. The admitted parabolic shape is more detrimental to column resistance than imperfection randomly distributed over column length; hence the approximation is conservative in terms of column safety.

6.3.3 Shear connection

Eurocode 4 design rules for composite columns assume full interaction between the steel section and the surrounding concrete, i.e. the slips at steel-concrete interfaces can be ignored. To remain consistent with Eurocode rules, the same assumption is retained for hybrid columns although the latter may be viewed as a fairly strong assumption for both composite and hybrid columns, particularly with deformable shear connectors. The consequence of this assumption on the ultimate load of hybrid columns will be evaluated by carefully analyzing the effect of the connection stiffness on the ultimate load using the nonlinear finite element model developed in B which takes into account the partial interaction.

The shear connection stiffness K_{sc} can be determined by $K_{sc} = k_{sc0}/d$ where k_{sc0} is the stiffness of a shear stud and d is spacing between the connectors. It is varied from low to high stiffness. For a certain value of the stiffness, the load-bearing capacity does not vary with increasing value of the connection stiffness and slips become very small so that we can assume full interaction. The value of this critical stiffness will be used for the parametric study in order to remain consistent with EC4.

The investigation on the effect of the stiffness K_{sc} and the interlayer slip distribution has been carried out on the pinned-pinned hybrid column, particularly the one with cross-section illustrated in Fig. 6.2a. Three different lengths corresponding to three different values of the relative slenderness $\bar{\lambda}$ (0.5, 1 and 2) are considered. The column is subjected to an eccentric load causing a symmetric

single curvature bending about the strong axis of the cross-section. The eccentricity ratio e/h is equal to 0.3 at both column extremities. It is worth to mention that the axial load is applied through an eccentric node linked rigidly to concrete node. The material properties are summarized in Table 6.2. In this case, a lin-

Table 6.2: Material properties.

Concrete		
$f_{ck} = 60$ MPa	$E_{cm} = 39.10$ GPa	$\varphi_{ef} = 1.5$
$\gamma_c = 1.5$	$\gamma_{cE} = 1.2$	
Reinforcing rebar		
$f_{sk} = 500$ MPa	$E_s = 210$ GPa	$\gamma_s = 1.15$
Steel profile		
$f_y = 355$ MPa	$E_a = 210$ GPa	$\gamma_a = 1.0$
Connector Stiffness		
$K_{sc} = 8$ MPa	$K_{sc} = 800$ MPa	$K_{sc} = 3000$ MPa
$K_{sc} = 7000$ MPa	$K_{sc} = \infty$ MPa	

ear elastic behavior of the connector is considered; the confinement of concrete is ignored and the residual stress distribution in the steel section is assumed to follow the diagram given in Fig. 6.4. The column is supposed to have an initial geometrical imperfection of $l_0/400$. The ultimate design capacity of the column is obtained by performing a nonlinear analysis using appropriate material laws and safety concept described in Section 6.3.1. The finite element results with a mesh consisting of 10 elements are shown in Table 6.3. The ratio between the bearing capacity of the column in partial interaction P_u and the one in full interaction $P_{u,\infty}$ is computed considering several values of connection stiffness K_{sc} and relative slenderness $\bar{\lambda}$. Regarding the boundary conditions for the interlayer slip at the column ends, two cases have been considered. In case A, interlayer slips are permitted at both ends of the column whereas in case B, the slips are prevented. It can be observed from Table 6.3 that when the interlayer slips at extremities

are prohibited (case B), the ultimate load in full interaction can be achieved for a moderate shear connection stiffness. However, with a low value of K_{sc} and no slips at the column ends (case B) the ultimate load is slightly below the one in full interaction. On the contrary, the ultimate load drops significantly for a column with low slenderness ratio and free slips at the column ends. In both cases (A and B), the ultimate load in full interaction can be achieved for columns with medium-to-high relative slenderness within a moderate shear connection stiffness.

Table 6.3: The ratio of bearing capacity of the column P_u to $P_{u,\infty}$.

$\frac{P_u}{P_{u,\infty}}$	Case A			Case B		
	$\bar{\lambda} = 0.5$	$\bar{\lambda} = 1$	$\bar{\lambda} = 2$	$\bar{\lambda} = 0.5$	$\bar{\lambda} = 1$	$\bar{\lambda} = 2$
$K_{sc} = 8$ MPa	0.72	0.72	0.76	0.98	0.96	0.92
$K_{sc} = 800$ MPa	0.90	0.99	1.00	1.00	1.00	1.00
$K_{sc} = 3000$ MPa	0.95	1.00	1.00	1.00	1.00	1.00
$K_{sc} = 7000$ MPa	1.00	1.00	1.00	1.00	1.00	1.00

6.3.4 Assessment of the EC2 version of moment magnification method

In the present section, the applicability of the EC2 version of the moment magnification method to hybrid columns is assessed by comparing its predictions against FE analysis results for hybrid column with cross-section HSRCC1 (see Fig. 6.2a). The concrete class is C60 and the effect of creep is taken into account ($\varphi_{ef} = 1.5$). It can be seen from Fig. 6.5a that in case of pure compression, the moment magnification method of EC2 gives unsafe results for low-to-moderate relative slenderness whereas the method provides conservative results for high relative slenderness. For columns subjected to single curvature bending and regardless of the load eccentricity (see Fig. 6.5b and Fig. 6.5c), the EC2 method

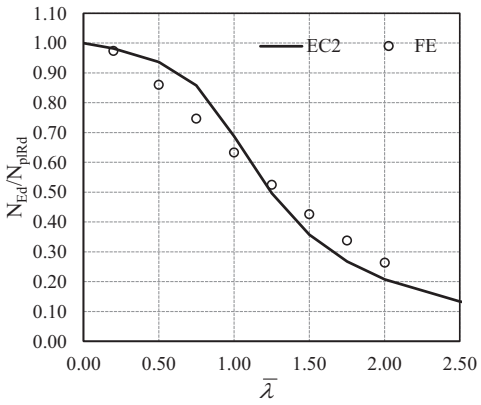

(a) Buckling curve.

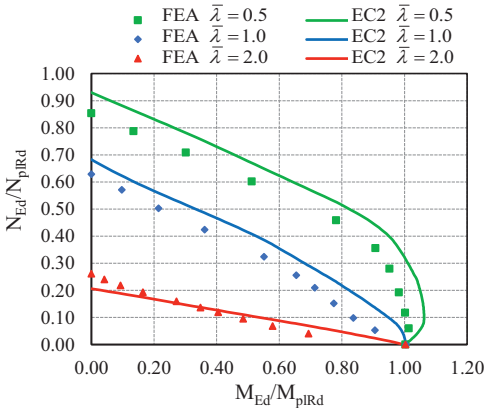

(b) Symmetrical single curvature bending ($r_m = 1$).

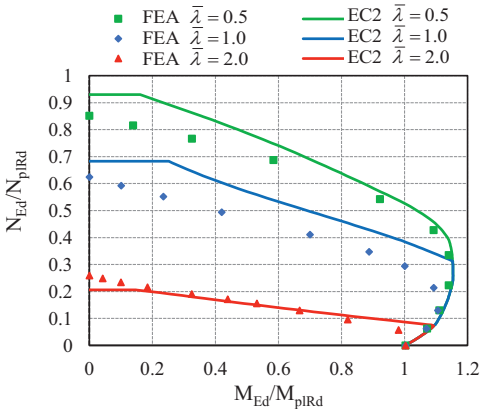

(c) Single curvature bending ($r_m = 0$).

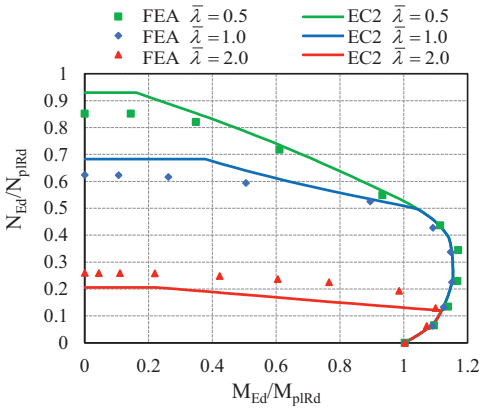

(d) Double symmetrical curvature bending ($r_m = -1$).

Figure 6.5: Comparison of simplified method of EC2 against FE analysis results.

overestimates the ultimate load for low-to-moderate relative slenderness ($\bar{\lambda} = 0.5$ to 1.0). The same conclusion applies for columns bent in double curvature under antisymmetric bending moment (see Fig. 6.5d) except for very high load eccentricities (close to pure bending). For high relative slenderness, EC2 method gives safe results except for columns bent in single curvature under large bending moment. Since this simplified method is based on the effective stiffness of the column EI, it can be concluded that the expression for the effective stiffness proposed by

EC2 cannot be applied in a straightforward fashion to hybrid column design. This effective stiffness should be modified by adjusting the factor K_c (see Eq. (6.4)) which depends on the relative slenderness of the column so that it becomes applicable to hybrid column. Moreover, the factor K_s which is applied to the stiffness can also be modified in order to account for the plastification of the steel section.

6.3.5 Assessment of the EC4 variant of the moment magnification method

In this section we pursue our study by an assessment of the performance of the EC4 version of the moment magnification method when applied to hybrid columns. Again a comparison of the predictions of the EC4 method against FE analysis results for hybrid column with cross-section HSRCC1 (see Fig. 6.2a) is carried out. The concrete class and effective creep ratio are the same as previous case (C60 and $\varphi_{ef} = 1.5$). Quite surprisingly, the EC4 version of the moment magnification method seems to perform less well. Indeed, for a hybrid column subjected to pure compression (see Fig. 6.6a) where the ultimate load of the column is characterized by the resistance in axial compression, the simplified method of EC4 gives safe results regardless of column relative slenderness. Apart from the later case, this method gives unsafe results for a large number of cases. For low load eccentricity, the ultimate load given by EC4 formulation is safe regardless of column relative slenderness (see Fig. 6.6b to Fig. 6.6d). For moderate load eccentricity, the EC4 method always overestimates the ultimate load. Under large bending moment, the EC4 method gives safe results, particularly for column under symmetric single curvature bending in the zone nearly pure bending. The conservative nature of the results can be attributed to the equivalent moment factor β, which, in the present case, is equal to 1.1.

Since this moment magnification method is based on the effective stiffness of the column EI, it can also be concluded that EC4 proposes an expression for effective stiffness that cannot be applied in a straightforward fashion to hybrid

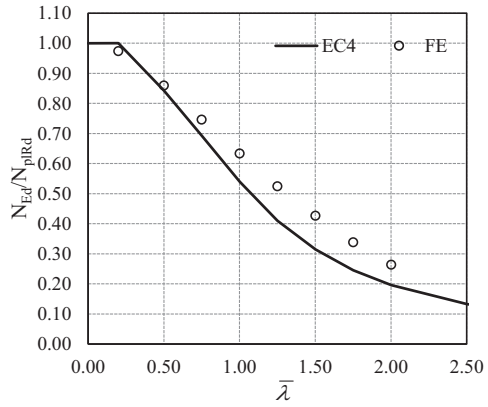

(a) Buckling curve.

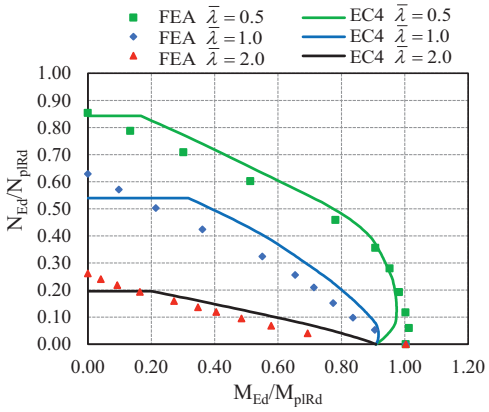

(b) Symmetrical single curvature bending ($r_m = 1$).

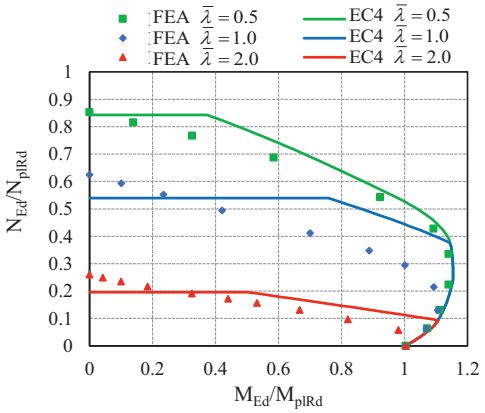

(c) Single curvature bending ($r_m = 0$).

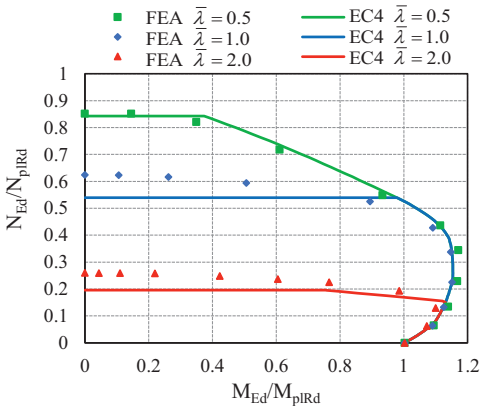

(d) Double symmetrical curvature bending ($r_m = -1$).

Figure 6.6: Comparison of simplified method of EC4 against FE analysis results.

column design. This effective stiffness should be modified by reformulating the factor $K_{e,II}$ as well as K_0. These factors should be minimized to reduce the value of the effective stiffness and as a result the ultimate load will be decreased. This modification is proposed in Section 6.4.

6.3.6 Results of the parametric study

The ultimate load for isolated hybrid columns with five different cross-section configurations (see Fig. 6.2) has been evaluated using both the finite element model and the moment magnification method proposed in EC2 and EC4. The accuracy of moment magnification method should be evaluated according to Appendix D of EN 1990 [146]. The application of the method given in this Appendix is rather straightforward provided that a large number of ultimate loads are available with the magnitude of the latter being influenced by a single parameter. It is much more complicated to apply this method for members subjected to axial load and bending moment where additionally, a large number of key parameters have to be taken into account. Because of this difficulty, an exact implementation of EN 1990-Appendix D cannot be rigorously followed while assessing the moment magnification method of EC2 and EC4. To evaluate the EC3 variant of the method for steel beam-column member, the ratio of the experimental or numerical failure load to the corresponding theoretical load has been used in [147]. Similarly, the ratio between the first order bending moment obtained via numerical simulation $(M1)_{FE}$ and the ones obtained with the simplified method $(M1)_{SM}$ was used to calibrate the simplified method of EC2 in [148]. However, this procedure is not appropriate in case the column is subjected to axial load only which leads this ratio to infinity. To overcome this difficulty, the ratio R expressed in Eq. (8.64) has been selected by Bonet et al. [130] as a reference value to evaluate the accuracy of their own proposal. This ratio is also adopted in our investigation.

$$R = \frac{R_{FE}}{R_{SM}} \tag{6.9}$$

where: $R_{FE} = \sqrt{\left(\frac{N_{FE}}{N_{pl,Rd}}\right)^2 + \left(\frac{M_{FE}}{M_{pl,Rd}}\right)^2}$ and $R_{SM} = \sqrt{\left(\frac{N_{SM}}{N_{pl,Rd}}\right)^2 + \left(\frac{M_{SM}}{M_{pl,Rd}}\right)^2}$.

Table 6.4 gives a summary of the results obtained with both EC2 and EC4 version of the moment magnification approach which are compared against FE analyses. In order to evaluate the contribution of the various parameters governing the ultimate load, the R ratio is first computed for all the considered cases (1140

data sets). The value of the R ratio is given as a function of each key variables: relative slenderness $\bar{\lambda}$, eccentricity e/h, steel contribution ratio δ, reinforcement ratio ρ, concrete characteristic strength f_{ck}, effective creep ratio ϕ_{ef} and the ratio r_m between the bending moment applied at the column ends. For every value of each parameter all corresponding values of R are given as discrete points.

To analyze the relative performance of the EC2 and EC4 variants of the moment magnification method, the graphs for the R ratio computed for each method for a given parameter are put as a pair. Regarding the contribution of the relative slenderness on variant of the method, two different graphs are provided. The first graph is for columns subjected to pure compression and the other for columns subjected combined compression and bending. The statistical distribution of R is represented along with its mean value r and the interval ($r+s$ and $r-s$) where s is the standard deviation. Both simplified methods show a rather wide discrepancy compared to FE analysis results. The most significant parameters are the slenderness of the column, the steel section contribution to the cross-section strength under pure compression δ as well as the geometrical reinforcement ratio ρ. Table 6.4 shows that for columns subjected to an axial load only (zero eccentricity), both simplified methods give unsafe results for low relative slenderness. In case the latter is moderate, the predictions of EC2 moment magnification method are unsafe while the EC4 one gives conservative results. Nevertheless, EC2 method provides reasonable results compared to EC4 method for high relative slenderness. For columns subjected to combined compression and bending moment, both codes provide unsafe results in most cases. In particular, the interaction curve given by EC2 moment magnification method without considering the creep effect ($\varphi_{ef} = 0$) is close to FE analysis results. However, EC2 becomes un-conservative if creep is considered ($\varphi_{ef} = 1.5$). Considering all cases, it was found that the mean value r and the standard deviation s are respectively equal to 0.996 and 0.104 for EC2 simplified method and 1.010 and 0.112 for EC4 simplified method. The percentage of R below 0.97 is 41.84% and 34.86% for EC2 and EC4 simplified method, respectively. As a general conclusion, it can be pointed out that mean

Table 6.4: Results of parametric study of EC2 and EC4 version of moment magnification method.

Variable	EC2 simplified method	EC4 simplified method
1. Relative slenderness	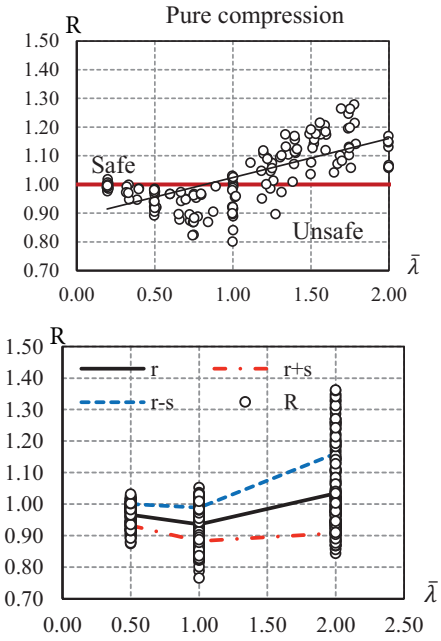	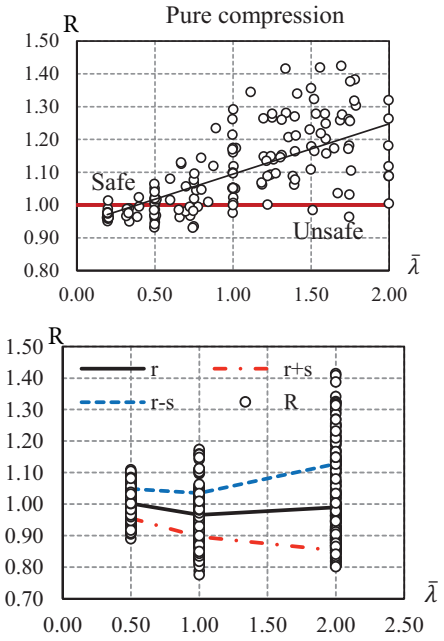
2. Eccentricity	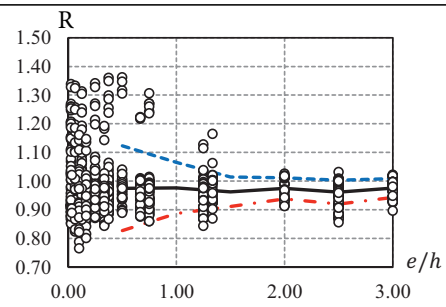	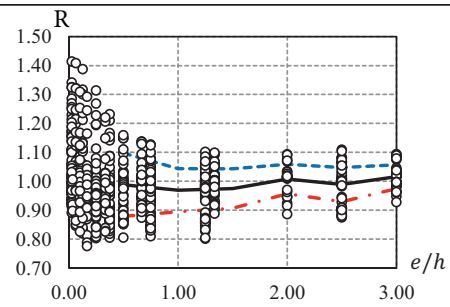

Continued on next page

Table 6.4 – continued from previous page

Variable	EC2 simplified method	EC4 simplified method
3. Steel contr. ratio	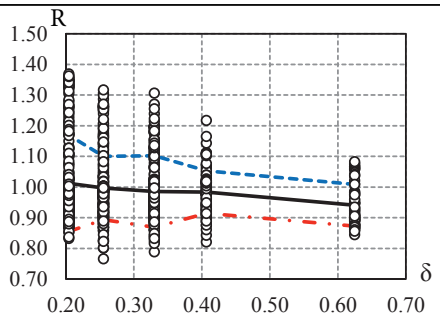	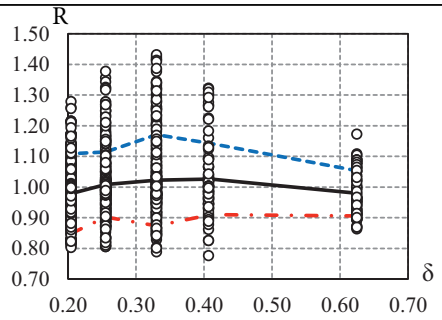
4. Geom. reinf. ratio	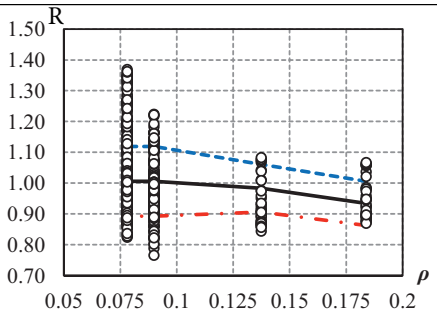	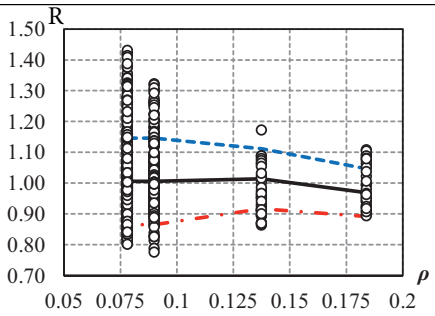
5. Concrete strength	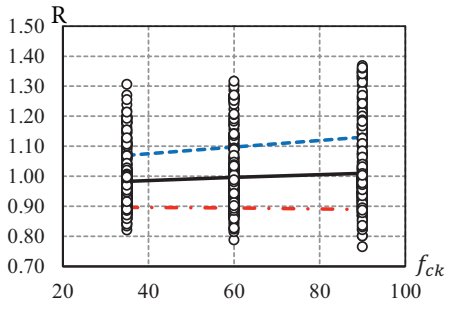	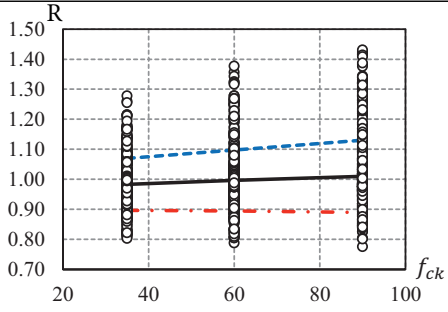
6. Effective creep ratio	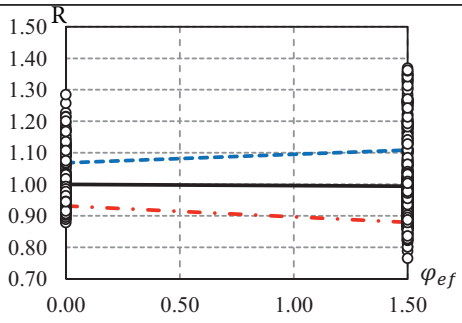	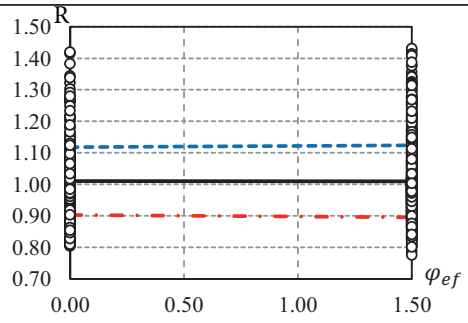

Continued on next page

Table 6.4 – continued from previous page

Variable	EC2 simplified method	EC4 simplified method
7. Histogram	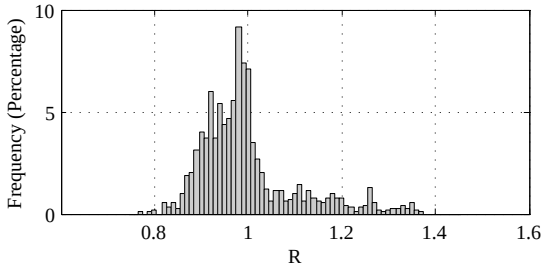	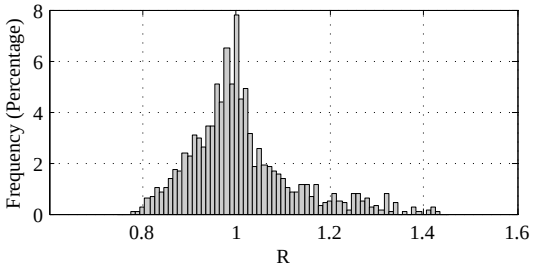

estimations of both design codes seem to be correct but that their shortcomings lead to a large scatter of the results.

6.4 Proposal of a moment magnification design method for hybrid columns

6.4.1 Further insight into the physical behavior of hybrid columns

Before suggesting new expressions for correction factors involved in the moment magnification method for hybrid column design, some effects are analyzed to get further insight into the physical behavior of hybrid columns.

6.4.1.1 Effect of sustained loads

The reduction of the load-bearing capacity due to creep is illustrated in Fig. 6.7a and Fig. 6.7b for different load eccentricities. The interaction curve of hybrid column with cross-section HSRCC1 subjected to eccentric load and bent in a symmetric single curvature is depicted in Fig. 6.7c where $N_{pl,Rd0}$ stands for the plastic design normal force and $M_{pl,Rd0}$ for the plastic bending moment of the

cross-section, both being considered without creep effect. Two values of the effective creep ratio are considered ($\varphi_{ef} = 0$ and $\varphi_{ef} = 1.50$). The concrete strength used in this study is C35. It can be seen that the plastic design moment of the cross-section with $\varphi_{ef} = 1.50$ is larger than that with $\varphi_{ef} = 0$. This difference comes from the ductility of the concrete which allows the compressed part of the steel section to yield before concrete crushes.

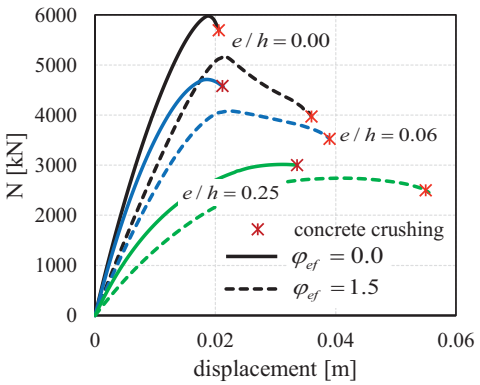

(a) Reduction of ultimate load due to creep for slenderness ratio $\bar{\lambda} = 1.0$.

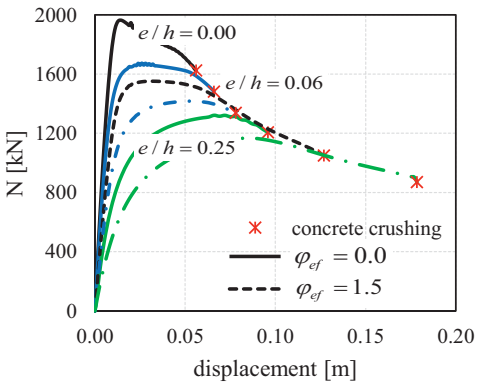

(b) Reduction of ultimate load due to creep for slenderness ratio $\bar{\lambda} = 2.0$.

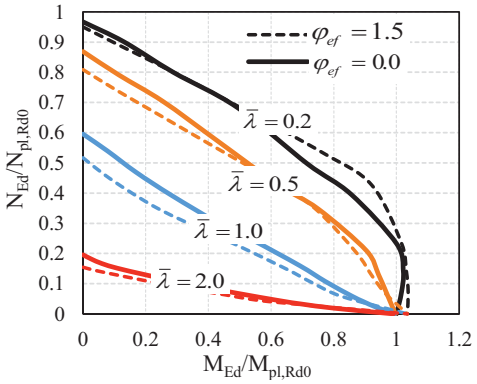

(c) Interaction curve.

Figure 6.7: Illustration of creep effect on slender hybrid column.

6.4.1.2 Effect of the residual stresses in the steel section

The buckling behavior of steel members is strongly influenced by the residual stresses. The distribution of the latter is shown in Fig. 6.4 for standard I-sections. The hybrid column with cross-section HSRCC1-3 are considered as well as the hybrid column with two steel profiles (HEB120) that are very close to each other (see Fig. 6.11a). The diameter of the rebar used for this column is ϕ12. The columns are modeled with concrete strength C35, structural steel yield stress 355 MPa and reinforcement yield stress 500 MPa. The columns were discretized using 20 elements. This discretization is sufficient to represent the imperfect parabolic shape of the columns. The column is subjected to the same eccentric loads at both ends. Residual stresses are incorporated in the model as a state of self-equilibrated initial stresses. The comparison of buckling and interaction curves considering and disregarding the residual stresses is given in Fig. 6.8 to Fig. 6.11b. The

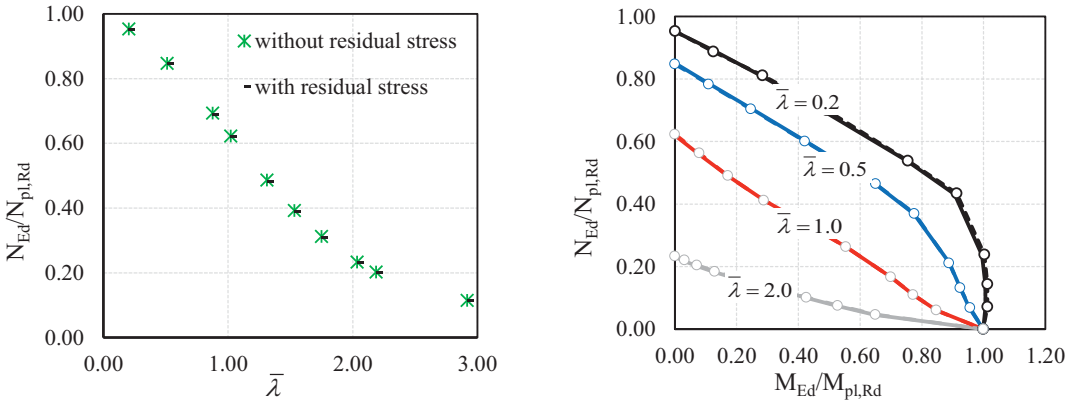

(a) Buckling curve.

(b) Interaction curve.

Figure 6.8: Effect of residual stress in buckling behavior of HSRCC1.

dash line (–○–) corresponds to the interaction curve when the residual stresses within the steel profile are not considered whereas the solid line (—) corresponds to the interaction curve with residual stresses. It can be seen that the residual stresses have a marginal effect on the behavior of hybrid columns and they can

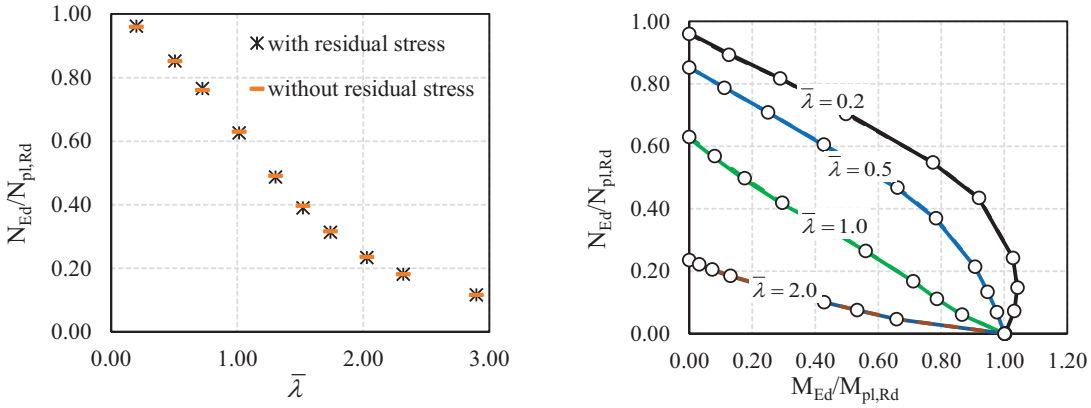

(a) Buckling curve. (b) Interaction curve.

Figure 6.9: Effect of residual stress in buckling behavior of HSRCC2.

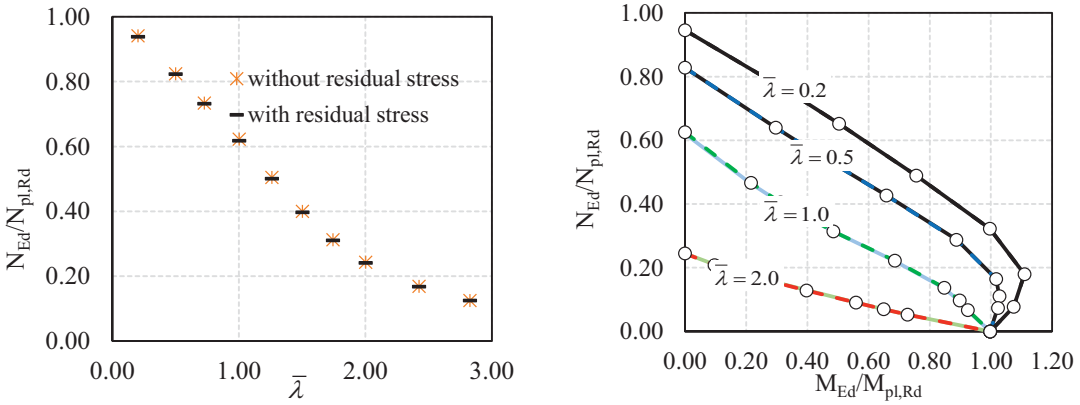

(a) Buckling curve. (b) Interaction curve.

Figure 6.10: Effect of residual stress in buckling behavior of HSRCC3.

be ignored. Therefore, it can be concluded that the structural steels behave as large rebars. Considering the above comments, it can be concluded that the new method for hybrid columns should be inspired from the EC2 variant rather than from the EC4 version.

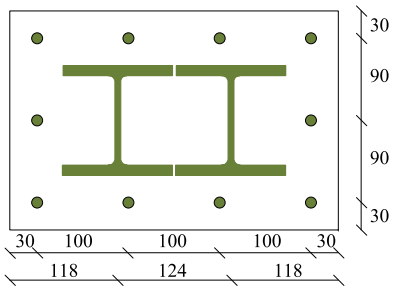

(a) Hybrid cross-section HSRCC6.

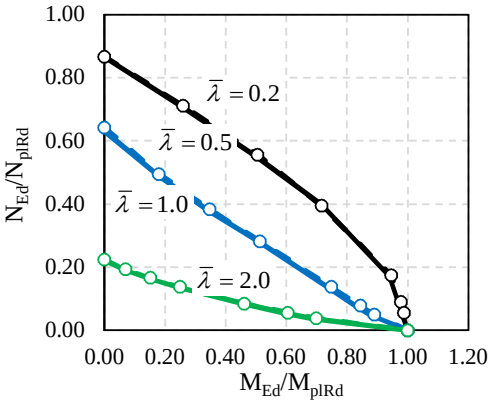

(b) Effect of residual stress on interaction curve.

Figure 6.11: Effect of residual stress in buckling behavior of hybrid column where the cross-section has two steel profiles very close to each other.

6.4.2 A proposal for the expression of the flexural stiffness EI applicable to hybrid columns subjected to combined axial load and uniaxial bending

The parametric study with 1140 data sets presented previously shows that both EC2 and EC4 version of the moment magnification method lead to unsafe results in half of case-studies (Table 6.1). It means that the effective flexural stiffness EI given in EC2 and EC4 are not appropriate for slender hybrid column design. Based on the outcome of the parametric study with 2960 cases including different yield stress of steel section, new expressions for β and the correction factors (K_s, K_a, K_c) involved in the definition of the effective flexural stiffness EI are proposed. By doing so, we are able to make the moment magnification method given in Eurocodes suitable for hybrid column design. The proposed simplified method based on moment magnification approach is summarized in the following.

The total design moment is determined by multiplying the first-order moment (including the effect of geometric imperfection) by the magnification factor k

which is defined as

$$k = \frac{\beta}{1 - \frac{N_{Ed}}{N_{cr}}} \tag{6.10}$$

where $\beta = 0.6r_m + 0.4 \geq 0.4$; and N_{cr} is the buckling load which is calculated by using the following expression for the flexural stiffness EI

$$EI = K_c E_{cd} I_c + K_s E_s I_s + K_a E_a I_a \tag{6.11}$$

with

$$K_c = k_1 k_2 / (1 + \varphi_{ef}) \tag{6.12}$$

$$K_s = 1 \tag{6.13}$$

$$K_a = \frac{0.76 \left(\frac{f_y}{f_{ck}}\right)^{0.0124}}{1 + 105\varphi_{ef}\exp(-0.078\lambda)} \leqslant 1 \tag{6.14}$$

$$k_1 = \sqrt{\frac{f_{ck}}{20}} \tag{6.15}$$

$$k_2 = n\frac{\lambda}{170} \leqslant 0.2 \tag{6.16}$$

$$n = \frac{N_{Ed}}{N_{pl,Rd}} \tag{6.17}$$

where the expressions of the correction factors K_c and K_s recommended in EC2 have been used. Further, since there is no steel profile in a reinforced concrete section, the correction factor K_a does not exist in EC2. If one compares these correction factors to those in EC4, they are totally different. In fact, due to compressive creep strains, as shown in Section 6.4.1.2, longitudinal steel compressive strains can exceed the yield strain. This implies that the steel modulus that collaborates in the effective stiffness EI of the hybrid column could not be the elastic modulus but should rather be the secant modulus which varies with concrete creep. Moreover, for slender columns, plastification in the compression zone of the steel section may not develop before instability. Hence, the secant modulus of steel should be a function of the creep coefficient φ_{ef} and the geometric slenderness λ. For higher values of the creep coefficient, the value of secant modulus of the steel section will be rather lower. However, for higher values of slenderness this modulus will be higher. Therefore, in addition to the previous cases already

analyzed, we need to investigate the effect of the steel yield stress on the ultimate load of hybrid columns. All cases previously analyzed with $f_y = 355MPa$ are now recalculated with $f_y = 235MPa$ and $f_y = 460MPa$. The objective is to study the effect of plastification of the steel sections, particularly for low yield stress. As a result, the correction factor K_a of EC4 is modified to take into account the effect of plastification of the steel section. This factor is calibrated based on the results of a parametric study with 2960 parameter sets (cross-sections, column effective slenderness and creep coefficient) performed by using the developed FE model.

The procedure employed to establish the expression of K_a is as follows. Let us consider a slender hybrid column with an initial imperfection w_0 subjected to axial loads and uniaxial bending, bent in a symmetric single curvature ($r_m = 1$), the ultimate first-order bending moment $M_{Ed,1}$ can be obtained with a nonlinear FE analysis for a particular axial load N_{Ed}. Likewise, it is also possible to compute the ultimate bending moment $M_{pl,N,Rd}$ of the cross-section of the column for the same axial force. By equating the second-order bending moment calculated with the moment magnification method to the ultimate bending moment of the column cross-section, the moment magnification factor k can be obtained. Finally, by making use of the critical buckling load formulation and the proposed form of effective stiffness expression, the correction factor K_a can be derived. This procedure has also been adopted in [130].

- First, the magnification factor is obtained:

$$k = \frac{M_{pl,N,Rd}}{M_{Ed,1}} \tag{6.18}$$

- This value allows the critical buckling load of the column to be computed:

$$N_{cr} = \frac{N_{FE}}{1 - \frac{M_{Ed,1}}{M_{pl,N,Rd}}} \tag{6.19}$$

- The flexural stiffness of the column can be computed from

$$EI = \frac{N_{cr} L^2}{\pi^2} \tag{6.20}$$

- Finally, the calibration factor K_a can be obtained as

$$K_a = \frac{EI - K_c E_{cd} I_c + E_s I_s}{E_a I_a} \tag{6.21}$$

6.4.3 Comparisons between proposed simplified method and FEA

In order to evaluate the contribution of the various parameters governing the ultimate load, the R ratio has been computed for all the considered cases (2960 data sets). The value of the R ratio is given as a function of the main variables: eccentricity e/h, geometric slenderness ratio λ and relative slenderness $\bar{\lambda}$, the latter being calculated according to EC4 formulation. For every value of each parameter all corresponding value of R are given as discrete points. In Fig. 6.12c, R is given with the mean value r, $r + s$ and $r - s$, where s is standard deviation. It can be seen that despite the wide dispersion at high relative slenderness ratio, the proposed formulation gives a relatively low scatter compared to FE analysis results. The standard deviations are equal to 0.0147, 0.0325 and 0.0712 for relative slenderness ratio $\bar{\lambda}$ equal to 0.5, 1 and 2 respectively. The frequency histogram shown in Fig. 6.12d was constructed using the proposed formulation. With a 0.005 precision, the percentage of the R ratio equal to 1 is 50.9%, and less than 1 is cumulatively 23.72% as can be seen on the histogram. The percentage of R below 0.97 is 10.34%. Its overall variability gives a good estimation of the mean value of the ultimate load with relatively small deviation. The mean value r and the standard deviation s provided by the proposed simplified method are respectively equal to 1.0022 and 0.0459 which have been improved compared to the ones given by EC2 simplified method ($r = 0.996$, $s = 0.104$) and EC4 simplified method ($r = 1.010$, $s = 0.112$). Based on these numerical results, we can conclude that the developed method gives the ultimate load of a slender hybrid column subjected to combined axial force and bending moment with sufficient precision.

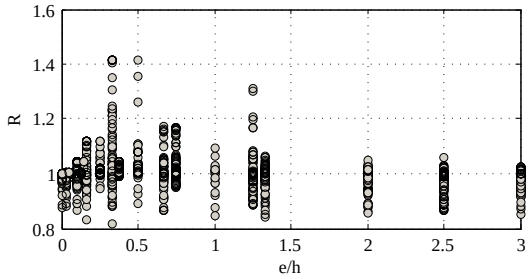

(a) Influence of eccentricity on the ultimate load of the hybrid column.

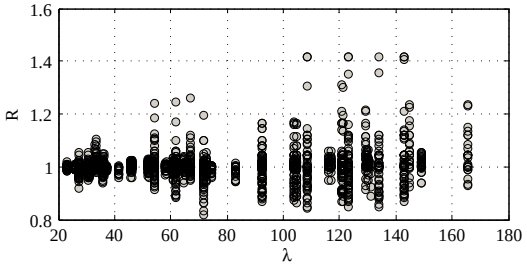

(b) Influence of geometric slenderness on the ultimate load of the hybrid column.

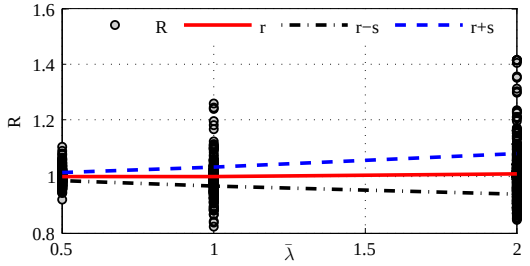

(c) Influence of relative slenderness on the ultimate load of the hybrid column.

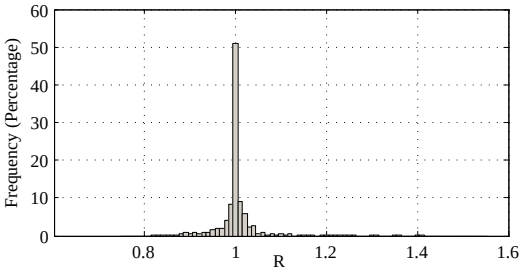

(d) Histogram of frequency of the R ratio.

Figure 6.12: Performance of the results given by the new simplified method.

6.5 Conclusion

Numerical investigations on the second-order effects in slender hybrid column subjected to combined axial load and uniaxial bending moment have been performed. One of the main objectives of this study was to evaluate the bending moment magnification method proposed in EC2 and EC4 when applied to hybrid columns. To do so, a FE model has been developed in which the geometrical/material nonlinearities as well as the partial interaction effect between the steel profiles and the surrounding concrete are taken into account. The FE model has been validated by comparing its predictions against experimental results for standard composite columns. To thoroughly analyze the applicability of EC2 and EC4 variants of the moment magnification method to hybrid columns, an extensive parametric study with 1140 data sets (cross-sections, column effective slenderness and creep

coefficient) has been carried out. The comparison between the results obtained with Eurocode simplified methods and with FEA shows that simplified methods of EC2 and EC4 lead to a wide scatter where the percentage of the ratio R lesser than 1 is cumulatively larger than 5%. It means that the proposed effective flexural stiffness EI of EC2 and EC4 are not appropriate for slender hybrid column design. It was observed that the secant modulus of compressed part of the steel section varies as a function of the creep coefficient φ_{ef} and the geometric slenderness λ. Therefore, in addition to the previous cases already analyzed, a further investigation of the effect of the steel yield stress on the ultimate load of hybrid columns has been carried out. This latter investigation was based on an extensive numerical parametric study with 2090 data sets. A simplified method has been proposed for hybrid column design. This method is developed within the context of Eurocodes, i.e. moment magnification approach. In the proposed method, new expressions for the correction factors (for the determination of effective flexural stiffness (EI)) are proposed in order to take into account the creep effect and the effect of plastification of the steel profiles. The comparisons between proposed simplified method and FE analyzes shows that the developed method provides the ultimate load for typical slender hybrid columns with an adequate accuracy.

The lack of the residual stress effects on the ultimate load of the hybrid columns as well as the destination of the method, which will occur in reinforced concrete buildings rather than in metal structures, led to development of this new formulation to be based on Eurocode 2 formulations. The proposed formulation is applicable for reinforced concrete columns (without an embedded steel shape) with respect to Eurocode 2 regulations. It notes, however, that by applying this method to a classical composite section, it gives a conservative result and more conservative than the one obtained from Eurocode 4 formulations. It can therefore lead to a consistency between the different formulations as the following. The "hybrid" approach (proposed formulation) can handle both reinforced concrete and hybrid columns, since it is developed based on Eurocode 2 formulations; and it can also be used for classical composite columns, while leading to less fa-

vorable ultimate load in the specific case of the only one embedded steel section for which a more precise formulation can be found in Eurocode 4.

Chapter 7

General conclusions and perspectives

***

7.1 Summary and concluding remarks

The development of a design guide for hybrid columns with several embedded steel profiles, subjected to combined loads is the objective of this thesis. Therefore, a FE model has been developed in which the geometrical/material nonlinearities as well as the partial interaction between the steel profiles and the surrounding concrete are taken into account. The results of the FE model have served as references in developing a new design method for hybrid columns. The development of the FE formulation was begun with the geometrically linear elastic analysis in which the exact expression of the stiffness matrix has been developed for the elastic hybrid beam-column in partial interaction. Both shear-rigid and shear-flexible model have been developed based on the exact stiffness matrix. The influences of shear flexibility of the encasing concrete component and the partial interaction on the overall behavior of the hybrid beam-column have been investigated by performing the analyses and comparing the results of both models. It has been found that the transverse displacement is more affected by shear flexibility than partial interaction. The deflection ratio of both model varies slightly following the increasing shear connection stiffness from low to high value.

To describe the geometrical nonlinearity, the co-rotational framework has been adopted and the motion of the element is decomposed into a rigid body motion and a deformational part using a local co-rotational frame, which continuously translates and rotates with the element but does not deform with it. The treatment of geometric nonlinearity is effectively undertaken at the level of discrete nodal variables with the transformation matrix between the local and global nodal entities being independent of the assumptions made for the local element.

The nonlinear FE model of hybrid beams under combined load has been developed based on the fiber beam model where the shear deformability of the concrete component is considered. To take into account the confinement effects, the 3d constitutive law for the encasing concrete component is adopted. Then, the plane stress condition for the concrete component is applied in order to condense the 3d formulation, derived from a 3d plastic model of the concrete material, into the 2d beam model. The developed FE model is implemented into the nonlinear geometry formulation by adopting the co-rotational framework. The static condensation has been applied in order to obtain the consistent tangent matrix in local co-rotational system. The FE model has been validated by comparing its predictions against experimental results of the hybrid beams conducted at Laboratory of Civil and Mechanical Engineering of INSA Rennes. Furthermore, the influence of the partial interaction on the overall behavior of the hybrid beams has been investigated. It has been found that the ultimate loads predicted by FE analysis agree well with those of the experimental results and that the shear connection stiffness plays a crucial role on the flexibility of the hybrid beam. From the numerical applications, it has been shown that the developed formulation provides a robust and reliable option in determining the ultimate load of hybrid beam-columns subjected to combined axial load, bending moment and shear force in a large displacement analysis.

Besides, numerical investigations on the second-order effects in slender hybrid

columns subjected to combined axial load and uniaxial bending moment have been performed. One of the main objectives of this study is to evaluate the bending moment magnification method proposed in EC2 and EC4 when applied to hybrid columns. To do so, a FE model is developed in which the geometrical/material nonlinearities, the geometrical imperfections, the residual stresses in steel profiles as well as the partial interaction effect between steel profiles and the encasing concrete are taken into account. Since slender hybrid columns subjected to combined axial load and bending moment are considered, the effects of shear deformability of concrete component can be ignored. As a result, Euler-Bernoulli beam kinematics and the uniaxial stress-strain behavior for each component (steel and concrete) of the hybrid beam-column element are adopted. Moreover, the developed model based on Euler-Bernoulli kinematic assumption is consistent with the finite element model proposed in the general methods of Eurocodes (EC2 and EC4) for designing a column subjected to combined axial load and bending moment. The comparison between the results obtained with Eurocode simplified methods (moment magnification method) and with FE analysis shows that simplified methods of EC2 and EC4 lead to a wide scatter where the unsafe factor ratio is cumulatively larger than 5%. It means that the proposed effective flexural stiffness EI of EC2 and EC4 are not appropriate for slender hybrid column design. As a result, a new simplified method has been proposed for slender hybrid column design within the context of Eurocodes, i.e. moment magnification approach. The proposed method is developed based on an insight into the physical behavior of slender hybrid columns. It has been observed that the secant modulus of compressed part of the steel section varies as a function of the creep coefficient φ_{ef} and the geometric slenderness λ. Consequently, in the proposed method, new expressions for the correction factors (for the determination of effective flexural stiffness (EI)) are proposed in order to take into account the creep effect and the effect of yielding in the steel profiles. The comparisons between proposed simplified method and FE analyses shows that the proposed method provides the ultimate load for typical slender hybrid columns with an adequate accuracy. To make the proposed simplified method more accessible for

designers, a simple design tool has been developed based on Matlab Compiler Runtime platform which is presented in Appendix C. The program is capable to perform a nonlinear analysis as well as a simplified analysis, based on moment magnification method, of reinforced concrete column with several embedded steel profiles subjected to combined axial load and uniaxial bending moment.

7.2 Perspectives

The FE model developed in Chapter 5 may serve as a primary reference in producing a design guide for hybrid beams subjected to combined loads (M-V). However, an insight into the physical behavior of hybrid beams under combined loads is required. Those requirements find their root in modeling the 3d constitutive law of concrete (with softening behavior) in which the hardening law and the damage plasticity model have to be introduced, variation of shear deformation over the depth of the concrete cross-section after cracking occurs, nonlinear distribution of axial deformation and other kinematic assumptions. The latter can be dealt with by adopting a more advanced beam theory which considers a nonlinear distribution of the kinematic variables.

While the thorough investigation on the second-order effects in hybrid columns has been performed in Chapter 6 to provide the design method for hybrid columns subjected to combined axial load and uniaxial bending moment, there are several factors that have not been considered. Among those factors are the biaxial bending and the lateral torsional buckling that may occur for a slender cross-section. Therefore, a 3d finite element model of the hybrid beam element has to be developed.

Appendix A

Geometrically elastic linear shear-rigid hybrid beam model

***

A.1 Fundamental equations

The governing equations describing the geometrically linear behavior of an elastic shear-rigid hybrid beam with n embedded sections in partial interaction are briefly outlined in this section. All variables subscripted with c belong to the encasing beam and those with subscript s belong to the embedded section. Quantities with subscript sc are associated with the shear connectors. The following assumptions are commonly accepted in all models to be discussed in this paper:

- connected members are made out of elastic, homogenous and isotropic materials;

- the cross-sections of all components remain plane and orthogonal to beam axis after deformation, though relative slips can develop along their interface;

- the lateral deflection v is assumed to be the same for all components;

- discretely located shear connectors are regarded as continuous.

A.1.1 Compatibility

Based on the above assumptions, kinematic equations relating the displacement components (u_i, v, θ) to the corresponding strain components (ϵ_i, θ, κ (Fig. A.1)) are derived for each component of the hybrid beam as follows:

$$\epsilon_i = \partial_x u_i, \qquad i = s1, s2, \cdots, sn, sc \tag{A.1}$$

$$v_c = v_{si} = v \tag{A.2}$$

$$\theta = \partial_x v \tag{A.3}$$

$$\kappa = \partial_x^2 v \tag{A.4}$$

The interlayer slip corresponds to the difference between axial displacements of embedded sections and of the encasing beam at the interface which is expressed as:

$$g_i = u_c - u_{si} - h_i\,\theta, \qquad i = 1, 2, \cdots, n \tag{A.5}$$

where $h_i = y_{si} - y_c$ is the distance between centroid of the embedded sections and the encasing element; i represents each embedded section.

A.1.2 Equilibrium

The equilibrium equations are derived by considering the free body diagrams of a differential elements dx located at an arbitrary position x (see Fig. A.2) in the hybrid beam. The interface connection between the embedded sections and the encasing beam is modeled by continuously distributed spring. The equilibrium conditions result in the following set of equations:

$$\partial_x N_{si} = -D_{sci}, \qquad i = 1, 2, \cdots, n \tag{A.6}$$

$$\partial_x N_c = \sum_{j=1}^{n} D_{scj} \tag{A.7}$$

$$\partial_x M = -V - \sum_{j=1}^{n} D_{scj} h_j \tag{A.8}$$

where

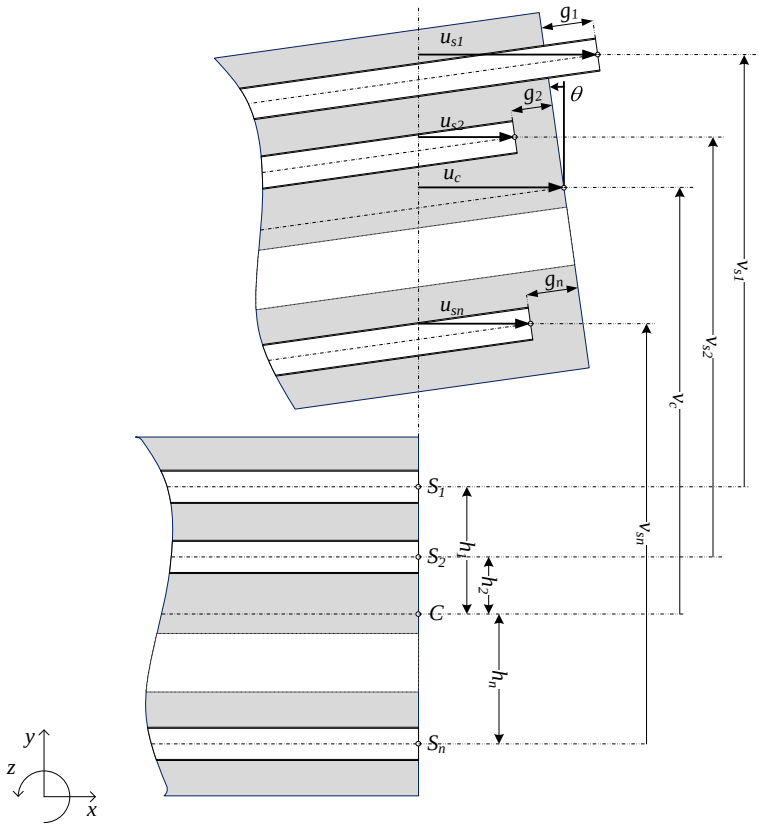

Figure A.1: Kinematic of shear-rigid hybrid beam-column.

- $\partial_x^i \bullet = \mathrm{d}^i \bullet / \mathrm{d}x^i$

- $h_i = y_{si} - y_c$ $(i = 1, 2, \cdots n)$ is the distance between the centroid of the k^{th} embedded section and the one of encasing beam cross-section;

- N_i, V_i, M_i $(i = s1, s2, \cdots sn, c)$ are the axial forces, the shear forces and bending moments at the centroid of component "i";

- D_{sci} $(i = 1, 2, \cdots n)$ are the slip forces per unit length at the interface of the k^{th} embedded section and the encasing beam;

- $V = \sum V_i$ is the sum of shear forces of each component;

- $M = \sum M_i$ is the sum of bending moments at centroid of each component.

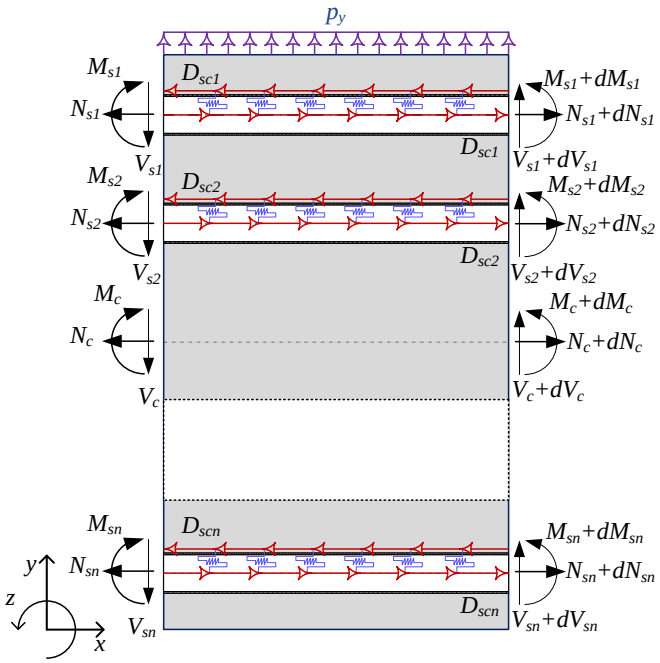

Figure A.2: Free body diagrams of an element at an arbitrary position x.

A.1.3 Constitutive relations

The generalized stress-strain relationships are simply obtained by integrating the appropriate uniaxial constitutive model over each cross-section. For a linear elastic material, these relationships lead to the following set of equations:

$$N_i = \int_{A_i} \sigma \, \mathrm{d}A_i = (EA)_i \, \epsilon_i, \qquad i = s1, s2, \cdots, sn, c \tag{A.9}$$

$$M_i = -\int_{A_i} y \, \sigma \, \mathrm{d}A_i = (EI)_i \, \kappa \tag{A.10}$$

where

- $(EA)_i = E_i \, A_i$ is the axial stiffness of each component;

- $(EI)_i = E_i \, I_i$ is the flexural stiffness of each component.

The parameters E_i, A_i and I_i are respectively the elastic modulus, the area and the second moment of area of the component "i". The above relations must be completed by the relationship between the shear bond force D_{sck} and the

interlayer slip g_k. The assumption of linear and continuous shear connection can be expressed by the following simple relationship between interface slips and shear flow:

$$D_{sci} = k_{sci}\, g_i, \qquad i = 1, 2, \cdots, n \tag{A.11}$$

where k_{sck} is the shear bond stiffness.

A.2 Derivation of the governing equations

The relationships introduced in Section A.1 are now combined to derive the equations governing the behavior of a hybrid beam with partial interaction. Combining the kinematic relations Eqs. (A.2-A.4) with the elastic law Eqs. (A.9-A.11) and inserting the outcome into the equilibrium equations Eqs. (A.6-A.8) produce the following set of differential equations:

$$(EA)_{si}\, \partial_x^2 u_{si} = -k_{sci}\, g_i \tag{A.12}$$

$$(EA)_c\, \partial_x^2 u_c = \sum_{j=1}^{n} k_{scj}\, g_j \tag{A.13}$$

$$(EI)_0\, \partial_x^3 v = -V(x) - \sum_{k=1}^{n} k_{sck}\, g_k\, h_k \tag{A.14}$$

The expression $(EI)_0$ stands for the sum of the flexural stiffness of each component i.e. $\Big(EI)_0 = \sum_{j=1}^{n} E_{sj}\, I_{sj} + E_c\, I_c\Big)$. Taking the derivative of the slip distribution relation Eq. (A.5) and making use of Eqs. (A.12-A.14), one arrives at the following coupled second-order system of differential equations where the unknown variables are the slip distribution at each interface:

$$\partial_x^2 \mathbf{g} - \Lambda \mathbf{g} = \frac{V(x)}{(EI)_0} \mathbf{h} \tag{A.15}$$

The components of the matrix Λ are given by

$$\Lambda_{kk} = k_{sck} \left[\frac{1}{(EA)_{sck}} + \frac{h_k^2}{(EI)_0} \right] \tag{A.16}$$

$$\Lambda_{kl} = k_{scl} \left[\frac{1}{(EA)_c} + \frac{h_k h_l}{(EI)_0} \right] \tag{A.17}$$

in which,

$$\frac{1}{(EA)_{sck}} = \frac{1}{(EA)_c} + \frac{1}{(EA)_{sk}}, \qquad k, l = 1, 2, \cdots n \tag{A.18}$$

A diagonalization of the matrix Λ will uncouple the above system of differential equations Eq. (A.15) and produce a set of n second-order ordinary equations. Let Λ_v and Λ_λ respectively be the matrix collecting the eigenvectors and the eigenvalues of Λ. Then, we have the following relationship:

$$\Lambda_\lambda = \Lambda_v^{-1} \Lambda \Lambda_v. \tag{A.19}$$

Subsequently, we insert the vector $\mathbf{g}$ obtained by pre-multiplying the vector $\tilde{\mathbf{g}}$ by the matrix Λ_v

$$\mathbf{g} = \Lambda_v \tilde{\mathbf{g}} \tag{A.20}$$

into Eq. (A.20) and make use of Eq. (A.19) to produce an uncoupled differential equation system:

$$\partial_x^2 \tilde{\mathbf{g}} - \Lambda_\lambda \, \tilde{\mathbf{g}} = \frac{V(x)}{(EI)_0} \bar{\mathbf{h}} \tag{A.21}$$

where $\bar{\mathbf{h}} = \Lambda_v^{-1} \mathbf{h}$ which gives the ordinary differential equation in n variables $\tilde{g}_k$ as follow:

$$\tilde{g}_i = C_{2i-1} \, e^{\sqrt{\lambda_i} x} + C_{2i} \, e^{-\sqrt{\lambda_i} x} + P_i, \qquad i = 1, 2, \cdots, n \tag{A.22}$$

A.3 Closed-form solution of the governing equations

In this section, we provide only the analytical solution of the governing equations for the general case of the interface connection (which means that $0 < k_{sck} < \infty$). The governing differential equation involves the single unknown variable $\tilde{\mathbf{g}}$. It is noteworthy that the exact solution of the governing differential equation Eq. (A.22) is contingent upon the distribution of the shear force $V(x)$. In order to simplify the development of the solution, we assume that the external distributed load on the element is constant. It results that the distribution of shear force is

linear, following the overall transverse equilibrium equation:

$$V(x) = -p_y\, x + C_{2n+6} \tag{A.23}$$

where C_{2n+6} is the shear force at the left hand side of the beam and is considered to be a constant of integration. The kinematic variables will be known while $\tilde{g}_k$ is found by solving the differential equation Eq. (A.22). Let $P_k(x)$ be the particular solution for non homogeneous differential equation Eq. (A.22). Hence, the general solution of $\tilde{g}_k$ is given by

- For $\lambda_i > 0$

$$\tilde{g}_i = C_{2i-1} e^{\sqrt{\lambda_k} x} + C_{2i} e^{-\sqrt{\lambda_i} x} + P_i(x), \qquad i = 1, 2, \cdots, n \tag{A.24}$$

- For $\lambda_i < 0$

$$\tilde{g}_i = C_{2i-1} \cos \sqrt{-\lambda_i} x + C_{2i} \sin \sqrt{-\lambda_i} x + P_i(x), \qquad i = 1, 2, \cdots, n \tag{A.25}$$

- For $\lambda_i = 0$

$$\tilde{g}_i = C_{2i-1} + C_{2i} x + P_i(x), \qquad i = 1, 2, \cdots, n \tag{A.26}$$

The particular solution of Eq. (A.22) is given by:

- For $\lambda_i \neq 0$

$$P_i(x) = \left(-C_{2n+6} + p_y x\right) \frac{\bar{h}_i}{\lambda_k (EI)_0}, \qquad i = 1, 2, \cdots, n \tag{A.27}$$

- For $\lambda_i = 0$

$$P_i(x) = \left(C_{2n+6} \frac{x^2}{2} - p_y \frac{x^3}{6}\right) \frac{\bar{h}_i}{(EI)_0}, \qquad i = 1, 2, \cdots, n \tag{A.28}$$

All $\tilde{g}_i$ are collected in a vector so the analytical solution can be written in a matrix form as follow:

$$\tilde{\mathbf{g}} = \mathbf{X}_{\tilde{g}} \mathbf{C} + \mathbf{Z}_{\tilde{g}} \tag{A.29}$$

with

$$\tilde{\mathbf{g}} = [\, \tilde{g}_1 \; \tilde{g}_2 \cdots \tilde{g}_n \,]^{\mathrm{T}} \tag{A.30}$$

and

$$\mathbf{C} = [\, C_1 \; C_2 \cdots C_{2n+6} \,]^{\mathrm{T}} \tag{A.31}$$

The components of matrix $\mathbf{X}_{\tilde{g}}$ and $\mathbf{Z}_{\tilde{g}}$ are respectively dependent on eigenvalues of Λ and external load p_y. In case Λ is positive definite i.e. $\lambda_k > 0$, we obtain the following expression of $\mathbf{X}_{\tilde{g}}$ and $\mathbf{Z}_{\tilde{g}}$ with $\alpha_k = \sqrt{\lambda_k}$.

$$\mathbf{X}_{\tilde{g}} = \begin{bmatrix} e^{\alpha_1 x} & e^{-\alpha_1 x} & 0 & 0 & \cdots & 0 & 0 & 0 & 0 & 0 & 0 & 0 & -\dfrac{\bar{h}_1}{\lambda_1 (EI)_0} \\ 0 & 0 & e^{\alpha_2 x} & e^{-\alpha_2 x} & \cdots & 0 & 0 & 0 & 0 & 0 & 0 & 0 & -\dfrac{\bar{h}_2}{\lambda_2 (EI)_0} \\ \vdots & \vdots & \vdots & \vdots & \ddots & \vdots & \vdots & \vdots & \vdots & \vdots & \vdots & \vdots & \vdots \\ 0 & 0 & 0 & 0 & \cdots & e^{\alpha_n x} & e^{-\alpha_n x} & 0 & 0 & 0 & 0 & 0 & -\dfrac{\bar{h}_n}{\lambda_n (EI)_0} \end{bmatrix} \tag{A.32}$$

and

$$\mathbf{Z}_{\tilde{g}} = \frac{p_y x}{(EI)_0} \begin{bmatrix} \dfrac{\bar{h}_1}{\lambda_1} & \dfrac{\bar{h}_2}{\lambda_2} & \cdots & \dfrac{\bar{h}_n}{\lambda_n} \end{bmatrix}^{\mathrm{T}} \tag{A.33}$$

Substituting Eq. (A.30) into Eq. (A.20), one gets

$$\mathbf{g} = \mathbf{X}_g \mathbf{C} + \mathbf{Z}_g \tag{A.34}$$

in which

$$\mathbf{X}_g = \Lambda_v \mathbf{X}_{\tilde{g}}; \qquad \mathbf{Z}_g = \Lambda_v \mathbf{Z}_{\tilde{g}} \tag{A.35}$$

A.3.1 Determination of displacement fields

We use the relations of kinematic variables in function of interlayer slip developed in Section A.2 to determine the displacement fields. Inserting the expression of shear force and Eq. (A.34) into Eq. (A.14), one obtains:

$$\partial_x^3 v = -\frac{1}{(EI)_0} \mathbb{I}_{2n+6} \mathbf{C} - \chi \mathbf{X}_g \mathbf{C} + \frac{p_y x}{(EI)_0} - \chi \mathbf{Z}_g \tag{A.36}$$

where

$$\chi = \frac{1}{(EI)_0}\left[\, h_1 k_{sc1}\ h_2 k_{sc2} \cdots h_n k_{scn}\,\right] \tag{A.37}$$

The curvature, rotation and deflexion can be derived by consequently once, twice and thrice integrating Eq. (A.36).

$$\kappa = \mathbf{X}_\kappa \mathbf{C} + Z_\kappa \tag{A.38}$$

$$\theta = \mathbf{X}_\theta \mathbf{C} + Z_\theta \tag{A.39}$$

$$v = \mathbf{X}_v \mathbf{C} + Z_v \tag{A.40}$$

where

$$\mathbf{X}_\kappa = \int \left[-\frac{1}{(EI)_0}\mathbb{I}_{2n+6} - \chi \mathbf{X}_g(x)\right] dx + \mathbb{I}_{2n+1} \tag{A.41}$$

$$\mathbf{X}_\theta = \int \mathbf{X}_\kappa dx + \mathbb{I}_{2n+2} \tag{A.42}$$

$$\mathbf{X}_v = \int \mathbf{X}_\theta dx + \mathbb{I}_{2n+3} \tag{A.43}$$

$$Z_\theta = \int Z_\kappa dx \tag{A.44}$$

$$Z_\kappa = \int \left[\frac{p_y x}{(EI)_0} - \chi \mathbf{Z}_g\right] dx \tag{A.45}$$

$$Z_v = \int Z_\theta dx \tag{A.46}$$

$$\mathbb{I}_{2n+1} = [0\ 0 \cdots 0\ 0\ 0 \cdots 0\ 1\ 0\ 0\ 0\ 0\ 0] \tag{A.47}$$

$$\mathbb{I}_{2n+2} = [0\ 0 \cdots 0\ 0\ 0 \cdots 0\ 0\ 1\ 0\ 0\ 0\ 0] \tag{A.48}$$

$$\mathbb{I}_{2n+3} = [0\ 0 \cdots 0\ 0\ 0 \cdots 0\ 0\ 0\ 1\ 0\ 0\ 0] \tag{A.49}$$

$$\mathbb{I}_{2n+4} = [0\ 0 \cdots 0\ 0\ 0 \cdots 0\ 0\ 0\ 0\ 1\ 0\ 0] \tag{A.50}$$

$$\mathbb{I}_{2n+5} = [0\ 0 \cdots 0\ 0\ 0 \cdots 0\ 0\ 0\ 0\ 0\ 1\ 0] \tag{A.51}$$

$$\mathbb{I}_{2n+6} = [0\ 0 \cdots 0\ 0\ 0 \cdots 0\ 0\ 0\ 0\ 0\ 0\ 1] \tag{A.52}$$

The axial displacement of concrete element can be determined from Eq. (A.13). It gives

$$\partial_x^2 u_c = \frac{1}{(EA)_c}\begin{bmatrix} k_{sc1} & k_{sc2} & \cdots & k_{scn} \end{bmatrix} \mathbf{g} \tag{A.53}$$

Integrating twice Eq. (A.53), one gets

$$u_c = \mathbf{X}_{u_c}\mathbf{C} + Z_{u_c} \tag{A.54}$$

where

$$\mathbf{X}_{u_c} = \int \left[\int \left(\frac{1}{(EA)_c} \begin{bmatrix} k_{sc1} & k_{sc2} & \cdots & k_{scn} \end{bmatrix} \mathbf{X}_g \right) dx \right] dx + x\mathbb{I}_{2n+4} + \mathbb{I}_{2n+5} \tag{A.55}$$

$$Z_{u_c} = \int \left[\int \left(\frac{1}{(EA)_c} \begin{bmatrix} k_{sc1} & k_{sc2} & \cdots & k_{scn} \end{bmatrix} \mathbf{Z}_g \right) dx \right] dx \tag{A.56}$$

The axial displacements of steel section can be determined by using the interlayer slip Eq. (A.5).

$$u_{si} = u_c - g_i - h_i\theta, \qquad i = 1, 2, \cdots n \tag{A.57}$$

Introducing Eq. (A.34), Eq. (A.39) and Eq. (A.54) into Eq. (A.57) leads to

$$u_{si} = \mathbf{X}_{u_{si}}\mathbf{C} + Z_{u_{si}} \tag{A.58}$$

where

$$\mathbf{X}_{u_{si}} = \mathbf{X}_{u_c} - \mathbf{X}_{gi} - h_i\mathbf{X}_\theta \tag{A.59}$$

$$Z_{u_{si}} = Z_{u_c} - Z_g - h_i Z_\theta \tag{A.60}$$

A.3.2 Determination of internal forces

Once the displacement fields are defined, one can use the linear elastic relationship (Eq. (A.9)-Eq. (A.10)) to obtain the nodal forces.

$$N_{si} = \mathbf{Y}_{N_{si}}\mathbf{C} + R_{N_{si}}, \qquad i = 1, 2, \cdots n \tag{A.61}$$

$$N_c = \mathbf{Y}_{N_c}\mathbf{C} + R_{N_c} \tag{A.62}$$

$$M = \mathbf{Y}_M\mathbf{C} + R_M \tag{A.63}$$

$$V = \mathbf{Y}_V\mathbf{C} + R_V \tag{A.64}$$

where

$$\mathbf{Y}_{N_{si}} = (EA)_{si}\partial_x \mathbf{X}_{usi}, \qquad i = 1, 2, \cdots n \tag{A.65}$$

$$\mathbf{Y}_{N_c} = (EA)_c \partial_x \mathbf{X}_{uc}(x) \tag{A.66}$$

$$\mathbf{Y}_M = (EI)_0 \mathbf{X}_\kappa \tag{A.67}$$

$$\mathbf{Y}_V = \mathbb{I}_{2n+6} \tag{A.68}$$

$$R_{N_{sk}} = (EA)_{sk}\partial_x Z_{usk}, \qquad k = 1, 2, \cdots n \tag{A.69}$$

$$R_{N_c} = (EA)_c \partial_x Z_{uc} \tag{A.70}$$

$$R_M = (EI)_0 Z_\kappa \tag{A.71}$$

$$R_V = -p_y x \tag{A.72}$$

A.4 Exact stiffness matrix

The direct stiffness method is used to derive the exact stiffness of the hybrid beam with n embedded sections. It can be obtained starting from the general expressions of the internal force and displacement fields. Let a hybrid beam element of length L be considered. Since the same transverse displacement is assumed, this element has $(2n + 6)$ degrees of freedom, see Fig. A.3. Applying the kinematic boundary conditions at $x = 0$ and $x = L$ leads to the relationship between the vector of constants of integration $\mathbf{C}$ and the vector of nodal displacements $\mathbf{q}$ as follows:

$$\mathbf{q} = \mathbf{X}\,\mathbf{C} + \mathbf{Z} \tag{A.73}$$

where,

$$\mathbf{q} = [\ u_{\mathrm{s}1,0} \quad \cdots \quad u_{\mathrm{c},0} \quad v_{\mathrm{c},0} \quad \theta_0 \quad u_{\mathrm{s}1,L} \quad \cdots \quad u_{\mathrm{c},L} \quad v_{\mathrm{c},L} \quad \theta_L\ ]^{\mathrm{T}} \tag{A.74}$$

$$\mathbf{X} = [\ \mathbf{X}_{s1,0} \quad \cdots \quad \mathbf{X}_{\theta,0} \quad \mathbf{X}_{s1,L} \quad \cdots \quad \mathbf{X}_{\theta,L}\ ]^{\mathrm{T}} \tag{A.75}$$

$$\mathbf{Z} = [\ \mathbf{Z}_{s1,0} \quad \cdots \quad \mathbf{Z}_{\theta,0} \quad \mathbf{Z}_{s1,L} \quad \cdots \quad \mathbf{Z}_{\theta,L}\ ]^{\mathrm{T}} \tag{A.76}$$

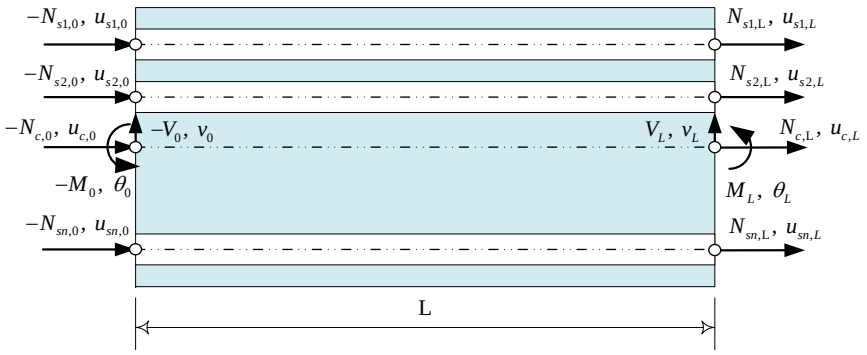

Figure A.3: Nodal forces and displacements of shear-rigid hybrid beam element.

The nodal displacements are independent, so the matrix $\mathbf{X}$ is reversible. Thus, the constants C_i are obtained in function of the nodal displacements q_i.

$$\mathbf{C} = \mathbf{X}^{-1}(\mathbf{q} - \mathbf{Z}) \tag{A.77}$$

The nodal forces can be expressed in compact form as:

$$\mathbf{Q} = \mathbf{Y}\mathbf{C} + \mathbf{R} \tag{A.78}$$

where,

$$\mathbf{Q} = [\ -N_{s1,0} \quad \cdots \quad -N_{c,0} \quad -V_0 \quad -M_0 \quad N_{s1,L} \quad \cdots \quad N_{c,L} \quad V_L \quad M_L\ ]^{\mathrm{T}} \tag{A.79}$$

$$\mathbf{Y} = [\ -\mathbf{Y}_{N_{s1,0}} \quad \cdots \quad -\mathbf{Y}_{N_{c,0}} \quad -\mathbf{Y}_{V_0} \quad -\mathbf{Y}_{M_0} \quad \mathbf{Y}_{N_{s1,L}} \quad \cdots \quad \mathbf{Y}_{N_{c,L}} \quad \mathbf{Y}_{V_L} \quad \mathbf{Y}_{M_L}\ ]^{\mathrm{T}} \tag{A.80}$$

$$\mathbf{R} = [\ -R_{N_{s1,0}} \quad \cdots \quad -R_{N_{c,0}} \quad -R_{V_0} \quad -R_{M_0} \quad R_{N_{s1,L}} \quad \cdots \quad R_{N_{c,L}} \quad R_{V_L} \quad R_{M_L}\ ]^{\mathrm{T}} \tag{A.81}$$

Introducing Eq. (A.77) in Eq. (A.78), one obtains:

$$\mathbf{K}\,\mathbf{q} = \mathbf{Q} + \mathbf{Q}_0 \tag{A.82}$$

where

$$\mathbf{K} = \mathbf{Y}\,\mathbf{X}^{-1} \tag{A.83}$$

represents the exact stiffness of the element and

$$\mathbf{Q}_0 = \mathbf{K}\mathbf{Z} - \mathbf{R} \tag{A.84}$$

represents the nodal force due to the uniform external load p_y.

A.5 Treatment on boundary conditions

Due to the choice of each cross-section centroid as the degree of liberty, the boundary conditions require a special treatment in the case concentrated external loads are applied elsewhere on the cross-section. Let us first consider that prescribed displacement or rotation are applied at node m_i on the encasing beam cross-section with the distance d_m from its centroid node c_i. This situation requires a rigid link between the nodes c_i and m_i and a change of degrees of freedom from $\mathbf{q}$ to $\mathbf{p}$ with

$$\mathbf{q} = [\ u_{\mathrm{s1},0} \quad \cdots \quad u_{\mathrm{c},0} \quad v_0 \quad \theta_0 \quad u_{\mathrm{s1},L} \quad \cdots \quad u_{\mathrm{c},L} \quad v_L \quad \theta_L\ ]^{\mathrm{T}} \tag{A.85}$$

and

$$\mathbf{p} = [\ u_{\mathrm{s1},0} \quad \cdots \quad u_{\mathrm{m},0} \quad v_{\mathrm{m},0} \quad \theta_0 \quad u_{\mathrm{s1},L} \quad \cdots \quad u_{\mathrm{c},L} \quad v_{\mathrm{c},L} \quad \theta_L\ ]^{\mathrm{T}} \tag{A.86}$$

The displacements of the node m_i can easily be obtained as

$$\begin{bmatrix} u_{\mathrm{m},0} \\ v_{\mathrm{m},0} \end{bmatrix} = \begin{bmatrix} u_{\mathrm{c},0} \\ v_0 \end{bmatrix} + \begin{bmatrix} \cos\theta_0 - 1 & -\sin\theta_0 \\ \sin\theta_0 & \cos\theta_0 - 1 \end{bmatrix} \begin{bmatrix} -\sin\beta_0 \\ \cos\beta_0 \end{bmatrix} d_{\mathrm{m}} \tag{A.87}$$

which gives the following expression for small rotation:

$$\begin{bmatrix} u_{\mathrm{m},0} \\ v_{\mathrm{m},0} \end{bmatrix} = \begin{bmatrix} u_{\mathrm{c},0} \\ v_0 \end{bmatrix} + \begin{bmatrix} 0 & -\theta_0 \\ \theta_0 & 0 \end{bmatrix} \begin{bmatrix} -\sin\beta_0 \\ \cos\beta_0 \end{bmatrix} d_{\mathrm{m}} \tag{A.88}$$

Differentiation of Eq. (A.88) gives

$$\begin{bmatrix} \delta u_{\mathrm{m},0} \\ \delta v_{\mathrm{m},0} \end{bmatrix} = \begin{bmatrix} \delta u_{\mathrm{c},0} \\ \delta v_0 \end{bmatrix} - \begin{bmatrix} \cos\beta_0 \\ \sin\beta_0 \end{bmatrix} d_{\mathrm{m}}\, \delta\theta_0 \tag{A.89}$$

The internal force vector $\mathbf{Q}$ and tangent stiffness matrix $\mathbf{K}$ are consistent with the displacement vector $\mathbf{q}$ such that

$$\delta\mathbf{Q} = \mathbf{K}\, \delta\mathbf{q} \tag{A.90}$$

Consider now that $\mathbf{q}$ is related to the displacement vector $\mathbf{p}$ through

$$\delta\mathbf{q} = \mathbf{B}_{qp}\, \delta\mathbf{p} \tag{A.91}$$

Then, by equating the virtual work in both systems, the internal force vector $\mathbf{P}$ consistent with $\mathbf{p}$ is defined by

$$\delta\mathbf{p}^{\mathrm{T}}\,\mathbf{P} = \delta\mathbf{q}^{\mathrm{T}}\,\mathbf{Q} \tag{A.92}$$

which, using Eq. (A.91), gives

$$\mathbf{P} = \mathbf{B}_{qp}^{\mathrm{T}}\,\mathbf{Q} \tag{A.93}$$

where the non zero terms in the matrix $\mathbf{B}_{qp}$ are

$$\mathbf{B}_{qp\,(k,k)} = 1 \qquad k = 1, 2, \cdots, 2n+6 \tag{A.94}$$

$$\mathbf{B}_{qp\,(n+1,n+3)} = \cos\beta_0\, d_{\mathrm{m}} \tag{A.95}$$

$$\mathbf{B}_{qp\,(n+2,n+3)} = \sin\beta_0\, d_{\mathrm{m}} \tag{A.96}$$

A.6 Numerical application

A.6.1 Simply supported sandwich beam subjected to uniformly distributed load

A simply supported sandwich beam of length 4, 000 mm subjected to a uniformly distributed load of identity $p_y = 10$ kN/m, see Fig. A.4, has been modeled using the direct stiffness approach within one element. The cross-section of the beam consists of a concrete core of rectangular cross-section having a width of 100 mm and a depth of 200 mm, reinforced by two steel plates of 20 mm thickness attached to the top and bottom surfaces of the concrete. The composite action between the concrete core and the steel plates is provided by shear connectors. The deformability of those shear connectors postulates the partial shear interaction behavior of the sandwich beam. The elastic modulus of concrete and steel plates considered in this example are respectively $E_c = 34.5$ kN/mm^2 and $E_s = 200$ kN/mm^2.

The distributions of the interlayer slips are shown in Fig. A.5 using shear connector stiffness $k_{sc1} = 40$ MPa and $k_{sc2} = 5$ MPa respectively at top and bottom

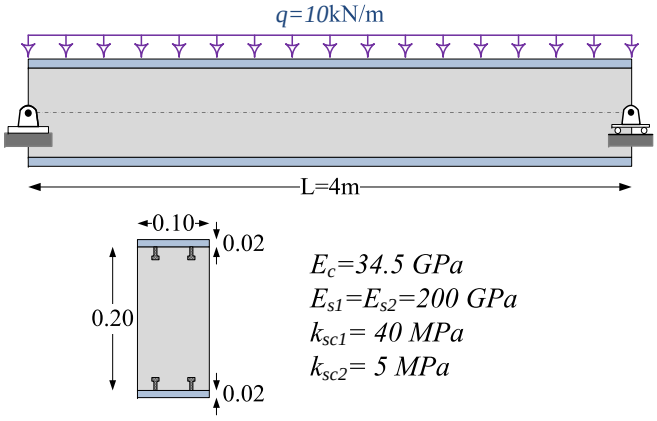

Figure A.4: Simply supported sandwich beam 4 m long subjected to a uniformly distributed load.

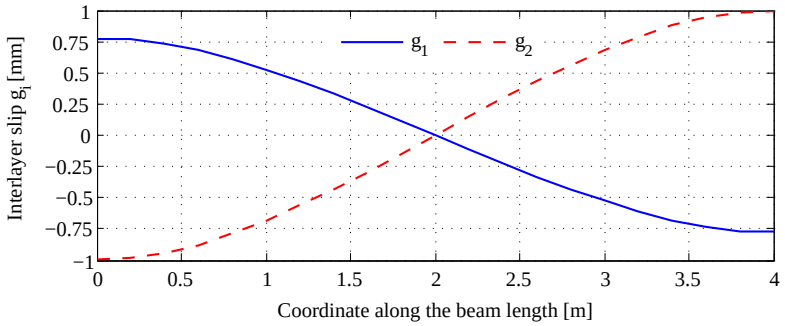

Figure A.5: Distributions of interlayer slips along the beam length.

surface of concrete core. An excellent agreement with the results of [42] is obtained. Furthermore, the effect of the degree of interaction has been investigated by considering different levels of the shear connector stiffness expressed in terms of dimensionless parameters k_1 and k_2 given by the following expression:

$$k_i = \sqrt{k_{sci}\left(\frac{1}{(EA)_{sci}} + \frac{h_i^2}{(EI)_0}\right)}L, \qquad i = 1, 2 \tag{A.97}$$

where the subscript "$i = 1$" represents the interface at top surface of concrete and "$i = 2$" for the one at bottom surface. Fig. A.6 and Fig. A.7 presents respectively the slip distributions at top and at bottom interface of the concrete core along the beam for a variety of dimensionless stiffness of the shear connections. As

expected, the interlayer slip decreases when its corresponding stiffness increases. The vertical displacement for all cases of shear connector stiffness is depicted in Fig. A.8. It can be seen that for the cases ($k_1 = 1$; $k_2 = 50$) and ($k_1 = 50$; $k_2 = 1$), the vertical displacements for each case are shown in the same curve. This is due to the symmetry of the system. The vertical displacement increases virtually with the decreasing connector stiffness.

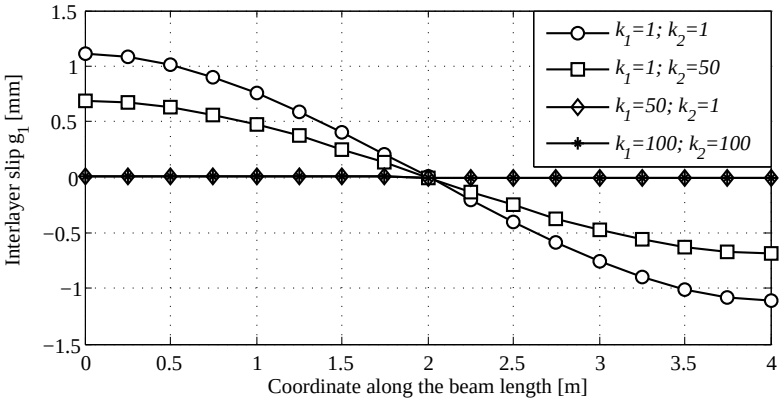

Figure A.6: Interlayer slip distribution for various shear connection stiffness.

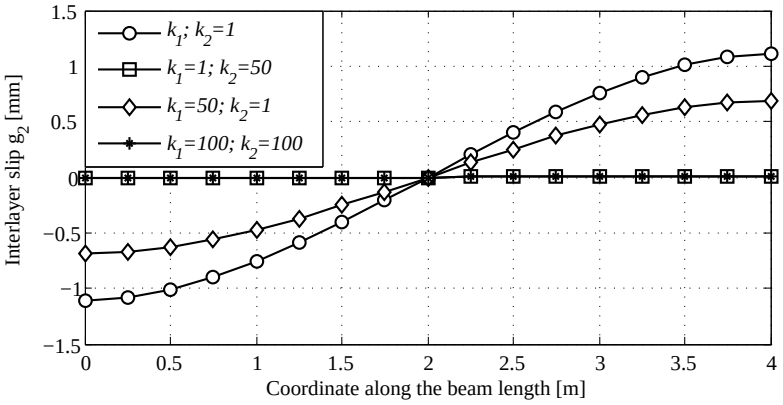

Figure A.7: Interlayer slip distribution for various shear connection stiffness.

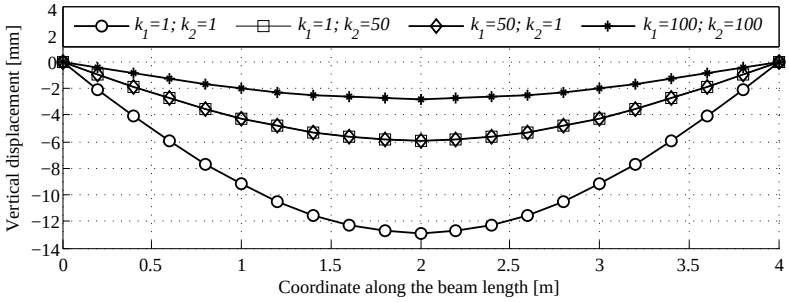

Figure A.8: Vertical displacement for various shear connection stiffness.

A.6.2 Hybrid column subjected to shear force

For this example, the analysis of elastic behavior of the concrete column with length of 10 m, having a width of 200 mm and a depth of 400 mm, reinforced by two steel profiles HEB100, see Fig. A.9, is performed using the direct stiffness approach within two elements based on the formulation developed in Section A.5. The column is subjected to a lateral load of 20 kN and compression axial force of 200 kN at free-end. The axial force is evenly distributed to concrete and steel sections through theirs axial stiffness. Two cases of the intermediate support are considered: one at the centroid of the concrete section (case A) and another one at the (outside) surface of the concrete section (case B). For case B, the eccentric node where the support is situated is linked rigidly to concrete node at centroid of the concrete cross-section. The composite behavior of the column in partial shear interaction is postulated by the deformability of shear connectors placed at the interfaces between those two materials. The elastic modulus of concrete and steel profiles considered in this example are respectively $E_c = 34.5$ kN/mm^2 and $E_s = 210$ kN/mm^2 and the shear connector stiffness $k_{sc1} = k_{sc2} = 3.87$ MPa are used at both interfaces. One can observe from Fig. A.10 that the position of the intermediate support influences the lateral deflection of the column. The column deflects more in case B where the support is located at the outside surface of the

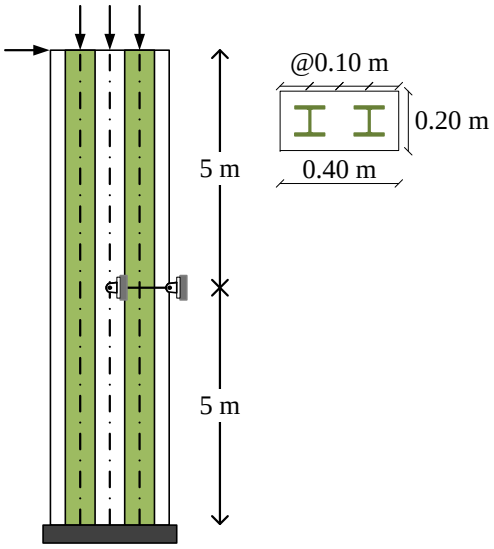

Figure A.9: Hybrid column with intermediate support.

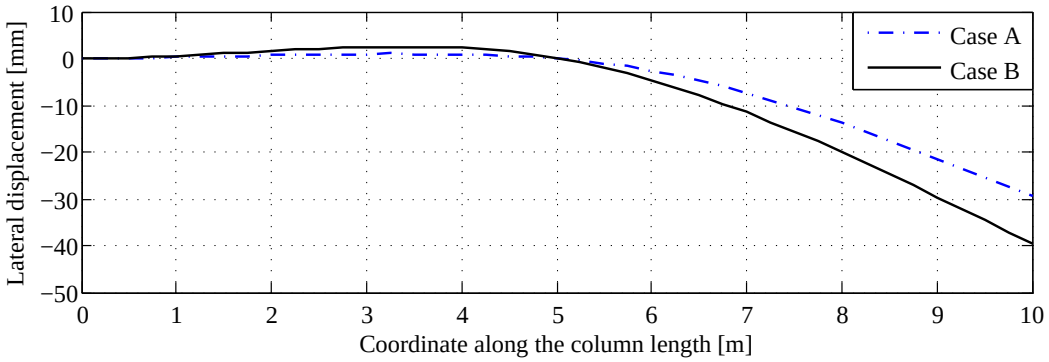

Figure A.10: Lateral displacement along the column length for each case.

cross-section. Nevertheless, the rotation and interlayer slip g_2 at free end in case B are reduced significantly comparing to case A, see respectively Fig. A.11 and Fig. A.12. This is due to the change of axial displacement of concrete component while the intermediate support is placed at outside surface, see Fig. A.13.

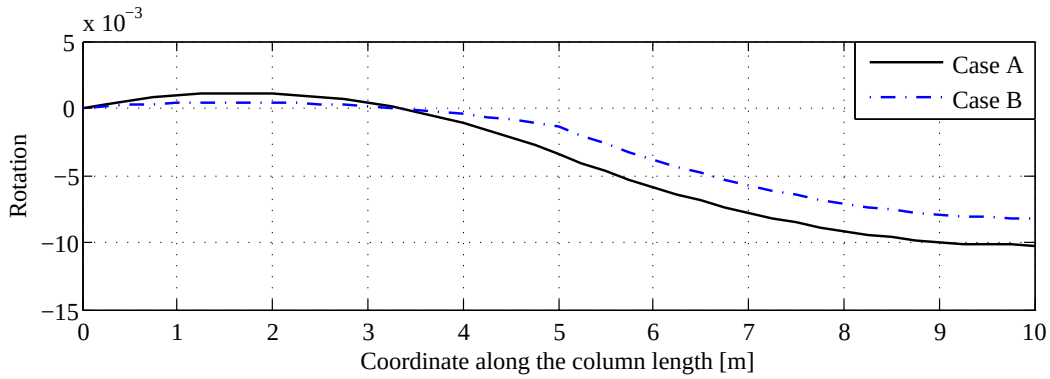

Figure A.11: Rotation along the column length for each case.

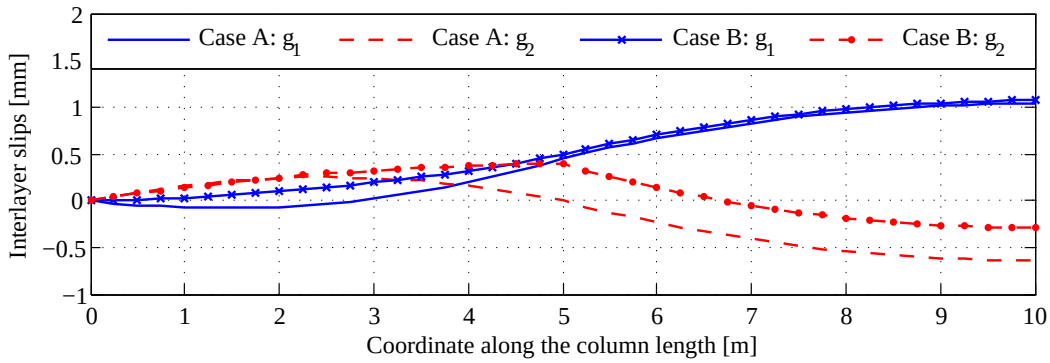

Figure A.12: Interlayer slips along the column length for each case.

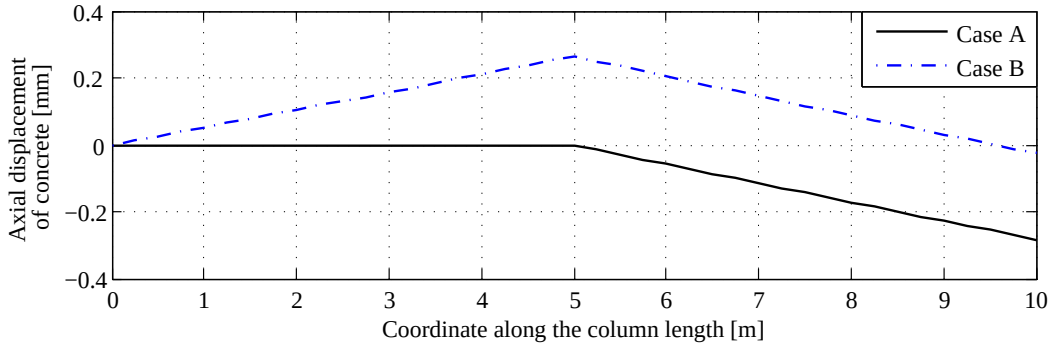

Figure A.13: Axial displacement of concrete component along the column length for each case.

A. GEOMETRICALLY ELASTIC LINEAR SHEAR-RIGID HYBRID BEAM MODEL

Appendix B

Geometrically nonlinear shear-rigid hybrid beam model

***

B.1 Introduction

In order to analyze the behavior of slender hybrid columns, a planar beam-column finite element formulation was developed based on Euler-Bernoulli kinematics and fiber cross-section discretisation. The co-rotational approach is adopted to take into account the geometry nonlinearity of the problem. The developed FE model is capable to consider the following aspects: a cross-section with more than one steel section in partial interaction; geometrical and material nonlinearities; initial imperfection; residual stresses; and concrete confinement. For the sake of clarity the FE formulation is presented for the case of hybrid column with two encased steel profiles. However, the concepts are also applicable to general case of several encased steel profiles. A more detailed deduction can be found in [149].

Let us consider a planar element with two steel sections fully encased in concrete and including shear connectors at the contact interface uniformly distributed along the element length. It is assumed that the interlayer slip can occur at the interface but there is no uplift. For the present case, the element has 10 global degrees of freedom in the fixed global coordinate system: global displacements

and rotation of the nodes (c_i and c_j) and slips (g_{ki}, g_{kj}) between the steel node s_k and concrete node $c_{i;j}$. Since all component are bent according to Euler-Bernoulli kinematics, the rotation of all components (steel sections and concrete section) at the end nodes are equal and that the slips (g_{ki}, g_{kj}) are perpendicular to the end cross-sections. The vector of global nodal displacements is defined by

$$\mathbf{p}_g = [\, u_{ci}\ v_{ci}\ \theta_i\ g_{1i}\ g_{2i}\ u_{cj}\ v_{cj}\ \theta_j\ g_{1j}\ g_{2j}]^{\mathrm{T}} \tag{B.1}$$

Due to the presence of the three rigid body modes in the global coordinate system, the corresponding element stiffness matrix is singular. Therefore, the linear local element is derived in the local system (x_l, y_l) without rigid body modes. The latter translates and rotates with the element as the deformation proceeds. In this local system, the element has seven degrees of freedom and the vector of local displacements is defined as

$$\mathbf{p}_l = [\bar{u}_{s1i}\ \bar{u}_{s2i}\ \bar{\theta}_i\ \bar{u}_{s1j}\ \bar{u}_{s2j}\ \bar{u}_{cj}\ \bar{\theta}_j] \tag{B.2}$$

B.2 Co-rotational formulation

The origin of the local coordinate system is taken at node c_i and the x_l-axis of the local coordinate system is defined by the line connecting the nodes c_i and c_j. These nodes are chosen to be at the centroid of concrete section in order to easily derive the kinematic relationships between the global nodal displacements and the local ones. The y_l-axis is perpendicular to the x_l-axis so that the result is a right-handed orthogonal coordinate system. The motion of the element from the original undeformed configuration to the actual deformed one can thus be separated in two parts. The first one, which corresponds to the rigid motion of the local frame, is described by the translation of the node c_i and the rigid rotation of the axes. The deformational part of the motion is always small in the local coordinate system and a geometrical linear element will be used.

According to the notations defined in Fig. B.1, the components of the local

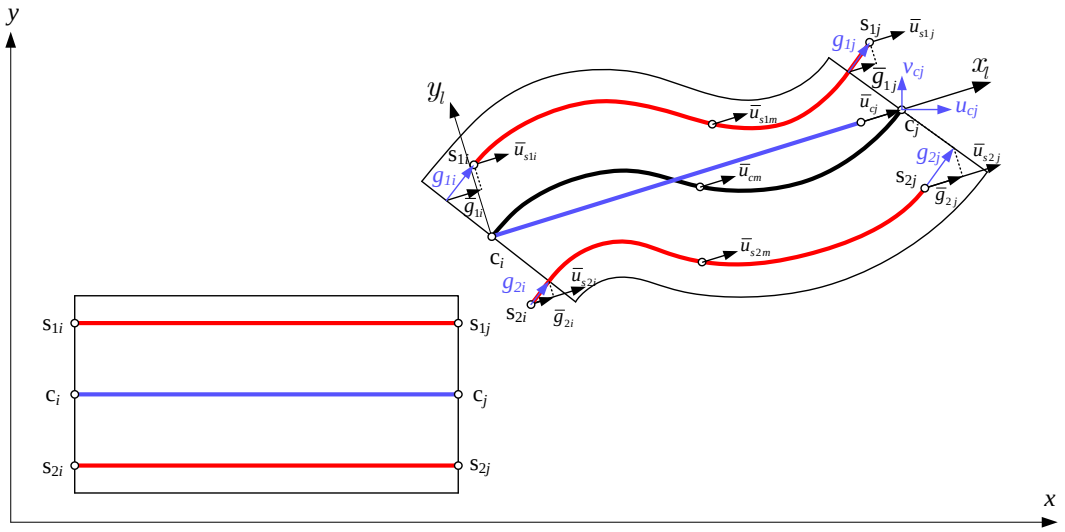

Figure B.1: Degrees of freedom and co-rotational kinematics.

displacement vector $\mathbf{p}_l$ can be computed from those of the global vector $\mathbf{p}_g$ as

$$\bar{u}_{\mathrm{c}j} = l_n - l_o \tag{B.3}$$

$$\bar{\theta}_i = \theta_i + \beta_o - \beta \tag{B.4}$$

$$\bar{\theta}_j = \theta_j + \beta_o - \beta \tag{B.5}$$

$$\bar{u}_{\mathrm{sk}i} = g_{\mathrm{k}i}\,\cos\bar{\theta}_i - h_{\mathrm{k}}\,\bar{\theta}_i \text{ with } k = 1 \text{ or } 2 \tag{B.6}$$

$$\bar{u}_{\mathrm{sk}j} = g_{\mathrm{k}j}\,\cos\bar{\theta}_j - h_{\mathrm{k}}\,\bar{\theta}_j \text{ with } k = 1 \text{ or } 2 \tag{B.7}$$

where

$$\cos\beta_o = \frac{1}{l_o}\left(x_{\mathrm{c}j} - x_{\mathrm{c}i}\right) \tag{B.8}$$

$$\sin\beta_o = \frac{1}{l_o}\left(y_{\mathrm{c}j} - y_{\mathrm{c}i}\right) \tag{B.9}$$

$$\cos\beta = \frac{1}{l_n}\left(x_{\mathrm{c}j} + u_{\mathrm{c}j} - x_{\mathrm{c}i} - u_{\mathrm{c}i}\right) \tag{B.10}$$

$$\sin\beta = \frac{1}{l_n}\left(y_{\mathrm{c}j} + v_{\mathrm{c}j} - y_{\mathrm{c}i} - v_{\mathrm{c}i}\right) \tag{B.11}$$

and l_o and l_n being the element length in initial and deformed configuration, respectively:

$$l_o = \sqrt{(x_{\mathrm{c}j} - x_{\mathrm{c}i})^2 + (y_{\mathrm{c}j} - y_{\mathrm{c}i})^2} \tag{B.12}$$

$$l_n = \sqrt{(x_{cj} + u_{cj} - x_{ci} - u_{ci})^2 + (y_{cj} + v_{cj} - y_{ci} - v_{ci})^2} \tag{B.13}$$

As can be seen from Eqs. (B.3) to (B.7), the local displacement vector $\mathbf{p}_l$ can be expressed as functions of the global one $\mathbf{p}_g$, i.e.:

$$\mathbf{p}_l = \mathbf{p}_l(\mathbf{p}_g) \tag{B.14}$$

Then, $\mathbf{p}_l$ is used to compute the internal force vector $\mathbf{f}_l$ and the tangent stiffness matrix $\mathbf{K}_l$ in the local system. Note that $\mathbf{f}_l$ and $\mathbf{K}_l$ depend only on the definition of the local strains and not on the particular form of Eq. (B.14). The transformation matrix $\mathbf{B}_{lg}$ between the local and global displacements is defined by:

$$\delta\mathbf{p}_l = \mathbf{B}_{lg}\delta\mathbf{p}_g \tag{B.15}$$

and is obtained by differentiation of Eq. (B.14). The global internal force vector $\mathbf{f}_g$ and the global tangent stiffness matrix $\mathbf{K}_g$, consistent with $\mathbf{p}_g$, can be obtained by equating the internal virtual work in both the global and the local system, i.e.:

$$\mathbf{f}_g = \mathbf{B}_{lg}^{\mathrm{T}}\mathbf{f}_l \qquad \mathbf{K}_g = \mathbf{B}_{lg}^{\mathrm{T}}\mathbf{K}_l\mathbf{B}_{lg} + \mathbf{H}_{lg} \qquad \mathbf{H}_{lg} = \left.\frac{\partial(\mathbf{B}_{lg}^{\mathrm{T}}\mathbf{f}_l)}{\partial\mathbf{p}_g}\right|_{\mathbf{f}_l} \tag{B.16}$$

$$\mathbf{B}_{lg}^{\mathrm{T}} = \begin{bmatrix} \frac{-s\,\lambda_{1i}}{l_n} & \frac{-s\,\lambda_{2i}}{l_n} & \frac{-s}{l_n} & \frac{c}{l_n} & \frac{-s\,\lambda_{1i}}{l_n} - c & -c & \frac{-s}{l_n} \\ \frac{c\,\lambda_{1i}}{l_n} & \frac{c\,\lambda_{2i}}{l_n} & \frac{c\,\lambda_{1i}}{l_n} - s & \frac{c\,\lambda_{2i}}{l_n} - s & \frac{c\,\lambda_{1i}}{l_n} - s & -s & \frac{c}{l_n} \\ \lambda_{1i} & \lambda_{2i} & 1 & 0 & 0 & 0 & 0 \\ -\cos(\theta_i - \alpha) & 0 & 0 & 0 & 0 & 0 & 0 \\ 0 & -\cos(\theta_i - \alpha) & 0 & 0 & 0 & 0 & 0 \\ \frac{s\,\lambda_{1i}}{l_n} & \frac{s\,\lambda_{2i}}{l_n} & \frac{s}{l_n} & \frac{s\,\lambda_{1j}}{l_n} + c & \frac{s\,\lambda_{2i}}{l_n} + c & c & \frac{s}{l_n} \\ \frac{-c\,\lambda_{1i}}{l_n} & \frac{-c\,\lambda_{2i}}{l_n} & \frac{-c}{l_n} & \frac{-c\,\lambda_{1j}}{l_n} + s & \frac{-c\,\lambda_{2j}}{l_n} + s & s & \frac{-c}{l_n} \\ 0 & 0 & 0 & \lambda_{1j} & \lambda_{1j} & 0 & 1 \\ 0 & 0 & 0 & -\cos(\theta_j - \alpha) & 0 & 0 & 0 \\ 0 & 0 & 0 & 0 & -\cos(\theta_j - \alpha) & 0 & 0 \end{bmatrix} \tag{B.17}$$

$$\mathbf{H}_{lg} = \frac{\omega_1\, z^{\mathrm{T}}}{l_n} + \omega_2\, r^{\mathrm{T}} + \omega_3\, t_{1i}^{\mathrm{T}} + \omega_3\, t_{2i}^{\mathrm{T}} + \omega_5\, t_{1j}^{\mathrm{T}} + \omega_6\, t_{2j}^{\mathrm{T}} + \omega_7\, \mathrm{I}_3^{\mathrm{T}} + \omega_8\, \mathrm{I}_8^{\mathrm{T}} \tag{B.18}$$

where

$$\omega_1 = \left[\, \xi_1 \;\; \xi_2 \;\; 0 \;\; -\sin(\theta_i-\alpha)\, f_l(1) \;\; -\sin(\theta_i-\alpha)\, f_l(2) \;\; -\xi_1 \;\; -\xi_2 \;\; 0 \;\; -\sin(\theta_i-\alpha)\, f_l(4) \;\; -\sin(\theta_i-\alpha)\, f_l(5) \,\right] \tag{B.19}$$

$$\omega_2 = \left[\; \xi_1 \;\; \xi_2 \;\; 0 \;\; 0 \;\; 0 \;\; \xi_1 \;\; \xi_2 \;\; 0 \;\; 0 \;\; 0 \;\right] \tag{B.20}$$

$$\omega_3 = \left[\; -\tfrac{s}{l_n} \;\; \tfrac{c}{l_n} \;\; 1 \;\; 0 \;\; 0 \;\; \tfrac{s}{l_n} \;\; -\tfrac{c}{l_n} \;\; 0 \;\; 0 \;\; 0 \;\right] f_l(1) \tag{B.21}$$

$$\omega_4 = \left[\; -\tfrac{s}{l_n} \;\; \tfrac{c}{l_n} \;\; 1 \;\; 0 \;\; 0 \;\; \tfrac{s}{l_n} \;\; -\tfrac{c}{l_n} \;\; 0 \;\; 0 \;\; 0 \;\right] f_l(2) \tag{B.22}$$

$$\omega_5 = \left[\; -\tfrac{s}{l_n} \;\; \tfrac{c}{l_n} \;\; 0 \;\; 0 \;\; 0 \;\; \tfrac{s}{l_n} \;\; -\tfrac{c}{l_n} \;\; 1 \;\; 0 \;\; 0 \;\right] f_l(4) \tag{B.23}$$

$$\omega_6 = \left[\; -\tfrac{s}{l_n} \;\; \tfrac{c}{l_n} \;\; 0 \;\; 0 \;\; 0 \;\; \tfrac{s}{l_n} \;\; -\tfrac{c}{l_n} \;\; 1 \;\; 0 \;\; 0 \;\right] f_l(5) \tag{B.24}$$

$$\omega_7 = \left[\; 0 \;\; 0 \;\; 0 \;\; \sin(\theta_i-\alpha)\, f_l(1) \;\; \sin(\theta_i-\alpha)\, f_l(2) \;\; 0 \;\; 0 \;\; 0 \;\; 0 \;\; 0 \;\right] \tag{B.25}$$

$$\omega_8 = \left[\; 0 \;\; 0 \;\; 0 \;\; 0 \;\; 0 \;\; 0 \;\; 0 \;\; 0 \;\; \sin(\theta_j-\alpha)\, f_l(4) \;\; \sin(\theta_j-\alpha)\, f_l(5) \;\right] \tag{B.26}$$

$$t_{1i} = \left[\; 0 \;\; 0 \;\; g_{1i}\cos(\theta_i-\alpha) \;\; \sin(\theta_i-\alpha) \;\; 0 \;\; 0 \;\; 0 \;\; 0 \;\; 0 \;\; 0 \;\right] - g_{1i}\cos(\theta_i-\alpha)\tfrac{z}{l_n} \tag{B.27}$$

$$t_{2i} = \left[\; 0 \;\; 0 \;\; g_{2i}\cos(\theta_i-\alpha) \;\; 0 \;\; \sin(\theta_i-\alpha) \;\; 0 \;\; 0 \;\; 0 \;\; 0 \;\; 0 \;\right] - g_{2i}\cos(\theta_i-\alpha)\tfrac{z}{l_n} \tag{B.28}$$

$$t_{1j} = \left[\; 0 \;\; 0 \;\; 0 \;\; 0 \;\; 0 \;\; 0 \;\; 0 \;\; g_{1j}\cos(\theta_j-\alpha) \;\; \sin(\theta_i-\alpha) \;\; 0 \;\right] - g_{1j}\cos(\theta_j-\alpha)\tfrac{z}{l_n} \tag{B.29}$$

$$t_{2j} = \left[\; 0 \;\; 0 \;\; 0 \;\; 0 \;\; 0 \;\; 0 \;\; 0 \;\; g_{2j}\cos(\theta_j-\alpha) \;\; 0 \;\; \sin(\theta_i-\alpha) \;\right] - g_{2j}\cos(\theta_j-\alpha)\tfrac{z}{l_n} \tag{B.30}$$

$$z = \left[\; s \;\; -c \;\; 0 \;\; 0 \;\; 0 \;\; -s \;\; c \;\; 0 \;\; 0 \;\; 0 \;\right] \tag{B.31}$$

$$r = \left[\; -c \;\; -s \;\; 0 \;\; 0 \;\; 0 \;\; c \;\; s \;\; 0 \;\; 0 \;\; 0 \;\right] \tag{B.32}$$

$$\mathrm{I}_3 = \left[\; 0 \;\; 0 \;\; 1 \;\; 0 \;\; 0 \;\; 0 \;\; 0 \;\; 0 \;\; 0 \;\; 0 \;\right] \tag{B.33}$$

$$\mathrm{I}_8 = \left[\; 0 \;\; 0 \;\; 0 \;\; 0 \;\; 0 \;\; 0 \;\; 0 \;\; 1 \;\; 0 \;\; 0 \;\right] \tag{B.34}$$

The choice of the slips as the degrees of freedom is indispensable for the robustness of the FE formulation. Due to this choice (see Eq. (B.1)) the boundary conditions require a special treatment in case external concentrated loads are not applied to the node located at the centroid of the column cross-section (origin of the local frame) but somewhere else on the cross-section.

Let us consider (see Fig. B.2) that prescribed displacement or rotation is applied at node m_i. This situation requires a rigid link between the nodes c_i and

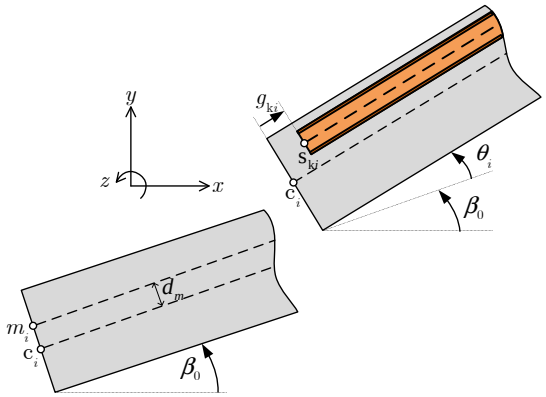

Figure B.2: Eccentric nodes in co-rotational frame.

m_i and a change of degrees of freedom from $\mathbf{p}_g$ to $\mathbf{p}_m$ with

$$\mathbf{p}_m = [\ u_{\mathrm{m}i}\quad v_{\mathrm{m}i}\quad \theta_i\quad g_{1i}\quad g_{2i}\quad u_{\mathrm{c}j}\quad v_{\mathrm{c}j}\quad \theta_j\quad g_{1j}\quad g_{2j}\ ]^{\mathrm{T}} \tag{B.35}$$

The internal force vector and tangent stiffness matrix consistent with $\mathbf{p}_m$ are then obtained by using the transformation matrix $\mathbf{B}_{gm}$. This gives

$$\delta\mathbf{p}_g = \mathbf{B}_{gm}\,\delta\mathbf{p}_m \quad \mathbf{f}_m = \mathbf{B}_{gm}^{\mathrm{T}}\,\mathbf{f}_g \quad \mathbf{K}_m = \mathbf{B}_{gm}^{\mathrm{T}}\,\mathbf{K}_g\,\mathbf{B}_{gm} + \mathbf{H}_{gm} \tag{B.36}$$

with

$$\mathbf{B}_{gm\,(k,k)} = 1 \text{ with } k = 1, 2, \cdots, 10 \tag{B.37}$$

$$\mathbf{B}_{gm\,(1,3)} = \cos(\beta_o + \theta_i)\,d_{\mathrm{m}} \tag{B.38}$$

$$\mathbf{B}_{gm\,(2,3)} = \sin(\beta_o + \theta_i)\,d_{\mathrm{m}} \tag{B.39}$$

and the only non zero term in the matrix $\mathbf{H}_{gm}$ is

$$\mathbf{H}_{gm\,(3,3)} = -\sin(\beta_o + \theta_i)\,d_{\mathrm{m}}\,f_g(1) + \cos(\beta_o + \theta_i)\,d_{\mathrm{m}}\,f_g(2) \tag{B.40}$$

B.3 Local displacement-based element

The geometrically linear element is derived in the local system (x_l, y_l). The local element has ten degrees of freedom (see Fig. B.3). The transverse displacement $\bar{v}$

is approximated using cubic Hermite interpolations. In order to avoid the curvature locking, three internal nodes (one for each component) are added in order to use quadratic shape function for axial displacement interpolation. However, for saving the calculation time, three degrees of freedom corresponding to the internal nodes will be statically condensed out thereafter to obtain the local displacement vector containing only the degrees of freedom at the element ends. The material

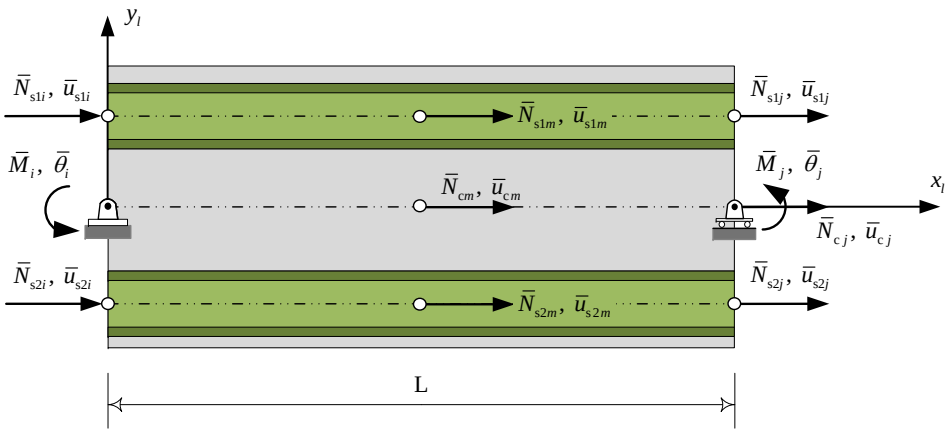

Figure B.3: Degree of freedoms of local linear element with two encased steel profiles.

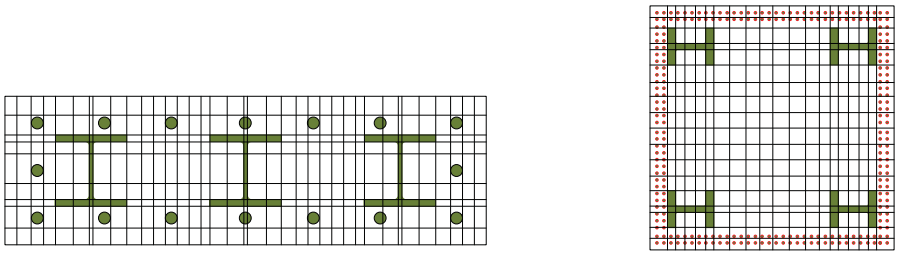

(a) Hybrid column with three encased steel profiles.

(b) Mega column with four encased steel profiles.

Figure B.4: Fiber discretization of sections.

non-linearity is taken into account by adopting the distributed plasticity model

with fiber section discretization (see Fig. B.4). Each fiber is fed with a uniaxial constitutive model.

B.4 Comparison against the experimental results

To the best of our knowledge, there is no available experimental results for buckling test on RC column with multi-embedded steel profiles (hybrid columns) in technical literature. Nevertheless, a couple of experimental compression-bending tests on steel-concrete shear walls with vertical steel encased profiles was conducted by Dan et al. [8] and by Zhou et al. [7]. The dimensions of the tested specimens are such that they cannot be considered as slender columns. Therefore, the developed finite element model is validated by comparing its prediction against ten test results of eccentrically loaded slender composite columns [150, 151] and six test results of short composite columns [152]. For the sake of clarity, in this study we denote seven specimens tested by Al-Shahari et al. [150] as CESC1-CESC7, three specimens tested by Morino et al. [151] as CESC8-CESC10, and six concrete encased steel composite short columns tested by Chen and Yeh [152] as SCESC1-SCESC6. The geometrical and material properties of the above-mentioned specimens are summarized in Table B.1 .

All composite column specimens are pinned at both ends. The columns CESC1-CESC10 are loaded with the same eccentricity at both extremities. The concrete region is subdivided into three parts as suggested by Mirza and Skrabek [153]. The highly confined concrete zone is taken from the web of the steel section to each flange, and the partially confined concrete zone is from the parabolic border of the highly confined concrete zone to the centerlines of the transverse reinforcement as illustrated in Fig. B.5. The confinement factor for highly confined concrete varied from 1.10 to 1.97 and for partially confined concrete varied from

Table B.1: Specimen dimensions and material properties.

Specimen	B×D (mm)	kL (mm)	Structural steel	Long. bar	e/D	f_c (MPa)	f_y (MPa)	f_s (MPa)
CESC1	230×230	2000	H100×96×5×8	4ϕ12	0.3	20.5[a]	337	459
CESC2	230×230	2000	H100×96×5×8	4ϕ12	0.3	13.7[a]	337	459
CESC3	230×230	2000	H140×133×5.5×8	4ϕ12	0.3	20.5[a]	307	459
CESC4	230×230	2000	H140×133×5.5×8	4ϕ12	0.3	28.2[a]	307	459
CESC5	230×230	3000	H140×133×5.5×8	4ϕ12	0.3	28.2[a]	307	459
CESC6	230×230	3000	H100×96×5×8	4ϕ12	0.17	20.5[a]	337	459
CESC7	230×230	3000	H100×96×5×8	4ϕ12	0.17	13.7[a]	337	459
CESC8	160×160	960	H100×100×6×8	4ϕ6	0.25	21.1[a]	345	460
CESC9	160×160	2400	H100×100×6×8	4ϕ6	0.25	23.4[a]	345	460
CESC10	160×160	3600	H100×100×6×8	4ϕ6	0.25	23.3[a]	345	460
SCESC1	280×280	1200	H150×150×7×10	12ϕ16	0.0	29.5[b]	296	350
SCESC2	280×280	1200	H150×150×7×10	12ϕ16	0.0	28.1[b]	296	350
SCESC3	280×280	1200	H150×150×7×10	12ϕ16	0.0	29.8[b]	296	350
SCESC4	280×280	1200	H150×75×5×7	12ϕ16	0.0	28.1[b]	303	350
SCESC5	280×280	1200	H150×75×5×7	12ϕ16	0.0	26.4[b]	303	350
SCESC6	280×280	1200	H150×75×5×7	12ϕ16	0.0	29.8[b]	303	350

[a]Concrete cube strength

[b]Concrete cylinder strength

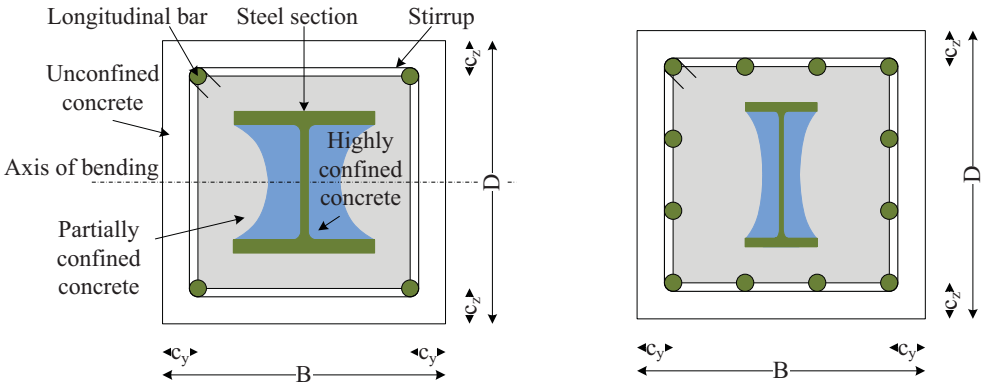

(a) Specimen CESC1-CESC10.

(b) Specimen SCESC1-SCESC6.

Figure B.5: Specimen dimension and regions for unconfined, partially confined and highly confined concrete.

1.08 to 1.50 depending on spacing of the stirrups, as given by [154]. The concrete outside the ties is not confined. The effect of residual stresses in structural steel

is included and the initial imperfection is taken equal to $l_0/1000$ in which l_0 is the effective length.

For all numerical simulations, the modified concrete stress-strain model proposed by Kent and Park [87] in compression is adopted. For concrete in tension, linear stress-strain relationship up to tensile strength and linear tensile softening with fracture energy 0.12 N/mm are assumed. The stress-strain relationships of structural steel recommended by EC3 [58] and reinforcing bar recommended by EC2 [11] are adopted. All test specimens are modeled with the developed FE model using 6 elements. In Table B.2, the predictions of the model are compared against test results. A good agreement between numerical and experimental results can be observed. Indeed, the mean value of numerical-experimental load capacity ratio for sixteen cases is very close to 1 and the corresponding standard deviation is only 6%. Furthermore, it is worth to mention that, in most cases, the FE model predictions are on the safe side.

Table B.2: Comparison between tests and finite element results.

Specimen	$\bar{\lambda}$	P_{Test} [kN]	P_{FE} [kN]	P_{FE}/P_{Test}
CESC1[150]	0.36	654	641	0.98
CESC2[150]	0.34	558	553	0.99
CESC3[150]	0.34	962	813	0.85
CESC4[150]	0.36	949	924	0.97
CESC5[150]	0.55	900	822	0.91
CESC6[150]	0.54	813	764	0.94
CESC7[150]	0.51	704	646	0.92
CESC8[151]	0.25	740	600	0.81
CESC9[151]	0.63	504	493	0.98
CESC10[151]	0.95	412	378	0.92
SCESC1[152]	0.19	4220	4261	1.01
SCESC2[152]	0.19	4228	4239	1.00
SCESC3[152]	0.19	4399	4641	1.06
SCESC4[152]	0.19	3788	3606	0.95
SCESC5[152]	0.18	3683	3615	0.98
SCESC6[152]	0.19	3893	3873	0.99
Mean	-	-	-	0.95
Cov	-	-	-	0.06

B. GEOMETRICALLY NONLINEAR SHEAR-RIGID HYBRID BEAM MODEL

Appendix C

Simple design tool - HBCol

***

C.1 Description of the program

A freeware program accessible at `http://hybridcolumnstruc.weebly.com/`, HBCol is a simple design tool capable to perform the nonlinear analysis of hybrid column reinforced by several embedded steel profiles subjected to combined axial load and uni-axial bending moment. The users are also able to carry out a new design method proposed by the author to accurately predict the ultimate load of hybrid columns. Moreover, a nonlinear analysis of reinforced concrete column is also available by choosing "Without Steel Section" in Steel Section Panel/Choose Box.

In this program, co-rotational framework is used for a large displacement analysis. The advantage of using the co-rotational approach is that the geometrical linear finite element formulation can be reused and automatically be transformed into geometrical nonlinear formulation. In local frame, the hybrid column with three encased steel profiles is divided into 4 sub-elements: 3 for structural steel profiles and 1 for reinforced concrete. This division leads to 16 degrees of freedom for one element where the internal nodes for axial displacement have been introduced to avoid shear locking problem. Eurocode 2 and 4 material laws for steel profile, rebar as well as concrete are adopted to take into account the non-

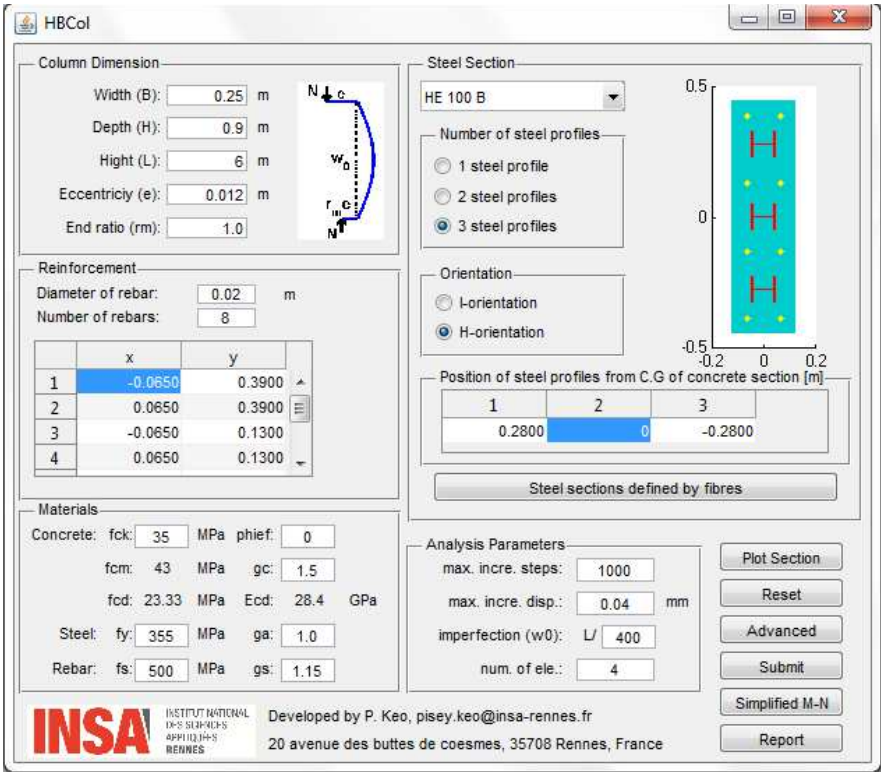

Figure C.1: Interface of HBCol program.

linear material effect. The residual stresses in steel profiles are considered. In this first version, the slips between steel and concrete component at extremities of the member are constraint to zero and the full interaction is assumed by providing relatively high rigidity of the connector. The relatively high rigidity of the connector is determined by:

$$k_{sc} = \frac{E_{cm}\, A_g}{b\, l} \tag{C.1}$$

where E_{cm}, A_g, b and l are respectively elastic modulus of concrete, area of cross-section, width of cross-section and column height.

The new design method is developed within the context of Eurocodes, i.e. moment magnification approach. In the new method, new expressions for the correction factors (for the determination of effective flexural stiffness EI of the column) are proposed, see Section 6.4.2 in order to take into account the creep effect and the

effect of plastification of steel profiles.

C.2 Input data

The program requires some basic input data like geometry of the column, the arrangement of reinforcing bar, steel section, material properties and parameters for the analysis, see Fig. C.1. Besides, the user may also define steel shapes by fibers for the simplified analysis. However, the steel shapes defined by fibers are not considered in the nonlinear FE analysis.

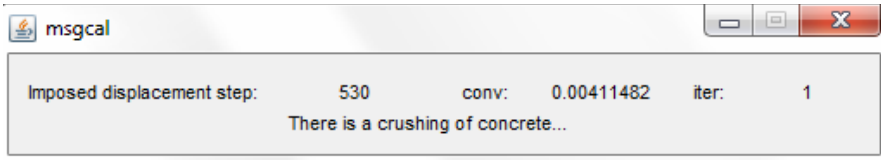

Figure C.2: Message box.

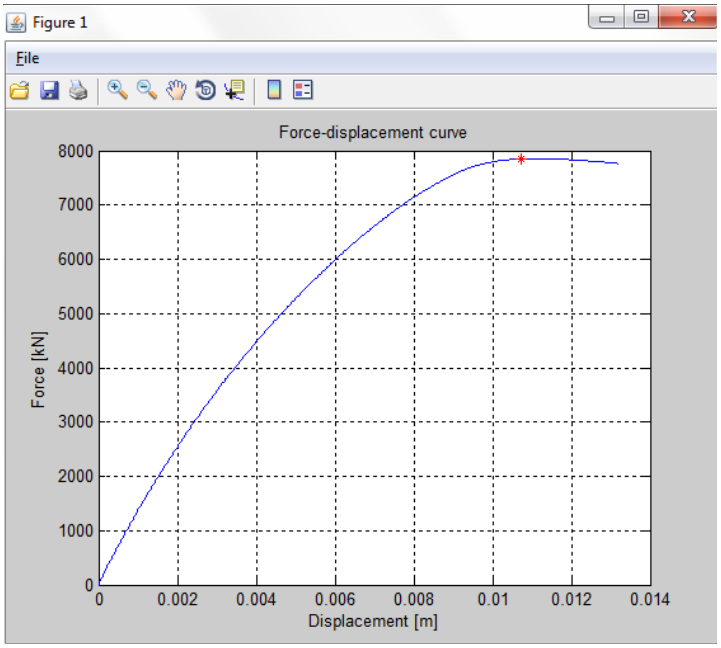

Figure C.3: Load-displacement curve.

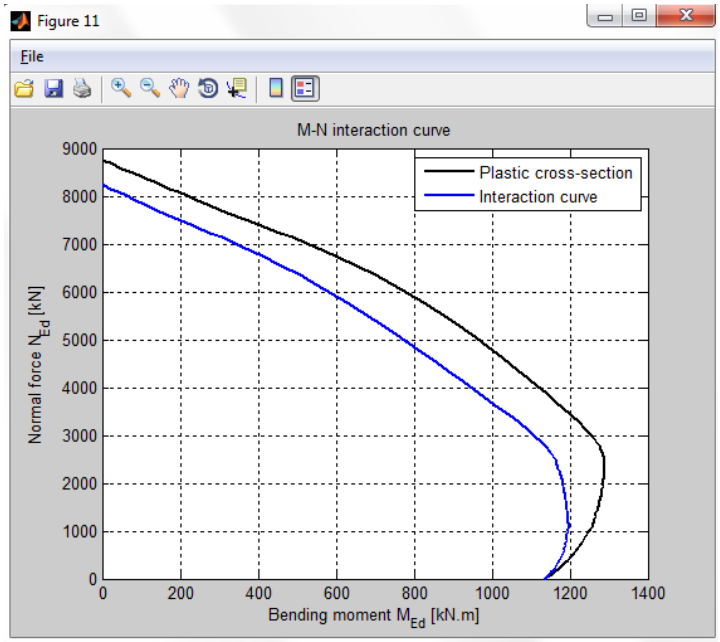

Figure C.4: M-N interaction.

C.3 Result of analysis

Whilst the nonlinear FE analysis is performed, the message box Fig. C.2 is appeared stating that the analysis is being executed. The nonlinear FE analysis is terminated if the non convergence is occurred or the imposed displacement step reaches a certain number after the peak load. Then, the load-displacement curve is provided, see Fig. C.3. Fig. C.4 shows the result of simplified method. Two curves are provided. The black one corresponds to the plastic resistance of hybrid/rc cross-section using pivot method. The blue one represents the M-N interaction curve provided by the new design method.

C.4 Report of analysis

When the analysis of hybrid column has been performed, the user is able to generate the report file given in the form of html format.

Chapter 8

Résumé en français

***

A short summary of the thesis in french.

8.1 Introduction

Dans les immeubles de grande hauteur en béton armé, les poteaux et les murs sont souvent renforcés par plusieurs profils acier noyés dans le béton car le renforcement traditionnel par les barres d'armature n'est plus suffisant. Ces éléments, qualifiés d'hybrides, ne peuvent être traités par les règlements relatifs aux structures en béton armé tels que l'Eurocode 2 [11], ni par les règlements dédiés aux structures mixtes comme l'Eurocode 4 [12] qui couvrent le cas des éléments contenant un seul profil métallique.

Dès lors, bien que de tels éléments soient utilisés régulièrement, les praticiens ne disposent d'aucun règlement applicable pour leur dimensionnement. Le projet de recherche Européen RFCS SMART COmposite COnstruction a pour objectif de combler ce vide, par la rédaction d'un guide de dimensionnement pour les éléments hybrides en s'appuyant sur une recherche théorique et expérimentale. Le travail de cette thèse s'inscrit dans ce projet d'envergure et apporte une contribution au volet théorique et numérique de cette recherche. Ce travail a but

de développer un outil de simulation et une méthode de dimensionnement dédiée aux poteaux hybride soumis à un chargement combiné (charge critique). Pour atteindre cet objectif, nous développons des modèles théoriques et numériques de complexité croissante.

Dans la **première partie** de cette thèse, les équations fondamentales (cinématique, équilibre, comportement) d'une poutre hybride élastique en l'interaction partielle sont présentées. Les équations du problème en déplacement sont développées et résolues par une technique de décomposition en valeurs propres. Une attention particulière est apportée à la détermination des constantes d'intégration. La solution analytique ainsi obtenue sert à construire la matrice de raideur exacte pour l'analyse élastique linéaire d'une poutre hybride en interaction partielle.

Dans la **seconde partie** de cette thèse, nous proposons une nouvelle formulation élément fini pour le calcul non linéaire en grande déplacement d'un poteau hybride en tenant compte des glissements qui se produisent à chaque interface acier-béton. Pour ce faire, nous considérons l'approche co-rotationnelle dans laquelle le mouvement de l'élément se décompose en un mouvement de corps rigide et en une partie déformable décrite dans le repère co-rotationnel local qui se déplace de manière continue et tourne avec l'élément mais qui ne se déforme pas avec celui-ci. Cette méthode bien connue permet de transposer en non-linéaire, les éléments développés dans un contexte géométriquement linéaire. La matrice de raideur exacte développée dans la première partie est utilisée pour l'élément local.

Dans la **troisième partie** de cette thèse, nous abordons le comportement matériellement non-linéaire des poutres/poteaux hybrides en interaction partielle soumis à l'action combinée d'un effort compression, d'un moment de flexion et d'un effort de cisaillement. Le modèle de fibre est adopté dans lequel l'état de contrainte triaxiale du béton est considéré. Un critère de type « Cap Model » ne dépendant que du premier et second invariant est considéré pour le béton. Le confinement créé par les cadres est pris en compte dans le modèle. Le schéma implicite est retenu

et une stratégie de condensation permet d'éliminer les deux contraintes normales non-nulles qui sont dans le plan de la section. Cette technique de condensation permet de passer d'une formulation en plasticité 3D au modèle de comportement de type poutre 2D.

Dans la **dernière partie** de cette thèse, les outils précédemment développés sont utilisés pour évaluer la pertinence des méthodes simplifiées de l'Eurocode 2 et 4, dans le cas spécifique des poteaux hybrides soumis à un effort normal et à un de moment de flexion uni-axial. Dans un premier temps, l'élément fini développé est modifié en considérant la cinématique d'Euler-Bernoulli pour chacun des composants. Ensuite, cet élément fini est utilisé pour traiter 1140 cas différents de poteaux hybrides, destinés à couvrir les différentes typologies possibles et afin de disposer d'une base de données suffisamment large qui permet de jauger de la pertinence des méthodes simplifiées de l'Eurocode 2 et de l'Eurocode 4. Les résultats indique clairement que la méthode d'amplification du moment (version EC2 et EC4) ne sont pas satisfaisante. Dans un second temps, la base de données est étendue à 2960 configurations, ce qui permet de calibrer une nouvelle version de la méthode d'amplification du moment. Cette nouvelle méthode sera proposée aux organismes de normalisation.

8.2 Modélisation d'une poutre hybride dans le domaine élastique

La grande majorité des articles scientifiques sur les poutres mixtes multicouches en interaction partielle traite du cas des poutres à deux couches [14, 22, 24, 27, 30] ; si bien que la littérature technique sur les poutres multicouches voire les poutres hybrides renforcées par plusieurs profils est nettement moins abondante. Chui et Barclay [36] et Schnabl et al. [37] ont proposé un modèle analytique exact pour la poutre élastique à trois couches, où l'épaisseur ainsi que le module de Young des couches sont arbitraires. Sousa et al. [38] a développé une solution analytique pour les poutres multicouches isostatiques en supposant que la rotation de la

section transversale est identique pour chacune des couches. Skec et al. [39] ont proposé des modèles mathématiques avec des solutions analytiques pour l'analyse de poutres multicouches en élasticité linéaire. Ranzi [40] a proposé deux types d'éléments finis de type « déplacement » pour objectif d'évaluer le comportement de ces éléments finis de poutre multicouche en interaction partielle face au verrouillage. Pour les fonctions de formes polynomiales classiques, il est montré que l'élément avec nœud interne caractérise bien le comportement de la poutre en interaction partielle alors que l'élément sans nœud interne souffre des problèmes de verrouillage.

Une formulation élément fini reposant avec matrice de rigidité exacte offre la possibilité de générer un élément fini sans verrouillage. Ces éléments sont très attrayants en raison de leur précision, l'efficacité de calcul et l'indépendance de la solution vis-à-vis de la discrétisation spatiale. Heinisuo [41] a proposé une formulation élément fini utilisant la matrice de rigidité exacte pour les poutres droites, linéairement élastiques avec trois et cinq couches. Sousa [42] a développé une formulation analytique et a déduit l'expression de la matrice de rigidité exacte pour les poutres multicouches partiellement connectés avec l'hypothèse que le déplacement transversal ainsi que la rotation de la section droite est le même pour toutes les couches.

Dans cette section, nous étendons les travaux de Sousa [42] en considérant que la rotation des sections droites est différente pour chacune des couches. Nous déduisons la solution analytique et une nouvelle formulation « élément fini » pour l'analyse des poutres hybrides en interaction partielle sur la base de la matrice de rigidité exacte dont l'expression est déduite de la solution analytique.

8.2.1 Equation d'équilibre

Les équations d'équilibre sont obtenues en considérant l'état équilibre d'un élément de longueur infinitésimal dx soumis à une charge répartie p_y, voir Fig. 8.1. La connexion à l'interface entre le profil acier et le béton est modélisée par un

ressort distribué continu. Les conditions d'équilibre se traduisent par l'ensemble d'équations suivantes :

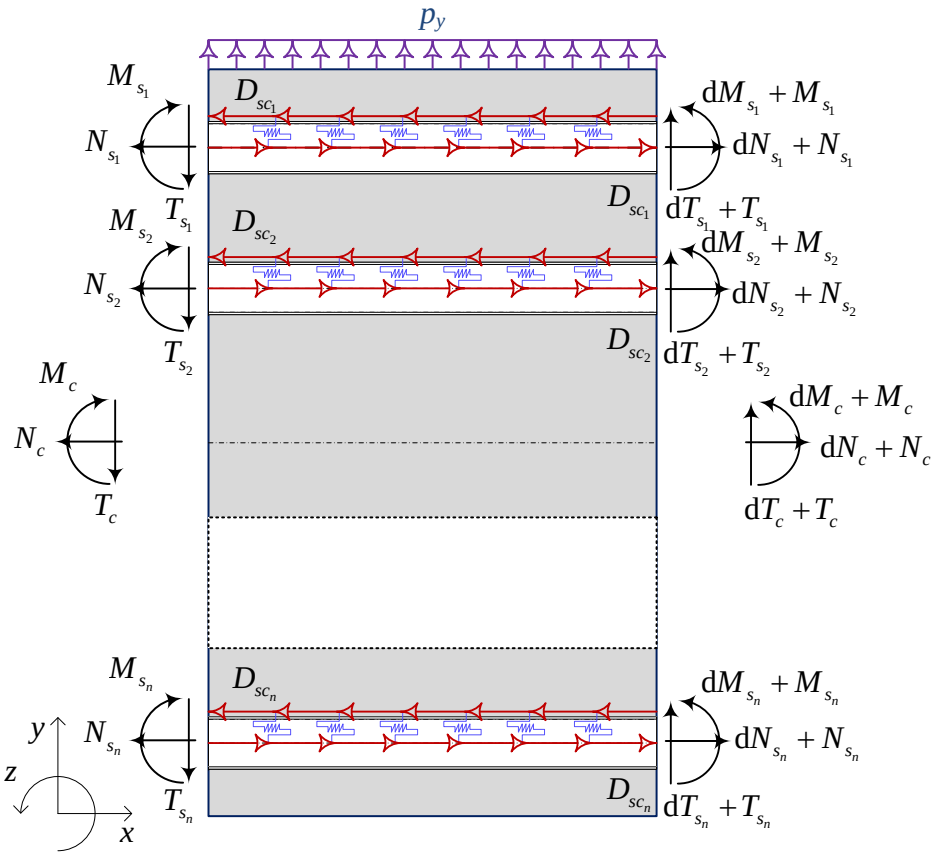

Figure 8.1: Élément infinitésimal d'une poutre hybride.

$$\partial N_{s_i} + D_{sc_i} = 0, \qquad i = 1, 2, \cdots n \tag{8.1}$$

$$\partial N_c - \sum_{j=1}^{n} D_{sc_j} = 0 \tag{8.2}$$

$$\partial M_c + \partial M_s + T + \sum_{j=1}^{n} h_j D_{sc_j} = 0 \tag{8.3}$$

$$\partial T + p_y = 0 \tag{8.4}$$

où $\partial \bullet = \mathrm{d} \bullet / \mathrm{d}x$, $M_s = \sum_{j=1}^{n} M_{s_j}$ et $T = \sum_{j=1}^{n} T_{s_j} + T_c$.

8.2.2 Relations cinématiques

En considérant que pour l'élément enrobant (qui en pratique est en béton) de la poutre hybride, la section droite reste plane mais n'est pas nécessairement normale à l'axe neutre, voir Fig. 8.2, on obtient les relations suivantes :

$$\epsilon_i = \partial u_i \qquad i = s_1, s_2, \cdots, s_n, c \tag{8.5}$$

$$\theta_c = \partial v - \gamma_c \tag{8.6}$$

$$\kappa_c = \partial \theta_c \tag{8.7}$$

$$\theta_{s_i} = \partial v \qquad i = 1, 2, \cdots, n \tag{8.8}$$

$$\kappa_{s_i} = \partial \theta_{s_i} \qquad i = 1, 2, \cdots, n \tag{8.9}$$

Les éléments enrobés se déforment selon les hypothèses cinématique d'Euler-Bernoulli. Les glissements se produisent aux interfaces acier-béton qui résultent des déplacements relatifs. Les rotations étant petites, on peut assimiler la tangente à l'angle, ce qui fournit :

$$g_i = u_c - u_{s_i} - h_i \theta_c, \qquad i = 1, 2, \cdots, n \tag{8.10}$$

8.2.3 Loi de comportement

Le champ des contraintes se déduit du champ de déformation à l'aide de la relation de comportement des matériaux. Par définition, les efforts internes résultent de l'intégration du champ de contrainte sur la section droite :

$$N_i = \int_{A_i} \sigma \, \mathrm{d}A_i = (EA)_i \, \epsilon_i \tag{8.11}$$

$$M_i = -\int_{A_i} y \, \sigma \, \mathrm{d}A_i = (EI)_i \, \kappa_i \tag{8.12}$$

$$T_c = \int_{A_c} \tau \, \mathrm{d}A_c = (GA)_c \, \gamma_c \tag{8.13}$$

$$D_{sc_i} = k_{sc_i} \, g_i, \qquad i = 1, 2, \cdots, n \tag{8.14}$$

où E_i, G_i, A_i et I_i sont respectivement le module élastique de Young, le module de cisaillement, l'aire de la section et le moment d'inertie de la section "i"; k_{sci} désigne la rigidité de la connexion.

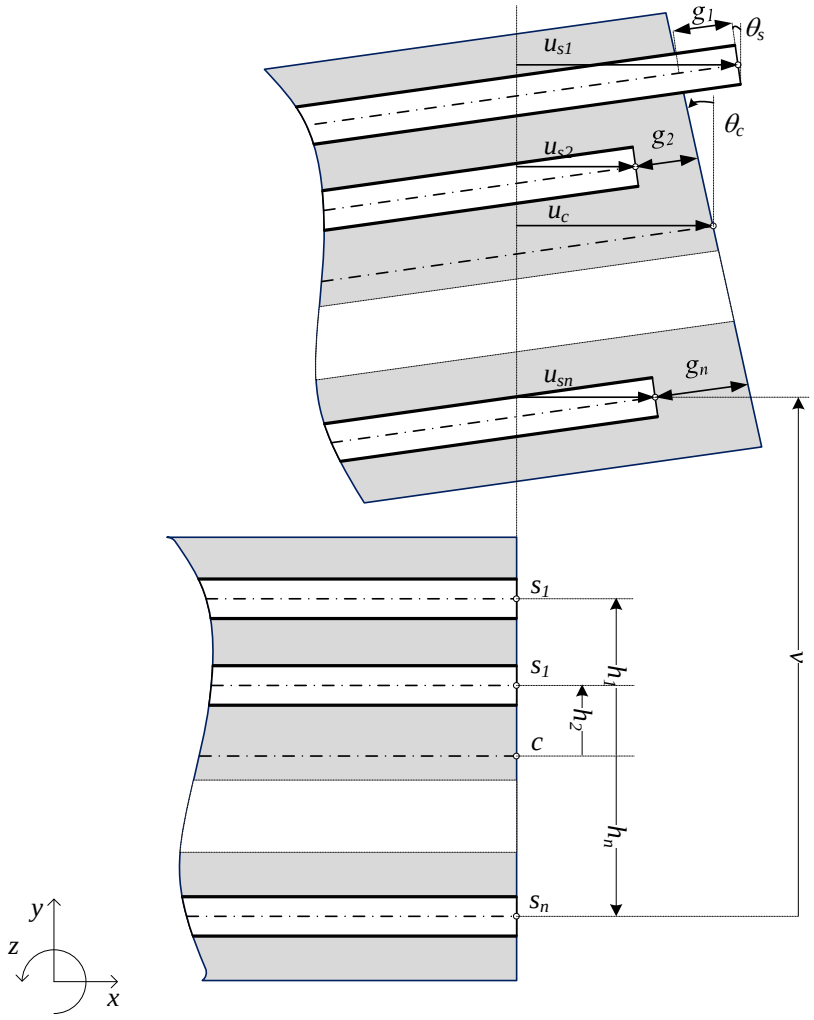

Figure 8.2: Cinématique de la poutre hybride.

8.2.4 Solution analytique et matrice de rigidité exacte dans le cas élastique linéaire

Les relations(8.1-8.14) sont maintenant combinées pour établir les équations gouvernant le comportement d'une poutre hybride en l'interaction partielle. En combinant les équations cinématiques (8.5-8.7) avec les équations du comportement élastique (8.11-8.14) et en insérant le résultat dans les équations d'équilibre (8.1-

8.3) se produit l'ensemble des équations différentielles suivantes :

$$(EA)_{s_i}\,\partial^2 u_{s_i} = -k_{sc_i}\,g_i, \qquad i = 1, 2, \cdots, n \tag{8.15}$$

$$(EA)_c\,\partial^2 u_c = \sum_{i=1}^{n} k_{sc_i}\,g_i \tag{8.16}$$

$$(EI)_0\,\partial^3 v = -T - \sum_{i=1}^{n} k_{sc_i}\,g_i\,h_i + (EI)_c\,\partial^2 \gamma_c \tag{8.17}$$

où $(EI)_0 = (EI)_s + E_c I_c$ et $(EI)_s = \sum_{i=1}^{n} E_{s_i} I_{s_i}$. En combinant les relations cinématiques, d'équilibre et de loi du comportement avec les équations (8.15-8.17), on obtient un system des équations différentielles couplées où les variables sont les glissements aux interfaces et la déformation de cisaillement collectée dans le vecteur $\mathbf{s}$:

$$\partial^2 \mathbf{s} - \mathbf{A}\,\mathbf{s} = \mathbf{h} \tag{8.18}$$

dans laquelle la matrice $\mathbf{A}$ est composée de paramètres provenant de la géométrie et de la rigidité de la section ; et le vecteur $\mathbf{h}$ dépend de l'effort tranchant total sur la section transversale.

Le system d'équations différentielles couplées (8.18) peut être résolu en diagonalisant la matrice $\mathbf{A}$, ce qui conduit à un système de n équations différentielles ordinaires du second-ordre.

Il est à noter que la solution exacte de (8.18) requiert la connaissance de la distribution de l'effort tranchant $T(x)$. Pour simplifier le développement de la solution, on suppose que la charge extérieure est répartie et constante sur l'élément de la poutre hybride. Par conséquence, la distribution de l'effort tranchant est linéaire suivant l'équilibre transversal de la section. On a donc :

$$T(x) = -p_y\,x + C_{2n+8} \tag{8.19}$$

où C_{2n+8} est l'effort tranchant à l'extrémité gauche de la poutre et est considéré comme une constant d'intégration dont la valeur sera fixée par les conditions aux

limites. En résolvant le system d'équations différentielles (8.18), on obtient :

$$\mathbf{g} = \mathbf{X}_g\mathbf{C} + \mathbf{Z}_g \tag{8.20}$$

$$\gamma_c = \mathbf{X}_{\gamma_c}\mathbf{C} + Z_{\gamma_c} \tag{8.21}$$

où la matrice $\mathbf{X}$ contient des fonctions exponentielles de x et Z est une fonction de la charge répartie p_y.

En introduisant (8.20-8.21) dans (8.15-8.17) et résolvant pour chaque variable cinématique, on obtient les relations suivantes :

$$v = \mathbf{X}_v\mathbf{C} + Z_v \tag{8.22}$$

$$\theta_s = \mathbf{X}_{\theta_s}\mathbf{C} + Z_{\theta_s} \tag{8.23}$$

$$\theta_c = \mathbf{X}_{\theta_c}\,\mathbf{C} + Z_{\theta_c} \tag{8.24}$$

$$u_c = \mathbf{X}_{u_c}\mathbf{C} + Z_{u_c} \tag{8.25}$$

$$u_{s_i} = \mathbf{X}_{us_i}\mathbf{C} + Z_{us_i}, \qquad i = 1, 2, \cdots, n \tag{8.26}$$

Une fois que les déplacements sont déterminés, on peut utiliser la loi de comportement élastique linéaire (8.11-8.13) pour déterminer les efforts nodaux.

$$N_{s_i} = \mathbf{Y}_{Ns_i}\mathbf{C} + R_{Ns_i}, \qquad i = 1, 2, \cdots n \tag{8.27}$$

$$N_c = \mathbf{Y}_{N_c}\mathbf{C} + R_{N_c} \tag{8.28}$$

$$M_s = \mathbf{Y}_{M_s}\mathbf{C} + R_{M_s} \tag{8.29}$$

$$M_c = \mathbf{Y}_{M_c}\mathbf{C} + R_{M_c} \tag{8.30}$$

$$T = \mathbf{Y}_T\mathbf{C} + R_T \tag{8.31}$$

où la matrice $\mathbf{Y}$ se décompose des fonctions exponentielle de x and R est une fonction de la charge répartie p_y. Comme nous avons le même déplacement transversal sur la section transversale, l'élément de la poutre hybride avec n sections noyées dans le béton a $(2n + 8)$ degrés de liberté, voir Fig. 8.3. Considérons un élément de la poutre hybride de longueur L, en appliquant les conditions aux limites en $x = 0$ et $x = L$, on obtient une relation entre les déplacements nodaux et les constantes d'intégration:

$$\mathbf{q} = \mathbf{X}\,\mathbf{C} + \mathbf{Z} \tag{8.32}$$

où

$$\mathbf{q} = [\ u_{s_1,0} \quad \cdots \quad u_{c,0} \quad v_{c,0} \quad \theta_{s,0} \quad \theta_{c,0} \quad u_{s_1,L} \quad \cdots \quad u_{c,L} \quad v_{c,L} \quad \theta_{s,L} \quad \theta_{c,L}\ ]^{\mathrm{T}},$$
$$\mathbf{Z} = [\ \mathbf{Z}_{us_1,0} \quad \cdots \quad \mathbf{Z}_{\theta_s,0} \quad \mathbf{Z}_{\theta_c,0} \quad \mathbf{Z}_{us_1,L} \quad \cdots \quad \mathbf{Z}_{\theta_s,L} \quad \mathbf{Z}_{\theta_c,L}\ ]^{\mathrm{T}} \text{ et}$$
$$\mathbf{X} = [\ \mathbf{X}_{us_1,0} \quad \cdots \quad \mathbf{X}_{\theta_s,0} \quad \mathbf{X}_{\theta_c,0} \quad \mathbf{X}_{us_1,L} \quad \cdots \quad \mathbf{X}_{\theta_s,L} \quad \mathbf{X}_{\theta_c,L}\ ]^{\mathrm{T}}.$$

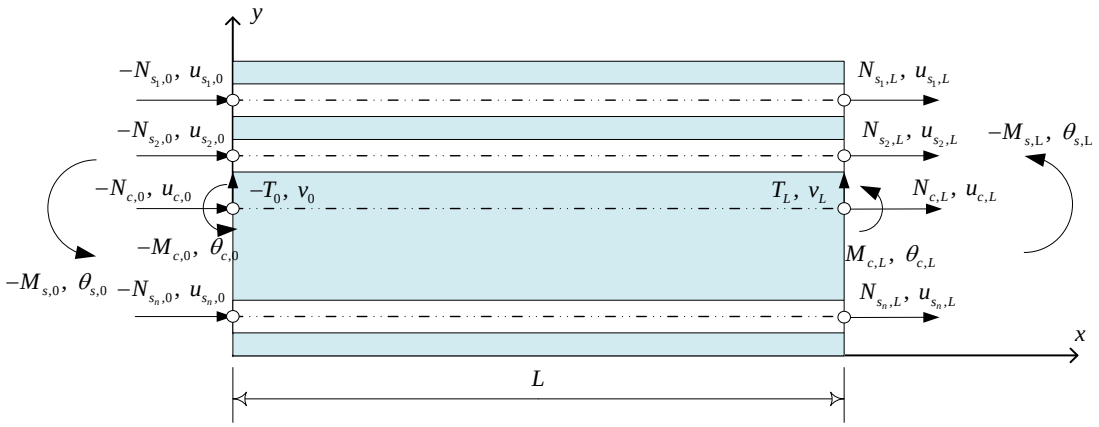

Figure 8.3: Degrés de liberté de l'élément de la poutre hybride.

Les forces nodales peuvent être exprimées par :

$$\mathbf{Q} = \mathbf{Y}\,\mathbf{C} + \mathbf{R} \tag{8.33}$$

où

$$\mathbf{Q} = [\ -N_{s_1,0} \quad \cdots \quad -M_{c,0} \quad N_{s_1,L} \quad \cdots \quad M_{c,L}\ ]^{\mathrm{T}},$$
$$\mathbf{Y} = [\ -\mathbf{Y}_{N_{s_1,0}} \quad \cdots \quad -\mathbf{Y}_{M_{c,0}} \quad \mathbf{Y}_{N_{s_1,L}} \quad \cdots \quad \mathbf{Y}_{M_{c,L}}\ ]^{\mathrm{T}} \text{ et}$$
$$\mathbf{R} = [\ -\mathbf{R}_{N_{s_1,0}} \quad \cdots \quad -\mathbf{R}_{M_{c,0}} \quad \mathbf{R}_{N_{s_1,L}} \quad \cdots \quad \mathbf{R}_{M_{c,L}}\ ]^{\mathrm{T}}.$$

En combinant (8.32) avec (8.33), on a :

$$\mathbf{K}\,\mathbf{q} = \mathbf{Q} + \mathbf{Q}_0 \tag{8.34}$$

où $\mathbf{K} = \mathbf{Y}\mathbf{X}^{-1}$ représente la matrice de rigidité exacte d'un élément et $\mathbf{Q}_0 = \mathbf{K}\mathbf{Z} - \mathbf{R}$ représente les forces nodales équivalent à la charge extérieure uniformément répartie p_y.

8.3 Modélisation d'une poutre hybride élastique en grand déplacement

Afin d'analyser l'effet des non-linéarités géométriques sur le comportement d'une poutre hybride, nous proposons un élément fini spécifique de poutre plane construit dans un contexte co-rotationnel. Dans cette approche, la configuration déformée de l'élément est définie par un mouvement « corps rigide » de la configuration initiale superposé à une déformation de la poutre dans un repère local. Dans ce repère, les déplacements sont petits et donc la relation entre les relations cinématiques sont linéaires.

8.3.1 Cinématique de l'élément de poutre hybride en description co-rotationnelle

Dans le repère global, l'élément possède deux nœuds pour la partie béton aux extrémités de l'élément. La cinématique des profils acier est définie en supposant qu'il n'y a pas de mouvement transversal relatif acier-béton ; il n'y a dès lors, à chaque extrémité de l'élément, qu'un seul degré de liberté spécifique représentant le glissement entre le profil acier et le béton. Dans le repère local, la matrice de rigidité exacte peut être utilisée. En conséquence, les nœuds intermédiaires utilisés pour éviter le problème de verrouillage numérique, rencontré dans les éléments finis polynomiaux d'ordre inférieur, ne sont pas nécessaires. Les notations utilisées sont définies sur Fig. 8.4 et Fig. 8.5. Les coordonnées des nœuds c_i et c_j dans le repère global (x, y) sont (x_{ci}, y_{ci}) et (x_{cj}, y_{cj}), respectivement.

L'élément a $2(n + 4)$ de degrés de liberté : les déplacements et les rotations globales des nœuds (c_i and c_j) et les glissements (g_{ki}, g_{kj}). La rotation de chaque profil à l'extrémité est la même (hypothèse de Bernoulli) et les glissements (g_{ki}, g_{kj}) dans le repère global sont perpendiculaires aux sections transversales des profils.

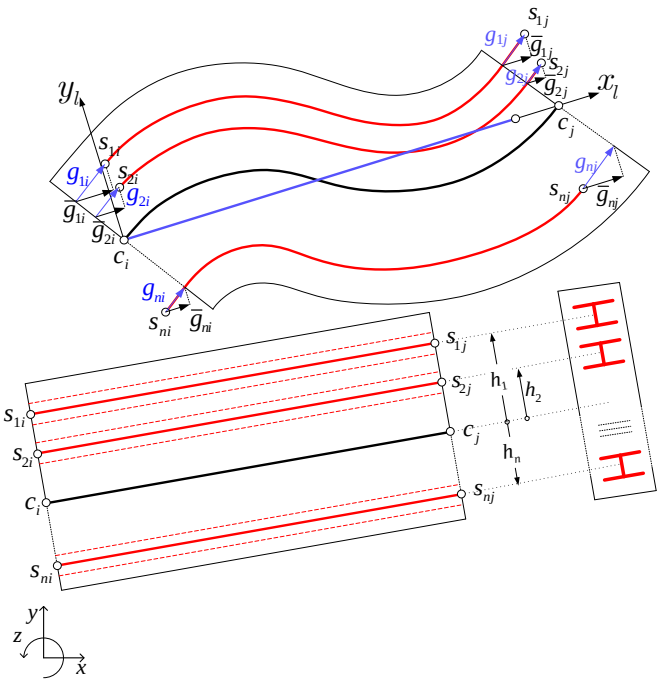

Figure 8.4: Glissements dans la poutre hybride en grande déplacement.

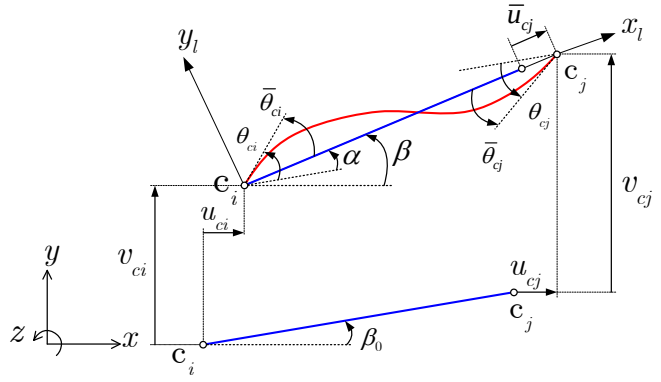

Figure 8.5: Déplacement et rotation de section.

8.3.2 Formulation de l'élément de poutre hybride en description co-rotationnelle

Une étape clé dans la méthode de co-rotationnel est d'établir la relation entre les variables locales et globales. Celle-ci est accomplie en effectuant un change-

ment des variables entre les quantités globales et locales. La deuxième étape consiste à supprimer les mouvements « corps rigide » du champ de déplacement de l'élément. Cette étape est réalisée en calculant les déplacements locaux en utilisant les relations cinématiques linéaires.

Considérons deux systèmes de coordonnées différents repéré par l'indice i et j. Supposons que le vecteur force interne $\mathbf{f}_i$ et la matrice de rigidité tangente $\mathbf{K}_i$ sont compatibles avec le vecteur de déplacement $\mathbf{p}_i$ de telle sorte que

$$\delta\mathbf{f}_i = \mathbf{K}_i\,\delta\mathbf{p}_i \tag{8.35}$$

Considérons maintenant que le vecteur $\mathbf{p}_i$ est lié au vecteur de déplacement $\mathbf{p}_j$ par

$$\mathbf{p}_i = \mathbf{B}_{ij}\,\mathbf{p}_j \tag{8.36}$$

En égalant le travail virtuel dans les deux systèmes, le vecteur de la force interne $\mathbf{f}_j$ conforme à $\mathbf{p}_j$ est défini par

$$\delta\mathbf{f}_j = \mathbf{B}_{ij}^{\mathrm{T}}\,\delta\mathbf{f}_i \tag{8.37}$$

L'expression de la matrice tangente de rigidité $\mathbf{K}_j$, cohérente à $\mathbf{p}_j$ est obtenue en différenciant l'équation (8.37) et en combinant le résultat avec (8.35) et (8.36) :

$$\mathbf{K}_j = \mathbf{B}_{ij}^{\mathrm{T}}\,\mathbf{K}_i\,\mathbf{B}_{ij} + \mathbf{H}_{ij} \qquad \mathbf{H}_{ij} = \left.\frac{\partial(\mathbf{B}_{ij}^{\mathrm{T}}\,\mathbf{f}_i)}{\partial\mathbf{p}_j}\right|_{\mathbf{f}_i} \tag{8.38}$$

De l'idée décrite ci-dessus, la formulation de l'élément de la poutre co-rotationnelle peut être obtenue en utilisant trois changements consécutifs de variables et quatre vecteurs de déplacement différents suivants :

$$\mathbf{p}_l = [\bar{u}_{\mathrm{s}1i}\ \bar{u}_{\mathrm{s}2i}\ \cdots\ \bar{u}_{\mathrm{sn}i}\ \bar{u}_{\mathrm{c}i}\ \bar{v}_{\mathrm{c}i}\ \bar{\theta}_{\mathrm{s}i}\ \bar{\theta}_{\mathrm{c}i}\ \bar{u}_{\mathrm{s}1j}\ \bar{u}_{\mathrm{s}2j}\ \cdots\ \bar{u}_{\mathrm{sn}j}\ \bar{u}_{\mathrm{c}j}\ \bar{v}_{\mathrm{c}j}\ \bar{\theta}_{\mathrm{s}j}\ \bar{\theta}_{\mathrm{c}j}]^{\mathrm{T}} \tag{8.39}$$

$$\mathbf{p}_e = [\ \bar{\theta}_{\mathrm{s}i}\ \ \bar{\theta}_{\mathrm{c}i}\ \ \bar{u}_{\mathrm{c}j}\ \ \bar{\theta}_{\mathrm{s}j}\ \ \bar{\theta}_{\mathrm{c}j}\ \ \bar{g}_{1i}\ \ \bar{g}_{2i}\ \ \cdots\ \ \bar{g}_{ni}\ \ \bar{g}_{1j}\ \ \bar{g}_{2j}\ \ \cdots\ \ \bar{g}_{nj}\ ]^{\mathrm{T}} \tag{8.40}$$

$$\mathbf{p}_a = [\ \bar{\theta}_{\mathrm{s}i}\ \ \bar{\theta}_{\mathrm{c}i}\ \ \bar{u}_{\mathrm{c}j}\ \ \bar{\theta}_{\mathrm{s}j}\ \ \bar{\theta}_{\mathrm{c}j}\ \ g_{1i}\ \ g_{2i}\ \ \cdots\ \ g_{ni}\ \ g_{1j}\ \ g_{2j}\ \ \cdots\ \ g_{nj}\ ]^{\mathrm{T}} \tag{8.41}$$

$$\mathbf{p}_g = [u_{\mathrm{c}i}\ v_{\mathrm{c}i}\ \theta_{\mathrm{c}i}\ \theta_{\mathrm{s}i}\ g_{1i}\ g_{2i}\ \cdots\ g_{ni}\ u_{\mathrm{c}j}\ v_{\mathrm{c}j}\ \theta_{\mathrm{c}j}\ \theta_{\mathrm{s}j}\ g_{1j}\ g_{2j}\ \cdots\ g_{nj}]^{\mathrm{T}} \tag{8.42}$$

8.4 Modélisation du comportement non-linéaire d'une poutre hybride

L'élément fini de poutre classique ne considère que les contraintes axiales agissant sur la section transversale et n'est pas en mesure de décrire précisément la réponse de l'élément de structure sous l'effet du couplage entre le cisaillement, la compression et le moment de flexion. Au cours des dernières décennies, il y a eu un effort de recherche pour surmonter cette limitation en adoptant la théorie de poutre de Timoshenko ou même la théorie de poutre exacte. Les différences entre les modèles proposés dans la littérature sont liées aux hypothèses cinématiques de la déformation de cisaillement prises au niveau de la section, au type de relations constitutives multiaxiales et aussi à la formulation élément fini basées sur l'approche de la rigidité ou la flexibilité [117, 122, 124–126]. Egalement, la stratégie d'intégration des lois d'évolutions élastoplastiques est un élément différentiant.

Cette partie vise à développer une nouvelle formulation éléments fini basée sur un modèle de fibre en considérant un critère 3D pour le béton enrobant et en prenant en compte l'effet de confinement provoqué par les étriers. Le pseudo-état plan de contraintes pour l'élément en béton est appliqué afin de condenser la formulation 3D pour obtenir les relations constitutives reliant les variables cinématiques dans le plan aux efforts généralisés caractérisant la poutre 2D. Pour ce faire, nous appliquons la stratégie proposée par Klinkel et Govindjee [127] pour l'état plan de contraintes dans lequel les contraintes agissantes dans le plan de la section doivent être mises à zéro. La rigidité tangente cohérente est fournie par la condensation statique standard de la matrice de rigidité tangente matérielle 3D. Pour tenir compte de la contribution de l'armature transversale sur les effets de confinement du béton, nous étendons cet algorithme en imposant l'équilibre transversal entre la fibre béton et l'acier transversal.

8.4.1 Équations fondamentales

Des relations cinématiques (8.5-8.10), on note le vecteur des déformations généralisées de la section $\hat{\mathbf{e}}$ lié aux déplacements par les relations cinématiques suivantes :

$$\hat{\mathbf{e}} = \hat{\partial}\mathbf{d} \tag{8.43}$$

où

$$\hat{\mathbf{e}}^{\mathrm{T}} = [\epsilon_{s_1}\ \epsilon_{s_2}\ \cdots\ \epsilon_{s_n}\ \kappa_s\ \epsilon_c\ \kappa_c\ \gamma_c\ g_1\ g_2\ \cdots\ g_n]\,, \tag{8.44}$$

$$\mathbf{d}^{\mathrm{T}} = [u_{s_1}\ u_{s_2}\ \cdots\ u_{s_n}\ u_c\ v\ \theta_c] \tag{8.45}$$

et

$$\hat{\partial}^{\mathrm{T}} = \begin{bmatrix} \partial & 0 & \cdots & 0 & 0 & 0 & 0 & 0 & -1 & 0 & \cdots & 0 \\ 0 & \partial & \cdots & 0 & 0 & 0 & 0 & 0 & 0 & -1 & \cdots & 0 \\ \vdots & \vdots & \ddots & \vdots & \vdots & \vdots & \vdots & \vdots & \vdots & \vdots & \ddots & \vdots \\ 0 & 0 & \cdots & \partial & 0 & 0 & 0 & 0 & 0 & 0 & \cdots & -1 \\ 0 & 0 & \cdots & 0 & 0 & \partial & 0 & 0 & 1 & 1 & \cdots & 1 \\ 0 & 0 & \cdots & 0 & \partial^2 & 0 & 0 & \partial & 0 & 0 & \cdots & 0 \\ 0 & 0 & \cdots & 0 & 0 & 0 & \partial & -1 & -h_1 & -h_2 & \cdots & -h_n \end{bmatrix} \tag{8.46}$$

Les équations d'équilibre (8.1-8.4) peuvent être exprimées sous la forme compacte suivante :

$$\widetilde{\partial}\mathbf{D} + \mathbf{P}_e = 0 \tag{8.47}$$

dans laquelle

$$\mathbf{D}^{\mathrm{T}} = [N_{s_1}\ N_{s_2} \cdots N_{s_n}\ M_s\ N_c\ M_c\ T_c\ D_{sc_1}\ D_{sc_2} \cdots D_{sc_n}]\,, \tag{8.48}$$

$$\mathbf{P}_e^{\mathrm{T}} = [0\ 0 \cdots 0\ 0\ p_y\ 0] \tag{8.49}$$

et

$$\widetilde{\partial} = \begin{bmatrix} \partial & 0 & \cdots & 0 & 0 & 0 & 0 & 0 & 1 & 0 & \cdots & 0 \\ 0 & \partial & \cdots & 0 & 0 & 0 & 0 & 0 & 0 & 1 & \cdots & 0 \\ \vdots & \vdots & \ddots & \vdots & \vdots & \vdots & \vdots & \vdots & \vdots & \vdots & \ddots & \vdots \\ 0 & 0 & \cdots & \partial & 0 & 0 & 0 & 0 & 0 & 0 & \cdots & 1 \\ 0 & 0 & \cdots & 0 & 0 & \partial & 0 & 0 & -1 & -1 & \cdots & -1 \\ 0 & 0 & \cdots & 0 & -\partial^2 & 0 & 0 & \partial & 0 & 0 & \cdots & 0 \\ 0 & 0 & \cdots & 0 & 0 & 0 & \partial & 1 & h_1 & h_2 & \cdots & h_n \end{bmatrix} \tag{8.50}$$

La formulation faible (variationnelle) des équations d'équilibre est donc donnée par

$$\int_L \delta d^{\mathrm{T}}\, \widetilde{\partial}\mathbf{D}\, \mathrm{d}x = 0 \tag{8.51}$$

dans laquelle la force volumique est ignorée. En développant cette équation, on a :

$$\int_L \delta \hat{\mathbf{e}}^{\mathrm{T}}\, \mathbf{D}\, \mathrm{d}x = \delta \mathbf{q}^{\mathrm{T}}\, \mathbf{Q} \tag{8.52}$$

où

$$\delta \mathbf{q}^{\mathrm{T}} \mathbf{Q} = \left[\sum_{j=1}^{n} \delta u_{s_j}\, N_{s_j} + \delta u_c\, N_c + \delta \theta_s\, M_s + \delta \theta_c\, M_c + \delta v\, T \right]_0^L \tag{8.53}$$

La méthode de Newton-Raphson est adoptée pour résoudre l'équation (8.52). La matrice de rigidité tangente de l'élément à l'itération $i-1$, est déterminée par

$$\mathbf{K}^{i-1} = \int_L \mathbf{B}^{\mathrm{T}}\, \mathbf{k}^{i-1}\, \mathbf{B}\, \mathrm{d}x \tag{8.54}$$

et le vecteur des forces nodales hors-équilibre au cours de l'itération est

$$\mathbf{Q}_R^{i-1} = \int_L \mathbf{B}^{\mathrm{T}}\, \mathbf{D}^{i-1}\, \mathrm{d}x \tag{8.55}$$

où $\mathbf{B} = \hat{\partial}\mathbf{N}(x)$, $\mathbf{k} = \frac{\partial \mathbf{D}}{\partial \hat{\mathbf{e}}}$ et $\mathbf{N}(x)$ est la fonction d'interpolation du champ de déplacement.

8.4.2 Comportement non-linéaire de la section

Le comportement non linéaire d'une poutre hybride soumise à un chargement combiné dépend largement des hypothèses faites sur la distribution de la contrainte et de déformation sur la section transversale. Il est supposé ici que les sections transversales des profils acier sont soumises uniquement à des déformations axiales alors que la déformation de l'élément en béton produit déformations axiales et des déformations de cisaillement. En conséquence, une relation contrainte-déformation uni-axiale pour la barre d'armature longitudinale et le profilé peut être utilisée et un modèle 3D du béton avec une stratégie de condensation doit être adopté. En raison de la complexité de ce dernier, ce qui suit est seulement consacré à la description de l'élément en béton.

Les équations constitutives de l'état 2D de contrainte-déformation de la fibre de béton sont obtenues en écrivant les déformations dans le plan et en appliquant l'état plan de contrainte sur la loi du comportement 3D. Par conséquent, les contraintes actives et les déformations hors-plan sont obtenues. Dans la direction transversale (direction y, ainsi que z), les armatures transversale sont supposées être distribuées uniformément avec un rapport volumétrique ρ^{st}. Cette hypothèse est faite dans le but de prendre en compte les effets de confinement dans le béton. Les exigences de compatibilité imposent que la déformation verticale ε_y^c et latérale ε_z^c dans le béton est égale à la déformation transversale ε_y^{st} et latérale ε_z^{st} dans les armatures, respectivement. Les contraintes résultantes le long de la direction y et z sont obtenues en additionnant les contraintes axiales dans l'armature transversal σ_y^{st} et σ_z^{st} aux contraintes axiales dans le béton σ_y^c et σ_z^c, respectivement. En conséquence, la relation contrainte-déformation 3D du problème peut être écrite comme suit :

$$\begin{bmatrix} \mathrm{d}\sigma_x^c \\ \mathrm{d}\sigma_y \\ \mathrm{d}\sigma_z \\ \mathrm{d}\tau_{xy}^c \end{bmatrix} = \left(\begin{bmatrix} C_{11}^{ep} & C_{12}^{ep} & C_{13}^{ep} & C_{14}^{ep} \\ C_{21}^{ep} & C_{22}^{ep} & C_{23}^{ep} & C_{24}^{ep} \\ C_{31}^{ep} & C_{32}^{ep} & C_{33}^{ep} & C_{34}^{ep} \\ C_{41}^{ep} & C_{42}^{ep} & C_{43}^{ep} & C_{44}^{ep} \end{bmatrix} + \begin{bmatrix} 0 & 0 & 0 & 0 \\ 0 & \rho_y^{st} E_y^{st} & 0 & 0 \\ 0 & 0 & \rho_z^{st} E_z^{st} & 0 \\ 0 & 0 & 0 & 0 \end{bmatrix} \right) \begin{bmatrix} \mathrm{d}\epsilon_x^c \\ \mathrm{d}\epsilon_y^c \\ \mathrm{d}\epsilon_z^c \\ \mathrm{d}\gamma_{xy}^c \end{bmatrix} \tag{8.56}$$

où $\mathbf{C}^{ep}$ est la rigidité tangente cohérente dans le problème de la section de béton. Pour obtenir l'opérateur tangent cohérent, qui répond à la condition particulière des contraintes du modèle poutre, la tangente matérielle doit être condensée. En introduisant $\bar{\sigma}_p^{\mathrm{T}} = [\sigma_y \, \sigma_z] = \mathbf{0}$ dans l'équation (8.56), on a

$$\mathrm{d}\overline{\boldsymbol{\sigma}}_p = \mathbf{C}_{pm} \, \mathrm{d}\overline{\boldsymbol{\epsilon}}^c + \mathbf{C}_{pp} \, \mathrm{d}\overline{\boldsymbol{\epsilon}}_p^c = 0, \tag{8.57}$$

D'où,

$$\mathrm{d}\overline{\boldsymbol{\epsilon}}_p^c = -\mathbf{C}_{pp}^{-1}\mathbf{C}_{pm} \, \mathrm{d}\overline{\boldsymbol{\epsilon}}^c. \tag{8.58}$$

où $\bar{\varepsilon}^{c,\mathrm{T}} = \left[\varepsilon_x^c \, \gamma_{xy}^c\right]$, $\bar{\varepsilon}_p^{c,\mathrm{T}} = \left[\varepsilon_y^c \, \varepsilon_z^c\right]$, $\mathbf{C_{pm}} = \begin{bmatrix} C_{21}^{ep} & C_{24}^{ep} \\ C_{31}^{ep} & C_{34}^{ep} \end{bmatrix}$, et $\mathbf{C_{pp}} = \begin{bmatrix} C_{23}^{ep} + \rho_y^{st} E_y^{st} & C_{23}^{ep} \\ C_{32}^{ep} & C_{33}^{ep} + \rho_z^{st} E_z^{st} \end{bmatrix}$. Le remplacement de l'équation (8.58) dans (8.56) conduit à la relation tangente cohérente entre les contraintes actives et les déformations dans le plan du béton comme suit :

$$\overline{\mathbf{k}}^c = \mathbf{C}_{mm} - \mathbf{C}_{mp}\mathbf{C}_{pp}^{-1}\mathbf{C}_{pm} \tag{8.59}$$

La matrice de rigidité tangente de la section de poutre hybride est donc :

$$\mathbf{k} = \begin{bmatrix} \mathbf{k}_s & \mathbf{0} & \mathbf{0} \\ \mathbf{0} & \mathbf{k}_c & \mathbf{0} \\ \mathbf{0} & \mathbf{0} & \mathbf{k}_{sc} \end{bmatrix} \tag{8.60}$$

dont ses composantes sont

$$\mathbf{k}_s = \begin{bmatrix} \overline{EA}_{s_1} & 0 & \cdots & 0 & -\overline{ES}_{s_1} \\ 0 & \overline{EA}_{s_2} & \cdots & 0 & -\overline{ES}_{s_2} \\ \vdots & \vdots & \ddots & \vdots & \vdots \\ 0 & 0 & \cdots & \overline{EA}_{s_n} & -\overline{ES}_{s_n} \\ -\overline{ES}_{s_1} & -\overline{ES}_{s_2} & \cdots & -\overline{ES}_{s_n} & \overline{EI}_s \end{bmatrix}, \tag{8.61}$$

$$\mathbf{k}_c = \begin{bmatrix} \int_{A_c} \overline{k}_{11}^c \mathrm{d}A + \overline{EA}_{sl} & -\int_{A_c} (y - y_c)\overline{k}_{11}^c \mathrm{d}A - \overline{ES}_{sl} & \int_{A_c} \overline{k}_{12}^c \mathrm{d}A \\ -\int_{A_c} (y - y_c)\overline{k}_{11}^c \mathrm{d}A - \overline{ES}_{sl} & \int_{A_c} (y - y_c)^2 \overline{k}_{11}^c \mathrm{d}A + \overline{EI}_{sl} & \int_{A_c} (y - y_c)\overline{k}_{12}^c \mathrm{d}A \\ \int_{A_c} \overline{k}_{21}^c \mathrm{d}A & -\int_{A_c} (y - y_c)\overline{k}_{21}^c \mathrm{d}A & \int_{A_c} \overline{k}_{22}^c \mathrm{d}A \end{bmatrix}, \tag{8.62}$$

et

$$\mathbf{k}_{sc} = \begin{bmatrix} k_{sc_1} & 0 & \cdots & 0 \\ 0 & k_{sc_2} & \cdots & 0 \\ \vdots & \vdots & \ddots & \vdots \\ 0 & 0 & \cdots & k_{sc_n} \end{bmatrix} \tag{8.63}$$

8.4.3 Applications numériques

Trois essais expérimentaux de poutres hybrides soumises à la flexion en 3 points, réalisés au Laboratoire de Génie Civil et Génie Mécanique de l'INSA de Rennes sont sélectionnés afin d'évaluer l'exactitude du modèle proposé. Le spécimen a une longueur de 5 m et une section rectangulaire de 25 cm x 90 cm, renforcée par huit barres d'armature longitudinales de 20 mm de diamètre, voir la Figure 6. Les armatures transversales (étriers) composées barres d'armature de 14 mm de diamètre. Les spécimens (BW, CW et CWHC) sont renforcés par trois HEB100 profilés en acier totalement enrobés dans la section en béton armé. Pour les spécimens CW et CWHC, les connecteurs (goujons Nelson H3L16) avec un espacement de 20 cm sont soudés à l'âme du profilé assurant le mécanisme de transfert de force entre le profil d'acier et le béton. Les barres d'armatures sont placées de la même façon dans tous les spécimens, sauf l'écartement de l'étrier. Les caractéristiques du matériau en MPa sont données dans Tableau 8.1. La simulation numérique des essais est conduite en discrétisant les spécimens sont modélisés en 12 éléments. Le poids propre est considéré comme une charge répartie appliquée au niveau de l'élément. Le déplacement vertical à mi-portée est appliqué de façon incrémentielle (déplacement contrôlé) jusqu'à la rupture. En ce qui concerne la loi de comportement, nous considérons la relation contrainte-déformation suivante : le cap modèle est retenu pour le béton; et la loi en élastique parfaitement plastique pour les aciers profilés, les armatures et les connexions de cisaillement longitudinal. Les courbes de force-déplacement obtenues à partir du modèle élément fini développé, sont comparées à celles obtenues à partir des essais expérimentaux

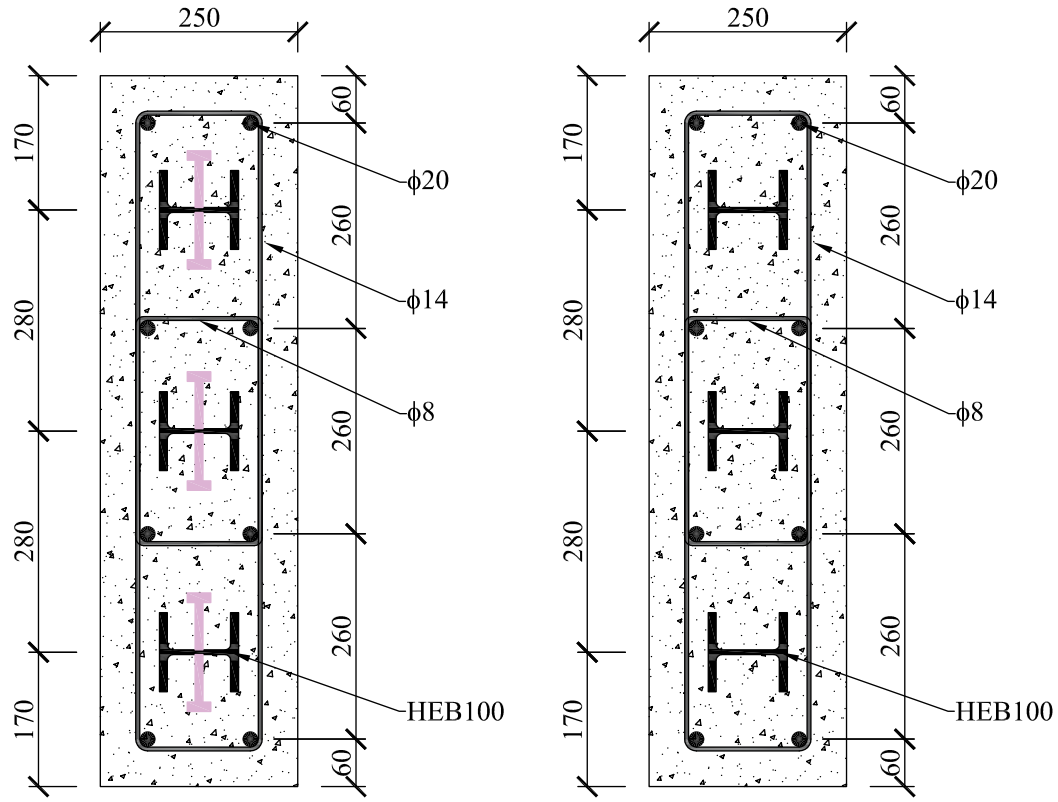

Figure 8.6: Section transversale des spécimens.

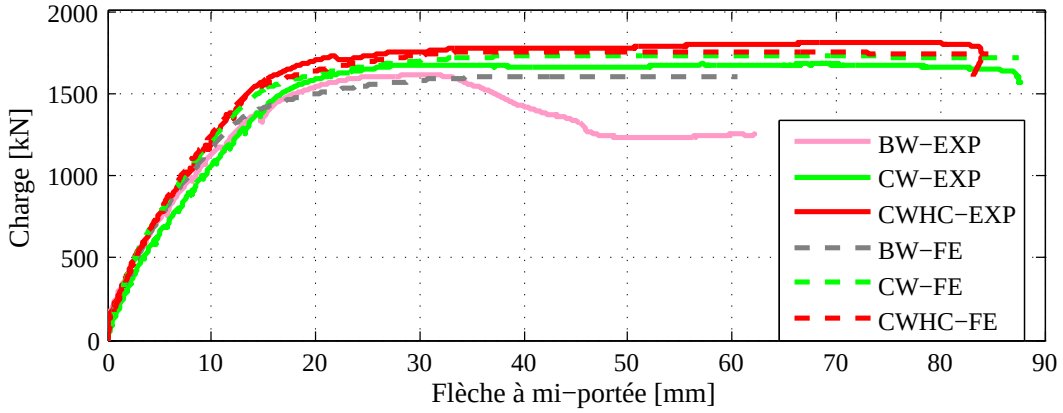

Figure 8.7: Comparaison des courbes de force-déplacement.

Fig. 8.7. Les courbes des résultats expérimentaux montrent que la déformation des spécimens est accompagnée de grands déplacements, ce qui montre leur comportement ductile quand soumis à un chargement monotone. Les charges ultimes de BW, CW et CWHC prédites par l'analyse numérique correspondent bien à celles des résultats expérimentaux.

Tableau 8.1: Caractéristiques des matériaux.

	Béton		Armature long.		Armature Trans.		Profilé	
Spécimen	f_{cm}	E_{cm}	f_s	E_s	f_{st}	E_{st}	f_y	E_y
BW	31.50	31040	383.91	210740	633.26	207460	462.7	214450
CW	32.00	31187	383.91	210740	633.26	207460	462.7	214450
CWHC	31.63	31078	383.91	210740	633.26	207460	462.7	214450

in MPa

8.5 Dimensionnement des poteaux hybrides en instabilité

Cette partie présente une étude numérique sur les effets du second-ordre dans les poteaux hybrides. Afin d'analyser le comportement non linéaire des poteaux hybrides, une formulation spécifique d'élément fini de poutre plane de type Bernoulli en description co-rotationnelle totale est utilsée. Dans le repère local, des nœuds intermédiaires sont utilisés pour l'interpolation quadratique du déplacement axial. Les efforts et les déplacements à ces nœuds sont statiquement condensés au niveau local pour être compatible au champ de déplacement dans le repère global. L'état de déformation, les contraintes et les efforts internes sur la section sont obtenus par une discrétisation multi-fibres de la section. Les détails du développement de l'élément fini, ainsi que de la validation par rapport à des résultats d'essai, peuvent être trouvés dans [13]. L'élément fini permet de traiter une connexion acier-béton partielle ; à ce stade la méthode simplifiée a été développée pour une connexion totale. Les simulations qui vont suivre ont donc été faites en adop-

tant une raideur de connexion importante qui annule à une tolérance près tout glissement. Il est à noter cependant que des travaux préliminaires montrent que cette connexion complète n'est pas toujours nécessaire pour optimiser la charge de ruine. Cet élément fini est utilisé pour traiter 1140 cas différents de poteaux hybrides, destinés à couvrir les différentes typologies possibles, afin de disposer d'une base d'évaluation de la pertinence des méthodes simplifiées de l'Eurocode 2 et de l'Eurocode 4 pour de tels éléments. Enfin, ces méthodes simplifiées ne donnant pas satisfaction, la base de données est étendue à 2960 configurations, afin de servir au calibrage d'une nouvelle méthode simplifiée.

8.5.1 Méthodes de dimensionnement en instabilité des poteaux des Eurocodes 2 et 4

Pour dimensionner en instabilité un poteau, tant l'Eurocode 2 que l'Eurocode 4 permettent de recourir à une analyse non linéaire géométrique et matérielle. Les hypothèses et coefficients de sécurité des deux normes sont cohérents, et serviront par la suite de base à la définition des modèles éléments finis de l'étude paramétrique. Toutefois, cette méthode est lourde à mettre en œuvre, et les deux Eurocodes proposent des méthodes simplifiées. Dans l'Eurocode 4 une seule méthode de dimensionnement est proposée. Le moment du second ordre est obtenu à partir du moment du premier ordre multiplié par le facteur d'amplification $k = \beta/(1 - N_{Ed}/N_{cr})$. Ensuite, la résistance de la section sous l'effet combiné de l'effort normal et du moment du second ordre doit être vérifiée. Dans l'expression de k, β dépend de la forme du diagramme de moments, et l'expression de N_{cr} est établie en prenant en compte la fissuration et le fluage du béton. L'Eurocode 2 propose deux méthodes de dimensionnement des poteaux en béton armé, appelées respectivement la méthode de la rigidité nominale et de la courbure nominale. La première repose sur le même principe d'amplification des moments que l'Eurocode 4. Dans la mesure où les éléments hybrides sont intermédiaires entre les poteaux en béton armé et les poteaux mixtes, il a été décidé de n'étudier que la méthode de la rigidité nominale, afin de faciliter la synthèse entre les deux normes.

Les expressions mathématiques des méthodes de l'Eurocode 2 et de l'Eurocode 4 sont résumées dans Tableau 8.2.

Tableau 8.2: Méthodes de calcul d'amplification des moments de l'Eurocode 2 et 4.

Moment du second ordre : $M_{Ed,2} = k\, M_{Ed,1}$ Raideur effective : $EI = K_c E_{cd} I_c + K_s E_s Is + K_a E_a I_a$	
EC2	**EC4**
$k = 1 + \dfrac{\beta}{\dfrac{N_{cr}}{N_{Ed}} - 1}$, $\beta = \dfrac{\pi^2}{c_0}$	$k = 1 + \dfrac{\beta}{1 - \dfrac{N_{Ed}}{N_{cr,eff}}}$
$N_{cr} = \dfrac{\pi^2 EI}{L^2}$; $k1 = \sqrt{\dfrac{f_{ck}}{20}}$; $k_2 = n\,\dfrac{\lambda}{70} \leq 0,2$;	$\beta = 0,66 + 0,44 r_m \geq 1$,
$n = \dfrac{N_{Ed}}{A_c f_{cd}}$; $K_c = \dfrac{k_1 k_2}{1 + \phi_{ef}}$; $K_s = K_c = 1$;	$N_{cr,eff} = \dfrac{\pi^2 EI}{L^2}$
$w_0 = L/400$	$K_c = 0,45$; $K_s = K_a = 0,9$
	w_0 selon la section

8.5.2 Évaluation des méthodes EC2 et EC4 pour les poteaux hybrides : étude paramétrique

8.5.2.1 Description de l'échantillon utilisé

Le modèle élément fini a été utilisé pour effectuer une étude paramétrique extensive, afin de vérifier l'applicabilité des méthodes de l'Eurocode 2 et 4 décrites au paragraphe précédent aux éléments hybrides. La charge ultime de 1140 poteaux différents a été calculée par les éléments finis, et comparée à celle obtenue par les méthodes simplifiées. 5 sections différentes, notées HSSRC1-5, ont été étudiées (Fig. 8.8).

Dans l'étude paramétrique, la limite élastique de l'acier des profils et des armatures est considérée constante, l'effet du ratio de résistance du béton par rapport à résistance de l'acier étant pris en compte en faisant varier la classe de béton. Les variables de l'étude paramétrique sont résumées au Tableau 8.3. Trois

valeurs d'élancement réduit $\bar{\lambda}$ différentes et trois classes de béton, sont considérées. L'étude porte sur trois formes de diagrammes de moment : constant, triangulaire ou bitriangulaire, défini par le ratio entre les moments d'extrémité r_m ($r_m = 1\,;\,0\,;\,-1$). Le moment maximal est défini par un excentrement de l'effort normal noté e, pour lequel une valeur variant de 0 à 3 fois la hauteur de la section est considérée. Le coefficient de fluage effectif est considéré soit avec une valeur nulle, soit avec une valeur de 1,5 correspondant au ratio classique entre les charges à court terme et à long terme. Le rapport δ entre la résistance axiale de la section acier, et la résistance totale de la section, varie de 0.2 à 0.62, ce dernier ratio important étant obtenu grâce à la section HSRCC4.

Tableau 8.3: Résumé des variables de l'étude paramétrique.

Section	S1; S2; S3; S4; S5
Béton	C35/45; C60/75; C90/105
f_{sk}	500 MPa
f_y	355 MPa
$\bar{\lambda}$	0.5; 1.0; 2.0
$\frac{e}{h}$	0.0-3.0
δ	0.2-0.62
φ_{ef}	0; 1.5

8.5.2.2 Définition du modèle numérique

Le comportement matériel du béton et de l'acier a été défini en conformité avec les règles de l'Eurocode 2 et de l'Eurocode 4. Les lois adoptées sont représentées sur la Figure 10. Le module de l'acier a été pris égal à 210 000 MPa. Les valeurs de Ecm, ϵ_{c1}, ϵ_{cu1}, ont été choisies selon les prescriptions de l'Eurocode 2.

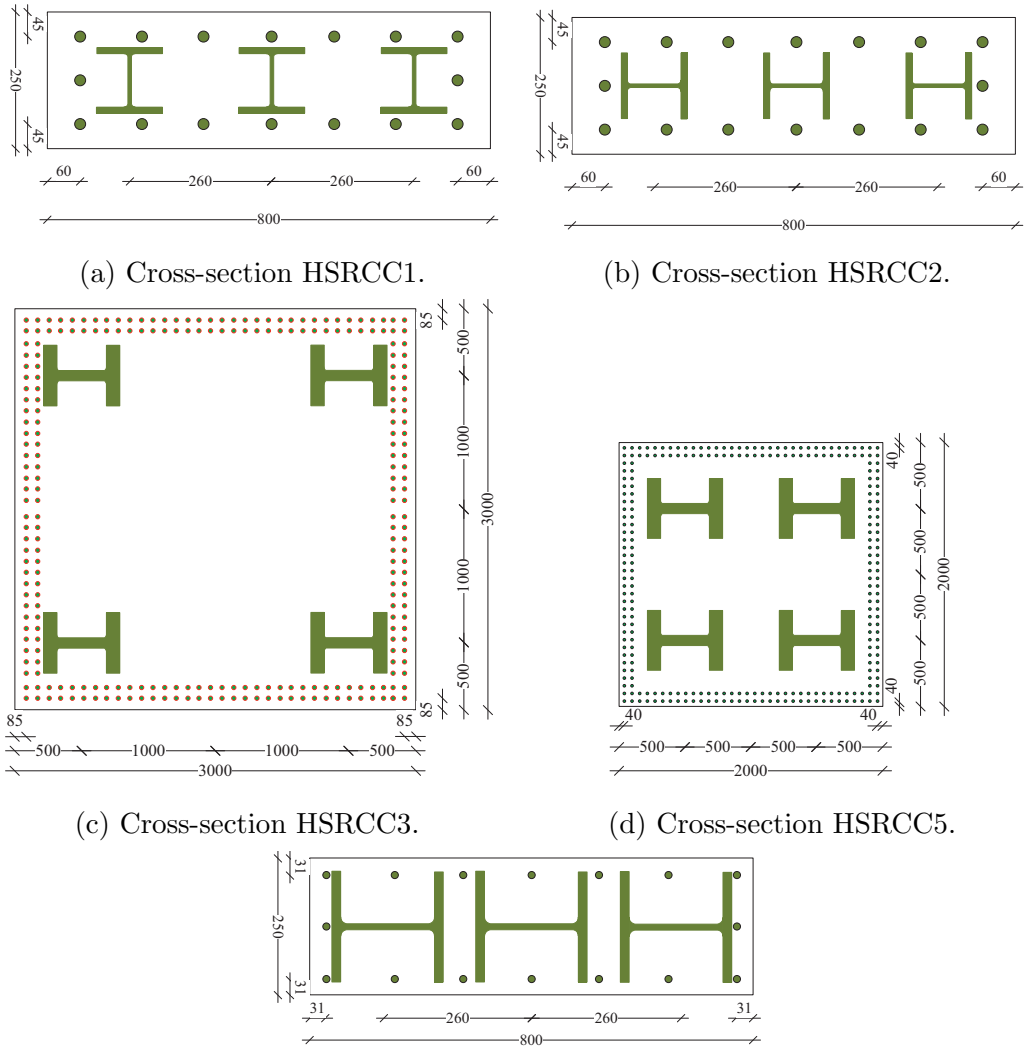

(a) Cross-section HSRCC1.

(b) Cross-section HSRCC2.

(c) Cross-section HSRCC3.

(d) Cross-section HSRCC5.

(e) Cross-section HSRCC4.

Figure 8.8: Cross-sections considered in parametric study.

Le calcul numérique prend en compte les contraintes résiduelles existant dans les profils métalliques (Figure 11), ainsi qu'une imperfection géométrique sinusoïdale dont son amplitude diffèrent selon les normes. Pour des profils métalliques, une valeur de L/1000 est proposée par l'Eurocode 3, alors que l'Eurocode 2 propose une valeur de $L/400$ pour les poteaux en béton. Dans la mesure où le mode constructif, qui fixe la précision de la forme générale des poteaux hybrides, et de

la position des profils métalliques, est de type béton, il a été décidé d'adopter une imperfection géométrique avec une amplitude de $L/400$. Comme annoncé, une

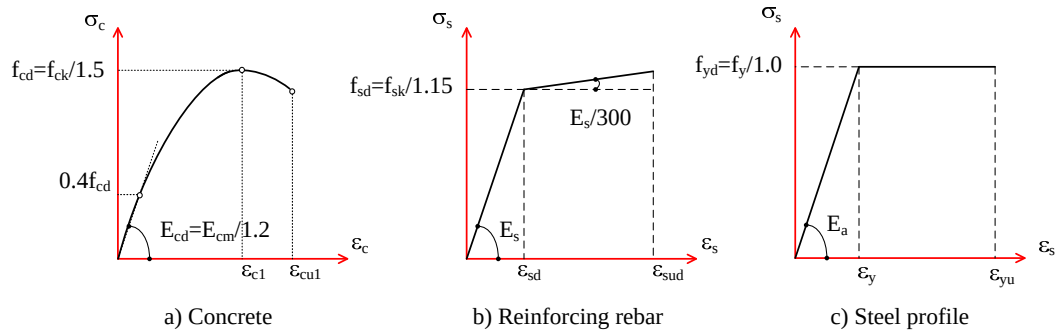

Figure 8.9: Lois constitutives utilisées dans le modèle élément fini.

connexion complète est imposée, à l'instar des recommandations de l'Eurocode 4.

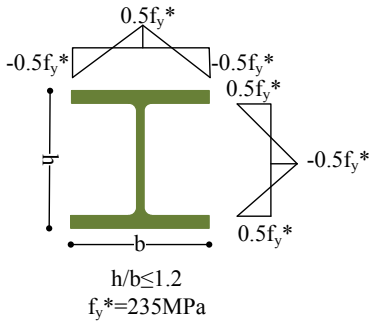

Figure 8.10: Distribution de contraintes résiduelles considérée dans le calcul.

8.5.2.3 Résultat des comparaisons

A titre d'illustration, les résultats obtenus pour différents élancements et cas de chargements pour la section HSRCC1 sont dessinés sur la Figure 12 et 13. La classe de béton adoptée est C60, et le coefficient de fluage effectif 1,5. Fig. 8.11, les prédictions de la méthode simplifiée de l'Eurocode 2 sont comparées aux résultats

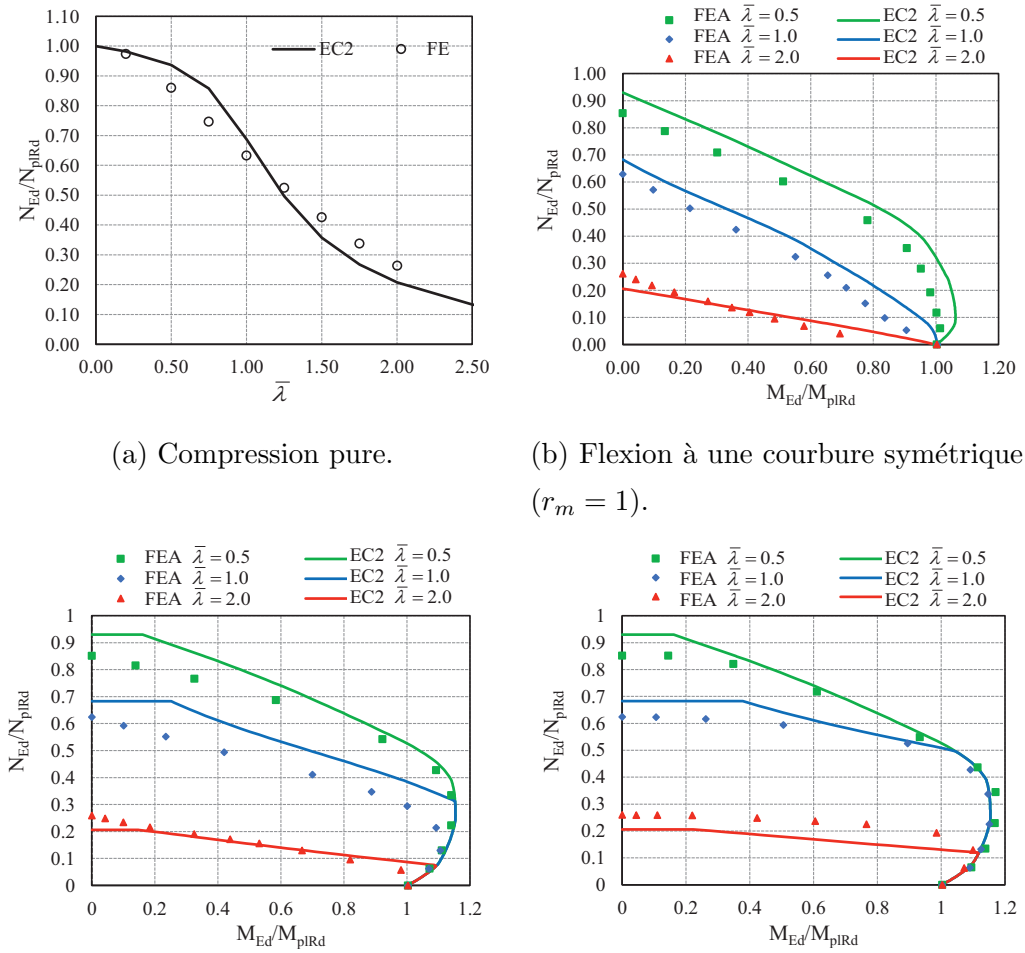

(a) Compression pure.

(b) Flexion à une courbure symétrique ($r_m = 1$).

(c) Flexion à une courbure ($r_m = 0$).

(d) Flexion à double courbure ($r_m = -1$).

Figure 8.11: Comparaison de la méthode simplifiée Eurocode 2 aux résultats d'éléments finis – section HSRCC1.

de la méthode d'éléments finis. Fig. 8.11a, dans le cas de la compression pure, il apparait que la méthode simplifiée de l'Eurocode 2 est insécuritaire pour les faibles élancements. Fig. 8.11b et Fig. 8.11c, dans le cas des colonnes soumises à une flexion avec une courbure, de nouveau l'Eurocode 2 donne des résultats insécuritaires pour les élancements faibles à modérés ($\bar{\lambda} = 0,5$ à 1 Des résultats similaires sont observés en cas de flexion avec double courbure, sauf pour les cas

proches de la flexion pure (Fig. 8.11d), où la méthode EC2 donne de bons résultats.

Fig. 8.12, la même comparaison est effectuée pour la méthode simplifiée de l'Eurocode 4. Les prévisions de l'Eurocode 4 sont globalement moins bonnes. Sous compression pure (Fig. 8.12a), la formulation de l'Eurocode 4 donne globalement les résultats sécuritaires. Dans les autres cas (Fig. 8.12b à Fig. 8.12d), l'EC4 donne des résultats conservatifs pour les faibles et les fortes excentricités. Par contre, pour les cas intermédiaires, les résultats sont insécuritaires, parfois largement. Afin d'évaluer de façon globale la qualité des résultats obtenus par les méthodes simplifiées pour les 1140 cas de l'analyse paramétrique, pour chaque cas, le ratio R suivant a été établi :

$$R = \frac{R_{FE}}{R_{SM}} \tag{8.64}$$

avec $R_{FE} = \sqrt{\left(\frac{N_{FE}}{N_{pl,Rd}}\right)^2 + \left(\frac{M_{FE}}{M_{pl,Rd}}\right)^2}$ et $R_{SM} = \sqrt{\left(\frac{N_{SM}}{N_{pl,Rd}}\right)^2 + \left(\frac{M_{SM}}{M_{pl,Rd}}\right)^2}$ où $(N_{FE},\, M_{FE})$ étant le couple sollicitant à la ruine dans le calcul par éléments finis, $(N_{SM},\, M_{SM})$ celui obtenu par l'analyse simplifiée, et $N_{pl,Rd}$, $M_{pl,Rd}$ l'effort normal et le moment de résistance correspondante. Lorsque R est supérieur à 1, l'approche simplifiée est sécuritaire. Les histogrammes de R obtenus pour les deux méthodes simplifiées sont dessinés sur Fig. 8.13.

Les moyennes des deux distributions sont proches de 1 : 0.996 pour la méthode Eurocode 2, 1.01 pour la méthode Eurocode 4. Les écarts types sont proches, 0.104 pour l'EC2 et 0.112 pour l'EC4. Le pourcentage de cas amenant à une insécurité notable est estimé par le nombre de cas pour lequel R est inférieur à 0.97. Il est de 41.84 % pour l'Eurocode 2, et 34.86 % pour l'Eurocode 4. Ces pourcentages importants montrent que les méthodes simplifiées des deux normes en vigueur en Europe ne sont pas applicables aux poteaux hybrides.

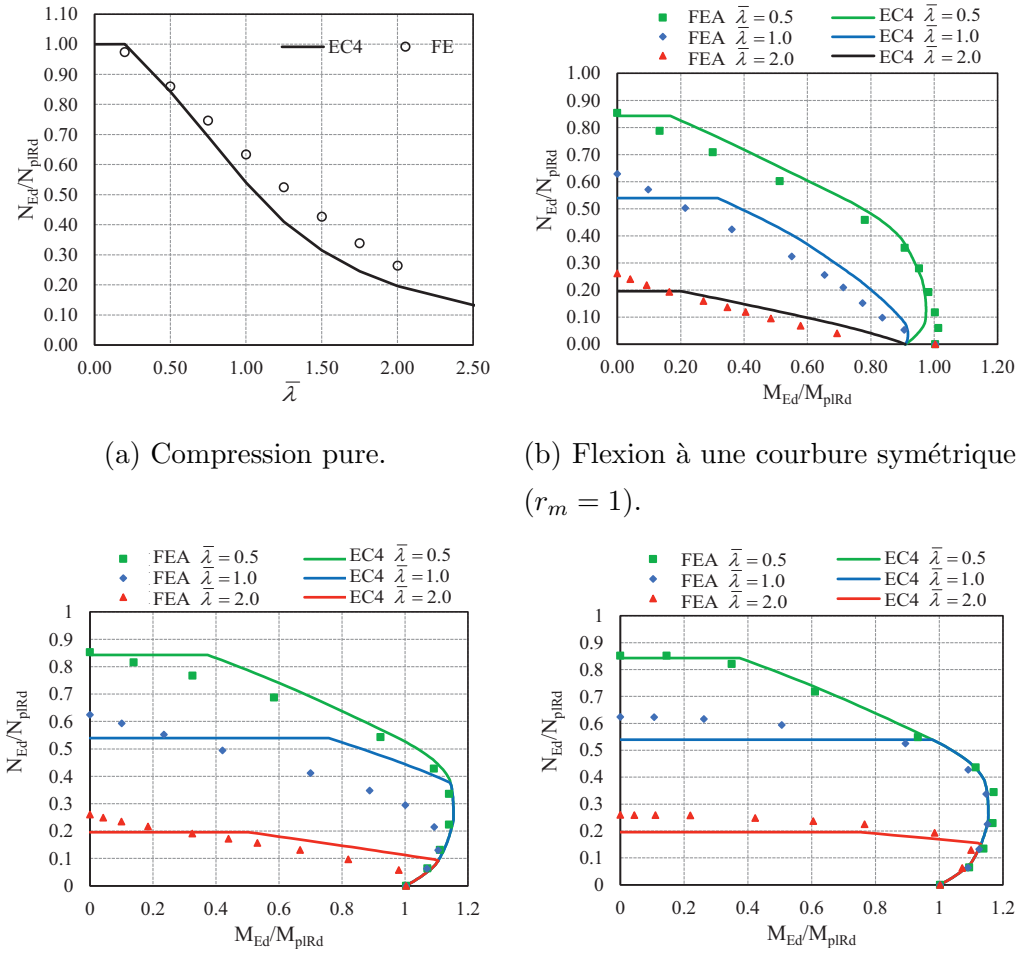

(a) Compression pure.

(b) Flexion à une courbure symétrique ($r_m = 1$).

(c) Flexion à une courbure ($r_m = 0$).

(d) Flexion à double courbure ($r_m = -1$).

Figure 8.12: Comparison of simplified method of EC4 against FE analysis results.

8.5.3 Proposition d'une nouvelle méthode simplifiée

8.5.3.1 Analyses complémentaires

Afin de déterminer comment définir la méthode simplifiée la plus adaptée, l'effet de différents paramètres a été étudié dans le détail. Le résultat le plus remarquant porte sur l'effet des contraintes résiduelles. Il apparait que celles-ci n'ont pas d'effet sur la charge ultime. Les profils étant excentrés par rapport au centre

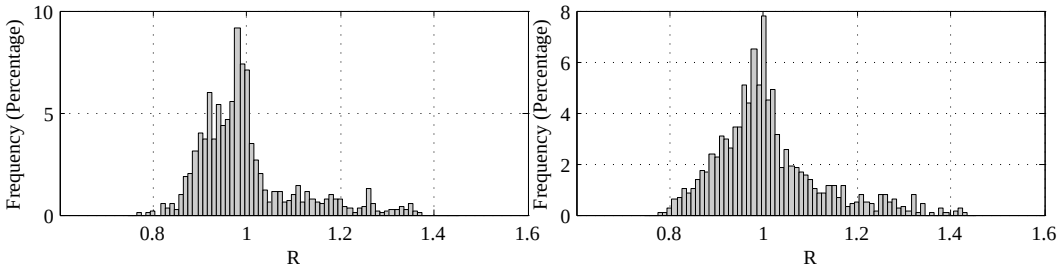

(a) Eurocode 2. (b) Eurocode 4

Figure 8.13: Histogrammes du ratio R pour les méthodes simplifiées de l'Eurocode 2 et 4.

de gravité de la section du béton, ils sont soumis à un effort normal important qui diminue l'effet des contraintes résiduelles, et l'on peut en conclure qu'ils se comportent plus comme des armatures, que comme des profilés fléchis. Par conséquent, il est plus pertinent de développer la nouvelle méthode simplifiée sur base de la méthode EC2, plutôt que de l'EC4, puisque l'EC4 intègre explicitement, au travers de la définition d'imperfections équivalentes, l'effet des contraintes résiduelles, alors qu'elles apparaissent négligeables pour les poteaux hybrides.

Ensuite, l'étude paramétrique générale a été portée à 2964 cas, en faisant varier la limite d'élasticité des profils. Des cas complémentaires ont été ajoutés avec des profils en S235 et S355. Il a été montré qu'une forte dépendance de l'état des profils à la ruine à l'élancement du poteau, au coefficient de fluage et au rapport des résistances du béton et de l'acier. En effet, le fluage conduit à une plastification partielle des profilés en augmentant la déformation du béton, et donc à une diminution de leur raideur. Cet effet est moins prononcé pour les forts élancements, pour lesquels les déformations, lorsque l'instabilité se déclenche, sont limitées, et donc dans ce cas le profil n'est pas plastifié.

8.5.3.2 Nouvelle méthode simplifiée

Partant des constatations précédentes, et en s'inspirant des travaux de Bonet et al. [130], une nouvelle méthode d'amplification des moments a été développée.

Le moment du second ordre, qui devra être comparé au moment résistant de la section compte tenu de l'effort normal appliqué Mpl,N,Rd, est obtenu en multipliant le moment du premier ordre par :

$$k = \frac{\beta}{1 - \frac{N_{Ed}}{N_{cr}}} \tag{8.65}$$

où $\beta = 0,6r_m + 0,4 \geq 0,4$; et N_{cr} est l'effort critique élastique calculé en utilisant l'expression de la rigidité en flexion efficace suivante :

$$EI = K_c E_{cd} I_c + K_s E_s I_s + K_a E_a I_a \tag{8.66}$$

avec

$$K_c = k_1 k_2 / (1 + \varphi_{ef}) \tag{8.67}$$

$$K_s = 1 \tag{8.68}$$

$$K_a = \frac{0.76 \left(\frac{f_y}{f_{ck}}\right)^{0.0124}}{1 + 105\varphi_{ef}\exp(-0.078\lambda)} \leqslant 1 \tag{8.69}$$

$$k_1 = \sqrt{\frac{f_{ck}}{20}} \tag{8.70}$$

$$k_2 = n\frac{\lambda}{170} \leqslant 0.2 \tag{8.71}$$

$$n = \frac{N_{Ed}}{N_{pl,Rd}} \tag{8.72}$$

8.5.3.3 Validation de la méthode simplifiée

L'histogramme du ratio R calculé pour la nouvelle méthode simplifiée est représenté sur Fig. 8.14. La moyenne de la distribution vaut 1,0022 avec son écart type 0,0459. Le fractile à 5% est obtenu pour $R = 0,93$. Afin d'être sécuritaire, les valeurs de ratio R devraient donc être pondérées par un coefficient de sécurité de 1,07.

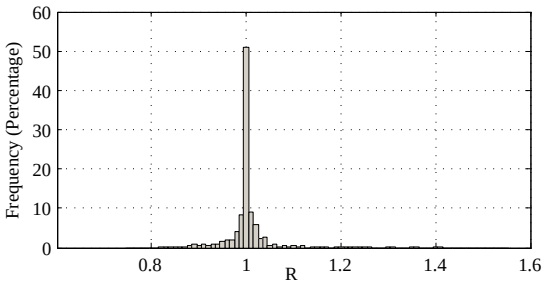

Figure 8.14: Histogramme de fréquence du ratio R pour la nouvelle méthode simplifiée.

8.6 Conclusion

Le développement d'outil de simulation numérique et de guide de dimensionnement pour les colonnes hybrides avec plusieurs profils en acier noyés dans le béton, soumises aux charges combinées a été l'objectif de cette thèse. Un modèle « élément fini » a été développé dans lequel la non-linéarité géométrique et matérielle ainsi que l'interaction partielle entre les profilés acier et le béton sont prises en compte. Les résultats du modèle élément fini ont été servis comme des références dans le développement d'une nouvelle méthode de dimensionnement pour les colonnes hybrides. La construction de ce modèle s'est faite graduellement en commençant par construire la matrice de raideur élastique exacte pour les poutres/poteaux hybrides. Ensuite ; l'approche co-rotationnelle nous a permis d'étudier ces même structures dans un contexte de grands déplacements. Enfin, une analyse fine nous a conduits à construire une stratégie numérique nous permettant de construire une loi de comportement élasto-plastique à partir des modèle 3D et surtout en prenant en compte l'influence des étriers. Tous ces outils ont été validés en comparant les prédictions du modèle aux résultats expérimentaux. Enfin, nous avons mené une étude numérique sur les effets de second ordre dans les colonnes hybrides élancés soumis à un chargement combiné de compression axiale et moment de flexion. Un des principaux objectifs de cette étude était de définir et valider une méthode de dimensionnement en instabilité applicable aux poteaux hybrides. Pour ce faire, le modèle « élément fini » développé dans

lequel la non-linéarité géométrique et matérielle, les imperfections géométriques, les contraintes résiduelles dans les profils d'acier ainsi que l'effet d'interaction partielle entre des profilés acier et le béton sont prises en compte a été utilisé à cette fin. En outre, le modèle mis au point avec la cinématique d'Euler-Bernoulli est compatible avec le modèle élément fini proposé dans les méthodes générales des Eurocodes (EC2 et EC4) pour le dimensionnement d'une colonne en béton armé et mixte. La comparaison entre les résultats obtenus avec des méthodes simplifiée de l'Eurocode (méthode d'amplification du moment) et avec l'analyse par éléments finis montre que la méthode simplifiée de l'EC2 et l'EC4 conduit à une grande dispersion où la moitié des cas sont insécuritaires. Cela signifie que les rigidités à la flexion en vigueur proposées par l'EC2 et l'EC4 ne sont pas appropriées pour le dimensionnement de la colonne hybride élancée. En conséquence, une nouvelle méthode simplifiée a été proposée dans le contexte des Eurocodes, à savoir l'approche d'amplification du moment. La méthode proposée est développée sur la base d'une étude approfondie sur le comportement physique de la colonne hybride. L'analyse des résultats ayant montré que les profils se comportent comme des armatures, et que les contraintes résiduelles ont un rôle négligeable - alors qu'elles sont un paramètre central de la méthode de l'Eurocode 4. Au vu de ces observations, la nouvelle méthode proposée est développée comme une extension de la méthode de l'Eurocode 2. La continuité par rapport à ce règlement est dès lors assurée ; il a par ailleurs été montré que la nouvelle méthode donne des résultats conservatifs, quoique moins précis que la méthode de l'EC4, pour les poteaux mixtes au sens de l'Eurocode 4. On peut donc affirmer que cette nouvelle méthode s'insère de façon cohérente dans la normalisation existante.

Bibliography

***

[1] D. Holmes, Trends in American High-rise Construction, Urbanophile LLC, 2013.

[2] G. Craighead, High-rise security and fire life safety, Butterworth-Heinemann, 2009.

[3] S. Morino, Recent developments in hybrid structures in Japan-research, design and construction, Engineering structures 20 (4) (1998) 336–346.

[4] C. W. Roeder, Overview of hybrid and composite systems for seismic design in the United States, Engineering structures 20 (4) (1998) 355–363.

[5] R. Wong, The construction of Super High-rise Composite Structures in Hong Kong, in: 2nd International Structural & Construction Conference, Rome, Italy, vol. 1, CRC Press, 107, 2003.

[6] R. F. Mast, M. Dawood, S. H. Rizkalla, P. Zia, Flexural strength design of concrete beams reinforced with high-strength steel bars, ACI Structural Journal 105 (5).

[7] Y. Zhou, X. Lu, Y. Dong, Seismic behaviour of composite shear walls with multi-embedded steel sections. Part I: experiment, The Structural Design of Tall and Special Buildings 19 (6) (2010) 618–636.

[8] D. Dan, A. Fabian, V. Stoian, Theoretical and experimental study on composite steel-concrete shear walls with vertical steel encased profiles, Journal of Constructional Steel Research 67 (5) (2011) 800 – 813.

[9] C. W. Roeder, R. Chmielowski, C. B. Brown, Shear connector requirements for embedded steel sections, Journal of Structural Engineering 125 (2) (1999) 142–151.

[10] J. A. Wium, J.-P. Lebet, Simplified calculation method for force transfer in composite columns, Journal of Structural Engineering 120 (3) (1994) 728–746.

[11] EN 1992-1-1, Eurocode 2: Design of Concrete Structures: Part 1-1: General Rules and Rules for Buildings, 2004.

[12] EN 1994-1-1, Eurocode 4: Design of composite steel and concrete structures: Part 1-1: General Rules and Rules for Buildings, 2004.

[13] P. Keo, H. Somja, Q.-H. Nguyen, M. Hjiaj, Simplified design method for slender hybrid columns, Journal of Constructional Steel Research 110 (2015) 101–120.

[14] N. M. Newmark, C. P. Siess, I. Viest, et al., Tests and analysis of composite beams with incomplete interaction, Proc. Soc. Exp. Stress Anal 9 (1) (1951) 75–92.

[15] U. Girhammar, V. Gopu, Composite Beam-Columns with Interlayer Slip-Exact Analysis, Journal of Structural Engineering 119 (4) (1993) 1265–1282.

[16] Y.-F. Wu, D. J. Oehlers, M. C. Griffith, Partial-interaction analysis of composite beam/column members, Mechanics of Structures and Machines 30 (3) (2002) 309–332.

[17] C. Faella, E. Martinelli, E. Nigro, Steel and concrete composite beams with flexible shear connection: exact analytical expression of the stiffness matrix

and applications, Computers & Structures 80 (11) (2002) 1001 – 1009, ISSN 0045-7949.

[18] G. Ranzi, M. Bradford, B. Uy, A direct stiffness analysis of a composite beam with partial interaction, International Journal for Numerical Methods in Engineering 61 (5) (2004) 657–672.

[19] U. A. Girhammar, D. H. Pan, Exact static analysis of partially composite beams and beam-columns, International Journal of Mechanical Sciences 49 (2) (2007) 239–255.

[20] R. Xu, Y. Wu, Static, dynamic, and buckling analysis of partial interaction composite members using Timoshenko's beam theory, International Journal of Mechanical Sciences 49 (10) (2007) 1139–1155.

[21] S. Schnabl, M. Saje, G. Turk, I. Planinc, Analytical solution of two-layer beam taking into account interlayer slip and shear deformation, Journal of structural engineering 133 (6) (2007) 886–894.

[22] Q.-H. Nguyen, E. Martinelli, M. Hjiaj, Derivation of the exact stiffness matrix for a two-layer Timoshenko beam element with partial interaction, Engineering Structures 33 (2) (2011) 298–307.

[23] R. Xu, G. Wang, Variational principle of partial-interaction composite beams using Timoshenko's beam theory, International Journal of Mechanical Sciences 60 (1) (2012) 72–83.

[24] M. R. Salari, E. Spacone, P. B. Shing, D. M. Frangopol, Nonlinear analysis of composite beams with deformable shear connectors, Journal of Structural Engineering 124 (10) (1998) 1148–1158.

[25] A. Ayoub, F. C. Filippou, Mixed formulation of nonlinear steel-concrete composite beam element, Journal of Structural Engineering 126 (3) (2000) 371–381.

[26] A. Dall'Asta, A. Zona, Non-linear analysis of composite beams by a displacement approach, Computers & structures 80 (27) (2002) 2217–2228.

[27] A. Dall'Asta, A. Zona, Slip locking in finite elements for composite beams with deformable shear connection, Finite Elements in Analysis and Design 40 (13) (2004) 1907–1930.

[28] A. Ayoub, A force-based model for composite steel–concrete beams with partial interaction, Journal of Constructional Steel Research 61 (3) (2005) 387–414.

[29] F. Gara, G. Ranzi, G. Leoni, Displacement-based formulations for composite beams with longitudinal slip and vertical uplift, International journal for numerical methods in engineering 65 (8) (2006) 1197–1220.

[30] G. Ranzi, A. Zona, A steel–concrete composite beam model with partial interaction including the shear deformability of the steel component, Engineering Structures 29 (11) (2007) 3026–3041.

[31] S. Schnabl, M. Saje, G. Turk, I. Planinc, Locking-free two-layer Timoshenko beam element with interlayer slip, Finite Elements in Analysis and Design 43 (9) (2007) 705–714.

[32] J.-M. Battini, Q.-H. Nguyen, M. Hjiaj, Non-linear finite element analysis of composite beams with interlayer slips, Computers & structures 87 (13) (2009) 904–912.

[33] A. Zona, G. Ranzi, Finite element models for nonlinear analysis of steel–concrete composite beams with partial interaction in combined bending and shear, Finite Elements in Analysis and Design 47 (2) (2011) 98–118.

[34] E. Martinelli, Q.-H. Nguyen, M. Hjiaj, Dimensionless formulation and comparative study of analytical models for composite beams in partial interaction, Journal of Constructional Steel Research 75 (2012) 21–31.

[35] M. Hjiaj, J.-M. Battini, Q.-H. Nguyen, Large displacement analysis of shear deformable composite beams with interlayer slips, International Journal of Non-Linear Mechanics 47 (8) (2012) 895–904.

[36] Y. H. Chui, D. W. Barclay, Analysis of three-layer beams with non-identical layers and semi-rigid connections, Canadian Journal of Civil Engineering 25 (2) (1998) 271–276.

[37] S. Schnabl, I. Planinc, M. Saje, B. Čas, G. Turk, An analytical model of layered continuous beams with partial interaction, Structural engineering and mechanics 22 (3) (2006) 263–278.

[38] J. B. M. Sousa, A. R. da Silva, Analytical and numerical analysis of multilayered beams with interlayer slip, Engineering Structures 32 (6) (2010) 1671–1680.

[39] L. Škec, S. Schnabl, I. Planinc, G. Jelenic, Analytical modelling of multilayer beams with compliant interfaces, Structural Engineering and Mechanics 44 (4) (2012) 465–485.

[40] G. Ranzi, Locking problems in the partial interaction analysis of multilayered composite beams, Engineering Structures 30 (10) (2008) 2900–2911.

[41] M. Heinisuo, An exact finite element technique for layered beams, Computers & Structures 30 (3) (1988) 615 – 622, ISSN 0045-7949.

[42] J. B. M. Sousa Jr, Exact finite elements for multilayered composite beam-columns with partial interaction, Computers & Structures 123 (2013) 48–57.

[43] Y.-L. Pi, M. A. Bradford, B. Uy, Second order nonlinear inelastic analysis of composite steel–concrete members. I: theory, Journal of structural engineering 132 (5) (2006) 751–761.

[44] G. Ranzi, A. Dall'Asta, L. Ragni, A. Zona, A geometric nonlinear model for composite beams with partial interaction, Engineering Structures 32 (5) (2010) 1384–1396.

[45] J. B. M. Sousa Jr, C. E. Oliveira, A. R. da Silva, Displacement-based non-linear finite element analysis of composite beam–columns with partial interaction, Journal of Constructional Steel Research 66 (6) (2010) 772–779.

[46] T. Hozjan, M. Saje, S. Srpcic, I. Planinc, Geometrically and materially non-linear analysis of planar composite structures with an interlayer slip, Computers & Structures 114–115 (0) (2013) 1–17.

[47] Q.-H. Nguyen, M. Hjiaj, V.-A. Lai, Force-based FE for large displacement inelastic analysis of two-layer Timoshenko beams with interlayer slips, Finite Elements in Analysis and Design 85 (2014) 1–10.

[48] M. A. Crisfield, Non-Linear Finite Element Analysis of Solids and Structures. Volume 1: Essentials, John Wiley & Sons, Inc., 1991.

[49] L. E. Malvern, Introduction to the Mechanics of a Continuous Medium, Monograph, Englewood Cliffs, N.J. : Prentice-Hall, 1969.

[50] F. Engesser, Die knickfestigkeit gerader stäbe, W. Ernst & Sohn, 1891.

[51] T. Wang, Non-linear bending of beams with uniformly distributed loads, International Journal of Non-Linear Mechanics 4 (4) (1969) 389–395.

[52] J. G. Ollgaard, R. G. Slutter, J. W. Fisher, Shear strength of stud connectors in lightweight and normal-weight concrete, AISC Engineering Journal 8 (2) (1971) 55–64.

[53] W. Ramberg, W. R. Osgood, Description of stress-strain curves by three parameters, Tech. Rep. 902, National Advisory Committee for Aeronautics; Washington, DC, United States, 1943.

[54] M. Menegotto, P. Pinto, Method of analyis for cyclically loaded reinforced concrete frames including changes in geometry and non-elastic behavior of elements under combined normal force and bending, in: Proceedings, IABSE Symposium on Resistance and Ultimate Deformability of Structures Acted on by Well Defined Repeated Loads, Preliminary Rep., Lisbon, Portugal, 15–22, 1973.

[55] J. F. Stanton, H. D. McNiven, The development of a mathematical model to predict the flexural response of reinforced concrete beams to cyclic loads, using system identification, Tech. Rep. UBC/EERC 79-02, Earthquake Engineering Research Center, University of California, Berkeley, 1979.

[56] F. C. Filippou, E. Popov, V. Bertero, Effects of bond deterioration on hysterectic behavior of reinforced concrete joints., vol. 83, Earthquake Engineering Research Center, University of California, Berkeley, 1983.

[57] Comité Euro-International du Béton, CEB-FIP model code 2010, first completed draft, Lausanne, Switzerland, 2010.

[58] EN 1993-1-1, Eurocode 3: Design of steel structures: Part 1-1: General Rules and Rules for Buildings, 2005.

[59] F. E. Richart, A. Brandtzaeg, R. L. Brown, A study of the failure of concrete under combined compressive stresses, Tech. Rep. v.26, n.12, University of Illinois at Urbana Champaign, College of Engineering. Engineering Experiment Station, 1928.

[60] G. Balmer, Shearing strength of concrete under high triaxial stress-Computation of Mohr's Envelope as a Curve, Tech. Rep., Structural Research Laboratory Report SP-23, Denver, CO, 1949.

[61] K. William, E. Warnke, Constitutive model for the triaxial behavior of concrete, International association for bridge and structural engineering proceedings 19 (1975) 1–30.

[62] N. S. Ottosen, Nonlinear finite element analysis of concrete structures, Tech. Rep., Risoe National Lab., Roskilde (Denmark), 1980.

[63] S. Hsieh, E. Ting, W. Chen, A plastic-fracture model for concrete, International Journal of Solids and Structures 18 (3) (1982) 181–197.

[64] E.-S. Chen, O. Buyukozturk, Constitutive model for concrete in cyclic compression, Journal of engineering mechanics 111 (6) (1985) 797–814.

[65] D. Han, W.-F. Chen, A nonuniform hardening plasticity model for concrete materials, Mechanics of materials 4 (3) (1985) 283–302.

[66] M. Ortiz, A constitutive theory for the inelastic behavior of concrete, Mechanics of materials 4 (1) (1985) 67–93.

[67] Y. Ohtani, W.-F. Chen, Multiple hardening plasticity for concrete materials, Journal of engineering mechanics 114 (11) (1988) 1890–1910.

[68] H.-T. Hu, W. C. Schnobrich, Constitutive modeling of concrete by using nonassociated plasticity, Journal of Materials in Civil Engineering 1 (4) (1989) 199–216.

[69] J. Lubliner, J. Oliver, S. Oller, E. Onate, A plastic-damage model for concrete, International Journal of solids and structures 25 (3) (1989) 299–326.

[70] Y. D. Murray, B. A. Lewis, Numerical Simulation of Damage in Concrete., Tech. Rep., DTIC Document, 1995.

[71] H. D. Kang, K. Willam, B. Shing, E. Spacone, Failure analysis of R/C columns using a triaxial concrete model, Computers & Structures 77 (5) (2000) 423–440.

[72] D. Pelessone, A modified formulation of the cap model, Tech. Rep., Gulf Atomics Report GA-C19579 to the Defense Nuclear Agency, 1989.

[73] K.-J. Bathe, M. D. Snyder, A. P. Cimento, W. D. Rolph, On some current procedures and difficulties in finite element analysis of elastic-plastic response, Computers & Structures 12 (4) (1980) 607–624.

[74] W.-F. Chen, Plasticity in reinforced concrete, J. Ross Publishing, 2007.

[75] B. Doran, H. O. Köksal, Z. Polat, C. Karakoç, The use of Drucker-Prager criterion in the analysis of reinforced concrete members by finite elements, Turkish Chamber of Civil Engineers 9 (2) (1998) 1616–1625.

[76] G. Arslan, Sensitivity study of the Drucker–Prager modeling parameters in the prediction of the nonlinear response of reinforced concrete structures, Materials & design 28 (10) (2007) 2596–2603.

[77] Y. D. Murray, Users manual for LS-DYNA concrete material model 159, Tech. Rep., National Technical Information Service, Springfield, VA 22161, 2007.

[78] J. C. Simo, T. J. Hughes, Computational inelasticity, vol. 7, Springer Science & Business Media, 2006.

[79] J. C. Simo, Numerical analysis and simulation of plasticity, Handbook of numerical analysis 6 (1998) 183–499.

[80] E. A. de Souza Neto, D. Peric, D. R. J. Owen, Computational methods for plasticity: theory and applications, John Wiley & Sons, 2011.

[81] S. Popovics, A numerical approach to the complete stress-strain curve of concrete, Cement and concrete research 3 (5) (1973) 583–599.

[82] E. Thorenfeldt, A. Tomaszewicz, J. Jensen, Mechanical properties of high-strength concrete and application in design, in: Proceedings of the Symposium on Utilization of High Strength Concrete, Tapir, Trondheim, Norway, 149–159, 1987.

[83] J. B. Mander, M. J. Priestley, R. Park, Theoretical stress-strain model for confined concrete, Journal of structural engineering 114 (8) (1988) 1804–1826.

[84] G. Schickert, H. Winkler, Results of test concerning strength and strain of concrete subjected to mulit-axial compressive stress, Tech. Rep. Heft 277, Deutsche Ausschuss Fur Stahlbeton, Berlin, West Germany, 1977.

[85] L. Bing, R. Park, H. Tanaka, Stress-strain behavior of high-strength concrete confined by ultra-high-and normal-strength transverse reinforcements, ACI Structural Journal 98 (3).

[86] L. Bing, R. Park, H. Tanaka, Constitutive behavior of high-strength concrete under dynamic loads, ACI Structural Journal 97 (4).

[87] D. C. Kent, R. Park, Flexural members with confined concrete, Journal of the Structural Division 97 (7) (1971) 1969–1990.

[88] B. Scott, R. Park, M. Priestley, Stress-strain behavior of concrete confined by overlapping hoops at low and high strain rates, in: ACI Journal Proceedings, vol. 79, ACI, 13–27, 1982.

[89] R. P. Johnson, Composite structures of steel and concrete: beams, slabs, columns, and frames for buildings, John Wiley & Sons, 2008.

[90] J. O. Bryson, R. G. Mathey, Surface Condition Effect on bond Strength of Steel Beams Embedded in Concrete, in: ACI Journal Proceedings, vol. 59, ACI, 397–406, 1962.

[91] N. Hawkins, Strength of concrete-encased steel beams, Institution of Engineers (Australia) Civ Eng Trans CE15 (1–2) (1973) 29–45.

[92] C. W. Roeder, Bond stress of embedded steel shapes in concrete, in: Composite and mixed construction, ASCE, 227–240, 1985.

[93] M. Hamdan, Y. Hunaiti, Factors affecting bond strength in composite columns, in: Proceedings of the 3rd International Conference on Steel-Concrete Composite Structures. Fukuoka, Japan, 213–218, 1991.

[94] H. Hotta, H. Kihara, K. Takiguchi, A fundamental study on shear bond strength of steel encased reinforced concrete members, Proceedings Fracture Mechanics of Concrete Structures. Freibung, Germany 2 (1998) 1321–1330.

[95] J. A. Wium, J.-P. Lebet, Simplified calculation method for force transfer in composite columns, Journal of Structural Engineering 120 (3) (1994) 728–746.

[96] W.-Y. Lam, R. K.-L. Su, H.-J. Pam, Experimental study on embedded steel plate composite coupling beams, Journal of structural engineering 131 (8) (2005) 1294–1302.

[97] ACI Committee and American Concrete Institute and International Organization for Standardization, Building Code Requirements for Structural Concrete (ACI 318-08) and Commentary, American Concrete Institute, 2008.

[98] AISC Committee on Specifications, Specifications for Structural Steel Buildings, American Institute of Steel Construction, 2010.

[99] C. W. Roeder, R. Chmielowski, C. B. Brown, Shear connector requirements for embedded steel sections, Journal of Structural Engineering 125 (2) (1999) 142–151.

[100] R. Johnson, Resistance of stud shear connectors to fatigue, Journal of Constructional Steel Research 56 (2) (2000) 101–116.

[101] I. M. Viest, Investigation of stud shear connectors for composite concrete-steel T-beams, Journal of the american concrete institute 27 (8) (1956) 875–891.

[102] G. Driscoll, R. Slutter, Research on composite design at Lehigh University, in: Proceedings of the National Engineering Conference, 18–24, 1961.

[103] J. Chinn, Pushout Tests on Lightweight Composite Slabs, AISC Engineering Journal 2 (4) (1965) 129–134.

[104] I. B. Valente, P. J. Cruz, Experimental analysis of shear connection between steel and lightweight concrete, Journal of Constructional Steel Research 65 (10) (2009) 1954–1963.

[105] C. Davies, Small-scale push-out tests on welded stud shear connectors, Concrete 1 (9) (1967) 311.

[106] R. Mainston, J. B. Menzies, Shear connectors in steel-concrete composite beams for bridges. I. Static and fatigue tests on push-out specimens, Concrete 1 (9) (1967) 291.

[107] N. M. Hawkins, D. Mitchell, Seismic response of composite shear connections, Journal of Structural Engineering 110 (9) (1984) 2120–2136.

[108] L. An, K. Cederwall, Push-out tests on studs in high strength and normal strength concrete, Journal of Constructional Steel Research 36 (1) (1996) 15–29.

[109] C. Topkaya, J. A. Yura, E. B. Williamson, Composite shear stud strength at early concrete ages, Journal of Structural Engineering 130 (6) (2004) 952–960.

[110] S. S. Badie, M. K. Tadros, H. F. Kakish, D. L. Splittgerber, M. C. Baishya, Large shear studs for composite action in steel bridge girders, Journal of Bridge Engineering 7 (3) (2002) 195–203.

[111] C.-S. Shim, P.-G. Lee, T.-Y. Yoon, Static behavior of large stud shear connectors, Engineering structures 26 (12) (2004) 1853–1860.

[112] P.-G. Lee, C.-S. Shim, S.-P. Chang, Static and fatigue behavior of large stud shear connectors for steel–concrete composite bridges, Journal of Constructional Steel Research 61 (9) (2005) 1270–1285.

[113] J. Aribert, A. Labib, Modèle de calcul élasto-plastique de poutres mixtes à connexion partielle, Constr Métallique 4.

[114] R. Johnson, N. Molenstra, et al., Partial shear connection in composite beams for buildings, in: ICE Proceedings, vol. 91, Thomas Telford, 679–704, 1991.

[115] N. Gattesco, E. Giuriani, Experimental study on stud shear connectors subjected to cyclic loading, Journal of Constructional Steel Research 38 (1) (1996) 1–21.

[116] M. R. Salari, Modeling of bond-slip in steel-concrete composite beams and reinforcing bars, Ph.D. thesis, University of Colorado, 1999.

[117] F. J. Vecchio, M. P. Collins, Predicting the response of reinforced concrete beams subjected to shear using the modified compression field theory, ACI Structural Journal 85 (3) (1988) 258–268.

[118] E. C. Bentz, F. J. Vecchio, M. P. Collins, Simplified modified compression field theory for calculating shear strength of reinforced concrete elements, ACI Structural Journal 103 (4) (2006) 614–624.

[119] G. Ranzo, M. Petrangeli, A fibre finite beam element with section shear modelling for seismic analysis of RC structures, Journal of Earthquake Engineering 2 (03) (1998) 443–473.

[120] M. Petrangeli, P. E. Pinto, V. Ciampi, Fiber element for cyclic bending and shear of RC structures. I: Theory, Journal of Engineering Mechanics 125 (9) (1999) 994–1001.

[121] J. Bairan, A. Mari, Multiaxial-coupled analysis of RC cross-sections subjected to combined forces, Engineering Structures 29 (8) (2007) 1722–1738.

[122] A. Saritas, F. C. Filippou, Numerical integration of a class of 3d plastic-damage concrete models and condensation of 3d stress–strain relations for use in beam finite elements, Engineering Structures 31 (10) (2009) 2327–2336.

[123] S. Guner, F. J. Vecchio, Pushover analysis of shear-critical frames: formulation, ACI Structural Journal 107 (01) (2010) 63–71.

[124] S. Mohr, J. M. Bairan, A. R. Mari, A frame element model for the analysis of reinforced concrete structures under shear and bending, Engineering Structures 32 (12) (2010) 3936–3954.

[125] T. Mullapudi, A. Ayoub, Analysis of reinforced concrete columns subjected to combined axial, flexure, shear, and torsional loads, Journal of Structural Engineering 139 (4) (2012) 561–573.

[126] J. Navarro-Gregori, P. Miguel, M. Fernandez, J. R. Marti-Vargas, A theoretical model for including the effect of monotonic shear loading in the analysis of reinforced concrete beams, Engineering Structures 52 (2013) 257–272.

[127] S. Klinkel, S. Govindjee, Using finite strain 3D-material models in beam and shell elements, Engineering Computations 19 (8) (2002) 902–921.

[128] SMARTCoCo, Task 6.1: Resistance to combined bending and shear of composite wall with three encased steel profiles. Experimental Program, Tech. Rep., LGCGM, INSA Rennes, France, 2014.

[129] J. Bonet, P. Miguel, M. Fernandez, M. Romero, Biaxial bending moment magnifier method, Engineering structures 26 (13) (2004) 2007–2019.

[130] J. Bonet, M. Romero, P. Miguel, Effective flexural stiffness of slender reinforced concrete columns under axial forces and biaxial bending, Engineering Structures 33 (3) (2011) 881–893.

[131] V. Mavichak, R. W. Furlong, Strength and stiffness of reinforced concrete columns under biaxial bending, Tech. Rep., Center for Highway Research, University of Texas at Austin, 1976.

[132] S. Mirza, Flexural stiffness of rectangular reinforced concrete columns, ACI Structural Journal 87 (4).

[133] T. K. Tikka, S. A. Mirza, Nonlinear EI equation for slender reinforced concrete columns, ACI structural journal 102 (6).

[134] T. K. Tikka, S. A. Mirza, Nonlinear equation for flexural stiffness of slender composite columns in major axis bending, Journal of structural engineering 132 (3) (2006) 387–399.

[135] T. K. Tikka, S. A. Mirza, Nonlinear EI equation for slender composite columns bending about the minor axis, Journal of structural engineering 132 (10) (2006) 1590–1602.

[136] T. K. Tikka, S. A. Mirza, Effective flexural stiffness of slender structural concrete columns, Canadian Journal of Civil Engineering 35 (4) (2008) 384–399.

[137] B. Westerberg, Slender column with uniaxial bending, International Federation for Structural Concrete (fib), Tech. Rep. 16, Design examples for 1996 FIP recommendations practical design of structural concrete, 2002.

[138] W. Austin, Strength and design of metal beam-columns, Journal of the Structural Division 87 (4) (1961) 1–32.

[139] J. Robinson, B. Fouré, A. Bourghli, Le flambement des poteaux en béton armé chargé avec des excentricités différentes à leurs extrémités, Tech. Rep., Institut Technique du Bâtiment et des Travaux Publics 1975; no. supplément au no. 333:74., 1975.

[140] N. S. Trahair, Design strengths of steel beam-columns, Tech. Rep., Structural Engineering Report No 132, Department of Civil Engineering, University of Alberta, 1985.

[141] L. Duan, I. S. Sohal, W.-F. Chen, On beam-column moment amplification factor., Engineering Journal 26 (4) (1989) 130–135.

[142] P. K. Sarker, B. V. Rangan, Reinforced concrete columns under unequal load eccentricities, ACI Structural Journal 100 (4).

[143] T. K. Tikka, S. A. Mirza, Equivalent uniform moment diagram factor for reinforced concrete columns, ACI Structural Journal 101 (4).

[144] T. Bogdan, H. Degée, A. Plumier, C. Campian, A simple computational tool for the verification of concrete walls reinforced by embedded steel profiles., in: 15th World Conference on Earthquake Engineering 2012 (15WCEE), Lisbon, Portugal, Sociedade Portuguesa de Engenharia Sismica (SPES), 16002–16011, 2012.

[145] R. Bergmann, G. Hanswille, New design method for composite columns including high strength steel, in: Composite Construction in Steel and Concrete V, ASCE, 381–389, 2006.

[146] EN 1990, Eurocode: Basic of structural design. Annex D: design by tests results, 2002.

[147] N. Boissonnade, R. Greiner, J.-P. Jaspart, J. Lindner, Rules for Member Stability in EN 1993-1-1: Background documentation and design guidelines, European Convention for Constructional Steelwork, Technical Committee 8-Stability, 2006.

[148] B. Westerberg, Second Order Effects in Slender Concrete Structures: Background to chapters 5.8, 5.9 and Annex H in EN 1992-1-1, Tech. Rep., Stockholm, Sweden: Brobyggnad (Bridge Structures), 2002.

[149] P. Keo, Q.-H. Nguyen, H. Somja, M. Hjiaj, Geometrical nonlinear analysis of hybrid beam-column with several encased steel profiles in partial interaction, Journal of Engineering Structures 100 (2015) 66–78.

[150] A. Al-Shahari, Y. Hunaiti, B. Ghazaleh, Behavior of lightweight aggregate concrete-encased composite columns., Steel & Composite Structures 3 (2) (2003) 97–110.

[151] S. Morino, C. Matsui, H. Watanabe, Strength of biaxially loaded SRC columns, in: Composite and mixed construction: proceedings of the U.S./Japan joint seminar, ASCE, 185–194, 1985.

[152] C. Chen, S. Yeh, Ultimate strength of concrete encased steel composite columns, in: Proceedings of the third national conference on structural engineering, 2197–206, 1996.

[153] S. Mirza, B. Skrabek, Reliability of short composite beam-column strength interaction, Journal of Structural Engineering 117 (8) (1991) 2320–2339.

[154] C.-C. Chen, N.-J. Lin, Analytical model for predicting axial capacity and behavior of concrete encased steel composite stub columns, Journal of Constructional Steel Research 62 (5) (2006) 424–433.

INSA de RENNES
Service des Formations

AVIS DU JURY SUR LA REPRODUCTION DE LA THESE SOUTENUE

Titre de la thèse:
Nonlinear analysis of steel-concrete hybrid members with application to stability design

Nom Prénom de l'auteur : KEO PISEY

Membres du jury :
- Monsieur COSTA NEVES Luis
- Monsieur MARTINELLI Enzo
- Monsieur LE GROGNEC Philippe
- Monsieur HJIAJ Mohammed
- Monsieur SOMJA Hugues
- Monsieur NGUYEN Quang Huy
- Monsieur LIMAM Ali
- Monsieur DENOËL Vincent

Président du jury : ALi LIMAM

Date de la soutenance : 27 Novembre 2015

Reproduction de la these soutenue

Thèse pouvant être reproduite en l'état
~~Thèse pouvant être reproduite après corrections suggérées~~

Fait à Rennes, le 27 Novembre 2015

Signature du président de jury
A- LIMAM

Le Directeur,

M'hamed DRISSI

Résumé

Le travail de cette thèse a pour but de développer des outils de simulation et une méthode de dimensionnement pour les poteaux hybrides soumis à des chargements combinés. La thèse est composée de 4 parties essentielles et comprend 6 chapitres. Dans la première partie, nous développons un élément fini poutre/poteau hybride élastique en interaction partielle avec matrice de raideur exacte. Cet élément fini découle de la solution analytique du système d'équations différentielles couplées obtenues en combinant les équations de champs (équilibre, cinématique et comportement). Les inconnues fondamentales sont les glissements aux interfaces et la déformation de cisaillement de l'élément principal. Ces équations sont résolues pour des conditions de chargement et des conditions aux limites arbitraires en accordant un soin particulier à la détermination des constantes d'intégration. Dans la seconde partie de cette thèse, nous proposons une formulation d'élément fini originale pour l'analyse en grand déplacement des poutres hybrides avec prise en compte des glissements qui se produisent à chaque interface acier-béton. La méthode de co-rotationnelle est retenue. Dans cette approche, le mouvement de l'élément se décompose en un mouvement de corps rigide et en une partie déformable définie dans un repère co-rotationnel local qui se déplace de manière continue avec l'élément mais qui ne se déforme pas avec ce dernier. Un choix judicieux des variables cinématiques locales accompagné des matrices de transformation correspondantes permet de transposer l'élément linéaire développé en partie 1 en un élément géométriquement non-linéaire performant. La partie 3 est consacrée à l'analyse non linéaire matérielle par élément finis de poutres hybrides en interaction partielle et soumise aux forces combinées de flexion et de cisaillement. Dans la formulation élément fini proposée, nous adoptons la discrétisation par fibres et une modèle 3D de comportement du béton avec prise en compte des états plans ce qui permet de reproduire rigoureusement l'effet du confinement et l'action des étriers. En partie 4, nous évaluons la pertinence de la méthode d'amplification des moments proposées dans l'Eurocode 2 et 4 à évaluer la charge ultime de poteaux hybrides soumis à une combinaison de charge axiale et de moment de flexion uni-axial. Dans un premier temps, nous conduisons une étude paramétrique sur 1140 cas différents de poteaux hybrides; étude destinés à couvrir les différentes typologies possibles, afin de disposer d'une base de résultats permettant d'évaluer la pertinence des méthodes simplifiées de l'Eurocode 2 et de l'Eurocode 4 pour de tels éléments. Cette étude a été réalisée à l'aide d'un élément fini non-linéaire (géométrique et matériel), avec une hypothèse de Bernouilli pour tous les composants du poteau hybride. Il ressort de cette étude que ces méthodes simplifiées ne peuvent être appliquées aux poteaux hybrides. Sur base de l'analyse d'un nombre de cas plus important (2960 configurations), la méthode d'amplification des moments est calibrée pour les poteaux hybrides.

Abstract

This thesis aims at developing simulation tools and a design method for hybrid beam-columns subjected to combined axial force, bending and shear. The thesis is divided in four main parts and comprises 6 chapters. In the first part, we develop a new finite element formulation based on the exact stiffness matrix for the linear elastic analysis of hybrid beam-columns in partial interaction taking into account the shear deformability of the encasing component. This element relies on the analytical solution of a set of coupled system of differential equations in which the primary variables are the slips and the shear deformation of the encasing beam. The latter is derived by combining the governing equations (equilibrium, kinematics, constitutive laws) and solved for a specific element with arbitrary boundary conditions and loading. Special care has been taken while dealing with the constants of integration. The second part of the thesis addresses a new finite element formulation for a large displacement analysis of elastic hybrid beam-columns taking into account the slips that occur at each steel-concrete interface. The co-rotational method is adopted in which the movement of the element is divided into a rigid body motion and a deformable portion in the local co-rotational frame which moves and rotates continuously with the element but does not deform with it. Appropriate selection of local kinematic variables along with corresponding transformation matrices allows transforming the linear finite element developed in Part 1 into a nonlinear one resulting in an efficient locking-free formulation. In Part 3, we derive a finite element formulation for materially nonlinear analysis of hybrid beam-columns with shear deformable encasing component, in partial interaction and subjected to the combined shear and bending. The fiber model is adopted with condensation of the 3D stress-strain relations which allow to account for confinement in a rigorous manner as well as the effect of the stirrups. Part 4 examines the adequacy of the moment magnification method given in Eurocode 2 and 4 to provide an accurate estimation of the ultimate load of hybrid columns subjected to a combination of axial load and uniaxial bending moment. The developed finite element model with a shear rigid encasing component is used to conduct a parametric study comprising 1140 cases to cover the various possible situations. The predictions of the model are compared against the values given by the simplified methods of Eurocode 2 and Eurocode 4. It is shown that these simplified methods does not give satisfactorily results. Based on the analysis of larger number of cases (2960 configurations), the moment magnification method has been calibrated for hybrid columns.

N° d'ordre : 15ISAR 30 / D15 - 30

Institut National des Sciences Appliquées de Rennes
20, Avenue des Buttes de Coëmes • CS 70839 • F-35708 Rennes Cedex
Tel : 02 23 23 82 00 - Fax : 02 23 23 83 96